Imperial College London
Department of Mechanical Engineering

The evolution of particulates across the sooting limit in turbulent premixed opposed jet flames

Hamed Shariatmadar

December 2020

Supervised by Professor R. P. Lindstedt

Submitted in part fulfilment of the requirements for the degree of
Doctor of Philosophy in Mechanical Engineering of Imperial College London
and the Diploma of Imperial College London

TO MY PARENTS!

Declaration of Originality

I hereby certify that the present thesis is in full the work of the author, with the work of others appropriately acknowledged.

Copyright Declaration

Acknowledgements

First and foremost, I would like to express my most sincere gratitude to Prof. R. P. Lindstedt for his supervision. He gave me the freedom to explore ideas and conduct research independently, but provided countless and enlightening guidance when needed. His guidance, support and encouragement made the completion of such complex project possible. Special thanks to Professor P. Aleiferis for the loan of SMPS to measure particle size distribution. I could present PSD results in the thesis as the data set completion to emission measurements.

I wish to thank Dr. Fabian Hampp for his help, advice and comments on the fundamentals of laser diagnostics. His comments facilitated the processes in the laser–based diagnostic experiments for the fuel–rich combustion. Special thanks also to E. Benbow, M. Holloway, K. Palmer, A. Munasinghe, J. Easton, E. Bekiri, T. Williams, A. M. Choda, K. Lewis and S. Dalrymple for their help and support on all fronts. I feel privileged to have known all of the wonderful people during my PhD. I would like to thank Dr. M. Schiener, Dr. L. Tian, Dr. P. Simatos, Ms. A. Tsopelakou for the great atmosphere in 208 and 674.

I also gratefully acknowledge the financial support of President scholarship scheme.

Publications

The work reported in the current thesis includes material from the following publications and presentations.

- H. Shariatmadar, F. Hampp, R.P. Lindstedt, Quantification of PAH concentrations in premixed turbulent flames crossing the soot inception limit, In press, Proc. Comb. Inst. 38 (2020).
- F. Hampp, H. Shariatmadar, R.P. Lindstedt, Quantification of low Damköhler number turbulent premixed flames, Proc. Combust. Inst. 37 (2019) 1047–1054.
- H. Shariatmadar, F. Hampp, R.P. Lindstedt, The evolution of incipient particle compositions across the sooting limit in turbulent premixed opposed jet flames, Submitted to Combust. Flame.
- H. Shariatmadar, R.P. Lindstedt, P. Aleiferis, Particle size distributions across the sooting limit in turbulent premixed opposed jet flames, In preparation.
- H. Shariatmadar, F. Hampp, R.P. Lindstedt, Quantification of the evolution of mean gaseous species concentrations across the sooting limit in turbulent premixed opposed jet flames, European Combustion Meeting Lisboa Portugal April 14–17, 2019.
- F. Hampp, H. Shariatmadar, R.P. Lindstedt, Low temperature chemistry in low Damköhler number, European Combustion Meeting Dubrovnik Croatia April 18–21, 2017.

Abstract

Soot formation in combustors is a complex process comprising highly intermittent interactions between physical and chemical processes across a wide range of time-scales. The influence of turbulence on the molecular pathways initiating particulate formation remains unquantified. Controlling soot emissions to the atmosphere will require overcoming large gaps in the understanding of soot formation/oxidation especially in turbulent combustion. The complexities of soot formation in turbulent flames suggests that the use of a flexible compact burner configuration with well–defined boundary conditions and precise control of flow characteristics is of significant advantage. The novel back–to–burnt opposed jet configuration features fractal grid generated turbulence and provides accurate control of flow parameters. The study includes the analyses of the overall flame structure of turbulent premixed ethylene/air flames, the relative concentrations of PAHs associated with soot inception and particle size distributions. The experiments covered a series of sooting flame conditions with variations in the equivalence ratio ($1.7 \leq \phi_{UN} \leq 2.2$), the total rate of strain ($255 \leq \mathrm{a}_T$ [s^{-1}] ≤ 610) and burnt gas temperature ($1400 \leq \mathrm{T}_{LN}$ [K] ≤ 1700). The conditions traverse the soot inception limit, e.g. the transition from lightly to heavily sooting flames, with non-intrusive ELS and PAH–PLIF combined probe sampling to quantify gaseous and PAH species using GC–TCD and GC–MS, respectively. The probe sampling features comprehensive sampling steps used to provide accurate concentrations of major gaseous, PAH species and particles with minimum losses. It is shown that the rate of strain exerts a substantial influence on both PAH concentrations and soot formation. Hence, it is likely that soot formation in turbulent flames becomes dominated by contributions from low strain regions. It is also found that the stoichiometry of the mixture controls the concentrations of PAHs associated with soot inception. The results obtained clearly show that benzo(a)pyrene is prevalent in flame structures and that relatively large amounts are condensed onto soot particles. A transition between bimodal and unimodal shapes of the particle size distributions shows strong competitions between oxidation, aggregation and surface growth processes in the turbulent flames.

Nomenclature

Abbreviation

AFM	Atomic force microscopy
AMDIS	Automated mass spectral deconvolution and identification system
BC	Boundary conditions
BCP	Burnt combustion products
BS	Beam splitter
BTB	Back–to–burnt
CARS	Coherent anti–stokes Raman spectroscopy
CFG	Cross fractal grid
CI	Chemical ionisation
CPC	Condensation particle counter
Da	Damköhler number
DG	Diluting gas
DMA	Differential mobility analyzer
DNS	Direct numerical simulation
DR	Dilution ratio
EDX	Energy dispersive X–ray
EI	Electron ionization
ELS	Elastic light scattering
EPA	Environmental protection agency
FBA	Flash back arrestor

FID	Flame ionization detector
FSM	Flame stabilising mesh
FTIR	Fourier transform infrared spectroscopy
GC	Gas chromatography
HACA	Hydrogen–abstraction–acetylene–addition
HCP	Hot combustion products
HIM	Helium–ion microscopy
IRO	Intensifier relay optics
ISF	International sooting flame (workshop)
JPDF	Joint transported probability density
Ka	Karlovitz number
LAS	Laser absorption spectroscopy
LB	Laser beam
LDV	Laser doppler velocimetry
LES	Large eddy simulation
LFC	Laminar flame calculation
LIF	Laser-induced fluorescence
LII	Laser-induced incandescence
LN	Lower nozzle
LS	Light sheet
MBMS	Molecular beam mass spectrometry
MFC	Mass flow controller
MS	Mass spectrometry
Nd:YAG	Neodymium-doped yttrium aluminium garnet
NEXAFS	Near–edge X-ray absorption fine structure
NIST	National institute of standards and technology
NOC	Nanoparticles or nano–organic carbon
OH-PLIF	Hydroxyl planar laser-induced fluorescence

p	Probe tip
PAH	Polycyclic aromatic hydrocarbons
PDF	Probability density function
PID	Proportional integral derivative
PIV	Particle image velocimetry
PM	Particulate matter
PP	Perforated platey
PSD	Particle size distribution
RSR	Resonance–stabilized radical
S	Sample
SANS	Small–angle neutron scattering
SAXS	Small–angle X-ray scattering
SEC	Size exclusion chromatography
SEM	Scanning electron microscope
SFC	Scientific committee for Food
SLM	Standard litre per minute
SMPS	Scanning mobility particle sizer
SP	Stagnation plane
STP	Standard temperature and pressure
SVF	Soot volume fraction
SVUV–PIMS	Synchrotron VUV photoionization mass spectroscopy
TCD	Thermal conductivity detector
TDLAS	Tunable diode laser absorption spectroscopy
TEM	Transmission electron microscope
TGA	Thermal gravimetric analysis
TOF	Time-of-flight
UN	Upper nozzle
UV	Ultraviolet

VUV–AMS	Ultraviolet aerosol mass spectrometer
WAXS	Wide-angle X-ray scattering
WHO	World Health Organisation
XPS	X–ray photoelectron spectroscopy

Latin symbol, upper case

$\dot{m}$	Mass flow rate [kg. s^{-1}]
$\dot{V}$	Volumetric flow rate [m^{3}. s^{-1}]
A	Einstein coefficients (spontaneous emission) [–]
B	Einstein coefficients (absorption) [–]
C	Cunningham slip correction [–]
d_i	Particle size [nm]
D_{kelvin}	Kelvin diameter [m]
D_p	Particle diameter [nm]
E	Electrical field strength [V. m^{-1}]
$f_{\nu,J}(T)$	Normalized Boltzmann fraction in the ground level [–]
g	Geometric factor [m^{2} . kg^{-1}]
I	Experimental signal intensities [–]
I_{laser}	Incident laser beam intensity [kg. m^{2}. s^{-2}]
L_I	Integral length scale of turbulence [m]
M	Molecular weight [kg/kmol]
N	Particle density number [m^{-3}]
N_0	Loschmidt number [m^{-3}]
n_i	Local number density [m^{-3}]
$q(T)$	Normalized collisional quenching rate at specific temperature [–]
Q_p	Aerosol flow rate [m^{3}. s^{-1}]
Q_{sh}	Sheath flow rate [m^{3}. s^{-1}]
R	Gas constant [J. mol^{-1}. K^{-1}]
S	Supersaturation ratio [–]

T	Temperature [K]
T_0	Initial temperature [K]
T_0	The temperature of the diluent [K]
T_{HCP}	Hot combustion product temperature [K]
T_{LN}	Lower nozzle temperature [K]
t_p	Purging time [s]
t_R	Residence time [s]
T_s	Sampling temperature [K]
t_s	Scan time [s]
T_{UN}	Upper nozzle temperature [K]
U	Flow velocity [m. s^{-1}]
V	Velocity [m. s^{-1}]
D	Nozzle diameter [m]
H	Nozzle separation [m]
I^{ν}	Laser irradiance [kg. s^3]
P	Pressure [kg. m^{-1}. s^2]
Re	Reynolds number [–]
Re_t	Turbulent Reynolds number [–]
RT	Retention time [s]
X	Axial coordinate [m]
X_i	Mole fraction [–]
Y	Radial coordinate [m]
Z	Perpendicular to X and Y coordinates [m]

Latin symbol, lower case

c	Reaction progress variable [–]
l	Depth of the measurement volume [m]
a	Rate of strain [s^{-1}]
a_b	Bulk rate of strain [s^{-1}]

a_T	Total rate of strain [s^{-1}]
a_t	Turbulent rate of strain [s^{-1}]
f_c	Carbon based mixture fraction [–]
m	Mass [kg]
n_{c_F}	The number of carbon atoms in the fuel [–]
n_{c_k}	The number of carbon atoms in species k [–]
n_i	Refraction index [–]

Greek letters

α	Probe tip angle [rad]
ΔP	Differential pressure [kg. m^{-1}. s^{2}]
δ_s	Surface tension [kg. m^{-1}. s^{-2}]
λ	Wavelength [nm]
μ	Dynamic viscosity [kg. m^{-1}. s^{-1}]
ν	Reactants kinematic viscosity [m^{2}. s^{-1}]
Ω	Collection solid angle [sr]
ϕ	Equivalence ratio [–]
ρ	Density [kg.m^{-3}]
σ_R	Rayleigh cross sections [m^{2}. sr^{-1}]
τ_I	Integral timescale of turbulence [s]
ε_r	Rate of dissipation within the reactants [m^{2}. s^{-3}]
ε_{sys}	Optical transmission efficiency [–]

Subscripts

0	Alignment at the origin
b	Bulk flow motion
HCP	Hot combustion products
I	Turbulent
LN	Lower nozzle
REF	Reference value

UN	Upper nozzle

Chemical species

1–$C_{11}H_{10}$	1–Methylnaphthalene (1–MN)
2–$C_{11}H_{10}$	2–Methylnaphthalene (2–MN)
$C_{10}H_8$	Naphthalene (A2)
$C_{11}H_{16}$	Pentamethylbenzene
$C_{12}H_{10}$	Acenaphthene
$C_{12}H_8$	Acenaphthylene
$C_{13}H_{10}$	Fluorene
C_2H_2	Acetylene
C_2H_4	Ethylene
C_3H_6	Propene
C_3H_8	Propane
$C_6H_4Cl_2$	1,4–Dichlorobenzene
C_6H_6	Benzene
C_7H_8	Toulene
CH_2O	Formaldehyde
CH_2	Methylene
CH_4	Methane
CO_2	Carbon dioxide
CO	Carbon monoxide
H_2	Hydrogen
O_2	Oxygen
a–$C_{14}H_{10}$	Anthracene
b–$C_{10}H_{14}$	Butylbenzene
b–$C_{18}H_{12}$	Benz(a)anthracene
bap–$C_{20}H_{12}$	Benzo(a)pyrene (B(a)P)
bb–$C_{20}H_{12}$	Benzo(b)fluoranthene

bj–$C_{20}H_{12}$	Benzo(j)fluoranthene
bk–$C_{20}H_{12}$	Benzo(k)fluoranthene
c–$C_{18}H_{12}$	Chrysene
d–$C_{10}H_{14}$	Diethylbenzene
e–C_8H_{10}	Ethylbenzene
f–$C_{16}H_{10}$	Fluoranthene
i–C_9H_{10}	Indane
p–$C_{14}H_{10}$	Phenanthrene
p–$C_{16}H_{10}$	Pyrene (A4)
p–$C_{20}H_{12}$	Perylene
p–C_9H_{12}	Propylbenzene
t–C_9H_{10}	Tetramethylbenzene
t–C_9H_{12}	Trimethylbenzene
x–C_8H_{10}	Xylene

Contents

List of Tables

List of Figures

Chapter 1

Overview

1.1 Background

The contribution of fossil fuels to world energy consumption is currently inevitable as it constitutes 85% of global annual energy demands [1]. Based on a report provided by US Department of Energy, the consumption of fossil fuels has doubled in the recent decade as more natural gas (fossil fuel) is used despite a trivial decrease in the percentage of coal consumption [2].

Renewable energy has also been in the centre of attention in the recent decade [3]. Although some industries invest in renewable energy for the sake of a clean environment, there are some significant uncertainties with renewable energy being considered as a complete replacement for fossil fuels. For instance, the raw materials of solar cells are made from quartz and coal with high purity. The materials need to be melted in furnaces, leading to the release of excessive carbon dioxide into the atmosphere [4]. Some solar facilities also need to burn natural gas for their operation depending on weather conditions [5]. Another main problem with renewable energy relates to storage issues. For instance, the global battery capacity (51 GIGA BTU) is much less than 1% of international annual energy use (546,000,000 GIGA BTU) [6].

There is still a long path to the establishment of new energy sources capable of replacing with fossil fuels. According to the U.S. Department of Energy projection, fossil fuels will still dominate as the energy source for at least 50 years [7]. The development of advanced combustion technologies that are highly efficient and produce low emissions is an increasingly crucial international priority. The advanced technologies can present broad implications for political stability, economic and environmental sustainability [8]. The major gaseous species, e.g. H_2O, CO and CO_2 also need to be considered. The rise in the release of CO_2 concentration leads to an increase in global temperature [9]. The Paris Agreement lays out national quotas on CO_2 emissions to control global temperature rise [10]. Carbon capture, carbon storage and reforestation are few possible proposed solutions to mitigate CO_2 emission [11]. The net–zero targets, adopted by the United Kingdom and France, contains a balance between the emissions level of generated greenhouse gas and that of removed from the atmosphere.

The products of incomplete combustion can be mainly categorised into major gaseous species, PAH (polycyclic aromatic hydrocarbons) and soot particulates. Such harmful products can stem from the fuel–rich combustion in practical combustors such as industrial furnaces, automotive, aircraft and diesel engines. For instance, particles from diesel exhaust include significant quantities of the Group 1 carcinogen benzo(a)pyrene (B(a)P) [12].

PAHs can exist as volatile, semi–volatile and particulate pollutants. Table 1.1 lists the PAH regulated by EPA, EU and SFC legislations, including the potential interferences [13–15]. The particle–bound air concentration of the human carcinogen PAH species, especially (B(a)P) a group 1 carcinogen, is subject to existing legislation. PAHs are capable of efficiently bounding to and be transported with atmospheric particles. The PAH infusion on the particle surface may undergo chemical changes in the atmosphere, leading to more toxic species such as oxygenated and nitrated PAHs [16]. Shirvastava et al. [17] demonstrate the potential shield of B(a)P from oxidation of the coating of viscous organic aerosol, which leads to stronger long–range transport, greater deposition fluxes, and substantially elevated lung cancer risk.

Polycyclic aromatic hydrocarbons (PAHs) are presumed to be the intermediates leading to soot formation [18]. Several possible factors are impacting their toxicity, causing severe environmental and human health effects [12, 19]. The factors include size, number, mass, morphology, surface area, surface charge, and chemical composition [20]. The operational losses are evident in combustion devices as a result of soot formation. For instance, the corrosion of turbine blades can stem from excessive quantities of soot [21]. Some practical combustors, e.g. some aircraft engines, are also recognized as being significant sources of ultrafine particles. Ultrafine particles associate with cardiovascular problems. Such particle sizes can readily translocate from the pulmonary system into the circulation [22]. There have been some regulations to limit the number and mass emission of generated particle sizes into the atmosphere for particles smaller than 10 μm (PM_{10}) and 2.5 μm ($PM_{2.5}$) [23]. The environmental protection agency (EPA) outlines a new standard regulation to envision the reduction in premature deaths as effects of soot generated form diesel vehicles and coal–fired power plants [24]. The air pollution standard can mitigate the negative impacts on human health, environment and the operational of practical combustors. Table 1.2 lists the standard concentration limit for pollutants ($PM_{2.5}$, PM_{10} and PAHs) present in the air proposed by European Union (EU) and World Health Organisation (WHO).

1.2 The objectives of work

Emissions of PAHs and soot particles are subject to stringent regulations and, therefore, quantitative data on concentrations and size distributions are of significance. Controlling carcinogenic emissions requires an understanding of critical steps in the growth mechanism from the transition of stable intermediate species to the formation of particulates [25]. The complexity of the soot formation process and its strong interactions with gas–phase chemistry and turbulence are of particular concern to turbulent flames

Table 1.1. PAH lists according to US Environmental Protection Agency (EPA), European Union (EU) and EU Scientific Committee for Food (SFC). The group shows the PAH carcinogenic levels. (Group 1): carcinogenic to humans; (Group 2A): probably carcinogenic to humans; (Group 2B): possibly carcinogenic to humans; (Group 3): not classifiable as to its carcinogenicity to humans.

Compound	MW	CAS	EPA	EU	SFC	Group
Naphthalene	128	91–20-3	×			
Acenaphthylene	152	208–96-8	×			
Acenaphthene	154	83–32-9	×			
Fluorene	166	88–73-7	×			Group 3
Phenanthrene	178	85–01-8	×			Group 3
Anthracene	178	120–12-7	×			Group 3
Fluoranthene	202	206–44-0	×			Group 3
Pyrene	202	129–00-0	×			Group 3
7H–Benzo(c)fluorene	216	205–12-9		×		Group 3
Benz(a)anthracene	228	56–55-3	×	×	×	Group 2B
Cyclopenta(c,d)pyrene	226	27208–37-3		×	×	Group 2A
Chrysene	228	218–01-9	×	×	×	Group 2B
5–methylchrysene	242	3697–24-3		×	×	Group 2B
Benzo(b)fluoranthene	252	205–99-2	×	×	×	Group 2B
Benzo(k)fluoranthene	252	207–08-9	×	×	×	Group 2B
Benzo(j)fluoranthene	252	205–82-3		×	×	
Benzo(a)pyrene	252	50–32-8	×	×	×	Group 1
Indeno(1,2,3–c,d)pyrene	276	193–39-5	×	×	×	Group 2B
Dibenzo(a,h)anthracene	278	53–70-3	×	×	×	Group 2A
Benzo(g,h,i)perylene	276	191–24-2	×	×	×	Group 3
Dibenzo(a,l)pyrene	302	191–30-0		×	×	Group 2A
Dibenzo(a,e)pyrene	302	191–65-4		×	×	
Dibenzo(a,i)pyrene	302	189–55-9		×	×	Group 2B
Dibenzo(a,h)pyrene	302	189–64-0		×	×	Group 2B

Table 1.2. The standard mean concentration limit for a number of pollutants ($PM_{2.5}$, PM_{10} and PAHs), where 1 and 2 stand for the regulation proposed by European Union and World Health Organisation (WHO). The limit concentration for B(a)P is provided for comparison.

Pollutant	Averaging period	Concentration^1	Concentration^2
$PM_{2.5}$	Annually (Daily)	25 (–) [μg/m^3]	10 (25) [μg/m^3]
PM_{10}	Annually (Daily)	50 (40) [μg/m^3]	20 (50) [μg/m^3]
B(a)P	Annually	1 [ng/m^3]	–

as found in practical applications [26, 27].

Despite extensive experimental and numerical studies of turbulent sooting flames, significant gaps in understanding remain. The challenges associated with experimental studies of turbulence-chemistry interactions are numerous, requiring careful selection of configurations and conditions. The challenges include the complex processes responsible for the chemical and physical evolution, the lack of laser–diagnostic techniques and sampling probe difficulties. As highlighted during the discussions in International Sooting Flame Workshop (ISF), experiments in turbulent flames are still highly desirable in burner configurations that feature well–defined boundary condition that are compatible with numerical calculations and that can be accurately implemented with reduced uncertainties and errors.

The current study presents a novel experimental process used to characterise soot formation/oxidation in premixed turbulent flames. A novel back–to–burnt opposed jet configuration [28–30] is here used to study turbulent ethylene–air flames that move from (effectively) lightly to heavily sooting conditions. The back-to-burnt opposed jet configuration can provide accurate control of the turbulent and chemical timescale of the flow from the soot inception limit to heavily sooting flames. Fractal grids are used to generate multi-scale turbulence directly. Simultaneous CH_2O/PAH–PLIF and Elastic Light Scattering (ELS) are used to identify the soot and PAH layers that are subsequently probed using GC–TCD/MS with the samples further analysed using Energy Dispersive X–ray spectroscopy (EDX) and Scanning Electron Microscopy (SEM). The particle size distribution is also measured using a scanning mobility particle sizer

(SMPS). The probe sampling features comprehensive sampling steps used to provide accurate measurements of PAH concentrations and PSDs with minimum particle losses in the extraction line. The current study provides quantitative information in relation to concentrations changes in gaseous and PAH species as well as particles as a function of (i) the total rate of strain, (ii) the reactant stoichiometry, and (iii) the counterflow hot combustion temperature. With the extensive data acquired and the detailed analysis performed, our understanding of trace gas species and particle emissions is advanced in premixed turbulent flames. The data are also of significance for the characterisation of probe designs, operational procedures and for the evaluation of experimental uncertainties in turbulent flames.

1.3 Structure of the thesis

The thesis consists of eight chapters. Chapter 2 contains information on the current state of knowledge in the field and information necessary to understand the results presented in the rest of the thesis. The fundamental concepts are discussed to provide insights on soot formation process for under both laminar and turbulent conditions. The experimental techniques are also categorised into laser diagnostics and probe measurements to present the basic backgrounds on the analyses of soot formation.

Chapter 3 outlines the experimental configurations, setups and conditions. The flame conditions are chosen to cover different sooting structures. The opposed jet configuration significantly facilitates the accurate control on the flow boundary conditions. The measurement techniques used in the current study include both laser diagnostics and probe sampling. In addition, probe effects, assessed using laser diagnostics, are presented in this chapter. The complementary measurement techniques permit robust conclusions on the soot oxidation/formation processes in the current turbulent flames.

Chapter 4 details the experimental steps related to the simultaneous laser diagnostics. The laser–based diagnostics were used to determine spatial distributions and to identify the interval of sampling points in the reaction zone layer, where the physical and chemical evolution plays a crucial role in the formation of particulates. The impact of rate of strain, equivalence ratio and burnt gas temperatures on signals are discussed for various sooting structures.

Chapter 5 covers the implemented experimental steps for the measurement of dominant gaseous species. Laminar flame calculations are also presented to support the interpretation of species growth and particle inception under different flame conditions. The difference in the profile distribution of species of laminar and turbulent cases shows the distinct impact of mixture and flow parameters.

The objective of Chapter 6 is to present information on soot nucleation under turbulent combustion condition. A standardised operational sampling procedure is outlined to minimise PAH losses within the system and sampling steps. The PAH profile distribution along the reaction zone layer indicates the impact of PAH species in the soot nucleation process for different equivalence ratios and rates of strain.

Chapter 7 contains the novel experimental process used to characterize particle size distributions in a premixed turbulent flames. The SMPS allows the quantification of the impact of the rate of strain and equivalence ratio on the particle size distributions along the stagnation point streamline. The data can significantly advance, in combination with the results from the laser–based diagnostics and GC–MS, the fundamental understanding of the particle formation and oxidation process in turbulent premixed sooting flames. The data can also further support the development and validation of numerical models.

Finally, the conclusions and future work are discussed in Chapters 8 and 9, respectively.

Chapter 2

Introduction

2.1 Overview

Interactions between turbulence and chemistry strongly impact the processes leading to soot formation in practical combustors due to the comparatively long chemical timescales. The control of soot emissions from practical devices requires an understanding of the controlling parameters leading to their formation in turbulent flows [25]. The current experiments, using premixed turbulent sooting flames, features an opposed jet burner configuration. Although target flames have been presented as part of the International Sooting Flame (ISF) workshop series, a significant demand on experimental data from compact turbulent flames with well–defined boundary conditions remain. A well–controlled experimental configuration, i.e. opposed jet burner, is here used to advance the fundamental understanding on particle inception, formation and oxidation in turbulent premixed flames.

In this Chapter, the fundamental concepts are provided in order to discuss the scope of the current thesis. Basic descriptions on turbulent combustion, fuel chemistry and soot formation process are presented to provide context. Experimental methods, used in soot formation studies, are also discussed.

2.1.1 Laminar sooting flames

Soot formation in laminar flame has been of particular interests to scientific communities for many years. Studies of soot inception under laminar conditions provide some guidance to the turbulent regime. Abid et al. [31] and Gua et al. [32] provided a careful quantification of soot particle size distributions in lightly and heavily sooting premixed laminar counterflow ethylene flames. The flames investigated in the current thesis represent the turbulent equivalent to the laminar flames presented by Wang and co–workers [31, 32] in terms of the mixture stoichiometries chosen. A combination of laser-induced fluorescence (LIF) and laser-induced incandescence (LII) has been used in counterflow diffusion flames [33, 34]. Quantitative measurements of intermediate gaseous species in flames were also performed by molecular beam mass spectrometry (MBMS) [35, 36]. Lindstedt and Waldheim [37] used the former data sets and a sectional model to show that it is necessary to account for the collision efficiency change when moving from PAHs to the van der Waals enhanced limit associated with particulates. Raj et al. [38] utilised a new multi–variate PAH population balance model to investigate the physical interactions between PAHs in laminar premixed flames. It was shown that the mass of the colliding PAHs, their collision diameters, and the flame temperature were important factors for the determination of the collision efficiency.
Johansson et al. [39] investigated the evolution of soot composition and the particle surface using a combination of laser-induced incandescence (LII) and X–ray photoelectron spectroscopy (XPS). Johansson et al. [40] studied soot precursors in a laminar counterflow diffusion flame using aerosol mass spectrometry coupled with tunable vacuum-ultraviolet radiation. Dominant peaks were found at m/z = 202, 226, 252, 276, and 300 amu. Johansson et al. [40] show that larger species can grow ahead of lighter ones and that PAH radical combination reactions provide fast routes for mass growth. Dillstrom et al. [41] noted the existence of common masses shown in the mass spectrum for different fuels.

Mercier et al. [42] concluded that the soot nucleation is the results of kinetic processes in laminar diffusion flame as the major part of the soot nucleation region is surrounded by PAH dimers. They concluded that soot nucleation coincided with the location of PAH dimers. Marinov et al. [43] found that stabilized radicals play an essential role in key reaction sequences leading to PAH and soot particles. Liu et al. [44] attribute the dominant reaction product to PAHs with 5–membered ring. Schulz et al. [45] and Commodo et al. [46] directly observed the chemical structures with 5–membered ring through using high–resolution of atomic force microscopy (AFM) in a premixed C_2H_4–air flame. For instance, indene and the indenyl radical show higher relative abundances in soot growth than 6–member ring structures [47, 48]. The higher abundances of such species reinforce the role of cross–linked aromatic compounds in the formation of particulates. Liu et al. [49] showed the importance level of chemical coalescence of moderate-sized PAHs into cross–linked three-dimensional structures as a probable pathway to soot nucleation. Sander et al. [50] developed a new optimised PAH-PP soot model to study the formation, growth and oxidation of soot in laminar premixed flames. The model included coalescence of primary particles and the composition of each individual primary particle. It was shown that the soot particle growth was significantly slower than in the gas-phase, and that steric hinderance could describe the lack of species capable of accessing active sites on PAHs inside a particle.

The weak intermolecular interactions and van der Waals forces, rather than covalent forces, are responsible for bond formation resulting from the majority of binary collisions [51, 52]. The mass growth can result from direct PAH condensation and gas–phase deposition onto the soot surface [53]. The representative nanoparticle samples were also collected on the probe and examined using scanning electron microscopy (SEM) and energy dispersive spectroscopy (EDX). Further, SMPS and SEM analyses revealed the nucleation, growth, aggregation and interaction of these nanoparticles formed in the flame, evidenced by the changes of particle morphology, averaged particle size and elemental composition [54]. Eaves et al. [55] suggest that smaller PAHs are the most important for the nucleation process, while small and large PAHs are essential for the condensation process.

The flame temperature and sooting conditions (lightly or heavily) are factors that impact the potential bimodality of PSDs. For instance, Zhao et al. [56] observed a bimodal shape in the particle size distribution at low temperatures. The PSD followed by a transition to a unimodal shape at higher temperatures. A bimodal size distribution function was also seen in slightly sooting premixed flames [57]. Botero et al. [58] utilised a differential mobility spectrometry (DMS) to study particle size distribution (PSD) for paraffin class hydrocarbons in a wick-fed burner. A unimodal PSD was detected at low flame heights, followed by a rapid evolution into multi-modal PSDs with larger particle diameters. Gleason et al. [59] investigated the impacts of temperature on soot volume fraction and dispersion index using multi–color pyrometry in ethylene counterflow diffusion flames at a constant rate of strain and equivalence ratio. The growth in soot volume fraction was found towards the stagnation plane, while the decrease in dispersion index leads to soot dehydrogenation proportional to flame temperature.

2.1.2 Turbulent sooting flames

Interactions of turbulence with soot, gas–phase chemistry and radiation impact practical applications [60]. Turbulent flames involve a complex coupling of fluid dynamics and chemical kinetics over wide ranges of spatial and temporal scales. The interaction of turbulence and chemistry influences the structure, the progress of reactions, the relationships among species concentrations, and the formation of pollutants [8]. For the particles, this changes the spatial trajectory and the history of gas conditions encountered. The change in trajectory can affect collisions with other particles, and the change in gas conditions affects the evolution of the particle through mass addition/removal and surface physical/chemical properties [61, 62]. During turbulent combustion, soot forms under the influence of a highly intermittent mixing process and a joint transported probability density (JPDF) approach [63] was used [26] to model soot PSDs [27, 64] using a fully coupled sectional model. Agreement similar to that expected in laminar flames was obtained, and it was further shown that local extinction effects resulted in soot being transported to leaner mixtures. Bisetti et al. [53] showed the importance of turbulence–related strain on soot formation. Mueller and Pitsch [65] used Large Eddy Simulation (LES) to study turbulence–chemistry interactions and found that small–scale interactions between turbulence, gas–phase chemistry, and soot have a significant impact. Yoo and Im [66] performed a two–dimensional DNS of a non–premixed flame. An increased soot volume fraction in turbulent flames, as compared to steady laminar flames, resulted from the rapid transport of soot particles out of high–temperature regions rather than enhanced chemistry. The occurrence of soot, PAH and OH and their spatial variations are strongly dependent on the properties of the flow field [67]. Tian et al. [68] used a fully coupled transported PDF approach featuring a 78-dimensional joint-scalar space, including enthalpy, gas phase species and 62 soot sections to show that soot may be transported to fuel lean mixtures and highlighted a correlation with local extinction events.

2.1.2.1 Target flames

The complexity of the soot formation process and its strong interactions with gas–phase combustion chemistry and turbulence are of particular concerns in the turbulent studies. Experiments in turbulent flames should be carried out for configurations suitable for the validation of numerical models. The relevant physics of the turbulent sooting characteristics should also be considered for widely approachable flame conditions to present more precise conclusions. There are still some problems and drawbacks for experimental and numerical studies of turbulent sooting flames. The drawbacks are attributable to a combination of factors, including (i) a lack of sensitive, accurate, noninvasive measurements of the physical and chemical characteristics of soot during

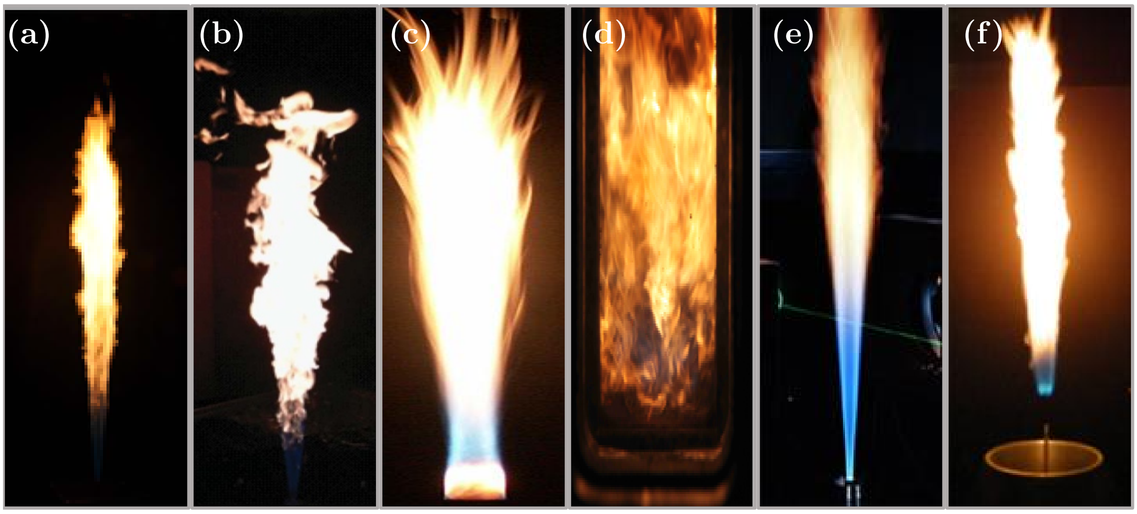

Figure 2.1. Photographs of target flames provided in the data sets of International Sooting Flame (ISF) workshop. (a) Adelaide jet flame; (b) Sandia flame; (c) Adelaide bluff body flame; (d) DRL swirl flame; (e) Delft III flame; (f) DLR–Lifted flame

Table 2.1. Brief details of target flames presented as part of ISF workshops covering fuel type, Reynolds number, pressure range and combustion type.

Target Flame	Fuel	Re	p (bar)	Type	Ref
Adelaide Jet	$C_2H_4/H_2/N_2$	5,000-15,000	1	Simple	[69–72]
Sandia	C_2H_4	20,000	1	Piloted	[73, 74]
Adelaide BB	C_2H_4/H_2	30,000	1	Bluff Body	[75, 76]
DLR Swirl	C_2H_4	Various	1–5	Premixed	[67, 77, 78]
Delft III	CH_4/N_2	9,700	1	Piloted	[79, 80]
DLR Lifted	C_2H_4	10,000	1	Lifted	[81, 82]

its development and evolution in combustors and (ii) computational limitations in simulating molecular–weight growth of large gas–phase species, the nucleation of species to particle formation, and the detailed chemistry involved in particle growth, chemical and physical evolution, and oxidation under combustion conditions. Experiments in turbulent flames are highly desirable in burner configurations that feature well–defined boundary condition, compatible with numerical calculations, that can be accurately implemented with reduced uncertainties and errors.

The sample photographs for the target flames used in the international sooting flame (ISF) workshop are shown in Fig. 2.1. As presented in Table 2.1, ethylene fuel blends have been at the centre of attention for the target flames. The geometry of the Adelaide jet flame includes a straight pipe burner with different diameters. Hydrogen is added to ethylene in this type of target flame. Hydrogen can present preferential diffusion effects leading to further complex issues. A Testo 350 flue gas analyser was used to measure NOx, CO, and CO_2, and the temperature profile distribution was measured via using R–type thermocouple. It was concluded that jet exit diameter and fuel flow rate linearly affect the soot yield, which was strongly dependent on both rate of strain and the flame volume. The main problems with the configuration include the control of boundary conditions and the flame perturbation due to intrusive probing methods. Accordingly, data obtained using LII to determine the soot volume fraction for different experimental conditions. Pure ethylene was used in the piloted Sandia flame. Simultaneous Rayleigh line imaging and OH–PLIF were used to study temperature and local extinction. The Rayleigh line imaging showed that the pilot flame can provide a homogeneous flow of hot products along the edge of the fuel jet. Soot layers entrained into vortical flow structures were also oberserved. Various optical setups have been used to study the turbulent sooting flame in the DLR premixed swirl burner. Soot volume fraction and temperature were measured via using LII and CARS, respectively, with OH–LIF and PIV also used to evaluate the flame conditions at different pressures, Reynolds number and equivalence ratios. It was found that the occurrence of soot, PAH and OH and their spatial variations were strongly dependent on the properties of the flow field. Arguably, a main problem with this target flame was the implementation of boundary conditions for the numerical analyses. The Delft III target flame contains methane as a fuel in contrast to other target flames in ISF workshop. Different laser techniques have been applied for this target flame, including Raman/Rayleigh/LIF/CARS temperature measurements and OH PLIF imaging at other laboratories. The accuracy of some species measurements in some locations was limited by high levels of fluorescence interference from soot precursors. The DLR lifted flame includes a simple burner geometry with ethylene used as reference fuel to study soot volume fraction (LII), velocity field (PIV), temperature (CARS) and mixture quantification upstream of ignition (Raman scattering). The lifted nature of the flame presents some additional complexities for modellers.

The current study aims to provide different flame conditions in a well–controlled opposed jet burner configuration. The reproducibility of the experimental condition is easily achievable by this type of burner. Different flame configurations can be obtained by adjusting the flow parameters. Such advantages assist the experimental sampling process and laser diagnostics in studying soot formation or oxidation in the turbulent regime. The work presented here takes advantage of this type of target flame to study gaseous species, PAH and particle size distribution in the premixed turbulent flame.

2.2 Combustion regimes

The practical operation of combustors determines the relevant combustion regimes. Wrinkled flames, corrugated flamelet and thin reaction zone regimes are examples of combustion modes applicable to conventional engine designs featuring self–sustained flames at comparably low turbulence levels. By contrast, the spread of the reaction zone region becomes of significance for novel combustion technologies operating in more distributed modes [83, 84]. A decrease in emission levels (e.g. NO_x) can be expected for such combustion technologies due to lower overall temperatures.

The current back–to–burnt (BTB) opposed jet configuration has distinct advantages for the systematic investigation of burning mode transitions from flamelet–like structures towards distributed reaction zones by means of chemical timescale variations [85]. Fig. 2.2 illustrates two distinct combustion regimes.

In the flamelet mode, changes in the structure of reaction and preheat zones are insignificant although the turbulence is capable of wrinkling the flame [86, 87]. Reactants and products are separated through thin reacting layers in this regime (i.e. bimodal statistics), and the internal flame structures are close to that of laminar flames [87–89].

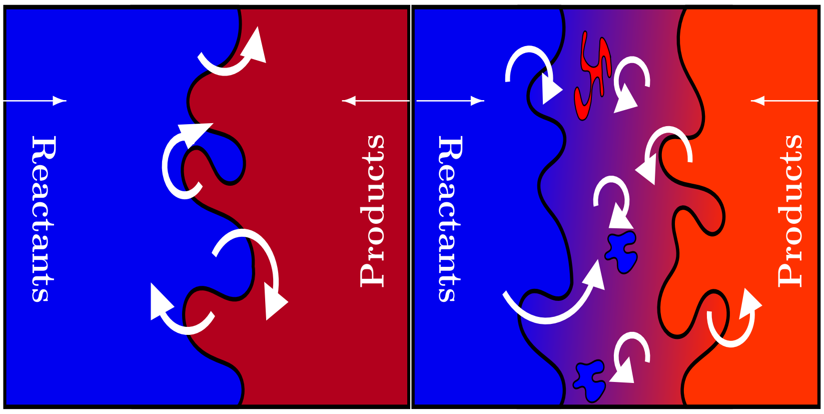

Figure 2.2. Combustion regimes applicable to opposed jet configuration. Left column: Thin reaction zone; Right column: Distributed reaction zone.

Such flames exhibit a clear flamelet–like structure with steep scalar gradients and a distinct dilatation direction with fast chemical activity [90–92].

By contrast, the distributed reaction mode precludes conventional flame propagation leading to strong deviations from bimodal structures. The increased turbulence–chemistry interactions can lead to an appearance of distributed reaction zones and increased uniformity in the temperature field. The broadening or fragmentation of a reaction zone is also strongly dependent on the chemical timescale. The bimodal statistics approach is not applicable for the quantification of such combustion zones. Spalding [93] and Hampp and Lindstedt [94] suggested that a multi–fluid approaches may be used as a possible extension to bimodal (two fluid) approaches, to quantify the intermediate fluid states. For instance, Hampp and Lindstedt [94] used simulatenous PIV, OH–PLIF and CH_2O–PLIF to identify fluid states.

In terms of the formation of PAHs and soot, the chemical time scales are long compared to the major chemical pathways and are hence much more likely to be distributed. Accordingly, the well–established need arises to solve additional transport equations for soot mass and number density [95, 96]. More recently, Schiener and Lindstedt [97] used a joint transported probability density (JPDF) approach to model soot PSDs.

2.3 Fuel chemistry

Lindstedt and Maurice [98] validated a detailed chemical kinetic mechanism for n–heptane combustion covering a wide range of conditions. It is found to be necessary to include both pyrolysis and radical reactions to predict intermediate species profiles. Furthermore, the distribution of intermediate species was found to be highly sensitive to the rate of the pyrolysis step. Fuel molecular structures can determine pyrolysis products and intermediate radical pools. Thus, the processes of soot inception, surface growth and oxidation can be distinct for different fuels.

Accordingly, soot formation has been studied for different fuel structures. The soot loading was seen to be comparably higher for propene and ethylene as compared to propane flames [99], sooting tendency as propene $>$ ethylene $>$ propane. The soot volume fraction of n–butane flame was reported a third of that of iso–butane at the same experimental conditions in counterflow flames [100]. In a further study, it was shown that propane and n–butane showed significantly higher sooting level in comparison to methane and ethane [101].

In the context of surrogate fuel blend for kerosene, Dagaut et al. [102] studied the oxidation of n–propylbenzene for different temperatures and equivalence ratios. Soot was not measured, but concentration profiles of 23 species (reactants, stable intermediates and final products) were obtained using probe sampling techniques. However, Choi et al. [103] conducted measurements to study the level of PAHs and soot for pure n–heptane, toluene and mixtures of n–heptane/toluene. It was observed that with the addition of toluene, soot inception occurred at lower flame heights and the primary particle size of soot aggregates was significantly reduced. Botero et al. [104] investigated the impact of fuel structures, i.e. pure aromatic hydrocarbons, on the soot mean mobility diameter and the number of particles. A smaller mean mobility diameter was observed for aromatic fuels substituted with aliphatic chains such as toluene and 1,2,4-trimethylbenzene. In another study, Botero et al. [105] used a differential mobility spectrometer (DMS) and transmission electron microscopy (TEM) to measure particle size distributions and particle morphology for different toluene/n-heptane blends. It was shown that the addition of toluene to n-heptane shifts the PSD and primary particles to larger diameters. The effects of dimethyl ether (DME) addition to ethylene fuel on sooting tendencies were investigated in counterflow diffusion flames using a laser scattering technique [106]. The results showed that the sooting region was appreciably reduced as DME was mixed with ethylene.

Since ethylene is a key intermediate in the fuel decomposition for a number of hydrocarbons, it has been considered as a primary reference fuel for soot formation investigations [107]. Camacho et al. [108] performed an extensive study of soot formation to evaluate the particle size distribution (PSD) in premixed ethylene/oxygen/argon flames. The flame temperature and thermodynamic reversibility strongly impact the soot formation and particle size distribution. For instance, soot suppression was remarkable at high temperatures and impacted particle size distributions. In a similar study [32], the PSDF was investigated in the premixed ethylene flames for various flame temperatures at $\phi = 1.8$ and 2.5. The PSDF was strongly dependent on gas–surface reactions, nucleation and coagulation. A simultaneous decrease in temperature and an increase in equivalence ratio favoured soot formation [109]. Figura et al. [110] studied the impact of pressure on the structure of ethylene/nitrogen/oxygen counterflow diffusion flames. It was observed that sooting tendency is a strong function of the aromatic content, especially at higher pressure.

2.4 Soot formation processes

Experimental and numerical analyses are complex in turbulent flames, even with an in–depth understanding of the physical processes of soot formation. The soot formation process should be distinct in turbulent flames as particle formation is coupled to the flame structure [111]. The major studies of soot formation–oxidation processes have been conducted for laminar flames as outlined above. The fundamental soot formation steps clearly remain and provide guidance for turbulent flames, though the influences of flow are much more complex.

The schematic of the soot formation process is shown in Fig. 2.3. The soot formation can be classified into different processes of (1) gas–phase precursor formation; (2) soot nucleation; (3) particle surface growth, particle coalescence and aggregation, PAH condensation and soot oxidation and fragmentation. The question mark in Fig. 2.3 indicates some of the current uncertainties among researchers on how soot inception initiates after PAH formation. Soot formation–oxidation processes have been discussed by Bock–horn [112], Frenklach [113], Mansurov [114] and McEnally et al. [18] amongst others.

2.4.1 Gas phase precursor formation

Polycyclic aromatic hydrocarbons (PAHs) are presumed to be the intermediates leading to soot formation [18]. There have been a large number of experimental and numerical investigations substantiating the inception of growth mechanisms from the transition of gas–phase species to particulates [25].

Multiple reaction mechanisms have been provided to clarify the contribution of PAH growths to soot particulates. For all proposed mechanisms, acetylene is the important intermediate species used as a building block for mass growths. Hydrogen–abstraction–C_2H_2–addition (HACA) is the most well–known mechanism presented by Frenklach et al. [115–118]. In this mechanism, hydrogen atom abstraction from stable molecules and acetylene addition to the radical site provide a continuous reaction of radical species, eventually leading to soot. The reaction sequences are presented in Eqs. (2.1)–(2.2). Thermodynamic and kinetic characteristics are the two main factors in the HACA mechanism [119]. Stein and Fahr [120] concluded that PAHs with their thermodynam-

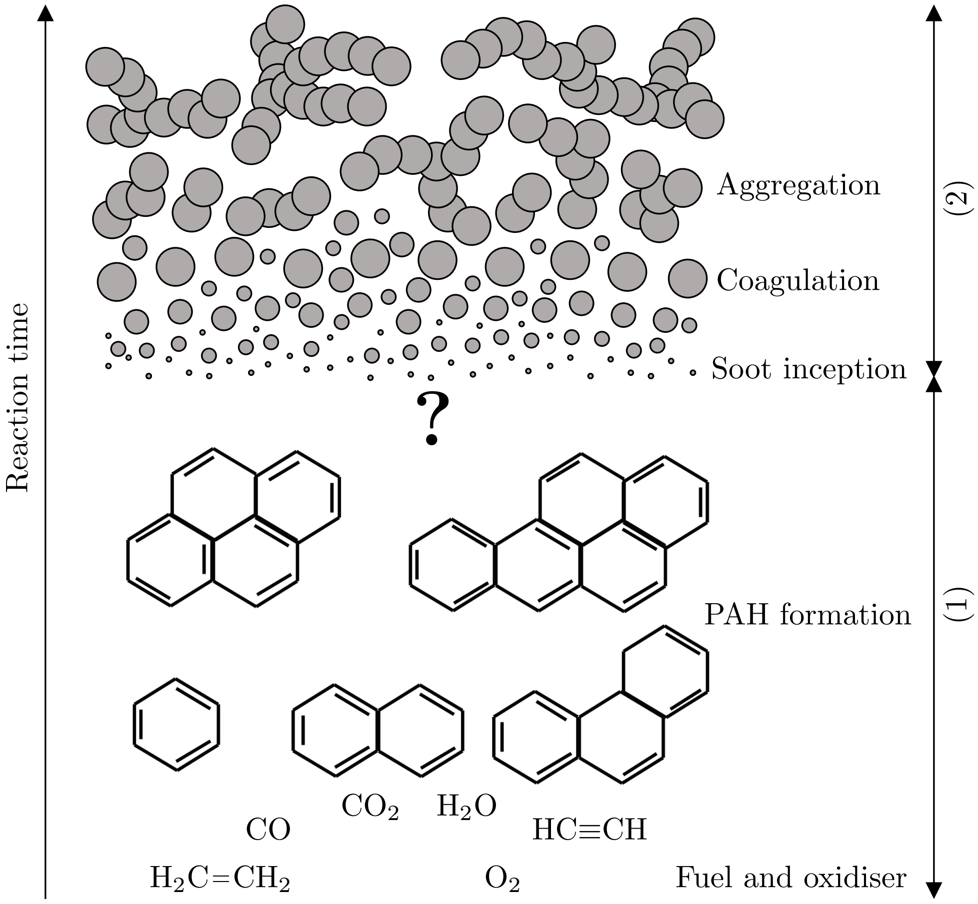

Figure 2.3. A scheme of the soot formation and oxidation process, based on Bock–horn [112]. (1) Molecular zone; (2) Particle zone: surface growth and oxidation. Question mark is representative of uncertainty on how particle inception initiates after PAH formation.

ics stability play an important key to soot formation.

$$\begin{aligned} &A_i + H \rightleftharpoons A_{i^-} + \mathrm{H}_2 \\ &A_{i^-} + \mathrm{C}_2\mathrm{H}_2 \rightleftharpoons A_i\mathrm{C}_2\mathrm{H}_2 \\ &A_i\mathrm{C}_2\mathrm{H}_2 + \mathrm{C}_2\mathrm{H}_2 \rightleftharpoons A_{i+1} \end{aligned} \tag{2.1}$$

$$\begin{aligned} &A_{i^-} + \mathrm{C}_2\mathrm{H}_2 \rightleftharpoons A_i\mathrm{C}_2\mathrm{H} + H \\ &A_i\mathrm{C}_2\mathrm{H} + \mathrm{C}_2\mathrm{H}_2 \rightleftharpoons A_{(i+1)^-} \end{aligned} \tag{2.2}$$

where A_i is aromatic species and A_{i^-} radical with i–number of rings.

There are several other reaction mechanisms, showing different pathways to PAH growth. For instance, Lindstedt et al. [98] have shown that additional pathways beyond the HACA sequence are required for fuels with aromatic content. It was found that the relative importance of species formation is a strong function of the parent fuel and oxidation conditions. Several competitive mechanisms were highlighted in the formation of both naphthalene and indene, and it was concluded that C_9H_8 and C_9H_7 are involved in the mass growth source that link five and six member ring structures. Lindstedt [47] underlined the crucial impact of isomerization and addition reactions as primary reaction channels, complementary to abstraction and decomposition paths in the soot mass growth processes. Such reaction classes are dependent on the fuel type and burning conditions. The interesting note is the unit ratio of naphthalene/indene explored for different fuels, reinforces the importance levels of both indene and naphthalene species in the soot growth. Leung and Lindstedt [121] also described a kinetic model for the combustion of $C_1 - C_3$ hydrocarbons. It was found that the the benzene formation stem from the reaction involving propargyl radicals, and the impact of reaction paths via C_4 species were comparatively insignificant.

Johansson et al. [40, 122] show the importance of non–stabilomer PAHs. The peri–condensed PAHs are also among the stable species and able to survive at flame environments. Johansson et al. [48] suggests the inclusion of chain reactions of resonance–stabilized radical (RSR) in a mechanism as a viable route to mass growth and soot formation. Ultraviolet aerosol mass spectrometer (VUV–AMS) was used to highlight the RSR sequence as shown in Fig. 2.4. Cyclopentadienyl, indenyl, vinylindene, fluorenyl, phenanlenyl, propargyl are among the essential RSR radicals. Elvati and Violi [123] also suggests that the attachment of aliphatic chains to aromatic rings can make the physical PAH stacks process possible based on the theory of collision energy.

2.4.2 Soot nucleation

The soot nucleation is the process where gas–phase species transition to condensed phase materials. There are still conjectural assumptions on how the nucleation process

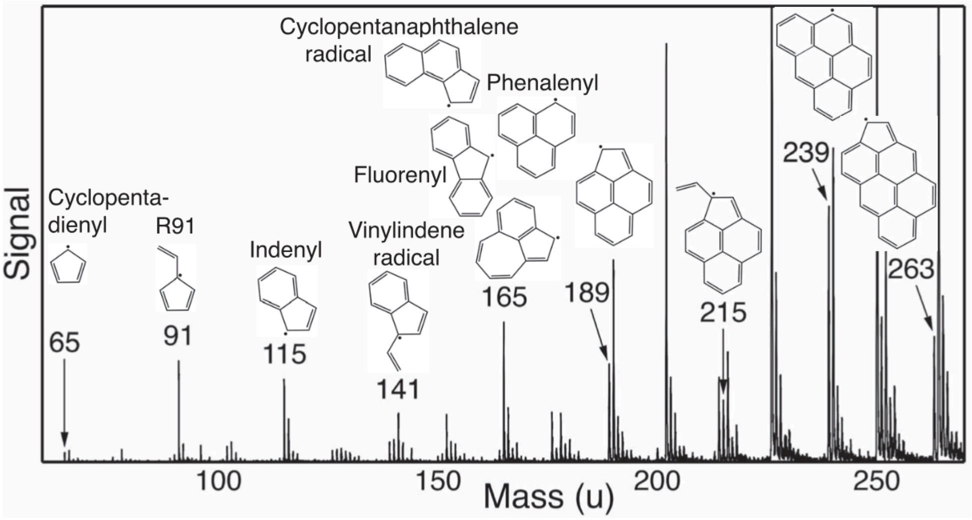

Figure 2.4. VUV-AMS spectrum demonstrating a sequence of radicals [48], substantiating the critical impact of cyclopentadienyl, indenyl, vinylindene, fluorenyl, phenanlenyl, propargyl on soot formation.

initiates. Studies support the prominent role of heavy PAHs in the soot nucleation. There are generally two theories on the soot nucleation. First, fullerene–like structure can be a representative of soot nucleation [119]. Kroto et al. [124] noted the high interactions of large concentrations of small hydrocarbons when large clusters are consumed throughout the nucleation process. The main problem with the theory is that the reaction process is too slow to generate soot inception from fullerene growth [118, 125]. The second theory suggests the coalescence of PAH species as a main route to the soot nucleation. Liu et al. [49] showed a strong relationship between the soot nucleation and the chemical coalescence of moderate–sized PAHs into cross–linked three–dimensional structures. The mass growth mechanism contains repetitive reaction sequences consisting of PAH reactions and C_2H_2 addition on the bridge and armchair sites of soot surface region [49]. D' Anna et al. [126, 127] refer the formation of three dimensional, cross–linked and ring–ring aromatic structures to soot nucleation process as presented in Eq. (2.3),

$$\begin{aligned} A_i + H &\rightleftharpoons A_{i\text{-}} + H_2 \\ A_{i\text{-}} + A_{j\text{-}} &\rightleftharpoons A_{i+j} + H \end{aligned} \tag{2.3}$$

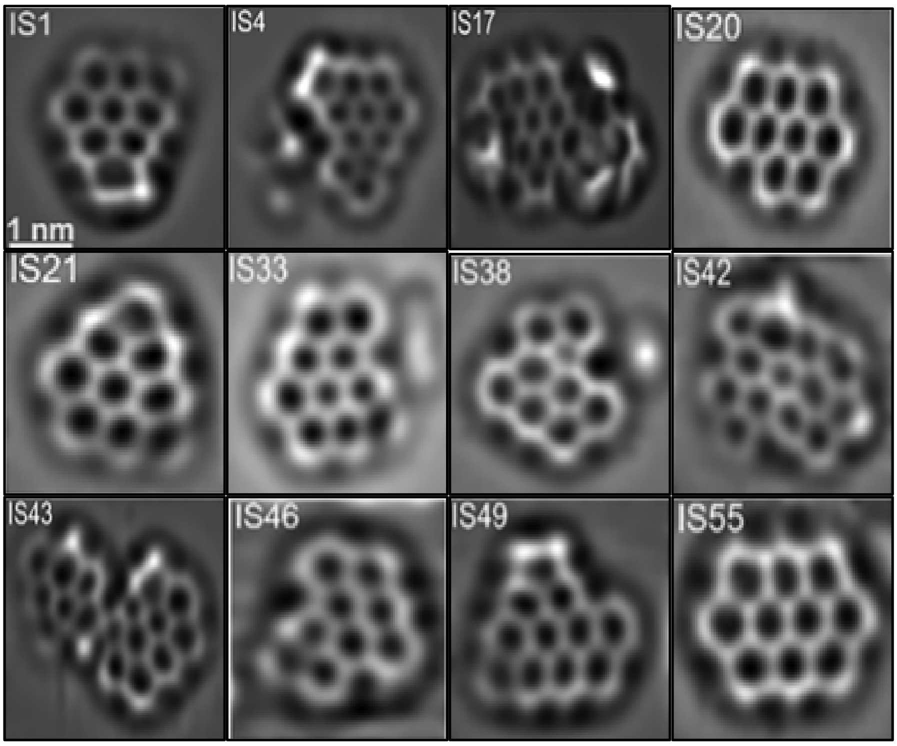

Figure 2.5. AFM images of identified PAH molecules and aliphatic chains/substituted benzenes found on the soot particles [45, 46], illustrating the frequency of penta–rings in the soot nucleation step.

where A_i is aromatic species and A_{i}- radical with i–number of rings. The subscripts of i and j refer to PAHs sizes.

Schulz et al. [45] and Commodo et al. [46] used a high–resolution AFM to identify the building blocks involving in incipient particulates as shown in Fig. 2.5. They showed the contribution of aromatic components, methyl and alkyl chains and penta–rings in the soot nucleation process as shown in the AFM images. Kholghy et al. [128] state that the soot nucleation is strongly proportional to PAH concentrations. They concluded that PAHs with higher concentrations, irrespective of their sizes, have a higher chance to collide with other PAHs and form larger clusters. The higher concentration of five carbon rings than their parent species was also highlighted, which suggests a direct relationship between the species with higher concentration and soot nucleation. Johansson et al. [48] proposed an alternative theory for soot nucleation process. In this theory, acetylene or vinyl play a key role in the mass growth of resonance–stabilized radicals (RSRs) in the first stage. In the second stage, the cluster of hydrocarbon

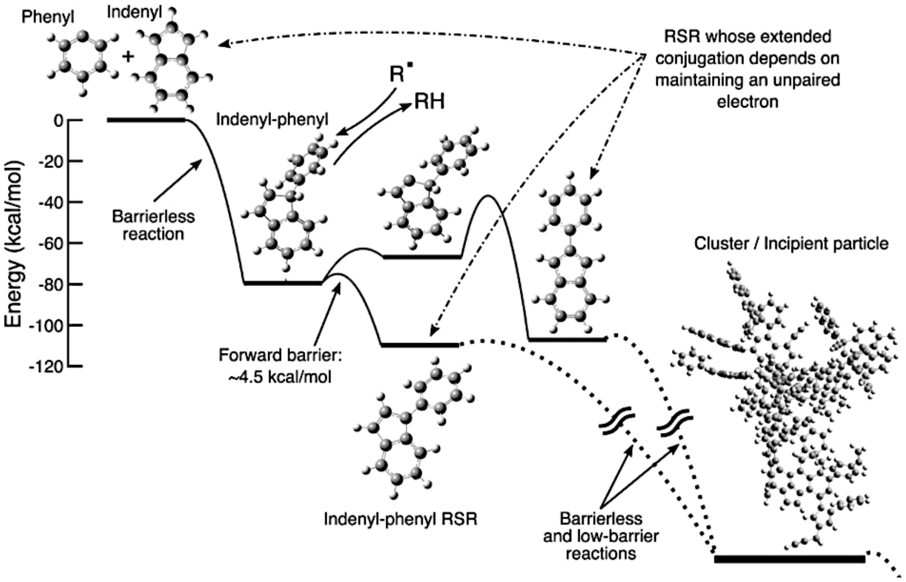

Figure 2.6. Representative potential energy surface for hydrocarbon clustering [48], suggesting the probable steps in the clustering process to soot growth.

species stems from the chain reactions of RSRs species. Stable PAHs and unsaturated aliphatic species are actively involved in the clustering process. Therefore, the growths can progress without a significant energy barrier for the activation reaction, leading to the formation of incipient particle compositions.

The potential energy diagram is shown in Fig. 2.6. The reactions shown are an exemplification of probable steps in the clustering process. When the incipient particle is formed, the chain reactions provide a route for soot growth (third stage).

The physical bonds between PAH species are crucial factors in soot nucleation [118]. With an increase in the size of aromatic species, the production of PAH dimers and trimers stems from the PAH collisions and the bonds between stacked PAHs. The weak intermolecular interactions and van der Waals forces, rather than covalent forces, are responsible for the bonds between PAH radicals in majority of the binary collisions [51, 52]. The mass growth can result from the direct PAH condensation and the gas–phase deposition onto soot surface [53]. Resonance–stabilised radicals can deposit/infuse on soot particles in the flame [111]. The incipient particle composition consists of aromatic structures with stacked PAHs linked together via van der Waals forces [129].

The heterogeneous particles–gas phase equilibrium is a crucial step in the soot formation process. The gas–phase PAH can adsorb on the surface of particles. The PAH condensation features a collision between a soot particulate and a gaseous PAH. In this process, the particle volume increases without the interference of the aggregation step. The rate of condensation can be defined by Eq. (2.4),

$$\dot{H}_{cond} = N_{PAH_g} \int_0^\infty \beta(\upsilon_{PAH_g}, \upsilon) n(\upsilon) d\upsilon \tag{2.4}$$

The rate of PAH_g condensation onto particles can be summarised by Eq. (2.5) when a sectional model with a disretisation of the particle volume υ is used.

$$\begin{aligned} \dot{H}_{cond} &= \beta(\upsilon_{PAH_g,\upsilon_i}) N_{PAH_g} N_i \\ N_i &= \int_{I_{\upsilon_i}} n(\upsilon) d\upsilon \end{aligned} \tag{2.5}$$

The rate of volume increase per particles ($G_{cond}(\upsilon_{PAH_g}, \upsilon_i)$) is defined as (Eq. (2.6)),

$$G_{cond}(\upsilon_{PAH_g}, \upsilon_i) = \frac{m_{PAH_g}.\dot{H}_{cond_i}}{\rho_{soot} N_i} \tag{2.6}$$

where m$_{PAH_g}$ is the molecular weight of PAH, N the particle number density, ρ the gas density, n(ν) the particle number density per unit size per unit of gas volume and β is the collision frequency between soot particles of different volume.

2.4.3 Soot surface growth and oxidation

The generated soot particles interact with gaseous species, and soot surface growth subsequently occurs. The process is the completion to soot inception step as soot particulates with heavily masses are formed via surface growth. The most important processes that determine the surface structure of the fine particles are surface growth and oxidation. Kennedy [130] concluded that the main percentage (90%) of soot masses is the result of the soot growth process. The abstraction reactions can be affected by the concentration level of important radicals like OH [117, 131]. The addition of PAH and acetylene on particle surface corresponds to soot mass growth [55, 132–134]. The soot growth process, shown in Fig. 2.7, illustrates the impact of acetylene addition and PAH reaction process. Pejpichestakul et al. [135] also found that the acetylene addition is the major pathway to soot growth. D' Anna et al. [136] show that soot mass growth is strongly proportional to PAH addition, even at a comparatively low temperature.

The particle–particle interactions or coagulation is the main process involved in the morphology and particle size distribution, while the majority of particulate mass stems from surface growth. Coalescence and aggregation are the results of collisional interactions between particles. The former contains a reduced area of the total surface as the existing boundary between particles disappears. The latter defines the particle stacking with point contact [137–139]. When surface growth stops, mature soot grows by agglomeration of polydisperse entities (e.g. spheres) and aggregates before oxidation takes over [140].

The coupling between gas–phase and surface reactions is one of the important factors [141]. Not only gas–phase composition affects surface kinetics, but it is demonstrated that the contribution of surface reactions to the gas–phase composition can be substantial. The competition between oxidation and formation process is an essential factor in the whole process discussed above, with OH and O_2 concentrations play a key roles in the oxidation of soot. Other species, such as the O atom and H_2O can also be contributors to oxidation [142, 143]. The main product produced via soot oxidation is CO. The oxidation rate by O_2 and OH is proportional to the number of radical sites and soot surface, respectively [144, 145]. Celnik et al. [146] presented an aromatic-site soot model to study the impact of O_2 oxidation on two to four ring aromatics. It was found that the oxidation rates were distinct for radicals on an armchair site, while the impact was reported to be same for all other radical sites. The radicals on an armchair site showed a higher activation energy.

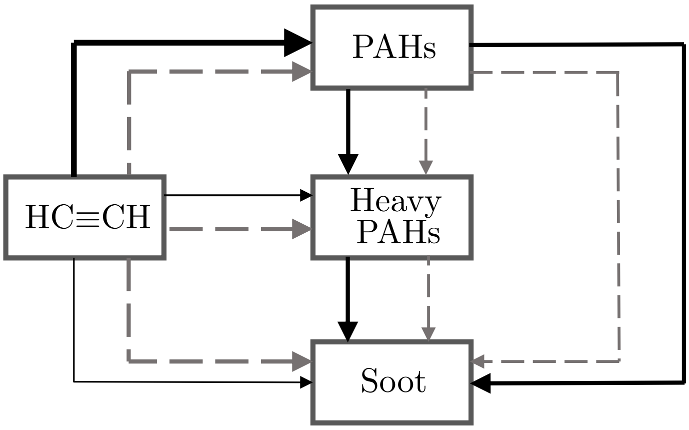

Figure 2.7. A diagram of soot particles growth showing the comparative contribution of PAH condensation reactions and HACA mechanism. Dashed and solid lines illustrate the impact of low and atmospheric pressure, respectively. The significance of each path corresponds to the thickness of arrows [135].

2.5 Experimental techniques

Experimental identification and characterisation of soot particles in combustion zones are tremendously important to our understanding of the mechanisms controlling particle formation, growth, and oxidation. Addressing outstanding questions in soot chemistry will require measurements of particle characteristics, such as composition, size, structure, morphology, abundance, and distribution, as they evolve during combustion. Experiments in soot studies can be categorised by two general techniques: laser diagnostics and probe sampling methods.

2.5.1 Laser diagnostics

One of the main advantages of the laser diagnostic is the non–intrusive feature. Several simultaneous laser diagnostic technique is usually utilised to provide details about size, structure, composition, and volume fraction of particles. Here, some of the relevant literature studies are described.

Sirignano et al. [145] used laser-induced fluorescence (LIF) to separate particulates with different aromatic constituent sizes. Two main high mass aromatics include sandwich–

like and highly packed structure. It was concluded that PAHs are kept together via van der Waals forces, while σ–bonds are the factor to maintain loose aromatic moieties. The main difficulty with the study is that the spectra used were too broad, and could not provide detailed information about specific species or functional groups. Sirignano et al. [145, 147] refer soot precursor particles to condensed phase, nanostructures, nanoparticles or nano–organic carbon (NOC). Their chemical and physical properties are among heavy aromatic molecules and solid particles. For this purpose, 266 nm excited LIF measurements can be used to distinguish between PAH and nano–structures. Bartos et al. [148] used simultaneous laser-induced incandescence (1064 nm), elastic scattering measurements (266 nm) and laser-induced fluorescence to study soot volume fraction and the impact of the gas–phase, the transition to nanostructures and then soot. It was shown that the existence of nanostructures is dominant to gas phase PAHs at 266 nm. At highly sooting flame conditions, soot volume fractions include the high level of nanostructures, implying that soot volume fraction is strongly proportional to surface growth. It was also noted the difficulty of individual probing of the domains in gas–phase, nanostructure and soot.

Commodo et al. [149] observed a change in the optical properties of the particles and attributed the effect to the presence of π–staked structure due to the onset of physical bonds between planes of polyaromatic units by van der Waals attractive forces [150], [151]. It was also declared that the growth of aromatic units involving in the soot formation process mostly occurs within the gas–phase. The results suggest that particle coagulation/coalescence has a major role in the initial soot formation, affecting both physical and chemical particle properties.

A combination of laser-induced incandescence (LII) and X–ray photoelectron spectroscopy (XPS) was used to study the maturity level of the bulk primary particle and particle–surface by Johansson et al. [20]. It was concluded that the evolution of particle surface and bulk material are unique in a flame. However, a wide range of particles with fine structures can result in a higher level of soot maturity.

Prior studies of soot formation process featuring laser diagnostic techniques [152–184] are summarised in Table 2.2. The laser technique is not capable of describing the existing interaction between species even if multiple laser diagnostic experiments are conducted simultaneously. As an example, the LII techniques can not heat all particles to the same level, influenced by other absorbing species.

2.5.2 Probe sampling

Probe sampling is usually used, as an interface to a detector, to extract major gaseous species, PAH and soot particles from flames. Table 2.3 lists the summary of techniques associated with the probe sampling to measure chemical compositions, physical structures and particle size distribution [185–203]. The sampling process can be carried out either online or offline, which is mainly dependent on the experimental procedures and the detectors' capabilities.

The probe configurations used in prior studies are entirely different in shape and material. The main problems with probing technique are the perturbation effects and sample losses in the extraction line. The perturbation effect can be minimised when mutual impacts of probe configuration and sampling conditions, i.e. suction pressure, are chosen suitably. The sample losses can be reduced when optimal probe sampling conditions (sampling line condition and nitrogen dilution) is implemented. Since there does not exist a standard probe configuration, all steps, including probe effects and sample losses, should be evaluated initially for different flame conditions either in laminar or turbulent flames. The technique applied in the current work is discussed in Chapter 3.

2.5.2.1 Chemical compositions

Table 2.3 lists the standard detectors utilised to quantify chemical compositions. The interface equipment (i.e. column), the operating condition and the instrument features are factors in the identification/quantification of chemical species.

The sampling process can be carried out either online or offline for chemical compositions. In the online analyses, the sampling line is directly connected to the detector. The filter unit is placed somewhere in the transfer line to capture large particles, and gaseous samples are drawn into the detector. When the sampling is conducted online, the results appearing on the detector signals potentially might not be a representative of correct analyses due to the potential losses in the extraction line. The length of the extraction line is also of significance as the existence of a thermal gradient in the system can result in species losses to the sampling line wall.

Gomez and co–workers [110, 204–207] inserted a microprobe radially using different inner and outer tip diameters. A straight quartz cylinder with a fine diameter was utilised to draw sample species using a vacuum pump. A combination of GC/TCD–FID–MS was used to quantify the spatial distribution of major gaseous and hydrocarbon species. Probes with different internal and external orifice diameters were used to collect samples without using inert gas dilution at pressures of 0.1 and 0.8 MPa. The internal and external diameters of the probes were selected in accordance with the flame thickness and pressure to reduce perturbations in the flame structure [207]. For instance, internal diameters of 0.10, 0.07 and 0.04 mm were used for pressures of 1, 4 and 8 atm, respectively [207]. The experiments were carried out in a laminar counterflow diffusion flame configuration. Figura et al. [204] repeated the experiments for pressures of 0.29 MPa and 2.5 MPa. The internal and outer diameters of probes, and relevant mixing layer thicknesses are shown in Table 2.4. The main problem with the sampling process is the probable losses of heavy hydrocarbon species during extraction (or in the filter unit) as aerodynamic quench, nitrogen dilution and a heated sampling line were not used in their experimental configuration.

Table 2.2. Summary of in-situ particle diagnostic techniques for studies of soot chemistry. SAXS – small-angle X-ray scattering, SANS – small-angle neutron scattering, WAXS – wide-angle X-ray scattering, UV – ultraviolet, LIF – laser-induced fluorescence, LII – laser-induced incandescence, ELS – elastic light scattering, NEXAFS – near-edge X-ray absorption fine structure, XPS – X–ray photoelectron spectroscopy, CARS – coherent anti-Stokes Raman spectroscopy.

Property	In-situ diagnostic
Soot formation	SAXS [152, 153]
Incipient particle size	SANS [154, 155]
Incipient particle fine structure	WAXS [155, 156]
Incipient particle composition	UV–visible spectroscopy [145, 157]
	LIF [158, 159]
Incipient particle volume fraction	Extinction [160]
	SAXS [154, 161]
	SANS [162]
Soot graphitization, growth, oxidation	Pulsed LII [163, 164]
Particle size, morphology	ELS [165, 166]
	SAXS [167, 168]
	SANS [169]
Particle fine structure	Multi-laser pulsed LII
Particle composition	Pulsed LII+extinction [170]
	Extinction [171]
	LIF [172, 173]
	NEXAFS [174]
	XPS [175]
Particle volume fraction	Pulsed LII [176, 177]
	ELS [178, 179]
	Extinction [180]
	Spectral soot emission [181]
	Laser-induced C or C_2 emission [182]
	Photoacoustic sensing [183]
Temperature	CARS [184]
Gaseous-phase species	

Table 2.3. Summary of probe sampling studies measuring chemical compositions, atom compositions, molecular mass, emission spectrum, soot structure and particle size distribution. GC – gas chromatography, TCD – thermal conductivity detector, FID – flame ionization detector, MS – mass spectrometry, HPLC – high performance liquid chromatography, MBMS – molecular beam mass spectrometry, TOF MS – time-of-flight mass spectrometry, SVUV-PIMS – synchrotron VUV photoionization mass spectroscopy, EDX – energy-dispersive X-ray spectroscopy, SEC – size exclusion chromatography, FTIR – fourier-transform infrared spectroscopy, TEM – transmission electron microscopy, SEM – scanning electron microscopy, AFM – atomic force microscopy, SMPS – scanning mobility particle sizer.

Property	Technique	Sampling method
Chemical compositions	GC–TCD [185, 186]	Online/Offline
	GC–FID [187, 188]	Online/Offline
	GC–MS [189–192]	Online/Offline
	HPLC [193]	Online/Offline
	MBMS [194, 195]	Online
	TOF–MS [122, 196]	Online/Offline
	SVUV–PIMS [197]	Online
Atom compositions	EDX [54]	Offline
Molecular mass	SEC [198]	Online/Offline
Emission spectrum	FTIR [199]	Online/Offline
Soot structures	TEM [200]	Offline
	SEM [201, 202]	Offline
	AFM [45, 46]	Offline
Particle size distribution	SMPS [32, 107]	Online
	TEM [203]	Offline
	AFM [119]	Offline

Table 2.4. Mixing layer thickness and microprobe dimensions [204]. D_i and D_o is inner and outer diameter, respectively, and δ_{mix} represent the mixing layer thickness.

Pressure (MPa)	D_i (mm)	D_o (mm)	δ_{mix} (mm)
0.29	0.07	0.15	4.76
2.5	0.02	0.09	1.62

The probes with a cone geometry are used with a molecular beam mass spectrometry (MBMS) to measure radical species. The MBMS schematic is shown in Fig. 2.8. Biordi et al. [208] conducted experimental studies to compare the extraction level of stable species as well as radicals for various types of sampling probes. It was suggested that a probe with an angle of 40°exhibits more advantages in comparison with other types. The flame perturbation and temperature effects were reported significantly lower for this case. Pauwels et al. [209] suggested using a quartz probe with a cone inside angle close to 40°and an orifice diameter about 100 μm. Flame perturbations were not observed for this probe. Struckmeier et al. [210] carried out experiments for a methane–oxygen–argon flame at ϕ= 1.4. The dimensions are presented in Table 2.5.

There was a direct relationship between the flame attachment to the probe wall and the opening angle. The probes with angles of 25° and 45° exhibited not only less disturbance of the flame, but also sufficient sample quenching. On the other hand, the flame was spread due to the perturbation for cone angles of 65° and 85°. Complete flame quench was observed at 1.5 mm and 6.5 mm from the cone aperture for 65° and 85°, respectively. The cone with an angle of 45°, a diameter of 0.125 mm and a length of 50 mm was considered as a standard configuration in their study. It was concluded that the cone geometry can have a significant impact on the species concentration. However, there was no change in species concentration with the various orifice diameters.

Niemann et al. [211] and Ergut et al. [212] used a tapered quartz tube without using an inside tube. It was pointed at that sampling probe can provide the precise detection of dominant gas species by using the aerodynamics of the orifice configuration even without sample dilution. Two concentric quartz tubes with outer diameters of 10 and 6 mm and an aperture diameter of 0.9 mm were used as a sampling probe for

Table 2.5. Summary of probes used with the MBMS sampling technique [208]. The cone length was considered 50 mm for all cases

Opening angle	Outer tip diameter (mm)	Height (mm)	Base diameter (mm)
25°	0.375	67.7	30
45°	0.050, 0.125, 0.325 0.375, 0.475 0.6, 0.7	50.5	40
65°	0.375	31.4	40
85°	0.375	25.6	45

a premixed ethylene jet flame by Faccinetto [213]. To slow down the condensation of particles and species and to quench the chemical reactions during the sampling, nitrogen flowed through the inner tube. Faccinetto [213] also performed comprehensive studies to investigate the effects of dilution, sampling time and probe aperture on the sample extraction. It was observed that a higher dilution rate did not have significant influences on the variation of heavier masses in comparison with that of light masses. Moreover, increasing the sampling line temperature can lead to more peaks in the mass intensities, especially for the light masses.

2.5.2.2 Soot structure

The sampling process is offline for the analyses of soot structure. There are generally two different sampling processes used to measure the soot structure. The first process is to use thermophoretic sampling. In this case, a carbon film or an atomically flat substrate is installed on the tip of the thermophoretic sampling system. The equipment is then shot into a flame for a short residence time. Then, the substrate is placed under TEM, AFM or SEM to identify the physical structure of soot. There are three main problems with the experimental steps. (i) The carbon film cannot be compatible with the high temperatures of flames. (ii) When particles coat onto the carbon film, there is a possibility of heavy aggregation between particles, which the soot structure cannot be precisely analysed using 2–D analyser (i.e. TEM). (iii) The quick thermophoretic

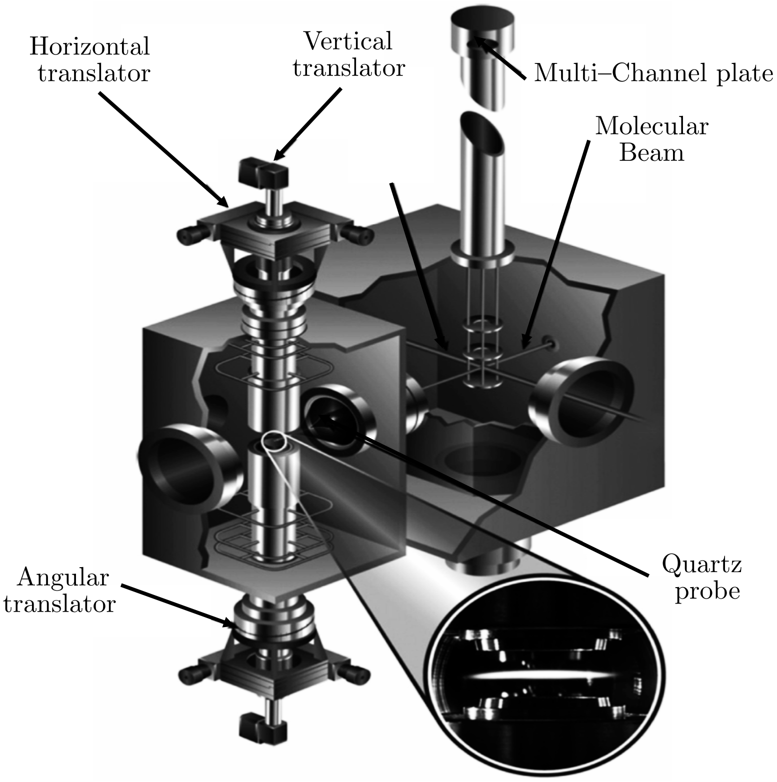

Figure 2.8. MBMS experimental setup used to measure chemical compositions [208]. The cone angle is a key parameter impacting the flame perturbation and species profile distribution.

sampling produces eddies and flame perturbation. The second option is to install the grid containing the substrate or carbon film somewhere in the transfer line to capture ultrafine particles. The sample losses in the transfer line should be minimised via applying suitable dilution and optimal operating conditions.

Amin et al. [203] used a transmission electron microscope (TEM) to analyse the impact of pressure on the soot morphology in counterflow ethylene flames. It was found that the mean primary particle diameter was a strong function of pressure. The mean diameter increased by a factor of three (from 17.5 to 47.1 nm) when the pressure was increased from 3 to 10 atm. Chemical structures with 5–membered ring were directly observed by Schulz et al. [45] and Commodo et al. [46] using high-resolution atomic force microscopy (AFM) in a premixed C_2H_4–air flame. This corroborates the role of cross–linked aromatic compounds in the formation of particulates.

Joo et al. [214] observed a substantial rise in the soot volume fraction with the increase in pressure. They referred the relationship between soot volume fraction and pressure to soot nucleation step and the coalescence of small soot particles. Moran et al. [215] conducted a numerical study to suggest a method to enhance TEM analyses by minimising potential errors. Such errors include the overlap and polydispersity of primary particles. Saffaripour et al. [216] noticed distinct physical structure differences between lean and rich flames. They observed smaller primary particles for lean flame conditions, while the impact of aggregation was evident in rich flames. Botero et al. [217] used a high resolution transmission electron microscopy (HRTEM) to study the morphology and nanostructure of soot particles produced using heptane, toluene, a volumetric mixture 50% heptane/50% toluene and a commercial gasoline. An algorithm was developed to enhance the image processing step by considering the interlayer-spacing between fringes in HRTEM. Longer and less curved fringes with more stacked layers were found for toluene flames. The reduced fringe length and increased tortuousity of soot from n-heptane flames stemmed from stronger oxidation.

2.5.2.3 Particle size distribution

Offline techniques to measure particle size distribution include AFM, TEM or SEM. Since the experiments are conducted offline, particular care should be taken to minimise particle losses along the extraction line. The process is time–consuming and expensive in comparison to the online SMPS method. Another problem with the above–mentioned offline techniques, e.g. AFM, TEM and SEM, are the analysing step. A large number of zones should be considered to provide the particle size distribution. Therefore, an analysis of a limited zone may not present the correct PSD. In some cases, the technique provides errors for particles with a high load of aggregations. In addition, particles with a diameter of $D_p \leq 10$ nm can be easily lost through the sampling process or within the instrument (TEM, AFM and SEM). Therefore, the results are not as robust as the SMPS technique. As the experiment is carried out online for SMPS, the optimum range of dilution should be initially quantified to minimise

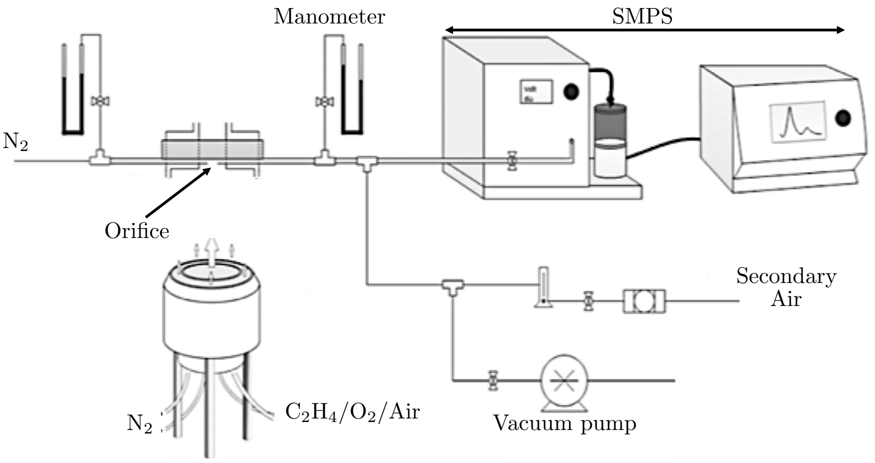

Figure 2.9. Experimental setup for measuring particle size distribution used by Wang and co–workers [218]. Optimum dilution ratio is used to minimise particle losses during extraction line; the dilution is varied via using different orifice sizes.

particle losses from the point of measurement to the detector. More details on SMPS experiments are presented in Chapter 7.

Almost all groups used a similar probe configuration with their respective sampling process for the measurement of particle size distribution, firstly utilised by Wang and co–workers [108]. The schematic is presented in Fig. 2.9. A steel tubular sampling probe was used to draw soot from the flame to the SMPS instrument. Nitrogen with a comparatively high level of dilution was injected to reduce particle losses within the extraction line.

One of the important factors for preserving the sample with minimum losses is the level of sample dilution. The impact of the dilution ratio on the total median mobility diameter and particle number density was studied to identify an appropriate limit of dilution at different flame conditions [218]. Nitrogen at 30 L/min was utilised to dilute the soot samples instantly. The dilution ratio was controlled by changing the probe pressure and nitrogen dilution. The former can be adjusted by regulating the pressure through the orifice. The latter can be monitored by using a set of probes with various orifice diameters. The limit provided the zone where the mobility diameter and particle number density were insensitive to variations of the dilution ratio. The optimum limit was reported for different flame structure. The dilution ratio limit was reported (250

– 750) and (5700 – 6500) for $\phi = 2.0$ and $\phi = 2.5$, respectively [32, 218]. For dilution ratios above the upper limit, sample losses occurred, especially for small particles. On the other hand, particle–particle coagulation was the main problem for dilution ratios below than the lower limit.

Aerodynamic probe configurations, with different probe diameters and angles, have been used to measure PAH and particle size distribution. The concentric tube is usually added to provide the sample dilution. It is necessary for PAH species and particles to be diluted for a sufficient quench of the chemical reactions [213]. Huang et al. [219] proposed a distinct configuration for gas and particle sampling probes. The particle sampling probe was diluted with N_2 although there was no dilution for gas sampling. Anderson et al. [220] designed two probes with distinct geometrical dimensions to detect gaseous species as well as particles. Anderson et al. [220] suggested that representative PM emission samples can be collected by gas probes although it was stated that it is necessary to perform a comprehensive study to explore an optimal design for gas probe over a wide range of engine conditions as well as dilution ratios.

Chapter 3

Experimental configuration

3.1 Introduction

A novel back–to–burnt opposed jet configuration [28–30] is here used to study turbulent ethylene–air flames that move from (effectively) lightly to heavily sooting conditions. The burner configuration and flow conditions are outlined in Section 3.2 and Section 3.3, respectively. The reasons for selecting a wide range of flame conditions are discussed in Section 3.3.2. The study features a combination of experimental techniques, including laser diagnostics and probe sampling, to infer the impact of changes in stoichiometry and rate of strain on the formation of particulates as discussed in Section 3.4. The details are provided to delineate the experimental setup for simultaneous laser diagnostics of ELS and PAH–PLIF in Section 3.5. Section 3.6 presents the details of probe sampling characteristics used to measure the concentrations of dominant gaseous species, PAH species and particles. The relevant measurement principles are discussed separately along with an uncertainty analysis. For instance, the probe effects are evaluated as functions of pressure suction and probe configuration. The ELS and PAH–PLIF are used to explain the sampling pressure impacts on the signals.

3.2 Burner configuration

A back–to–burnt opposed jet configuration offers noticeable advantages, including control of flow characteristics (chemical and turbulence time–scales [221]), aerodynamic flame stabilisation [222] and accurate boundary conditions [223]. In other words, the configuration assists in resolving issues with soot predictions along the burner centerline that have been found in simulations for coflow laminar diffusion flames.

Several different configurations of the opposed jet burner can be implemented based on the fuel and oxidiser streams. A non–premixed configuration is defined as a condition where an oxidiser stream is stabilised against the stream of fuel/diluted inert gas [224]. Twin flames corresponds to a case where identical premixed mixtures emerge from both nozzles with flames stabilised either side of the stagnation plane [225]. Lastly, the back–to–burnt (BTB) configuration features the stabilisation of a premixed fuel oxidation (reactant) stream against hot combustion products [226]. The latter configuration is utilised in the current study to assess the formation, growth, and oxidation of particles [227].

In prior studies conducted by our research group, experiments were primarily conducted under fuel lean conditions. Here, a brief background of previous studies is provided. Hampp et al. [94] investigated burning mode transitions from close to the corrugated flamelet into the distributed reaction zone regime by varying the stoichiometry of lean premixed DME/air flames at a constant turbulent Reynolds number ($\mathrm{Re}_t \simeq 380$) and a burnt gas state temperature of 1700 K using simultaneous Mie scattering, PIV and OH planar laser-induced fluorescence combined with a multi–fluid statistical description.

Lindstedt et al. [225] carried out experimental investigations for CH_4, C_2H_4 and C_3H_8 lean turbulent premixed flames over a wide range of Reynolds numbers to analyse flame structures. Goh et al. [228] performed a comprehensive study to investigate burning mode characteristics of premixed lean JP–10 flames by using particle image velocimetry (PIV) for Damköhler numbers from 0.3 to 6. A gradual combustion regime transition

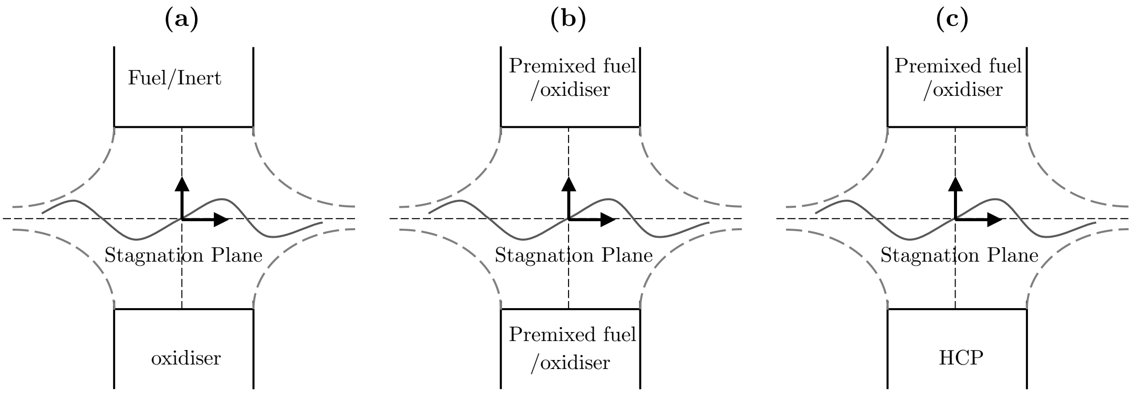

Figure 3.1. Opposed jet flame operation modes: (a) Non–premixed configuration with fuel/inert injected through the upper nozzle stabilised by the oxidiser from the lower nozzle; (b) Symmetric twin flame with identical premixed fuel/oxidiser mixtures injected through both nozzles. (c) Back–to–burnt configuration with premixed fuel/oxidiser injected through the upper nozzle and stabilised by hot combustion products emerging the lower nozzle.

was observed for $\phi < 0.6$. Rayleigh measurement and 1–D Raman were used to study the spatial profile distribution of species and the temperature profile in the opposed jet configuration [229]. Geipel et al. [230] utilised turbulence generating cross fractal grids in both lower and upper nozzle to increase the turbulent strain. Several experiments were performed to identify the optimum nozzle grid blockage with a high level of turbulence. It was found that a grid with a total area blockage of 65% provides the highest turbulent intensities with reasonable uniformity in radial fluctuations. The back–to–burnt opposed jet burner [228–232] features cross fractal grid, installed 50 mm upstream the upper nozzle exit, to generate turbulence multi-scale turbulence with significantly elevated levels [222, 223, 228, 230].

The extension of the opposed jet geometry to much more practical conditions has been achieved through the use of fractal grid generated turbulence, as shown in Fig. 3.2. The fractal grids should have a part to play in bridging the gap to practical devices. Cross fractal grids with different configuration were assessed by Geipel et al. [230]. The aim was to evaluate the rate of increase in the turbulence intensity as cross fractal grids were used instead of conventional plates. The turbulent flow was comparatively well developed at the nozzle exit. A further important point is that fractal grids generate multi–scale turbulence directly. The burner configuration used in the current study

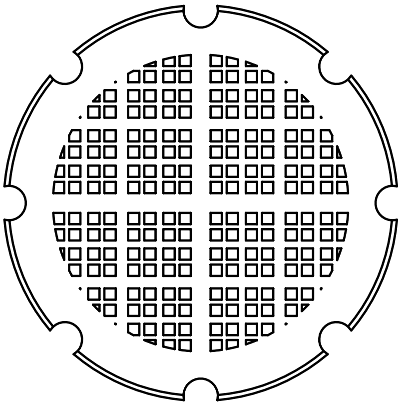

Figure 3.2. The well–developed cross fractal grid (CFG) used in the upper nozzle (UN) generating the required multi–scale of turbulence. The grid showed the best efficiency for the increase of turbulence intensity among other grid configurations [230].

is based on the established geometrical advancement presented by Geipel et al. [230]. The exception is that a lower nozzle with longer length (100 mm) is used to ensure HCP homogenisation at the nozzle exit.

3.2.1 Gas mixing system

A series of digital Bronkhorst mass flow controller (MFC) was used in the current study. A LabView interface facilitates the accuracy of flow rate adjustments. Fuels were supplied to each burner at a pressure of 4 bar (g). High purities of gaseous fuels were used: H_2 (99 %), N_2 (99 %) and 44–WW nitrogen pallet (99 %). One more nitrogen cylinder (99 %) was utilised to provide the desired dilution gas when probing techniques were used. The optimum nitrogen dilution gas can reduce species and particle losses within the sampling system. Nitrogen with 20 LPM is usually used at the beginning and end of the process to avoid flashback in the system in the upper nozzle.

The 44–WW nitrogen pallet is used as a source to maintain flame unaffected by environmental disturbances. A relief valve is used with the nitrogen pallet to provide simple, reliable, over–pressure protection. Special care should account for the pallet in the lab, and some initial leak process should be conducted to minimise probable safety risks. The ventilation system should be checked regularly to ensure the proper safety

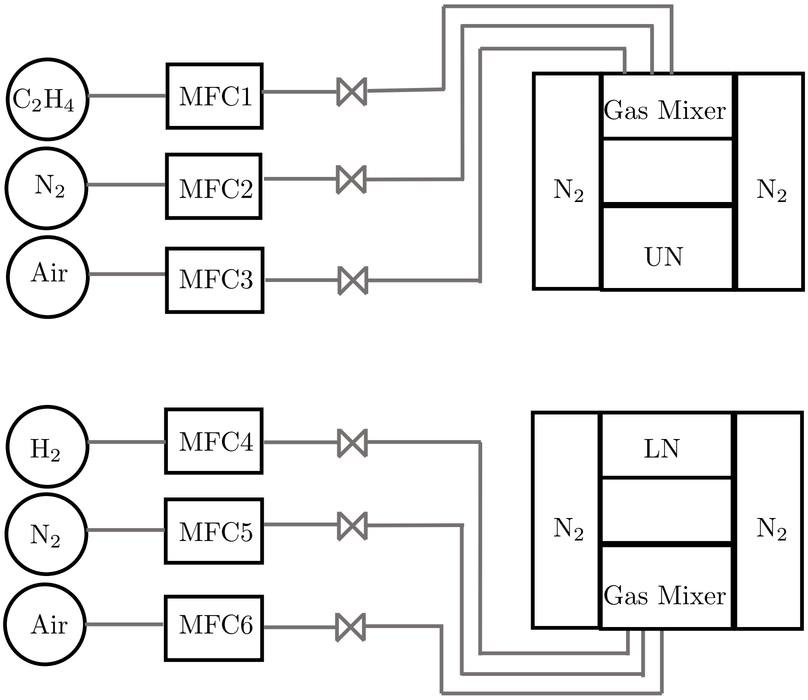

Figure 3.3. Gas supply and gas mixing system. MFC – mass flow controller; LN – lower nozzle; UN – upper nozzle; 44–WW – nitrogen pallet. The nitrogen with 20 LPM is used at the beginning and end of process to avoid flashback in the system in the upper nozzle. One more nitrogen cylinder is used to provide sample dilution when probe sampling is used.

conditions before initiating experiments.

3.3 Experimental conditions

The opposed jet configuration is depicted in Fig. 3.4. An opposed jet configuration, initially developed by Geyer et al. [229], subsequently modified and used to study combustion regime transitions under fuel–lean conditions [28, 29, 222, 232] is here used to study fuel–rich flames. The back–to–burnt opposed jet burner configuration features cross fractal grids, installed 50 mm upstream of the upper nozzle exit, to elevate turbulence levels. The turbulent and chemical time scales can be accurately controlled by individual parameters. Counterflowing hot combustion products (HCPs), produced by a stoichiometric hydrogen flame with a diluted fuel stream (H_2/N_2) resulting in burnt gas temperatures of 1400–1700 K, were used. The burnt gas was generated by

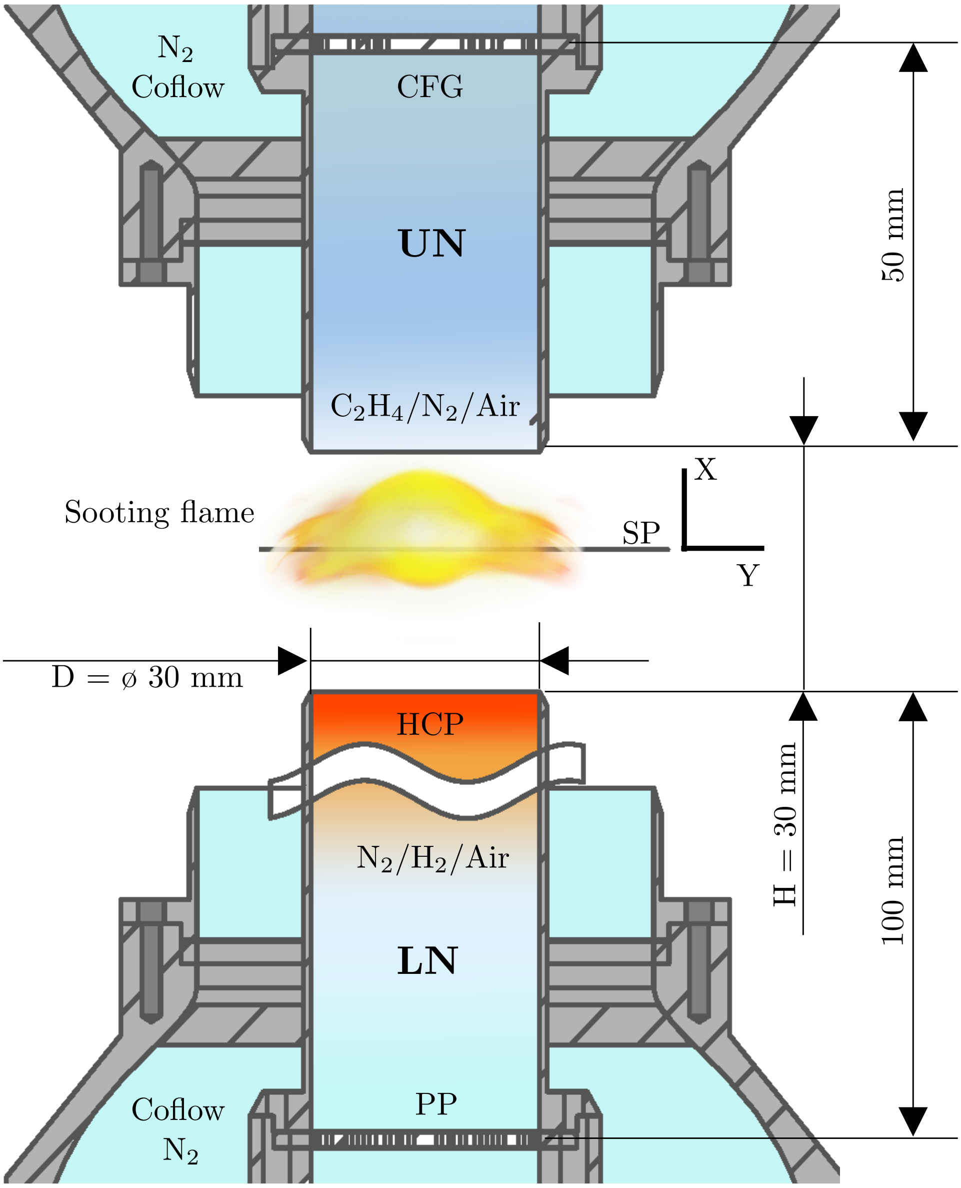

Figure 3.4. Schematic of the experimental configuration. Premixed fuel/air is introduced in the upper nozzle (UN) stabilised by hot combustion products (HCP) from a stoichiometric H_2/N_2/air flame in the lower nozzle (LN). CFG – cross fractal grid, PP – perforated plate, SP – stagnation plane.

stabilising flames on the perforated plate (PP) located 100 mm upstream of the lower nozzle (LN) exit. The HCPs are used to provide aerodynamic flame stabilisation. The HCP temperature was controlled by the N_2 and H_2 dilution rate. The temperature at the lower nozzle exit was measured using an R–type thermocouple. The equivalence ratio was maintained constant at $\phi_{LN} = 1.0$ to reduce differential leaning of the opposing UN reactants through mixing across the stagnation plane. The temperature of the air stream was regulated to 320 K to achieve repeatable conditions. The burner is surrounded by an annular shroud which provides nitrogen to shield the flame from environmental disturbances and limit the flame propagation. The premixed ethylene/air mixtures, injected through the upper nozzle, are stabilised against the HCPs. The elongated LN assured that the HCPs are in thermochemical equilibrium at the nozzle exit, providing a well–defined burnt gas state to the stagnation plane. The aerodynamic stabilisation of the stagnation plane in the proximity of the burner centre is achieved by jet momentum matching. The nozzle separation is set to the burner diameter for (close to) optimal flow stability [225]. The burner is equipped with a cooling water system to maintain the burner in a well–operated conditions as it can resist high temperature for a number of experiments over a long run time. An air dryer is used to filter moisture in the air. Several check valves are used in the pipelines prior to burners to avoid backflow in the fuel system line.

The experimental conditions adopted in the present work correspond to lightly and heavily sooting flames in premixed turbulent flames. A summary of the experimental conditions is presented in Table 3.1. The selected limit for probe measurement is to cover flames with different sooting characteristics. The reference (REF) flame contains a HCP temperature of $T_{HCP} = 1500$ K and a total rate of strain $a_T = 420$ s^{-1} and equivalence ratio of $\phi_{UN} = 2.0$.

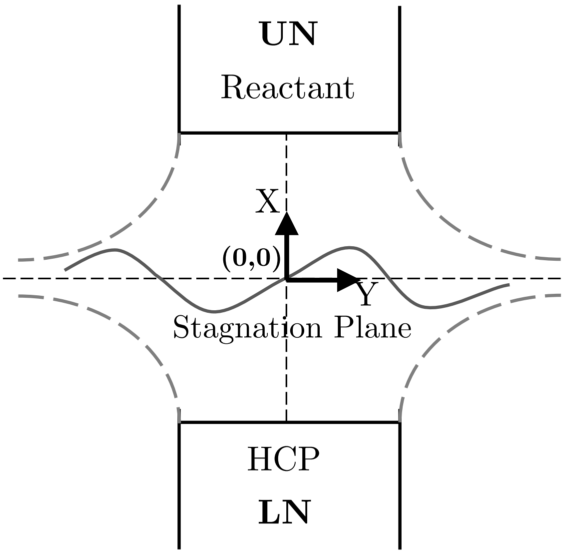

Figure 3.5. Coordinate system convention. UN – upper nozzle; LN – lower nozzle; HCP – hot combustion products, X – axial coordinate, Y – radial coordinate, Z coordinate is perpendicular to X and Y. A target plate was mounted on the burner to ensure that laser light sheet superposition is aligned appropriately. The ELS laser is used to adjust probe tip at Z = 0. Axial and radial coordinates of probe tip is adjusted using ELS camera.

Table 3.1. Experimental conditions used to study the impact of equivalence ratio, rate of strain and burnt gas temperature. The UN and LN fuels are C_2H_4 and H_2, respectively, and ϕ_{LN} = 1.0 with $\alpha = X_{H2}/X_{N2}$, where X indicates a mole fraction, used to control T_{HCP}, U is the upper nozzle bulk velocity and u' the velocity fluctuations. The reactant temperatures are T_r = 320 K, L_I = 3.9 ± 0.2 mm is the integral length scale of turbulence, $Re_t = u'L_I/\nu$ the turbulent Reynolds number and $a_t = (\varepsilon_r/\nu_r)^{1/2}$ is the turbulent, $a_b = 2U/H$ the bulk and $a_T = a_t + a_b$ the total rates of strain [233]. ε_r is the rate of dissipation in the reactants and ν is fluid viscosity [234]. Values shown in brackets feature only CH_2O/PAH–PLIF and ELS measurements.

Variation	Reactants	HCP	Rate of Strain
ϕ_{UN} [-]	(1.7), 1.8, 2.0, 2.2	2.0	2.0
a_b [s^{-1}]	120	120	80, (105), 120, (135), 160
a_t [s^{-1}]	300	300	175, (253), 300, (357), 450
a_T [s^{-1}]	420	420	255, (358), 420, (492), 610
Re_t [-]	72	72	50, (64), 72, (81), 94
U [m s^{-1}]	1.8	1.8	1.2, (1.6), 1.8, (2.0), 2.4
u' [m s^{-1}]	0.30	0.30	0.21, (0.26), 0.30, (0.33), 0.39
T_{HCP} [K]	1500	1400, 1500, 1600, 1700	1500
α [-]	0.51	0.43, 0.51, 0.64, 0.75	0.51

3.3.1 Flame parameters

Combustion in practical applications occurs in turbulent flows characterised by unsteady, chaotic and random motions. The turbulence can, at an indicative level, be characterised using critical quantities of kinetic energy and the integral length scale. The former accounts for the primary energy and momentum transport, and is proportional to the associated turnover velocity [235]. The latter is the characteristic length scale for the turbulent eddies and vortices. The non-dimensional parameter of Reynolds number (Re_t) is used to characterise turbulent flow and is calculated using Eq. (3.1),

$$Re_t = \frac{u' \; L_I}{\nu_r} \tag{3.1}$$

where ν_r is fluid viscosity. The integral length scale of turbulence and the velocity fluctuation (u') was inferred from hot wire anemometry and PIV, respectively. More details on the calculation of L_I and u' for the current conditions can be found elsewhere [233].

The rate of dissipation (ε_r) in the reactants can be determined using Eq. (3.2) for locally axisymmetric turbulence. The method was comprehensively explained by George and Hussein [234] as applied by Goh et al. [233],

$$\varepsilon_r = \nu_r \; . \; \left[-\overline{\left(\frac{\partial u}{\partial x}\right)^2} + 2 \; . \; \overline{\left(\frac{\partial u}{\partial y}\right)^2} + 2 \; . \; \overline{\left(\frac{\partial v}{\partial x}\right)^2} + 8 \; . \; \overline{\left(\frac{\partial v}{\partial y}\right)^2} \right] \tag{3.2}$$

The bulk rate of strain (a_b) is correlated with bulk velocity (U) and the distance between nozzles ($\mathrm{H} = 30$ mm), and is calculated based on Eq. (3.3),

$$a_b = \frac{2 \; U}{H} \tag{3.3}$$

The turbulent rate of strain is characterised by random velocity fluctuations leading to the movement of any two points on a flame surface further apart, and is the factors of dissipation rate of the turbulent kinetic energy (ε_r) within the reactants and kinematic viscosity as discussed by Peters [236]. The relationship of Kostiuk et al. [237] was used to estimate the turbulent rate of strain (a_t) as shown in Eq. (3.4),

$$a_t = \left(\frac{\varepsilon_r}{\nu_r}\right)^{1/2} \tag{3.4}$$

The magnitude of the total rate of strain can be calculated by the sum of the bulk and turbulent rate of strain as presented in Eq. (3.5),

$$a_T = a_b + a_t = \frac{2\,U}{H} + \left(\frac{\varepsilon_r}{\nu_r}\right)^{1/2} \tag{3.5}$$

3.3.2 Flame conditions

The photographs, shown in Fig. 3.6, illustrate the range of experimental conditions from lightly to the heavily sooting flames via bulk rate of strain and equivalence ratio adjustments as listed in Table 3.1. The selected flame conditions are the results of the interactions between physical and chemical processes, leading to the formation and oxidation of soot particulates. The formation of soot precursors or the oxidation of soot is affected by the flame motion, and the fluid mechanics governing the flame evolution. The interactions affect the structure of the turbulent flames, the progress of reactions, the relationships among species concentrations, and the formation of pollutants over wide ranges of spatial and temporal scales [8].

All flames are self–sustained (i.e. detach from the stagnation plane) [238]. The demise of PAH is aided by the elevated temperatures found in the nearly sooting flame $\phi_{UN} = 1.7$ and $a_T = 610$ s^{-1}) leading to enhanced oxidation. In contrast, flames at low rates of strain or high equivalence ratios are far richer and less hot than the lightly sooting flames, favouring the formation and survival of PAHs [239].

The current flame conditions, see Table 3.1, were selected to cover a range of scales

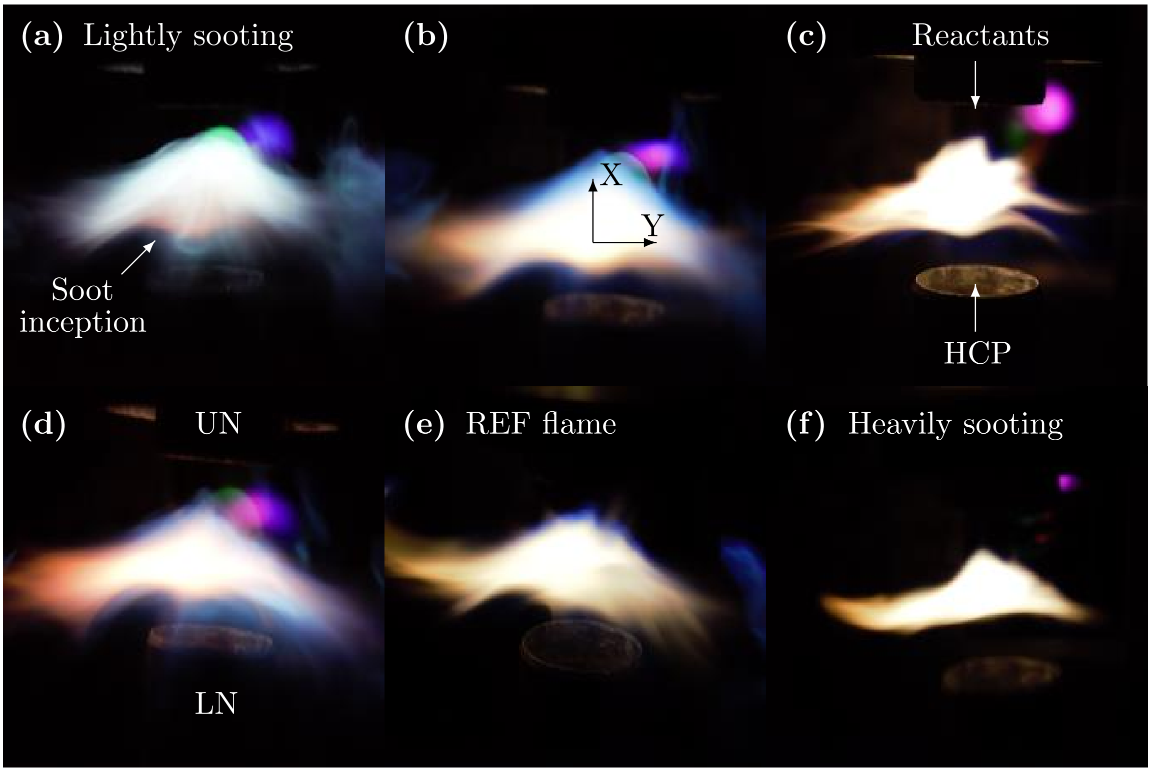

Figure 3.6. Sample photographs illustrating the experimental conditions used in the current study. Top row: ϕ_{UN} variation at a constant total rate of strain of a_T = 420 s^{-1} for (a) ϕ_{UN} = 1.7, (b) ϕ_{UN} = 1.8 and (c) ϕ_{UN} = 2.2; Bottom row: a variation of the rate of strain at constant ϕ_{UN} = 2.0 for (d) a_T = 610 s^{-1}, (e) a_T = 420 s^{-1} (Reference flame) and (f) a_T = 255 s^{-1}.

affecting the formation of soot and soot precursors. The flame with a stoichiometry of ϕ_{UN} = 1.7 and a_T = 420 s^{-1} is the lightest sooting condition shown and features a strongly intermittent appearance of soot. The soot layer thickness increases significantly with a decreasing rate of strain and increasing equivalence ratio with the flames becoming bright yellow/orange at ϕ_{UN} = 2.2 and a_T = 255 s^{-1}. The HCP temperatures of 1400, 1500 and 1600 K were chosen based on observed flame characteristics with higher luminosity at 1500 K than 1400 K and a change to pale yellow at 1600 K. Hampp and Lindstedt [85] have shown that the impact of the HCP temperature is comparatively modest for fuel–lean self–sustained flames that detach from the stagnation plane. The influence of the HCP on the flames is limited to soot oxidation at the stagnation plane and heat transfer between the flame and the HCP stream.

3.4 Measurement process

A schematic of various measurement methods used in the current study is depicted in Fig. 3.7. The flame structures are initially analysed using PAH/CH_2O–PLIF and elastic light scattering (ELS). The laser–based diagnostics were used to illustrate spatial distributions and to identify the ideal locations for probe sampling. The results from laser diagnostics show that physical and chemical evolution plays a crucial role in the formation of particulates over the reaction zone layer with the maximum intensity at $X/L_I = +0.5$ (close to the stagnation plane).

In the next step, the probe sampling is located at $X/L_I = +0.5$, and various dilution ratios applied. For PAH experiments, the optimum dilution ratio (DR) is in a range where no PAHs are found in the extraction line, and all PAHs are deposited on the filter unit. For SMPS experiments, the optimum dilution ratio is in the limit where the particle size distribution is independent of DR values.

When the optimum dilution ratio is quantified, the spatial distribution of PAH species and particulate matters are quantified for various experimental conditions. It is important to note that a different approach is used for the measurement of dominant gaseous species. These measurements are conducted without using dilution ports and with sodium sulfate in the filter unit to remove water vapour. More details are provided in relevant Chapters.

3.5 Optical diagnostics based measurements

A simultaneous laser diagnostics technique, including ELS and CH_2O–PAH PLIF, is used in the current study. The setup contains Spectra–Physics Quanta–Ray Lab–150, Nitron lasers, a nano–PIV laser. A light source, e.g. a Spectra–Physics Quanta–Ray Lab–150 with external frequency tripling, is used for the CH_2O–PLIF measurements.

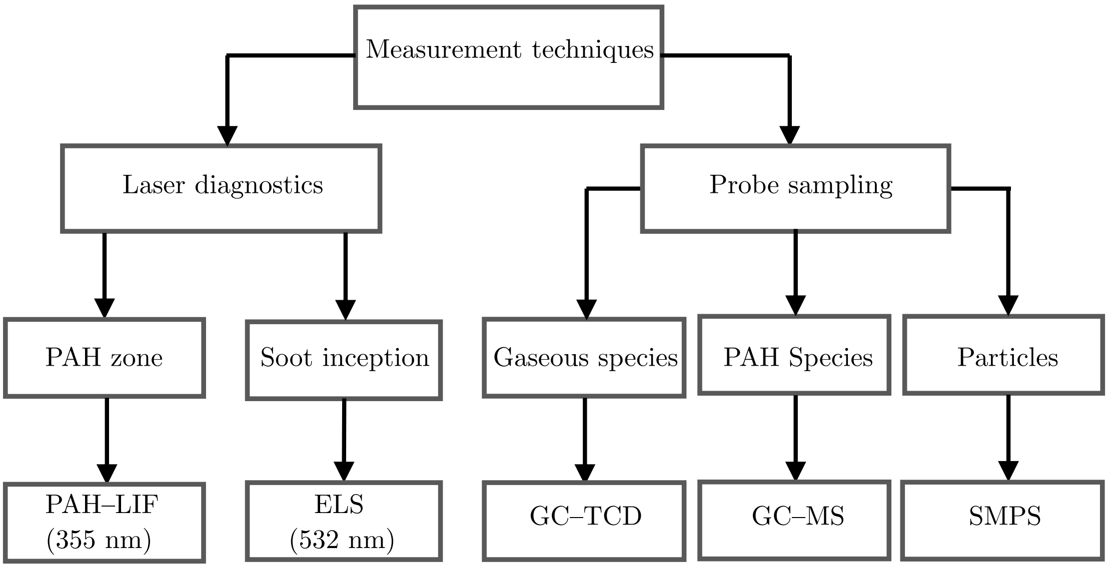

Figure 3.7. The measurement techniques used in the current study. PAH – polycyclic aromatic hydrocarbon, LIF – laser-induced fluorescence, ELS – elastic light scattering, GC – gas chromatography, TCD – thermal conductivity detector, MS – mass spectrometry, SMPS – scanning mobility particle sizer

The 3rd harmonics of the Nd:YAG laser at the wavelength of 355 nm is used to excite CH_2O and can be added to ELS setup. The CH_2O emission occurs at the wavelength of 380–470 nm, which allows the spectral separation using dichroic filters. More details on optical diagnostics setup are presented in Chapter 4.

3.6 Probing based measurements

Sampling pollutants inside fuel rich flames is a challenging endeavour as the incomplete combustion can lead to very high concentrations of PAHs and soot particles. The major losses in sampling system are caused by thermophoretic diffusion (temperature gradients), particle coagulation and sedimentation. To accurately measure emissions, samples should be diluted very quickly to prevent coagulation and formation of new aerosols through condensation of low volatility species.

There does not exist a standard sampling procedure. All the detailed pollutant studies to date have used distinct sampling system configurations to measure species and soot particulates. Scientific questions and engineering challenges are summarised here:

- A key question is if the same sampling probe system and configuration can be used for the measurement of gaseous and PAH species, and particulate.
- There is a need to evaluate whether the dilution probes are absolutely necessary for the precise sampling of PAH species and particles. In a case that dilution is needed, the difference in the level of dilution should be clarified to present the actual concentrations of PAH species and particles.
- The different processes should account for the low–loss detection of major gaseous species, PAH species and soot particulates. There is a need to develop optimal sampling approaches, including low–loss probes and transmission lines for gaseous, PAH species and particulates.
- A detailed analyses of particle evolution within sampling systems under typical operating conditions of temperature and suction pressure should be scrutinised.
- Another remaining question is whether an aerodynamic–quench sampling probe should be developed for the accurate measurements of species.

The impact of losses can only be dealt with by designing the system to maximize transport efficiency and then conducting careful characterization studies of each implementation to quantify the sampling losses and develop empirical equations for correcting important emission parameters. One of the novelties of the current study is to establish a sampling system with minimum sample losses for PAH species and particulates. As an example, a sampling process is divided into multi–stages consisting of collection, extraction and preparation to study incipient particle compositions. An optimum dilution range is applied to slow down the condensation of particles and PAH species, and to quench the chemical reactions appropriately [240]. The sampling process is conducted differently for major gaseous species, PAHs and soot particulates, while the same probe configuration is used.

3.6.1 Sampling system characteristics

3.6.1.1 Probe configuration

The designed quartz probe, manufactured by Hilgenberg GmbH, features aerodynamic quenching and individually adjustable probe tip and transfer–line nitrogen dilution as shown in Fig. 3.8. Quartz is extremely pure materials featuring very low thermal expansion, inert to most materials and with good chemical resistance at high temperatures. It is important to select an aperture for a probe such that there is a balance between the spatial resolution and collected substances. The probe tip orifice diameter is 286 μm (see Fig. 3.8) and thus below 10% of the current integral length scale of turbulence (L_I) to reduce interference effects [241]. This diameter further determines the spatial resolution and limits non-uniformities caused by gradients of the mean–field and turbulent fluctuations.

The aerodynamic shape of the probe is designed based on the recommendations of Fristrom and Westenberg [242]. An opening angle of 20 degrees minimises flame disturbance while providing sufficient sample quenching [210]. The probe tip divergence is less steep in the flame region and then increase significantly. The configuration limits flame perturbation effects.

3.6.1.2 Dilution box

A dual–port dilution box is to used to provide an appropriate range of dilution ratio for PAH species and particulates. The dilution can minimise the critical losses through the system. To avoid trapping gas residue in the sampling system and possible error from a sampling set to another, a flow of nitrogen is injected into the sampling system (between experimental sets) using two dilution ports.

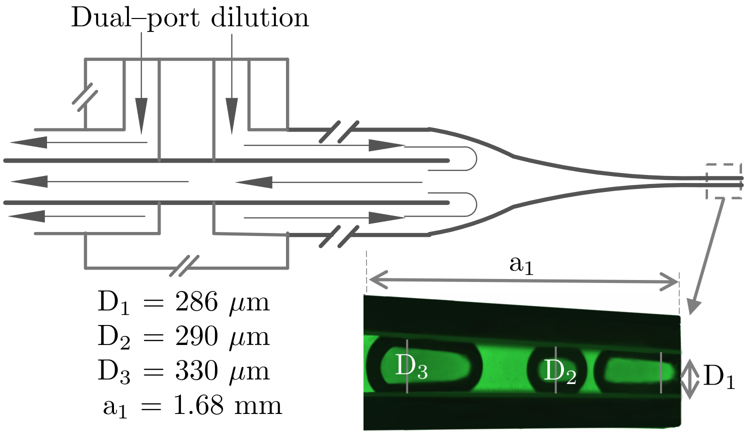

Figure 3.8. Quartz probe configuration used to measure chemical compositions and particle size distribution. The design principle is to provide the minimum flame perturbations and proper species/aerosol quenching. Nitrogen dual port dilution is used to apply the required optimum ratio with the aim of minimum species and particle losses in extraction line for PAH and particle size distribution, respectively.

3.6.1.3 Sampling line adjustments

The sampling line assembly can be traversed in the horizontal and vertical directions using linear translation stages, and the sampling location is calibrated using the optical setup. The ELS camera determines the X and Y position (i.e. $Y/L_I = 0$, and X/L_I in a step of 0.5) and the laser light sheet the alignment of the probe tip with the theoretical stagnation plane. An interline-transfer CCD–camera (LaVision Imager Intense) is utilised to adjust the location of the tip of the sampling probe. A Litron LG 175 laser at low power is used to align the probe tip with the laser light sheet to the burner centre; the probe is moved into the measurement region between the two nozzles until the laser light sheet edge is reflected from the probe tip. The required probe movements at various heights are calibrated for the measurement campaigns using the linear adjusters. The positioning of the sampling system (i.e. probe tip) on laboratory jacks and sliders enables a fine adjustment with an accuracy of about 0.1 mm.

3.6.1.4 Filter unit configuration

Different filter configurations were evaluated in terms of compound filtration/extraction efficiency according to the aim of the study. The filter unit is different for experiments performed to determine (i) major gaseous species (ii) PAH concentrations (iii) particle size distributions. (i) Preliminary results showed that the profile distribution of major gaseous species can be affected when the sample contains water vapour [241]. A filter unit consists of a series of quartz wool and sodium sulphate is used to remove water vapour [243]. (ii) PAH sampling experiments features a filter unit with a series of quartz wool and XAD. Direct analysis of the species concentration recorded with the quartz fibre filter in place can lead to incorrect conclusions for the PAH sampling experiments as discussed above. (iii) The filter unit configuration consists of quartz wool to filter particles in the bypass line and to provide the upper limit of desirable dilution ratio.

3.6.1.5 Sampling line pressure

One of the critical factors in the sampling collection process is to avoid pressure fluctuations along the extraction line. A large volume is usually recommended to prevent any pressure fluctuations while sampling species. The pressure fluctuation in the sampling system is shown in Fig. 3.10. The data were measured using a constant volume and leak–free setup, and the flow rate through the probe tip was inferred from the pressure increase. The static pressure (number 1 in Fig.3.9) is recorded using a pressure transducer (UNIK 5000; GE Measurement and Control).

The schematic is shown in Fig. 3.9. The pressure fluctuations are initially studied for several cases and new volumes are added into the sampling system accordingly. The dilution box is initially enclosed via a cylinder plate (in the absence of the quartz probe) to assess potential leaks in the system. The multiple valves are installed in the different locations of the sampling system, and the leak test was completed between parts step by step. As shown in the figure, there is no leak in the system (Cases 5 and

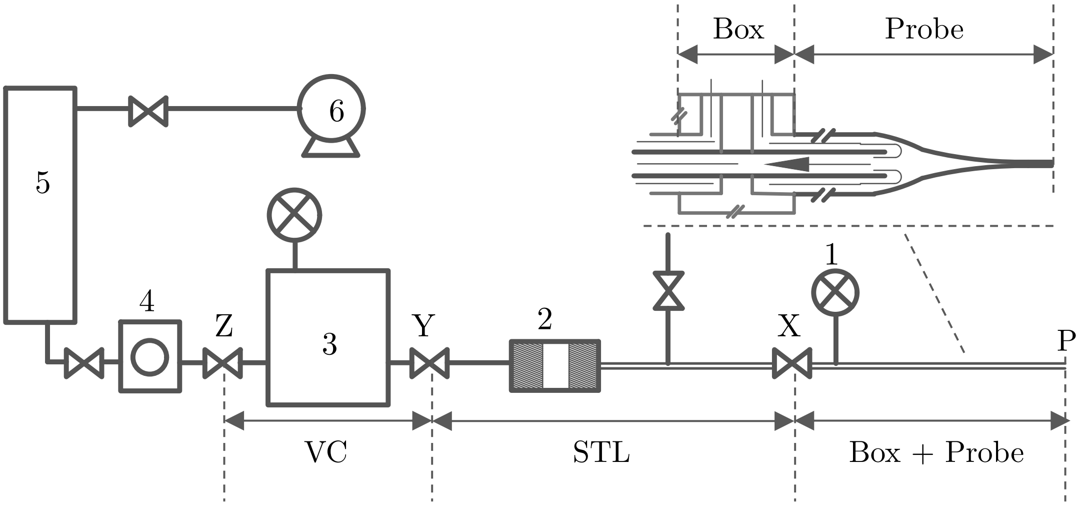

Figure 3.9. Sampling system tested for pressure fluctuations. 1) Pressure transducer; 2) Filter unit; 3) Vacuum chamber; 4) Vacuum regulator; 5) Vacuum volume; 6) Vacuum pump; X, Y and Z) Valve. STL – short transfer line; VC – vacuum chamber.

6) and the rate of increase in pressure versus time is negligible.

When probe sampling is connected directly to a vacuum pump (Valve X, Case 1), the pressure reaches ambient quickly. This illustrates the worst–case scenario while suction pressure lost after a short sampling time. When the short transfer line (STL) is added into the system (Valve Y, Case 2), the static pressure in the sampling system increase to atmospheric pressure after 25 seconds. Adding a long transfer line (LTL) (Case 3) leads to a constant pressure for further 10 seconds.

The existence of vacuum chamber (26.5 l volume) enhances the sampling collection process, and no pressure fluctuation is found within the sampling system. The static pressure can be constant irrespective of reasonable sampling time (Valve Z, Case 4). The differential pressure versus time is shown in Fig. 3.11. The pressure differential between flame and sampling system is controlled via using a vacuum regulator. The sampling probe offers an approximately constant sampling rate over a wide range of probe pressure. The sampling pressure is maintained constant at 20 mbar throughout the sampling probe study, and frequent leak tests are performed to preclude sample contamination. The pressure differential of $\Delta P = 20$ mbar also provides a minimum flame disturbance as discussed in Section 3.6.1.7.

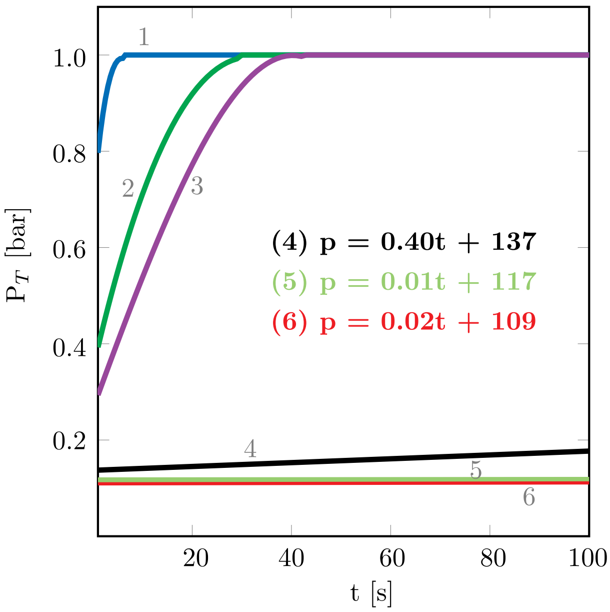

Figure 3.10. Pressure fluctuation based on volume used in the sampling system.(1) box + probe ; (2) STL + box + probe; (3) LTL + STL + box + probe; (4) black line: VC + STL + box + probe; (5) green line: VC + STL + box; (6) red line: box. STL – short transfer line, LTL – long transfer line, VC – vacuum chamber.

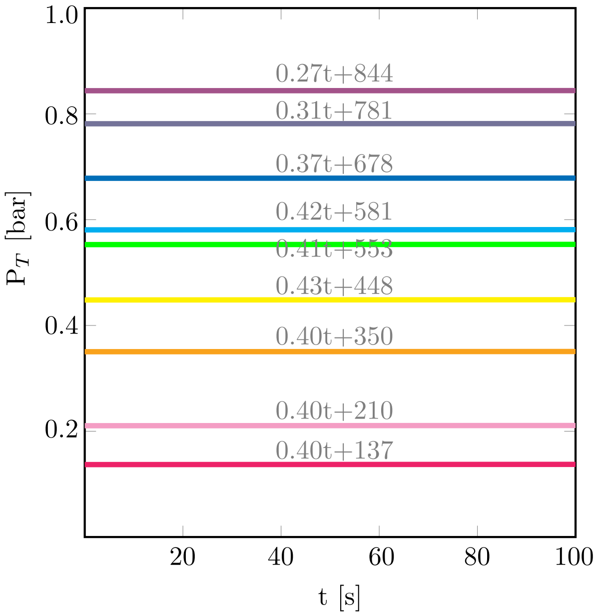

Figure 3.11. The static pressure in the sampling system versus time. The lines show the different static pressure in the sample line controlled using a vacuum regulator.

3.6.1.6 Sampling process

Sampling is initiated by connecting the transfer line and probe to the large vacuum vessels. A sampling time of about 10000 integral timescales of turbulence is used (120 s) to ensures statistical independence of the sample during which the sampling pressure is constant. The sampling process is terminated by disconnecting the suction probe from the vacuum system. A flow of nitrogen is injected into the sampling system using two dilution ports to avoid trapping residue in the sampling system and possible error from a sampling set to another. This process is repeated at the end of the sampling measurement for other experimental sets.

3.6.1.7 Probe effects

Probe sampling is a fairly well–established technique. However, it can disturb the flow and the temperature fields of a flame. A quantitative understanding of the probe effect is challenging as the mutual impact of probe configuration and sampling conditions (i.e. the applied ΔP for pressure suction) need to be taken into account for the evaluation of flame perturbations [244]. The probes that have been used so far are significantly different in size, opening angle, orifice diameter, from one experimental group to another. The recommendations given in the literature are probably not consistent, and a standard probe design does not exist.

Studies under laminar conditions provide relevant guidance. For example, the temperature gradient is reported to be less pronounced in the reaction zone than the region close to burnt gases [245] and it has been shown that probe effects are minimised when the flame is located far on the fuel side of the stagnation plane [244]. Also, flow perturbations were found to decrease with increasing burner-probe separation [246].

The experimental process faces challenges as the existence of a solid material can lead to the damage to the camera in a case that there is a laser reflection from the probe tip to the camera. Therefore, the whole process was conducted with specific care to eliminate any damage to optical devices. At the initial stage, the cameras are covered by the

Table 3.2. The peak shift and ratio of the signals (ELS and PAH–PLIF) for various suction pressures compared to the reference case without a probe. The number shown in the figure corresponds to the location of the peak value.

Number	ΔP (mbar)	Peak ratio		Peak shift	
		ELS	PAH	ELS	PAH
1	20	0.98	0.99	0	0
2	40	0.91	0.94	0	0.16 L_I
3	150	0.75	0.95	0.10 L_I	0.32 L_I
4	250	0.70	0.96	0.10 L_I	0.51 L_I

cap and the laser powers are gradually increased to ensure that there is no reflection from the probe tip to the camera. The probe impacts on ELS and PAH–PLIF signals are studied for different flame conditions after the operation procedure is finalised for the laser–probe experiments.

In turbulent flames, species profiles extend over a much broader spatial domain as a result of turbulent transport and flame-front folding [247], and it is reasonable to expect a reduced impact of the sampling probe. The PAH–PLIF and elastic light scattering are used to determine the flow perturbation of the probe at different suction pressures. The details on laser diagnostic methods are discussed in Chapter 4. The experiment is conducted for the reference (REF) flame at X/L_I = 0.5. The REF flame featured a HCP temperature of 1500 K, an equivalence ratio of $\phi_{UN} = 2.0$ and a total rate of strain of $a_T = 420$ s^{-1}.

The impact of sampling conditions on the PAH and ELS signals is shown in Fig. 3.12. The signals are normalised by the corresponding maximum value among the cases presented in each subfigure. The numbers (1–4) corresponds the peak value of signals at specific ΔP. The peak shifts and ratio of the signals, compared to the case without the probe, are presented in Table 3.2. The analysis shows that the mean PAH and ELS profile peak and location are not affected by the presence of the probe at a suction pressure of 20 mbar. At higher ΔP the profiles deviate from the undisturbed profiles. The peak value of the PAH–PLIF signal shifts by 0.51 × L_I (~ 2 mm) toward the reactants at ΔP = 250 mbar. The maximum ELS signal reduces by 30% at ΔP = 250 mbar.

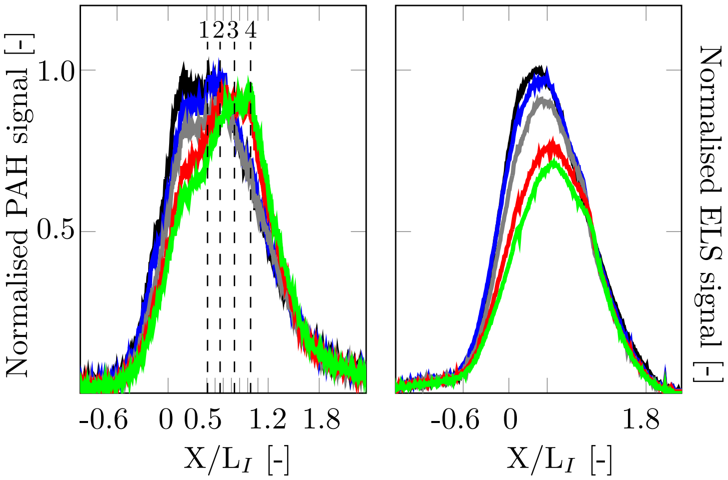

Figure 3.12. The probe effects on PAH–PLIF (left) and ELS (right) at different sampling pressure suction. Black (flame); Blue (ΔP = 20 mbar); grey (ΔP = 40 mbar); red (ΔP = 150 mbar); green (ΔP = 250 mbar). Signals are normalised by the corresponding maximum value among the cases presented in each subfigure.

3.6.1.8 Probe clogging

One potential source of errors is caused by clogging at the probe tip [248, 249]. The static pressure of the sampling line (pressure transducer) is recorded regularly for each set. In a case that there is a pressure fluctuation or sudden variation in the sampling line, the experiment is stopped to check any signs of probe clogging. The clogging at the probe tip is seen for the heavily sooting case of a_T = 255 s^{-1}, while the impact is not critical for all other experimental conditions. Wang and co–workers [218], and Roberts and co–workers [27] used a fine needle/wire to resolve orifice clogging between experimental cases. Camacho et al. [218] reduced the sampling time (50 s) to avoid clogging at the probe tip. The sampling time was chosen to provide a compromise between size distribution smearing at short times and orifice clogging at long scan times. In the current study, a different approach is chosen to minimise uncertainties, avoid experimental interferences or errors and potential probe cracking. The probe is disconnected from vacuum suction, and nitrogen flow is used to direct soot particulates to the outside of the probe tip. The sampling line assembly is traversed in X directions close to the burnt gas state using linear translation stage. The probe is at a point where there is no trace of particulates. Particle, clogged at the probe tip, will then burn at the high temperature and be pushed out with the assistance of the nitrogen flow.

3.7 Applied diagnostic techniques

3.7.1 Gas chromatography–mass spectrometry

Chromatography is defined as the separation of a mixture of compounds into individual components. Gas chromatography (GC) includes three steps for the separation and identification of a mixture. First, the sample is injected into the GC inlet. Second, the compounds in the sample interact with the column. Third, the elution of compounds at a different time is processed in the detector. The elution time is dependent on both compound molecular weight and boiling point. The GC inlet type is usually selected according to the kind of analysis, sample and the column. The GC column is an interface connecting the GC inlet to the detector and is located inside the oven. Each column has specific features, i.e. internal coating, capable of separating certain compounds. As an example, the Select–PAH column (CP7462) used in the PAH sampling experiments has the the capability to identify PAH and other aromatic species. For initial experiments, different columns including HP-5ms, Db–1 were used for mass spectrometer (MS) detector. It is found that the Select–PAH enhances selectivity towards PAHs, separating the isomers and enable the accurate analyses of PAHs.

The separation can be significantly enhanced by using an optimal gas flow and complex GC temperature profile. The identification of compounds is completed using a detector. An electrical signal proportional to the compound abundance is produced as each compound reaches the detector. Agilent ChemStation software is used to provide data analyses on chromatogram peaks. The detector type should be chosen based on the compounds of interests. For instance, the mass spectrometer (MS) can provide a precise analysis for heavy species up to $m/z = 300$ while the accuracy is a factor of the column and sample type. The mass spectrometer comprises three main components. (i) The ionisation is completed using either electron ionisation (EI) or chemical ionisation (CI). (ii) An analyser (quadrupole) accelerates and separates charged ions depending on their mass-to-charge-ratio (m/z). (iii) A detector (electron multiplier) identifies ions from the analyser. On the other hand, a thermal conductivity detector (TCD) provides the identification of gaseous species with low molecular weight, including CO and CO_2. The TCD chromatogram responses are the result of the difference between the thermal conductivity of compounds and the utilised carrier gas. A helium or hydrogen carrier gas is usually recommended for TCD due to a higher difference in the relative thermal conductivity in comparison to other gaseous compounds.

The ion count is a non–unit parameter. The response of the chromatographic system can be under the influence of routine variations and the detector response needs a regular calibration using known standard species. The normalisation of the compound peak value (to a reference peak), used by some research group, can lead to significant uncertainty. The sampling needs to be calibrated using standard solutions due to routine variation in the response of the chromatographic system. The performance of the GC interface or detector instrument can be evaluated by signal shapes, i.e. baseline, sharpness or noise. For instance, problems with sample preparation (i.e. the existence of residue or particles) and leak within the instrument can impact chromatogram responses. The performance of the detector response should be assessed as introduced in the Agilent manuals (dependent on the instrument type and model) [250]. For instance, the EM voltage, the ratio of some reference peaks needs a regular check and the implementation of precise tuning steps. The air leaks within the GC system are evaluated using the ratio (or absolute value) of air ($m/z = 28$) to water ($m/z = 18$). The relative ion abundance of $m/z = 69, 212, 512$ (Mass Spectrometer) should be in a limit provided by Agilent. The instrument needs a service (including the cleansing ion source or HED) if the ratios are not in the range provided by the manufacturer. The sampling injection should be initiated after a high system performance is ensured as bold in instrument instructions.

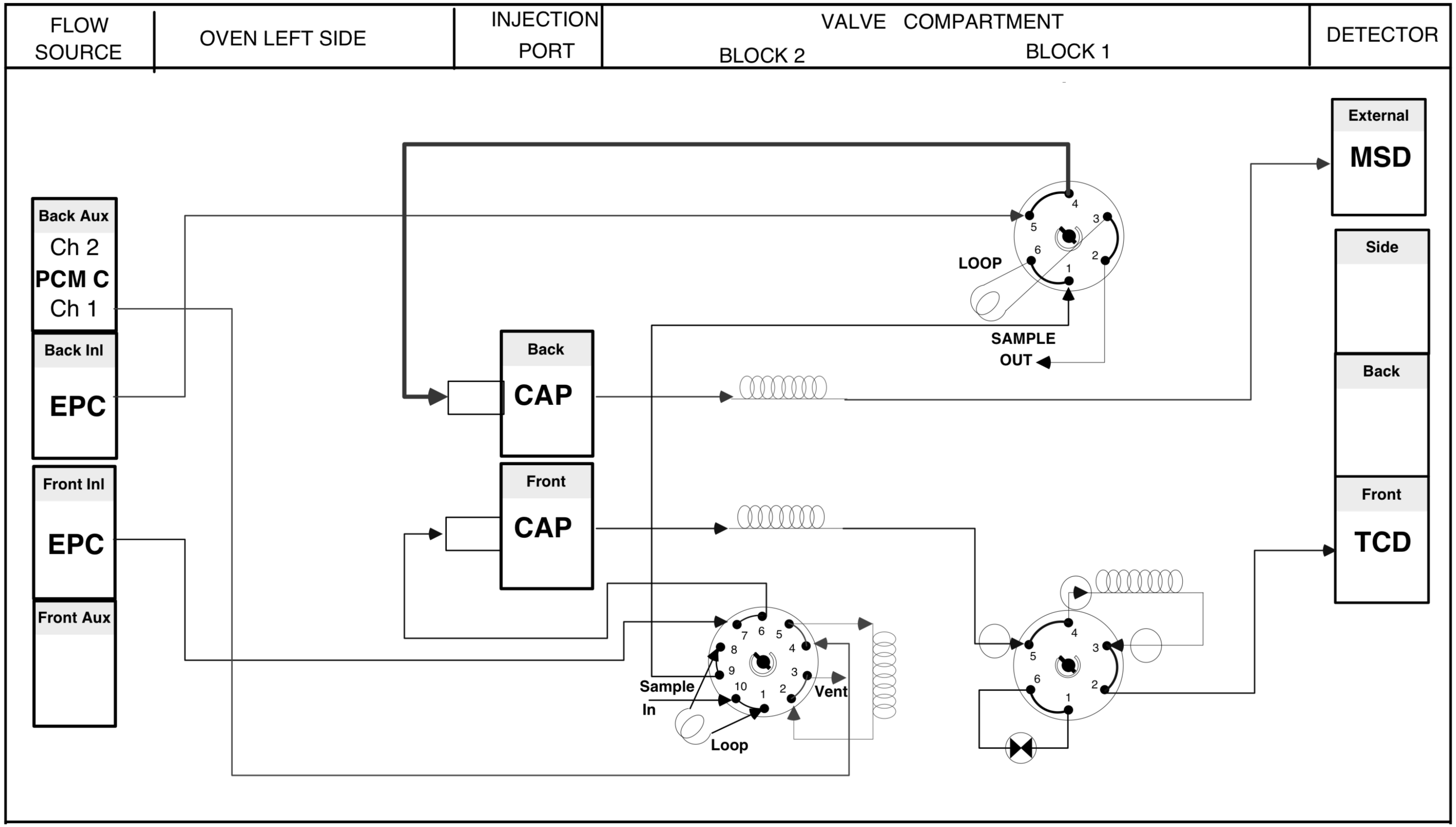

Figure 3.13. Schematic of valve system used for GC setup. PCM – pressure control modules; EPC – electronic pneumatic control; MSD – mass spectrometer detector; TCD – thermal conductivity detector; Inl – inlet; Aux – auxiliary.

3.7.2 Scanning mobility particle sizer

Scanning mobility particle sizer (SMPS) spectrometers, manufactured by TSI, are frequently used to quantify the size distribution of polydisperse aerosols [251, 252]. The current SMPS spectrometer system consists of an electrostatic classifier, a neutralizer, differential mobility analyzer (DMA), a nano enhancer and a condensation particle counter (CPC). The TSI 3938 1–nm SMPS model is used in the current study. Different setups can be used based on the particle size of interests. As an example, a nano DMA and long DMA are usually used to enable SMPS to measure particles with the size in the range of $D_p < 70$ nm and $D_p < 1000$ nm, respectively. In the current study, the 1–nm SMPS system provides particle sizes ranging from 4–40 nm. Long DMA setup can provide a size range between 8–230 nm depending on the instrument setting. A vacuum pump, connecting to the CPC and nano enhancer (when used), provides the required suction for the sampling particulates.

3.7.2.1 Soft X–ray

The function of the neutralizer is to apply an equilibrium charge distribution to the aerosol. The neutralizer uses a low–energy soft X–ray source to generate high concentrations of bipolar ions. These ions interact with incoming charged particles, and the product is a polydisperse aerosol flow with a known bipolar charge distribution.

3.7.2.2 Impactor

The impactor, mounted on the exit of the electro–classifier (model 3082), removes particles above a limit of particle size by inertial impaction. The nozzle size of the impactor provides the volume of the aerosol sample. The impactor with a nozzle size of 0.071 cm is used to provide the range of aerosol inlet flow from 0.6–2.1 (L/min).

The pressure drop across the impactor is used to adjust the aerosol flow rate. The aerosol flow is deflected 90° using an impactor plate to filter particles that are out of the desirable range. The particles below the limit can follow the streamline emerging out of impactor without contact.

3.7.2.3 Differential mobility analyzer

In the current study, long (model 3081) and nano (model 3086) DMA are utilised to provide a wide range of PSD for various flame structures. The fundamental of both DMAs operations is similar. The main feature of the nano DMA is an optimised flow path, used to minimise diffusion losses within the system and to enhance the resolution for particles. The schematic of nano DMA is shown in Fig. 3.14. The nano DMA includes a central cylindrical electrode with a controlled negative voltage and a grounded outer cylinder. The positively charged particles are attracted to a negative inner electrode. The DMA works based on the principle of the particles electrical mobility, as presented in Eq. 3.6. The aerosol is drawn into the nano DMA from the top and disperse into the outer electrode cylinder. The sheath flow is applied from the bottom of the nano DMA and then pass through the instrument emerging into the inner electrode cylinder. The desired particles, with specific size, are drawn into nano enhancer. However, the neutral particles are pulled out the DMA using excess airflow. The nano DMA model used in the current study is usually recommended for PSDs with particle diameter range below 50 nm. During mobility measurements, the sample and sheath flow through the nano DMA and long DMA were 1.5 and 15 L/min, respectively. These flow rates allow for particles to be classified in the range of 4–40 nm and 8–230 nm for nano DMA and long DMA, respectively. The nano DMA is cradled into nano enhancer to reduce diffusion losses within the SMPS instrument.

$$Z_p = \frac{V}{E} = \frac{n_p e C}{3\pi\mu D_p} \tag{3.6}$$

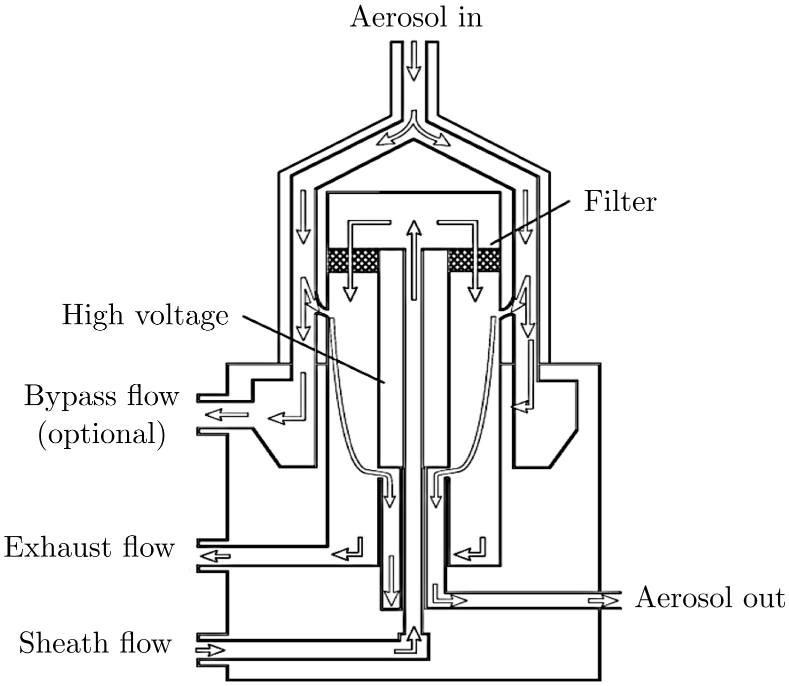

Figure 3.14. Schematic of nano DMA from TSI manual [253].

where Z_p is the capability of a charged particle to move in an electric field, V is particle velocity, E is electrical field strength, n_p is the number of charges/particle and e is the elementary unit of charge. μ is the viscosity of the gas, D_p is particle diameter, and C is Cunningham slip correction.

A nano enhancer is usually synchronised with the condensation particle counter (CPC) when there is a need to measure particle number concentration from 1 nm with a high resolution. The nano enhancer model used in the current study is the TSI 3777. Diethylene glycol (DEG $\geq$ 99%) is used as a working fluid to enable the nano enhancer measuring particles from 1 nm through a condensation process. A heated saturator is utilised to vaporise and diffuse DEG into the aerosol stream. A condenser in the system facilitates the DEG vapour condensation onto the particles in the sample stream.

The nano enhancer maintains a false count rate < 0.01 particle/cm^3 according to a 12–hr average. The DEG can limit the maximum size of the particle. The resulting particles are drawn out of the nano enhancer into the CPC. A critical orifice (operating below critical pressure) and a needle valve are utilised to precisely set 1.5 L/min (nominal) transport flow. A 0.85 L/min air flow into saturator is adjusted using a sheath

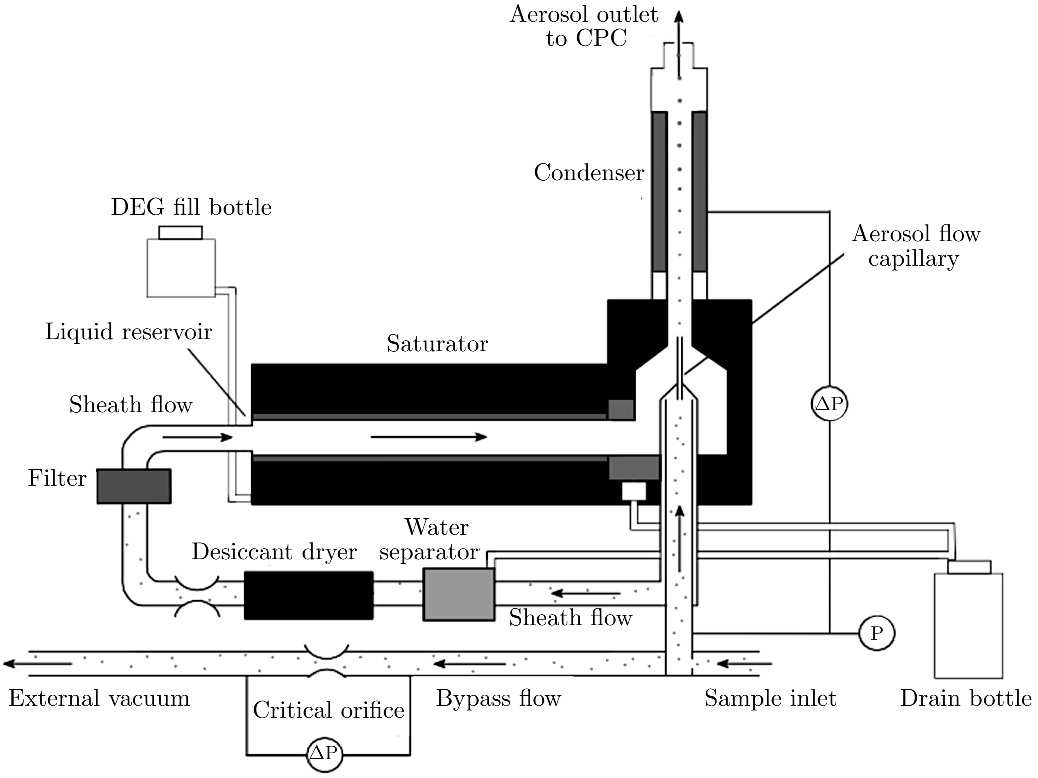

Figure 3.15. Schematic of nano enhancer from TSI manual [253].

air needle valve.

3.7.2.4 Condensation particle counter

The condensation particle counter (CPC) model used in the current study is the TSI 3772. The CPC contains three major components: (i) saturator; (ii) condenser; (iii) optics (detector). The aerosols coming out, from the the either nano enhancer (when used) or long DMA are exposed to further saturation and condensation processes, used to increase the particle sizes in a range, where they can be counted via using a laser–based optical system (photodetector). The smallest non-evaporating particle (D_{kelvin}) can be calculated based on Eq. (3.7),

$$\begin{aligned} D_{Kelvin} &= \frac{4\delta_s M}{\rho_L RT log S} \\ S &\equiv \frac{P_v}{P_{saturation}(T)} \end{aligned} \tag{3.7}$$

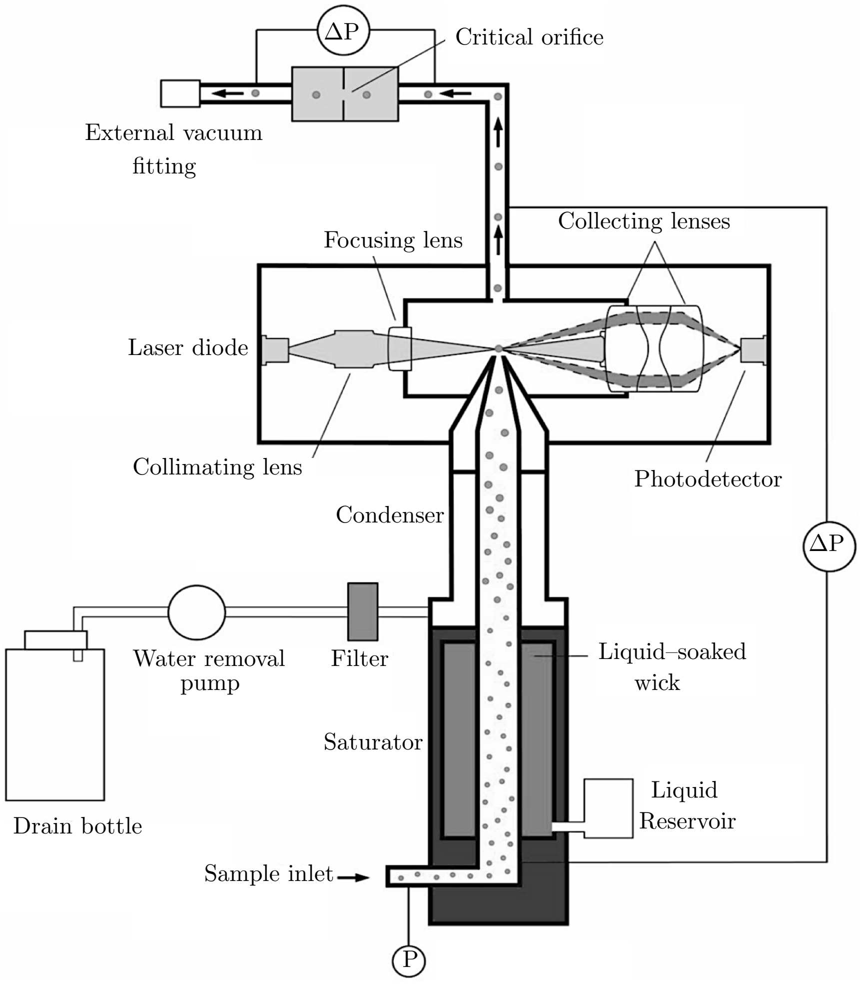

Figure 3.16. Schematic of condensation particle counter (CPC) from the TSI manual [253].

where D_{kelvin} is the Kelvin diameter and δ_s the surface tension of working fluid. M is the molecular weight of working fluid, ρ_L the density of working fluid, R the gas constant, T the temperature, and S the supersaturation ratio.

Butyl alcohol ($\geq$ 99.4%) is used as a working fluid for CPC. The orifice inside the CPC is utilised to maintain the aerosol flow constant. A vacuum pump is used to provide the required suction for the aerosol sample drawn into nano enhancer (when used) and the CPC. A water removal system is used (especially in hot/humid environments) to remove contamination of the working fluid of butanol (CPC) and DEG (nano enhancer) by condensed water vapour. Water removal keeps the CPC and nano enhancer operating at peak performance.

The instrument is capable of operating at pressures in the range of 75 to 105 kPa using a vacuum pump when a combination of long DMA and CPC is used. When the 1–nm SMPS system is used, a T–fitting is used to provide the vacuum range required for the nano enhancer 3777 and CPC 3772. The pump should provide at least 60 kPa in this case. The vacuum keeps 2.5 L/min of critical flow through the 3777–3772 combinations.

Chapter 4

Laser diagnostics measurements

4.1 Introduction

A simultaneous laser setup featuring PAH–PLIF and ELS is used to study the impact of gas burnt temperature, equivalence ratio and rates of strain on gaseous PAH, soot and nanostructures (liquid and solid phase) over the reaction zone in turbulent premixed flames. The fundamental concepts of PAH–PLIF and ELS are briefly discussed followed by standard terminologies used in sooting flame studies. The laser diagnostics and relevant uncertainties are provided in the current Chapter. The laser–based diagnostics were used to identify the reaction zone layers where the physical and chemical evolution plays a crucial role in the formation and oxidation of particulates. The spatial distributions of PAHs and particulates are determined using sampling probe experiments over the reaction zone layer identified by the laser diagnostics.

4.2 Elastic light scattering

Thermal gradients can be assessed using elastic light scattering (ELS). ELS has usually been utilised to present information on particle size distributions and particle volume fractions. In this technique, the energy transfer from the photons to ultrafine particles is limited based on criteria of particle diameter and laser wavelength ($d_p/\lambda \ll 1.0$) [254]. The ELS signal can be determined as follows (Eq. (4.1)),

$$I_R = I^{\nu} \cdot N \cdot \sigma_R \cdot \Omega \cdot l . \varepsilon_{sys} \tag{4.1}$$

where N is the total molecular number density, I^{ν} the laser irradiance, σ_R the Rayleigh cross sections, Ω the collection solid angle, l the depth of the measurement volume, ε_{sys} the collection efficiency. The Rayleigh cross sections (σ_R) can be obtained as follows [255],

$$\sigma_R = \sum_{i=1} X_i \cdot \sigma_{R,i} \tag{4.2}$$

where X_i is mole fraction of species i.

The higher signal intensity can represent a higher particle density or bigger particle size. ELS can present scattered lights from both particles and gaseous molecules. The Rayleigh cross sections of species ($\sigma_{R,i}$) can be calculated by Eq. (4.3) [256, 257],

$$\sigma_{R,i} = \frac{4 \cdot \pi r^2 (n_i - 1)^2}{N_0^2 \cdot \lambda^4} \tag{4.3}$$

where n_i is the species refractive index, λ the laser wavelength, N_0 the Loschmidt number. The Loschmidt number is defined as the number of particles (atoms or molecules) of an ideal gas in a given volume (the number density).

The ELS signal is a reciprocal function of wavelength as the degree of scattering increases with the decrease in the wavelength. The refraction indices and the corresponding Rayleigh quenching cross–sections are listed in Table 4.1 for some species.

Table 4.1. Species Rayleigh cross sections ($\sigma_{R,i}$) and refraction indices (n_i). Refraction index data are taken from Namer and Schefer [255] and $\sigma_{R,i}$ calculated by Eq. (4.3) for the wavelength $\lambda = 532$ nm.

Species	n_i	$\sigma_{R,i} \times 10^{-28}$ [cm^{-2}]
H	0.072	0.353
O	0.136	1.26
C	0.178	2.16
N	0.150	1.53
Air	0.293	5.85
O_2	0.273	5.08
N_2	0.300	6.13
H_2	0.144	1.41
CH_4	0.444	13.4
C_2H_4	0.636	27.6
C_2H_6	0.776	41.0
CO	0.340	7.87
CO_2	0.450	13.8
H_2O	0.255	4.43
OH	0.206	2.89
HO_2	0.343	8.01

As shown in Eq. (4.4), the ELS intensity is a strong function of particle size (d_i), number of particles (N_i), and the particles complex index of refraction (n). The sensitivity of signal to particle diameter is significant ($I \propto d^6$). Therefore, a simultaneous laser dianostics techniques including ELS can provide details about particle size and volume fraction [33, 177, 258–261]. This approximation is suitable for gas phase and nanostructures, i.e. molecular species and small spheroids. At the high levels of soot aggregation or coagulation, Debye or Mie scattering ($d_p \sim \lambda$) should be replaced with the Rayleigh approximation.

$$I = \frac{\pi^4}{4\lambda^4} \sum \left| \frac{n_i^2 - 1}{n_i^2 + 2} \right| N_i d_i^6 \tag{4.4}$$

Although elastic light scattering (ELS) can yield information about aggregate sizes and morphologies [262, 263], ELS is less selective than photoacoustic approaches and can give signals from other particles, such as fuel or water droplets [264].

4.3 Laser-induced fluorescence

Laser-induced fluorescence (LIF) is considered as few in–situ approaches are capable of measuring in–flame compositions. The physical and chemical evolution of the nanostructures can be processed using a wide range of fluorescence spectrums. The PAHs or nanostructures concentrations can be proportional to fluorescence intensity in a well–controlled environment when reabsorption effects remain negligible at low optical density [265, 266]. The laser wavelength can be qualitatively tuned to provide the required resonance for the species of interests. A combination of CH/OH–LIF has been frequently used to qualitatively provide data on the temporal evolution of flame fronts as well as the corresponding spatial distribution. Smaller PAHs mainly fluoresce in the spectrum range of 250 – 450 nm [267–269], while the heavy PAHs fluoresce at higher wavelengths.

The abundance of specific species is achieved via the quantum nature of the electronic energy levels in molecules [270]. LIF contains a process including (i) the absorption of a photon; (ii) the excitation to a higher energy state (excited state); (iii) the spontaneous emissions of photons while the species returns to the ground state. The last step includes three consecutive processes. First, the species reaches the lowest vibration with the minimum free energy of the higher electronic state. Second, the electron returns to the ground electronic state. The fluorescence emission happens at this stage. Third, the ultimate relaxation of the molecule from rotational states is obtained.

The energy level explains the specific wavelength of emissions. As mentioned, the nuclei vibration along the internuclear axis (B) and rotation of the molecule (ω) in space are included as important parameters in the discrete levels of excitation. The energy level can be summarised by Eq. (4.5),

$$E_{total} = E_{electronics} + \omega \cdot (\nu + \frac{1}{2}) + B \cdot J(J+1) \tag{4.5}$$

Where ν and J are quantum numbers corresponds to discrete levels of excitation vibration and rotation, respectively. The fluorescence signal S_F is calculated as follows (Eq. (4.6)),

$$S_f = g n_i V I_{laser} B \frac{A}{A+Q} \tag{4.6}$$

where i is the target species, n_i the local number density, g the geometric factor, V the probed volume, I_{laser} the incident laser beam intensity, A the Einstein spontaneous emission coefficients, and B the Einstein absorption coefficient.

The equation is simplified when the spontaneous emission coefficient is much lower than the quenching coefficient. The Boltzmann distribution can be used to define the electron distribution at different energy levels,

$$S_f \propto n_i \frac{f_{\nu,J}(T)}{q(T)} \tag{4.7}$$

where $f_{\nu,J}(T)$ is the normalized Boltzmann fraction in the ground state, and $q(T)$ is normalized collisional quenching rate at specific temperature.

The efficiency of the fluorescence process is dependent on the local chemical compositions and the corresponding temperature. The quenching rate coefficients are listed in Table 4.2 for some species [271]. The problems with LIF techniques are the uncertainties stemming from (i) fluctuations of laser energies and (ii) fluorescence quenching processes. Therefore, the quantification of species using LIF is a challenging task. The complexity is stronger for PAH–PLIF as PAHs species contain a mixture of distinct functional groups with broad spectra; the spectra of such species can also be overlap with each other. The infusion of PAHs on particles also leads to more complications. The qualitative analyses of light and heavy PAHs can be carried out using a spectrally–resolved LIF as the detection of heavier PAHs is distinguishable at higher wavelengths [272, 273].

Table 4.2. Quenching rate coefficient for common species [271].

Species	Quenching rate coefficient $q_i(T[k]) \times 10^{-13}$ [cm^{3}s^{-1}]
N_2	$4.47 \cdot T^{0.5} \cdot 0.4 \cdot e^{\frac{624}{T}}$
O_2	$4.37 \cdot T^{0.5} \cdot 8 \cdot e^{\frac{243}{T}}$
H_2O	$4.92 \cdot T^{0.5} \cdot 20 \cdot e^{\frac{434}{T}}$
H_2	$10.88 \cdot T^{0.5} \cdot 4.5 \cdot e^{\frac{224}{T}}$
CO_2	$4.16 \cdot T^{0.5} \cdot 11 \cdot e^{\frac{488}{T}}$
CO	$4.47 \cdot T^{0.5} \cdot 12 \cdot e^{\frac{397}{T}}$
CH_4	$5.07 \cdot T^{0.5} \cdot 11 \cdot e^{\frac{320}{T}}$
H	$15.0 \cdot T^{0.5} \cdot 14.5 \cdot e^{\frac{84}{T}}$
OH	$4.99 \cdot T^{0.5} \cdot 20 \cdot e^{\frac{384}{T}}$

4.4 Optical setup

The current laser diagnostic setup [29, 30] is schematically depicted in Fig. 4.1. The measurements feature a simultaneous CH_2O/PAH – PLIF and elastic light scattering (ELS). A frequency tripled (355 nm) Spectra–Physics Quanta-Ray Lab-150 Nd:YAG laser is used for CH_2O/PAH – PLIF and a frequency–doubled (532 nm) Litron Nano LG 175–10 Nd:YAG laser for the ELS measurements. The two spatially overlapped light sheets (i.e. ELS at 532 nm, light sheet height HLS = 27 mm, pulse power = 30 mJ; CH2O–PLIF at 355 nm, HLS = 18 mm, Power = 150 mJ) were located symmetrically around the theoretical stagnation plane. The light sheet thickness was estimated to 0.1 mm in the centre of the interrogation region using burn marks. In order to eliminate elastic scattering in the LIF detection systems, ELS is recorded 200 ns prior to LIF. Dichroic filters are used to spatially and spectrally segregate the signals.

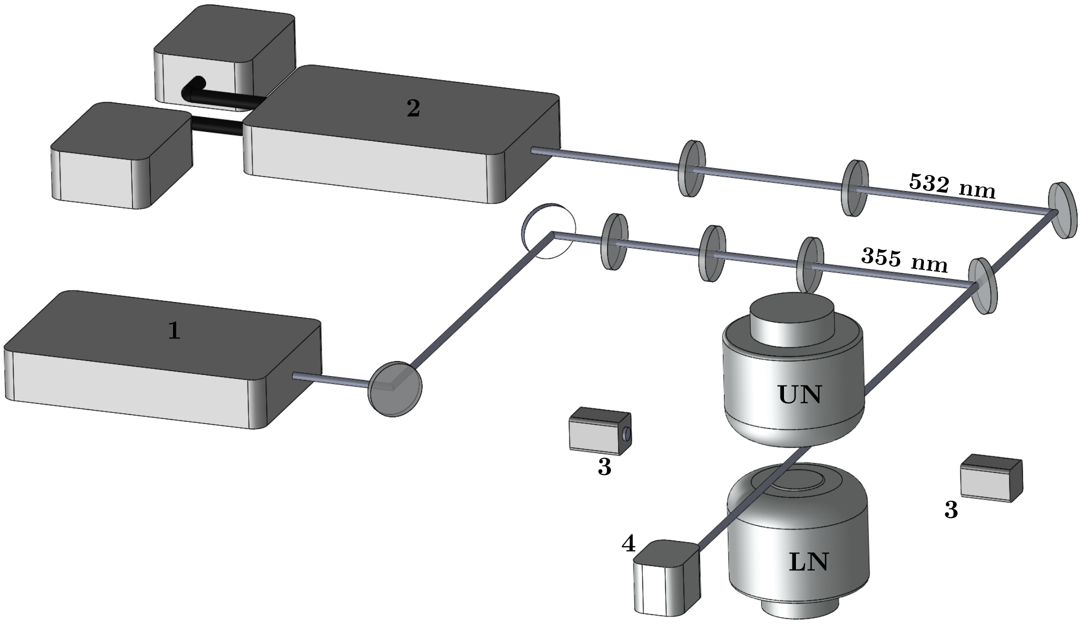

Figure 4.1. Laser diagnostics schematic: 1) Quanta–Ray laser; 2) Nano PIV; 3) Camera; 4) Beam dump; UN – Upper Nozzle; LN – Lower Nozzle.

4.4.1 LaVision software

LaVision Davis 8.1 [274] supports a large number of hardware components, all fully integrated and controlled by the software. The integration with DaVis allows the combination of various hardware components, such as three different cameras and lasers within the same measurement system. A large extensible library of built–in processing and filtering functions are provided within the software package.

4.4.2 Signal collection system

The ELS camera (LaVision LX 8M) is equipped with a 180 mm f/2.8 Sigma lens and a narrow width bandpass filter centred at 532 nm. A LaVision intensifier relay optic unit and intense imager camera are used to record the CH_2O/PAH–PLIF. The former is equipped with a 85 mm (f/1.2) lens and a 400 nm long-pass filter. An intensifier gate time of 70 ns and a low gain level of 60% minimises flame luminescence and noise. The detection system is calibrated using a multi-frequency target.

4.4.3 Noise reduction

In order to remove stray light scattering from the burner configuration, a rectangular aperture is installed prior to the burner. The resulting interrogation window provides a spatially constant background signal. The beam dump, aluminium sheets and laser safety curtains (purchased from Thorlabs) are used to minimise reflections of laser light.

4.4.4 Systematic uncertainty

A multi–step of alignment process was applied before each experiment to minimise systematic errors introduced by setup imprecision. A target plate was mounted on the burner to ensure that the laser light sheet superposition is aligned appropriately. The target plate was also utilised to control the camera alignment, and the resulting calibration images were used to provide image correction in the post–processing step. The alignment of the laser light sheet was also checked in the near and far–field. All cameras were mounted on lab jacks and sliders enabling precise adjustment within an accuracy of around 0.1 mm.

4.4.5 Image pre–processing

Alignment correction, noise removal and data reduction are the multi–steps included in the image pre–processing. Images of the multi–frequency calibration target from each camera system were used to create a standard coordinate system and eliminate any residual spatial misalignment. Calibration images were utilised to amend the spatial image separation because of the camera alignment. A pure air stream was used to present white image normalisation amending the average laser light sheet profile. To correct shot–to–shot fluctuations, a dynamic background subtraction was carried out. The impacts of light emitted from the hot nozzle, light from the burner assembly and flame luminescence were also removed from images. A purpose written algorithm was used for the image–processing step.

4.5 Terminology

In the current work, signal analyses of simultaneous ELS scattering and CH_2O/PAH–PLIF are carried out to distinguish between gaseous/condensed species and particles. The cross–correlation of the instantaneous ELS and CH_2O/PAH–PLIF images provides markers of soot and PAH zones. The CH_2O chemiluminescence is a useful marker for low–temperature chemistry, and the formaldehyde layer is appearing close to the reactants [275]. ELS can provide the identification of boundaries between PAH and soot for the signal analyses. Different flame structures are considered in the current project to present a comprehensive study on PAH growth and soot formation process.

Sample elastic light scattering and CH_2O/PAH–PLIF images are shown in Fig. 4.2 at soot inception ($\phi_{UN} = 1.7$) and heavily sooting ($\phi_{UN} = 2.0$) conditions. Descriptive labelling is provided in the images for the clarification of PAHs and particulate zones. The flame with an equivalence ratio of $\phi_{UN} = 1.7$ corresponds to lightly sooting condition with only a sporadic appearance of soot layers. By contrast, the reference flame ($\phi_{UN} = 2.0$) represents a sooting flame with a relatively thick soot layer. Soot nucleation, mass growth and PAHs condensation are enhanced considerably in the low-temperature region in the proximity of the stagnation plane ($X/L_I = 0.5$) in the richer flame [276, 277]. The superposition of a higher intensity at PAH–PLIF (the term of "soot") can be representative of interactions between primary particles, aggregates and condensed species close to a stagnation point. Interactions between turbulence and flame structures have not been well–investigated in sooting turbulent flames and fundamental research is required using simultaneous experimental techniques [60, 278, 279]. One of the major problems is the production of a large number of PAHs and particulates in the reaction layer. The excitation wavelength of species covers a broad range

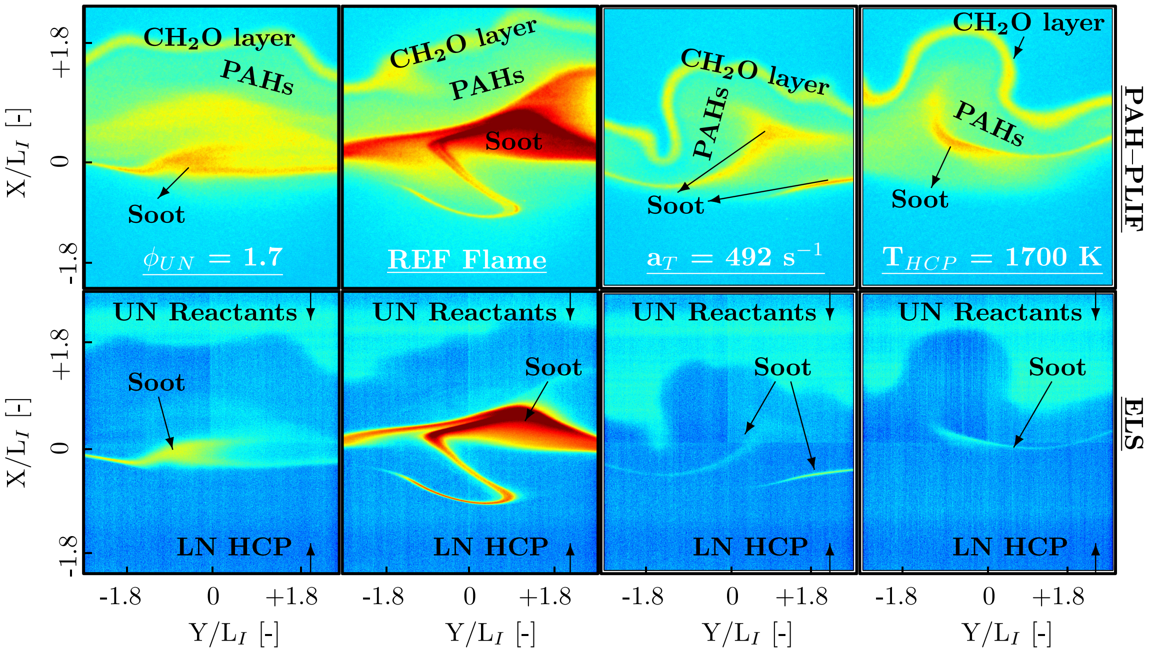

Figure 4.2. Laser diagnostic images obtained for CH$_2$O/PAH–PLIF (top) and ELS (bottom). 1st column: ϕ_{UN} = 1.7, a$_T$ = 420 s^{-1} and T$_{HCP}$ = 1500 K; 2nd column: ϕ_{UN} = 2.0, a$_T$ = 420 s^{-1} and T$_{HCP}$ = 1500 K; 3rd column: ϕ_{UN} = 2.0, a$_T$ = 492 s^{-1} and T$_{HCP}$ = 1500 K; 4th column: ϕ_{UN} = 2.0, a$_T$ = 420 s^{-1} and T$_{HCP}$ = 1700 K.

as it is close to impossible to attribute one wavelength to a specific species. Besides, it is impossible to distinguish condensed/gaseous species from each other as there exists a significant interaction between species. The gaseous/condensed species can infuse into particles, which can not be identified via laser diagnostic–based measurements.

4.6 Results and discussion

The impacts of the rate of strain, equivalence ratio and burnt gas temperature on the signals (PAH–PLIF and ELS) are shown in Fig. 4.3. The signals along the theoretical stagnation point streamline are normalised by the corresponding maximum for each subfigure. As shown, the extent of the turbulent reaction zone is ~ 2.4 L$_I$, consistent with Shariatmadar et al. [30] and Hampp et al. [29].

As shown in Fig. 4.3, clear differences in the patterns of CH$_2$O/PAH and ELS are observed for a wide of range of flame conditions. The flames exhibit significant dif-

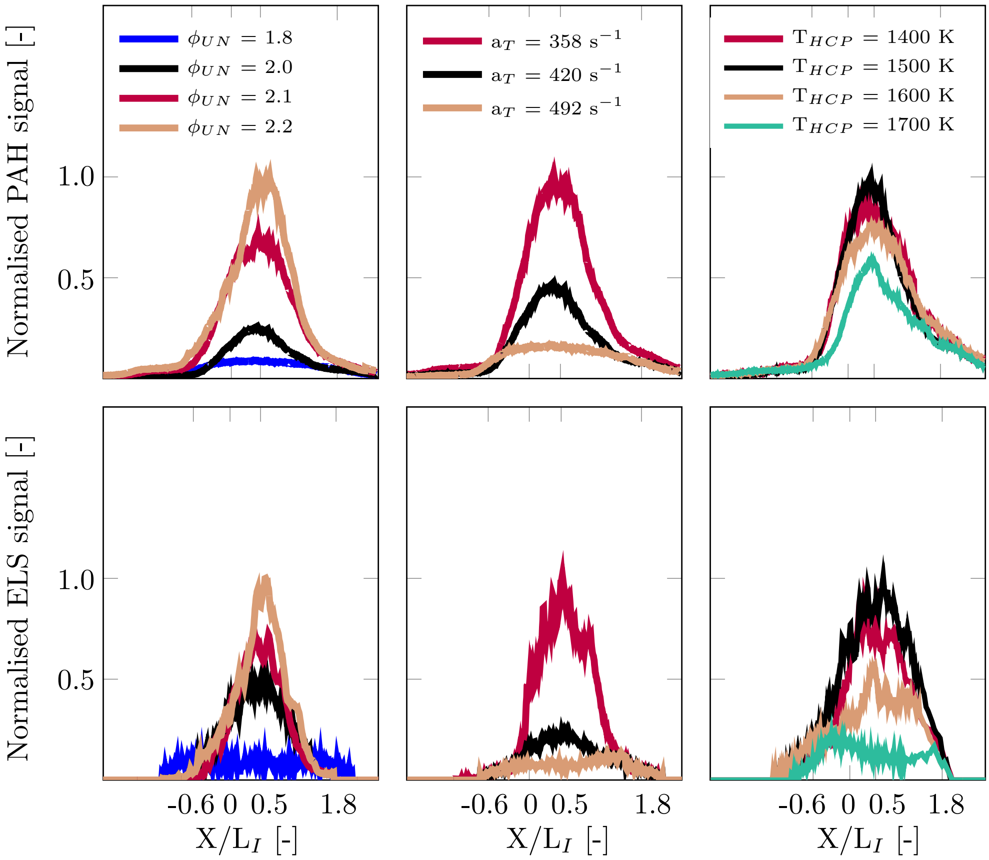

Figure 4.3. Normalised PAH–PLIF (top) and ELS (bottom) signals across the turbulent reaction zone for various equivalence ratios (left), total rates of strain (middle) and burnt gas temperature (right). Left column: $1.8 \leq \phi_{UN} \leq 2.2$, $a_T = 420$ s^{-1} and $T_{HCP} = 1500$ K; Middle column: $\phi_{UN} = 2.0$, $358 \leq a_T$ [s^{-1}] ≤ 492 and $T_{HCP} = 1500$ K; Right column: $\phi_{UN} = 2.0$, $a_T = 420$ s^{-1}, $1400 \leq T_{HCP}$ [K] ≤ 1700. Signals are normalised by the corresponding maximum value among the cases presented in each subfigure.

ferences in the production of soot, PAHs and their relative combinations. The peak ratios of the signals to the REF Flame are presented in Table 4.3. The analyses show that the occurrence of soot, PAH and nanostructure and their spatial variations are strongly dependent on the properties of the flow field (i.e. equivalence ratio and rate of strain) [67]. Overall, the results indicate that the both soot and PAH formation are exceptionally sensitive to the rate of strain and by implication to the local flow field conditions. The results further indicate that soot, in particular, can grow rapidly in regions of low rates of strain. The rate of increase in soot concentration (4.17) is higher than the increase for the gaseous PAH species (2.27) as the rate of strain is varied from $a = 420$ s^{-1} to $a = 358$ s^{-1}. The mean gaseous PAH peak (0.36) decreases slightly more

Table 4.3. Peak PAH–PLIF and ELS values at various experimental conditions normalised relative to the reference (REF) flame ($\phi_{UN} = 2.0, a_T = 420\,s^{-1}$ and $T_{HCP} = 1500$ K).

Case	PAH–PLIF	ELS
$\phi_{UN} = 1.80$	0.36	0.21
$\phi_{UN} = 2.00$	1.00	1.00
$\phi_{UN} = 2.10$	2.80	1.38
$\phi_{UN} = 2.20$	4.00	1.92
$a_T = 358$ s^{-1}	2.27	4.17
$a_T = 420$ s^{-1}	1.00	1.00
$a_T = 492$ s^{-1}	0.36	0.54
$T_{HCP} = 1400$ K	0.88	0.90
$T_{HCP} = 1500$ K	1.00	1.00
$T_{HCP} = 1600$ K	0.77	0.57
$T_{HCP} = 1700$ K	0.59	0.23

than soot (0.54) when the rate of strain is increased from $a_T = 420$ to $a_T = 492\,s^{-1}$. By comparison, the gaseous PAH concentrations are more influenced by the equivalence ratio. For instance, the gaseous PAH and soot particulates increase by a factor of 4 and 1.92 as equivalence ratio increase from $\phi_{UN} = 2.0$ to $\phi_{UN} = 2.2$, respectively. The two values are inevitably linked due to PAH condensation on soot particles.

The PAH concentrations are comparatively insensitive to the lower nozzle HCP temperature as shown in PAH signals (see Fig. 4.3). There is an increase in the PAH species concentration when the temperature is increased from 1400 to 1500 K, which is followed by a slight decrease at 1600 K. A decrease is also noted as the temperature is raised to 1600 and 1700 K. The trend correlates with the ELS signal. This implies a high level of competition between the soot formation and oxidation reactions with soot oxidation starting to take precedent at temperatures higher than 1600 K. The trend is stronger for soot with a reduction in the peak signal from 0.23 compared to 0.59 for PAH–PLIF. At higher temperature, decreased thermodynamic stability of soot precursors and reduced surface reactivity are expected to decrease soot formation [115] as shown in ELS signals (see Fig. 4.3 and Table 4.3). The reduced surface reactivity (e.g. the density of active sites per unit surface area) stems from a balance between PAH depletion in the gas phase and rates of surface reactions [280]. An increase in temperature can not only result in faster fuel decomposition to soot precursors and an enhancement of the molecular growth processes towards PAHs and soot particles, but also a faster increase in the oxidation rates of soot precursors/particles [281]. The temperature distribution can also impact the nucleation rate and fusing behaviour [282].

4.7 Conclusions

The impacts of burnt gas temperature, equivalence ratio and rate of strain on PAH distribution, soot inception have been discussed in this Chapter. Simultaneous PAH–PLIF and ELS were utilised to elucidate soot formation and oxidation processes in the reaction zone layer. As concluded, a higher equivalence ratio lead to a stronger relative PAH–PLIF response than ELS signals. It shows that PAH formation is favoured at higher equivalence ratio, regardless of sooting conditions. On the other hand, the relative increase for lower rate of strain is noticeable in ELS signals, showing significant loads of particles. At higher burnt gas temperature, decreased thermodynamic stability of soot precursors and reduced surface reactivity are expected to decrease soot formation while PAH concentration shows comparatively modest changes as the burnt gas temperature is varied.

The laser diagnostic measurements cannot precisely address some issues. These includes the ability to differentiate the gaseous PAH phase, the transition from molecular to solid nanostructures and soot formation. The identification of gaseous and condensed species, and the existing interaction between PAHs and particles cannot be precisely distinguished [148]. Turbulence presents challenges due to the increase in the rate of the mixing process and interaction between species. ELS can also be prone to interferences by other particle and extinction is susceptible to interferences by absorbing gas-phase species [129]. A probe sampling method is utilised to provide the spatial distribution of important species contributing to primary particle growth, aggregates and condensed species. Details are provided in the following Chapters.

Chapter 5

Flame structures

5.1 Introduction

The purpose of the work outlined in this chapter is to determine concentration profiles of major gaseous species under the influence of rate of strain and equivalence ratio along the burner centreline. Laminar flame calculations are performed to support the interpretation of species growth and particle inception as functions of equivalence ratio and rate of strain. The present flame series was also identified experimentally as suitable by means of simultaneous ELS and CH_2O/PAH–PLIF measurements as discussed in Chapter 4.

The analysis benefits from time–dependent data with minimal perturbations to the reacting environment [141]. Experimentally, it is critical to have more complete sets of data that include particle aerosol characterization along with flow parameters and concentrations of species, such as O_2, C_2H_2, CO and CO_2. For instance, acetylene plays an important role in soot formation, starting from the chemical initiation of combustion and fuel decomposition [18, 35, 283]. Acetylene provides a route to generate larger hydrocarbons and polycyclic aromatic hydrocarbon (PAH) species known to be precursors to soot formation [113, 119].

A sampling probe system is utilised to present major gaseous concentrations along the burner centerline. The experimental results are compared to laminar flame calculation to illustrate differences in species profile distributions between laminar and turbulent regimes.

Laminar flame calculations were used to reinforce the selection of the current flame condition as ideal for the study of soot inception and the transition to a heavily sooting flame. As discussed above, the present flame series was also identified experimentally as suitable using simultaneous ELS and CH_2O/PAH-PLIF measurements.

Laminar flame calculations also support the interpretation of species growth and particle inception. The inflow boundary conditions for the computational study matched the experimental data, i.e. identical air, H_2 and N_2 mole fractions and inlet temperature and velocity conditions. The computational domain also resembled that of the BTB experimental setup with the exception that the flow was laminar. Hence, only the impact of bulk strain (not the turbulent strain) is accounted for accurately in the simulations. However, computations were also performed based on the estimated total rate of strain ($a_T = a_b + a_t$) to provide an indication of the impact.

The computational domain was resolved by 233 distributed cells with local refinement in the reaction zone. The resolution is 36 μm. A detailed chemical mechanism featuring 358 species and 1789 reactions was applied. The details of the chemical reaction mechanism can be found in Lindstedt and Waldheim [37]. Calculations were performed to infer the corresponding temperature and species profiles contributing to soot growth and particle inception.

5.2 Sampling process

The sampling probe can provide the precise detection of gaseous species by using the aerodynamic effects of the orifice configuration as discussed in Chapter 3. The sampling process is conducted at ambient temperature and without using nitrogen dilution. The sampling pressure is maintained constant at 20 mbar throughout the study, and frequent leak tests are performed to preclude sample contamination. A tedlar bag is placed in the vacuum chamber to collect gaseous species, and a gas–tight syringe (purchased from ESSLAB) is used to inject the sample into the GC–TCD [284]. When a gas chromatography (GC) is used, it is necessary to eliminate any particles and water vapour from the gas sample [241]. It is confirmed that water vapour or particles can be retained or adsorbed onto the column and have a significant impact on the TCD peak of species signals (especially CO and CO_2) or lead to considerable noises. The adsorption of water into the column requires a bake–out process for either column or detector.

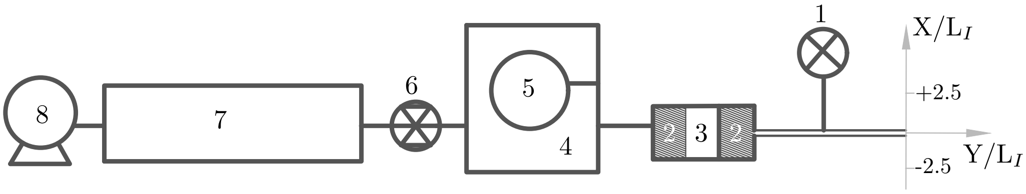

Figure 5.1. Sampling collection system used to measure major gaseous species over spatial locations $-2.5 \leq X/L_I \leq +2.5$. 1) Pressure transducer; 2) Quartz wool; 3) Sodium sulphate; 4) Vacuum chamber; 5) Tedlar bag; 6) Vacuum regulator; 7) Vacuum volume; 8) Vacuum pump. P is probe tip. The filter unit consists of quartz wool and sodium sulphate.

A series of quartz wool, XAD–2 resin, and sodium sulphate are utilised as a filter package to remove water vapour. The two nitrogen dilution ports here are utilised to remove residues between each experimental case. To avoid trapping gas residue in the sampling system, a small flow of nitrogen is injected into the sampling system.

The chemical analysis is performed by a gas chromatograph (Agilent 7890A) equipped with a thermal conductivity detector (TCD). A HP–PLOT Q and a HP–Moleseieve column (helium carrier gas) are used to quantify C_1–C_4 and CO, CO_2, N_2, O_2. The GC–TCD was calibrated regularly with Scotty gas mixtures (purchased from Agilent Technologies LTD) containing C_1 to C_4 hydrocarbons, N_2, CO and CO_2.

The accuracy of the GC/TCD analysis and the repeatability of the data is assured by repeated sampling at the same flame positions. A standardised operational procedure

Table 5.1. Flow conditions for the two parameter variations (ϕ [-] and a$_T$ [s^{-1}]) at constant gas burnt temperature of T = 1500 K. The UN and LN fuel is C_2H_4 and H_2, respectively and ϕ_{LN} is 1.0. U is the upper nozzle bulk velocity and u' the velocity fluctuations, T$_r$ = 320 K the reactant temperature, L$_I$ = 3.9 ± 0.2 mm is the integral length scale of turbulence, Re$_t$ the turbulent Reynolds number and α = X$_{H2}$/X$_{N2}$ = 0.51, where X is the respective mole fraction. Re$_t$ = $u'L_I/\nu$ is the turbulent Reynolds number and a$_t$ = $(\varepsilon_r/\nu_r)^{1/2}$ is the turbulent, a_b = $2U/H$ the bulk and a$_T$ = $a_t + a_b$ the total rates of strain [233]. ε_r is the rate of dissipation in the reactants and ν is fluid viscosity [234].

Variation	ϕ_{UN} [-]	T$_{HCP}$ [K]	a_T [s^{-1}]
ϕ [-]	1.8, 2.0, 2.2	2.0	2.0
a_b [s^{-1}]	120	120	80, 120, 160
a$_t$ [s^{-1}]	300	300	175, 300, 450
a$_T$ [s^{-1}]	420	420	255, 420, 610
Re$_t$ [-]	72	72	50, 72, 94
U [m s^{-1}]	1.8	1.8	1.2, 1.8, 2.4
u' [m s^{-1}]	0.30	0.30	0.21, 0.30, 0.39
α [-]	0.51	0.43, 0.51, 0.64	0.51

is used to enhance the repeatability of the sampling process. Each experimental set is repeated at least five times to assess the reproducibility. The total error and data repeatability is significantly enhanced by removing water vapour from the gaseous sample and routine calibration steps before sampling injection. The maximum cumulative error in measured concentrations (based on standard deviation) is estimated at ± 2.1% for major gaseous samples.

5.3 Results and discussion

Computed temperature profiles are shown in Fig. 5.2 and examples of calculated species profiles in Fig. 5.3. The peak temperature is significantly higher for lower bulk rates of strain. The spread in the temperature profile is also strongly evident at lower rates of strain. As shown in Fig. 5.3, indene and the indenyl radical show a higher rate of increase than naphthalene. This further supports the importance of such species in the formation of soot precursors. The PAH reactions (indene and the indenyl) play an important role in the early formation of incipient–soot precursors and provide

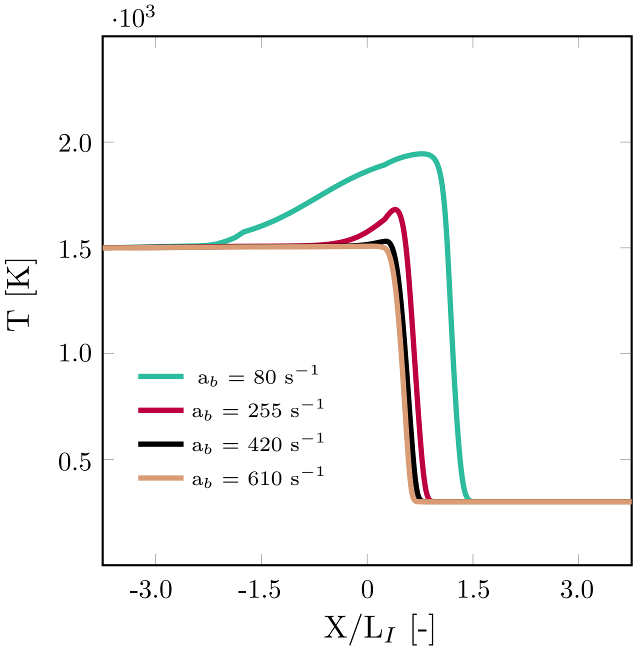

Figure 5.2. The computed temperature profiles at a constant stoichiometry of $\phi_{UN} = 2.0$ for different bulk rates of strain.

fast routes for mass growth. The rate of increase in species concentration is strongly influenced by the rate of strain. For instance, the peak concentration ratio of pyrene reduces by a factor of 830 when bulk rate of strain is increased from $a_b = 80$ to $a_b = 610$ s^{-1}. Also, the peak concentration of naphthalene reduced 506 times to further illustrate the impact of rate of strain on species growth from soot inception.

The flame conditions used in the current Chapter are listed in Table 5.1. The axial sample position was varied (11 points) along the stagnation point streamline in steps of 2 mm (about half of an integral length scale of turbulence) to include the (statistical) location of the PAH layer. The measured mole fractions of major gaseous species (N_2, O_2, CO, CO_2, CH_4, C_2H_2, C_2H_4, C_3H_6 and C_3H_8) extracted from samples taken in the turbulent reaction zone shown in Figs. 5.4–5.5. The presented results are on a dry basis with water vapour removed from the samples.

The formation/oxidation of species is strongly dependent on the reaction zone thickness and the heat release zone. There are considerable differences in turbulence-chemistry interactions with increasing equivalence ratio, from light to heavily sooting premixed flames, as observed by Duwig et al. [285]. The turbulence characteristics also control

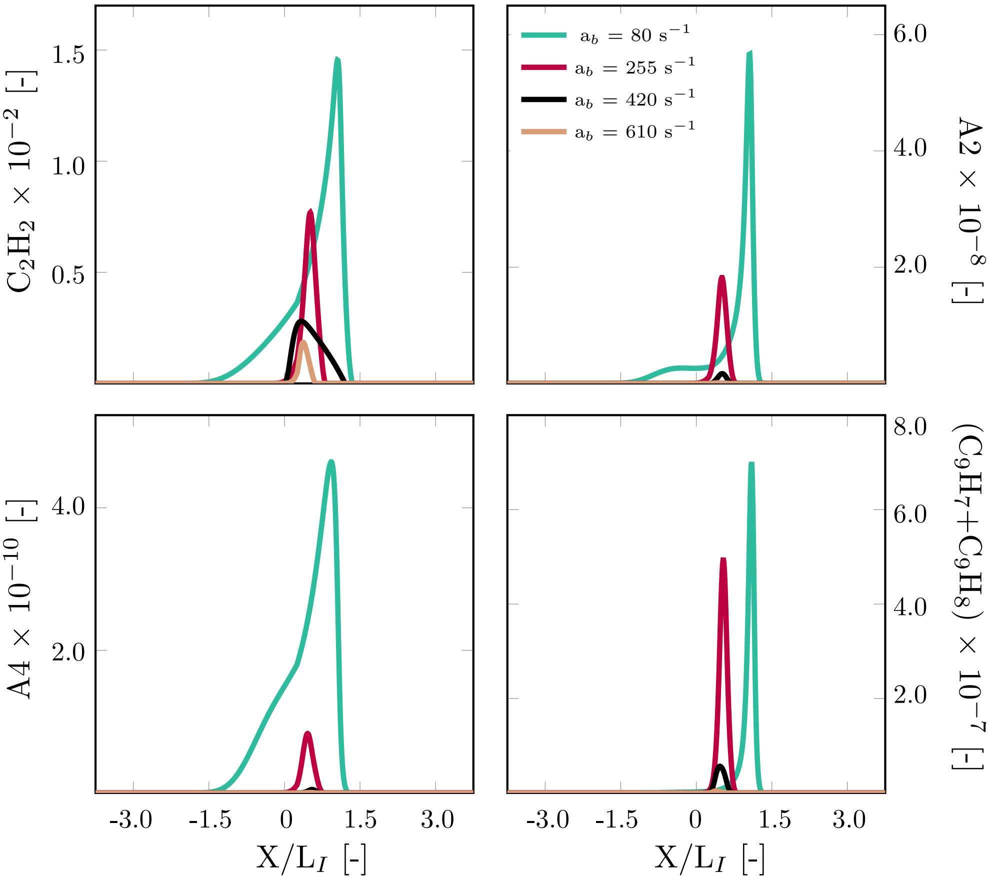

Figure 5.3. The calculated species profiles distribution at a constant stoichiometry of ϕ_{UN} = 2.0 along the burner centreline under the influence of rates of strain.

the spatial extent of the reaction zones [286].

The peak ratios of the measured mean concentrations of stable hydrocarbon species are presented in Table 5.2. In the lightly sooting flames, the decreasing acetylene profiles parallel the decreasing profiles of PAH and are in line with the absence of detected soot [285]. The PAH–PLIF signal increases by a factor of 4 from ϕ_{UN} = 2.0 to 2.2, while the acetylene concentration increases by a factor of 2.25. The corresponding increase in the ELS signal is a factor of 1.92, close to the increase in the acetylene concentration. It can be noted that the increase in the acetylene concentration with stoichiometry is less than for the C_3 species. This may be due to preferential depletion caused by acetylene addition to soot via HACA type mechanisms (c.f. [113]). A reduction in the formation of intermediate species is also observed for the major hydrocarbon species including CH_4, C_2H_2, C_3H_6 and C_3H_8 as the flame shifts from ϕ_{UN} = 2.0 to ϕ_{UN} =

Table 5.2. The peak ratio of major gaseous species for various experimental conditions including lightly and heavily sooting flame. The peaks are normalised with the corresponding maximum value of REF case.

Species	$\phi_{UN} = 1.80$	$\phi_{UN} = 2.20$	$a_T = 255$ s^{-1}	$a_T = 610$ s^{-1}
CH_4	0.37	1.60	2.28	0.43
C_2H_2	0.46	2.25	3.00	0.57
C_3H_6	0.20	2.46	3.00	0.40
C_3H_8	0.34	2.53	3.20	0.45

1.80. For instance, the concentrations of acetylene and methane reduce by 54% and 63%, respectively. A similar trend was also seen at a higher rate of strain ($a_T = 610$ s^{-1}) as the decrease was 60% for propene and 55% for propane. The reduction is due to both flame structure and turbulence effects [286]. The latter is capable of wrinkling the flame and leads to a Da number dependent species scattering within the reaction zone [87]. Thus, the interface thicknesses can become governed by the turbulent transport and mixing rather than reaction progress, suggesting a potentially significant impact of turbulence and rate of strain on the distribution within the flame structure. On the other hand, the mean concentration of species rises at lower rates of strain and higher equivalence ratios further indicating complex turbulence–chemistry interactions [287]. The growth rate of species is steeper at $a_T = 255$ s^{-1} as the growth was reported higher than 200% for acetylene, methane and propane.

The carbon based mixture fraction is calculated from seven carbon containing species (CO, CO_2, CH_4, C_2H_2, C_2H_4, C_3H_6 and C_3H_8) for both experimental data and the laminar flame computations on a dry basis (omitting the water concentrations and thus dividing the computational results by $1 - X_{H2O}$). The reaction progress variable is computed based on the fuel mass fraction (Y_F) [288] as shown in Eq. (5.1),

$$c = \frac{Y_F^1 - Y_F}{Y_F^1 - Y_F^2} \tag{5.1}$$

where subscripts 1 and 2 (in the equations) indicate values at fuel and air stream, respectively.

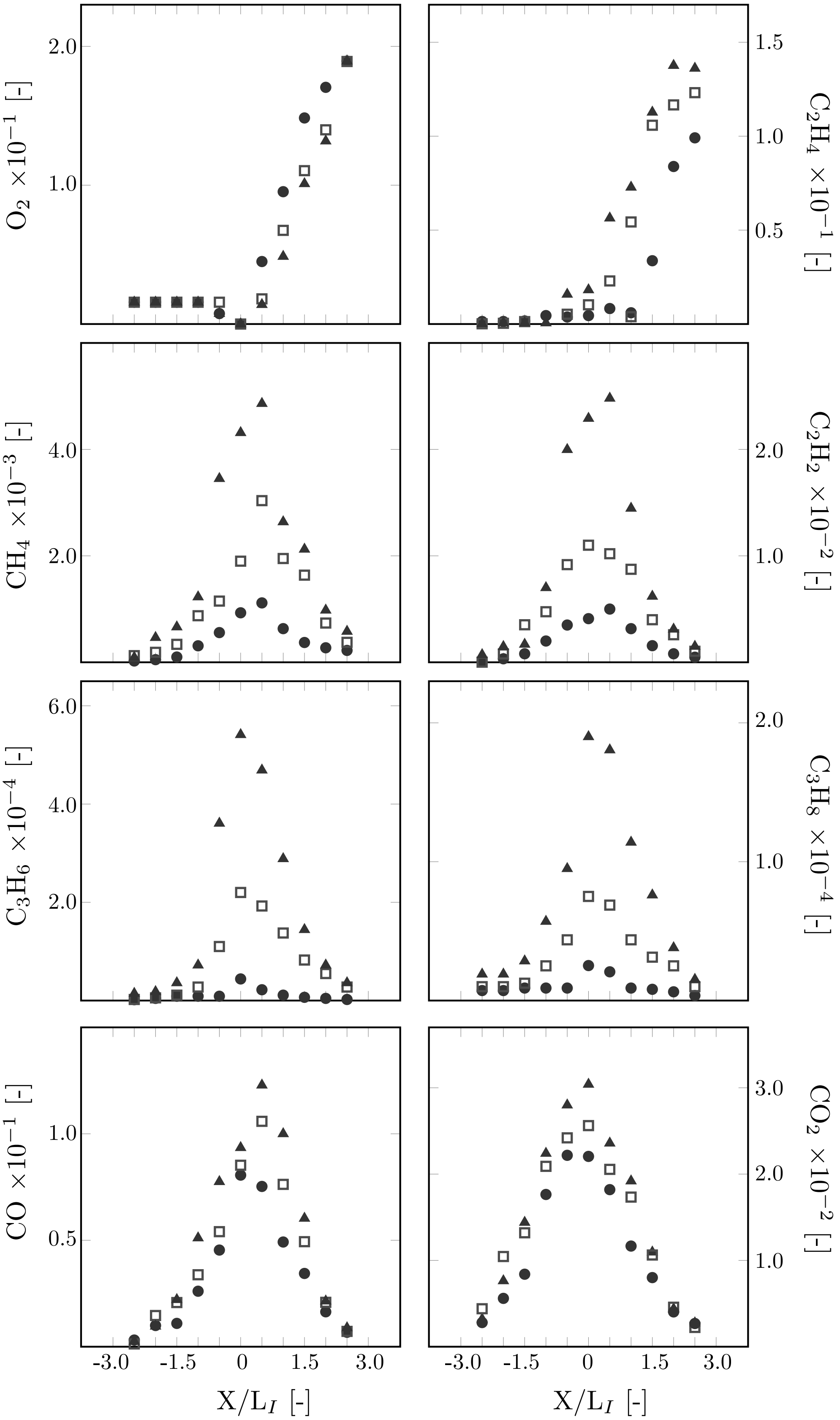

Figure 5.4. The impact of equivalence ratio on mole fractions of major gaseous species at different spatial locations for $a_T = 420\,s^{-1}$ and T_{HCP} = 1500 K. Circle – $\phi_{UN} = 1.8$; Square – $\phi_{UN} = 2.0$; Triangle – $\phi_{UN} = 2.2$. The filter unit, containing quartz wool and sodium sulphate, is used to remove water vapour from gaseous sample. X/L$_I$ > 0 is towards reactants and X/L$_I$ < 0 towards the hot combustion products.

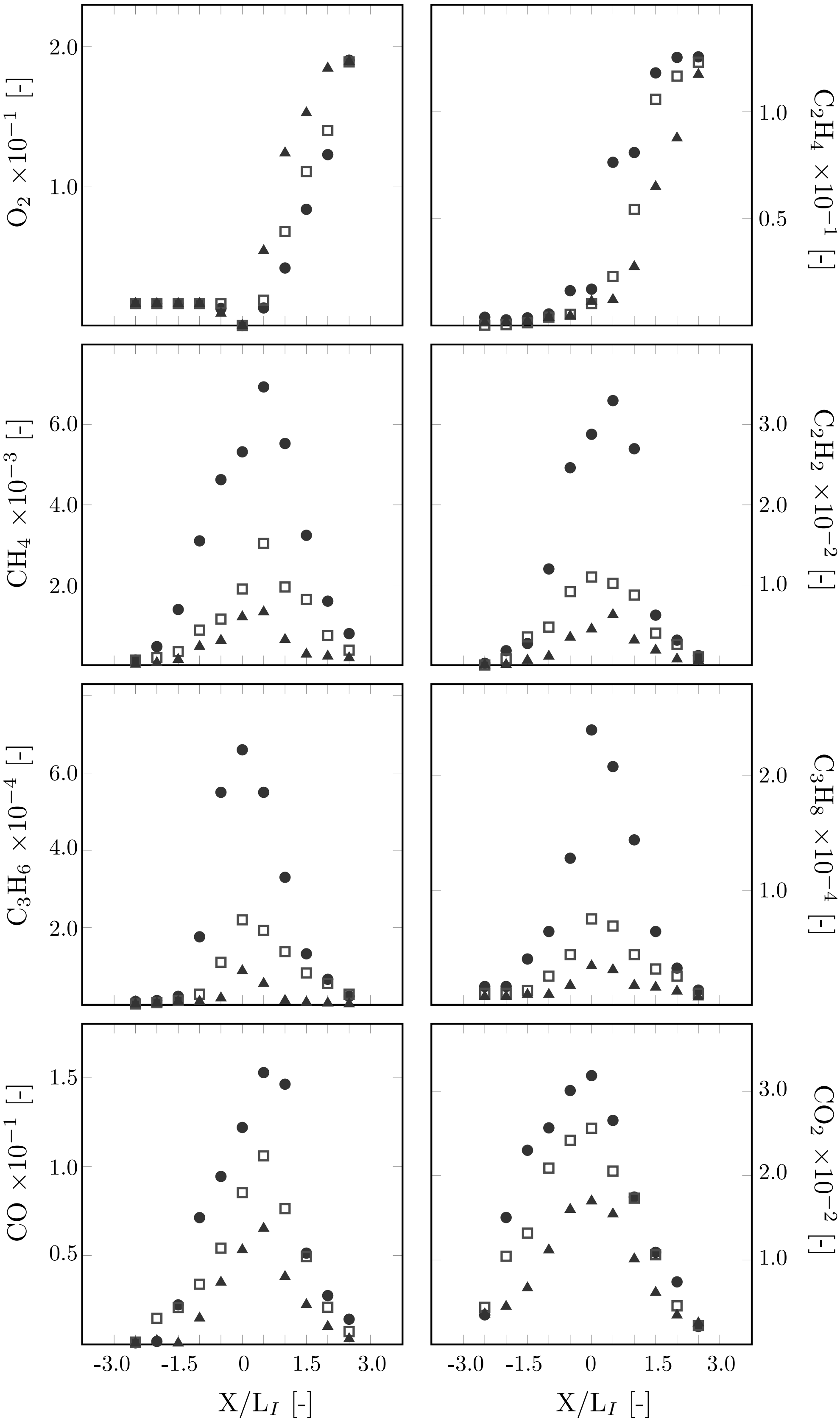

Figure 5.5. The impact of the rate of strain on mole fractions of major gaseous species at different spatial location for ϕ_{UN} = 2.0 and T_{HCP} = 1500 K. Circle – a_T = 225 s^{-1}; Square – a_T = 420 s^{-1}; Triangle – a_T = 610 s^{-1}. The filter unit, containing quartz wool and sodium sulphate, is used to remove water vapour from gaseous sample. X/L$_I$ > 0 is towards reactants and X/L$_I$ < 0 towards the hot combustion products.

The determination of major carbon containing species permit the tentative evaluation of the carbon based mixture fraction (f_c), defined by Eq. (5.2),

$$\mathrm{f}_c = \frac{\sum_{k=1}^{nsp} n_{C_k} X_k}{\sum_{k=1}^{nsp} X_k M_k} . (\frac{n_{C_F}}{M_F})^{-1} = \frac{M_F}{M} \frac{1}{n_{C_F}} \sum_{k=1}^{nsp} n_{C_k} X_k \tag{5.2}$$

where n_{C_k} denotes the number of carbon atoms in species k and n_{C_F} the number of carbon atoms in the fuel, and M is the mean molecular weight.

The reaction progress variable and mixture fraction profiles across the burner centreline are depicted in Figs. 5.6 and 5.7. The experimental conditions shown in Fig. 5.6 correspond to a total rate of strain of $255 \leq \mathrm{a}_T \leq 610$ at a constant stoichiometry of $\phi_{UN} = 2.0$ and a burnt gas temperature of $\mathrm{T}_{HCP} = 1500$ K. The experimental conditions corresponding to Fig. 5.7 is for equivalence ratios of $1.8 \leq \phi_{UN} \leq 2.2$ at a constant total rate of strain of $\mathrm{a}_T = 420$ s^{-1} and a burnt gas temperature of $\mathrm{T}_{HCP} = 1500$ K. The mixture fraction profiles indicate the influence of the rate of strain and also provide approximate limiting values for each case. The deviations occurring under some conditions in the region of the flame stabilisation point at $\mathrm{X/L}_I \simeq 0$ indicates the sensitivity to the probe insertion at this location. The impact is particularly notable at low and high rates of strain.

The measured mole fractions of major species at the two different limiting rates of strain (a_b and a_T) are mostly bounded by the flamelet computations for the reference flame shown in Fig. 5.8. The impact of turbulence is notable at lightly sooting conditions (e.g. $\phi_{UN} = 1.8$). However, the correlation with the estimated upper limit of the total rate of strain is noticeably stronger as shown in Fig. 5.9.

The deviation in the mixture fraction profile between the laminar flame computations and turbulent flame (i.e. the experiments) increases with the decrease in the total rate of strain, especially for the total rate of strain $\mathrm{a}_T = 255$ s^{-1}. The deviation around the stagnation plane might result from two problems. First, a stronger impact of probe effects might be expected for heavily sooting flame in comparison to all other experimental conditions. As discussed in Chapter 3, the clogging at the probe tip can be a problem for the heavily sooting case of $a_T = 255$ s^{-1}, while this effect is not critical for all other experimental conditions. Second, a significant proportion of carbon is converted to soot and also presents problems due to the radiative heat loss effects associated with such flames. Accordingly, additional transport equations for soot related properties (e.g. soot mass and number density) should be included with the calculations. Unsteady effects can also account for differences around the stagnation plane [289].

Conditional species profiles versus mixture fraction as a function of equivalence ratio are shown in Figs. 5.9–5.10 at a constant total rate of strain of $a_T = 420$ s^{-1} and a burnt gas temperature of $T_{HCP} = 1500$ K. The impact of the total rate of strain on the species profiles as a function of mixture fraction is provided in Figs. 5.11 and 5.12 at a constant stoichiometry of $\phi_{UN} = 2.0$ and a burnt gas temperature of $T_{HCP} = 1500$ K. It can be concluded that the laminar flamelet approximation may struggle to accurately predict species profiles in the current turbulent flames due to the strong impact of the rate of strain [290]. However, the overall local structures (i.e. major gaseous products) of the flames can be evaluated using elemental mixture fractions (e.g. carbon, hydrogen and oxygen) and correlations with concentrations are shown for many species.

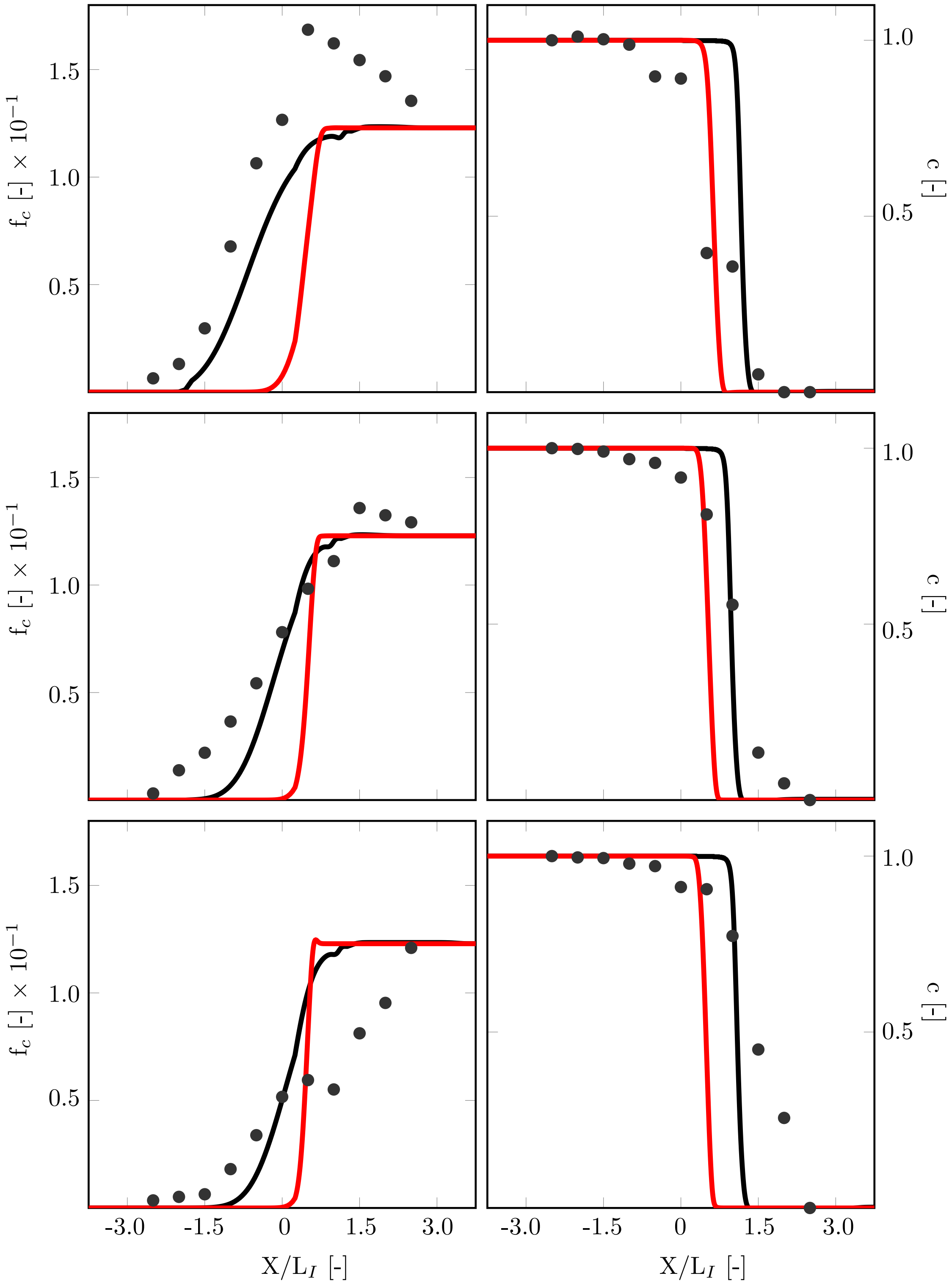

Figure 5.6. Profiles of mixture fraction (left) and reaction progress variable (right) along the stagnation point stream line for the reference flame (ϕ_{UN} = 2.0 and T$_{HCP}$ = 1500 K) with rates of strain. Circles are experiments. Top row: $a_T = 255\,s^{-1}$ (red line) and a$_b$ = 80 s^{-1} (black line); Middle row: $a_T = 420\,s^{-1}$ (red line) $a_b = 120\,s^{-1}$ (black line); Bottom row: $a_T = 610\,s^{-1}$ and $a_b = 160\,s^{-1}$. For consistency, computed data is based on dry mole fractions (i.e. divided by $1 - X_{H2O}$).

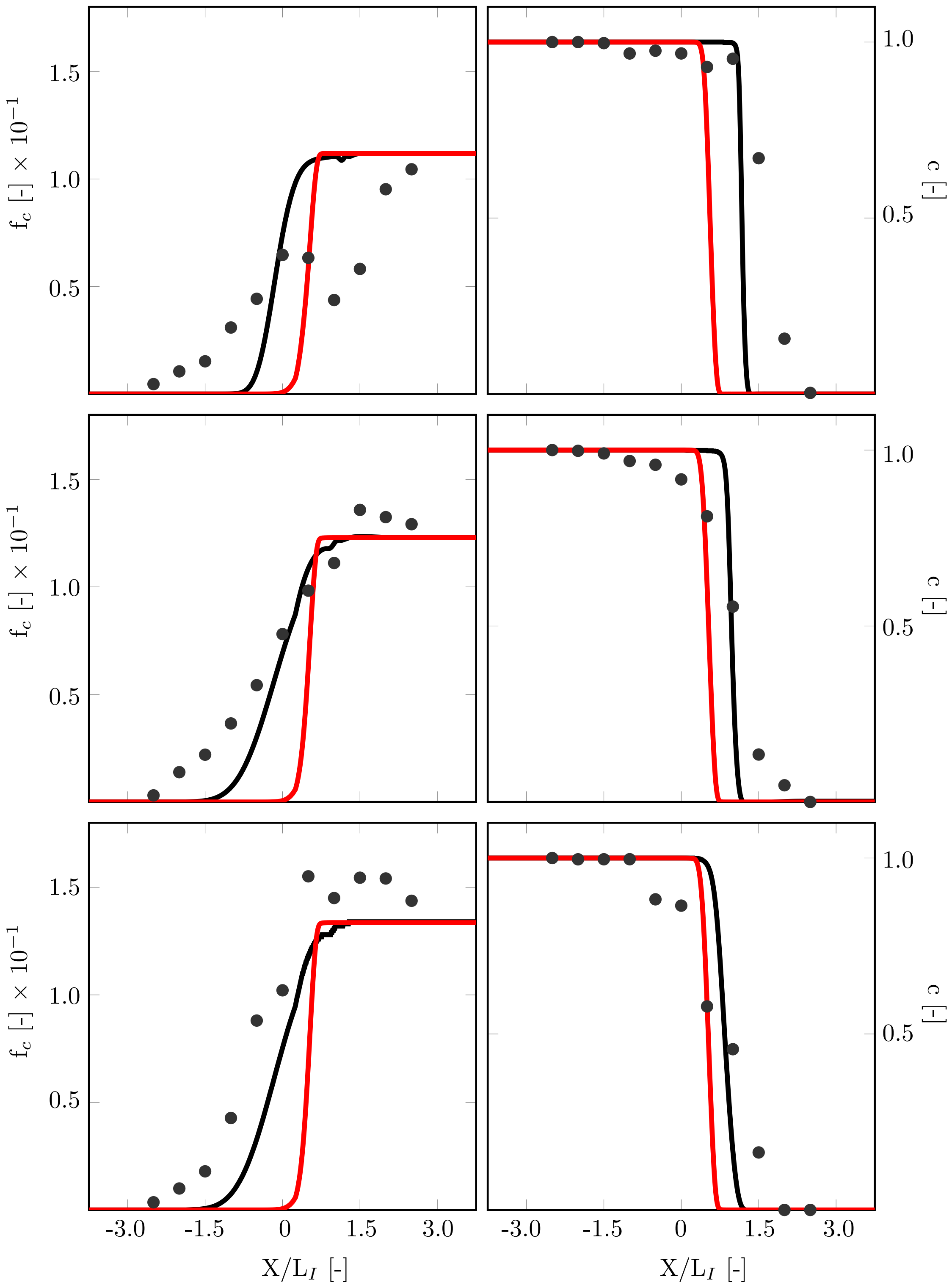

Figure 5.7. Profiles of mixture fraction (left) and reaction progress variable (right) along the stagnation point stream line at constant rates of strain with $a_T = 420\,s^{-1}$ (red), $a_b = 120\,s^{-1}$ (black) and $T_{HCP} = 1500$ K for different equivalence ratios. Top row: $\phi_{UN} = 1.8$; Middle row: $\phi_{UN} = 2.0$; Bottom row: $\phi_{UN} = 2.2$. Circles are experiments. For consistency, computed data is based on dry mole fractions (i.e. divided by $1 - X_{H2O}$).

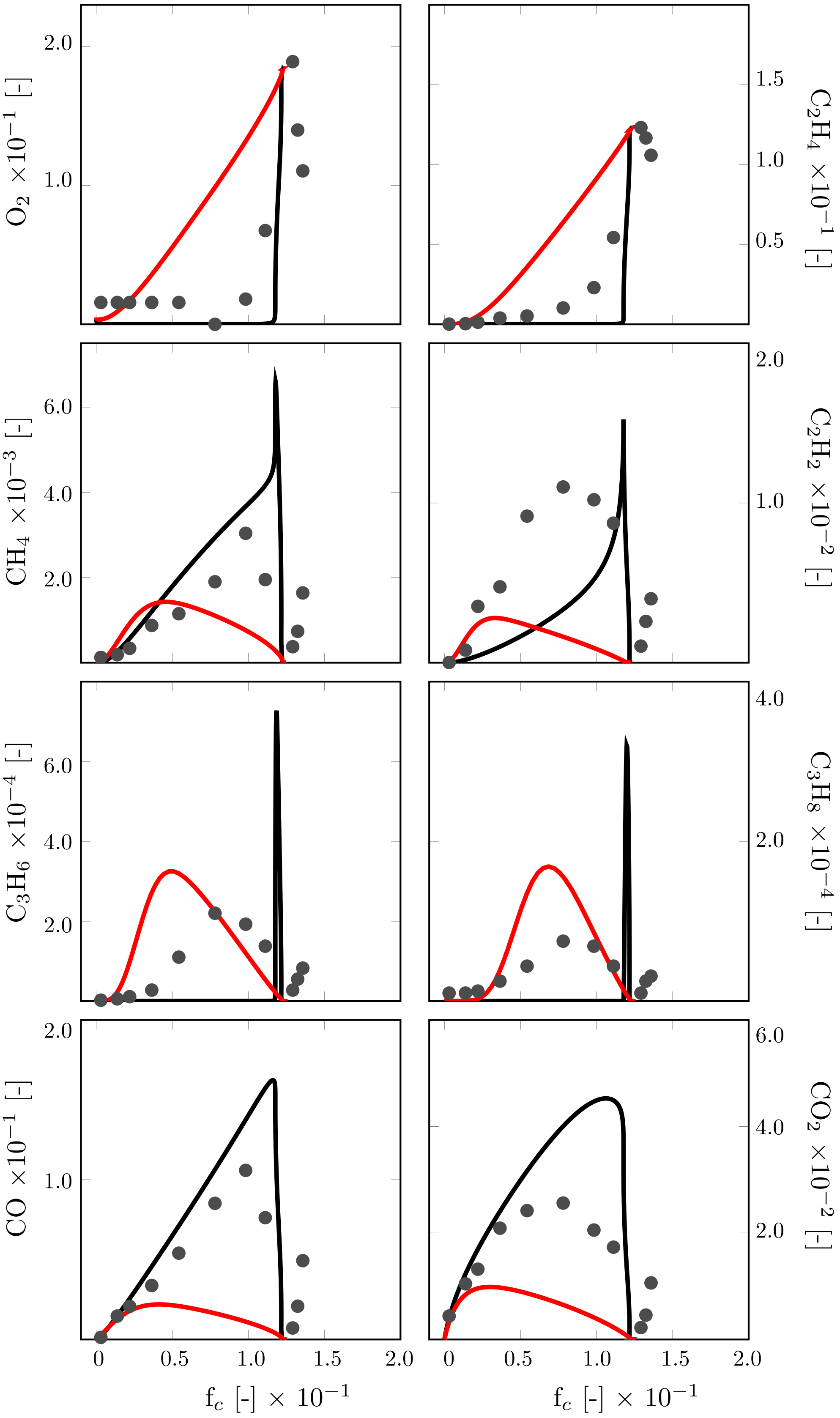

Figure 5.8. Species profile versus mixture fraction for $\phi_{UN} = 2.0$ at rates of strain of $a_T = 420\,s^{-1}$ (red) and $a_b = 120\,s^{-1}$ (black) and a burnt gas temperature of $T_{HCP} = 1500$ K. Experiments indicated by circles.

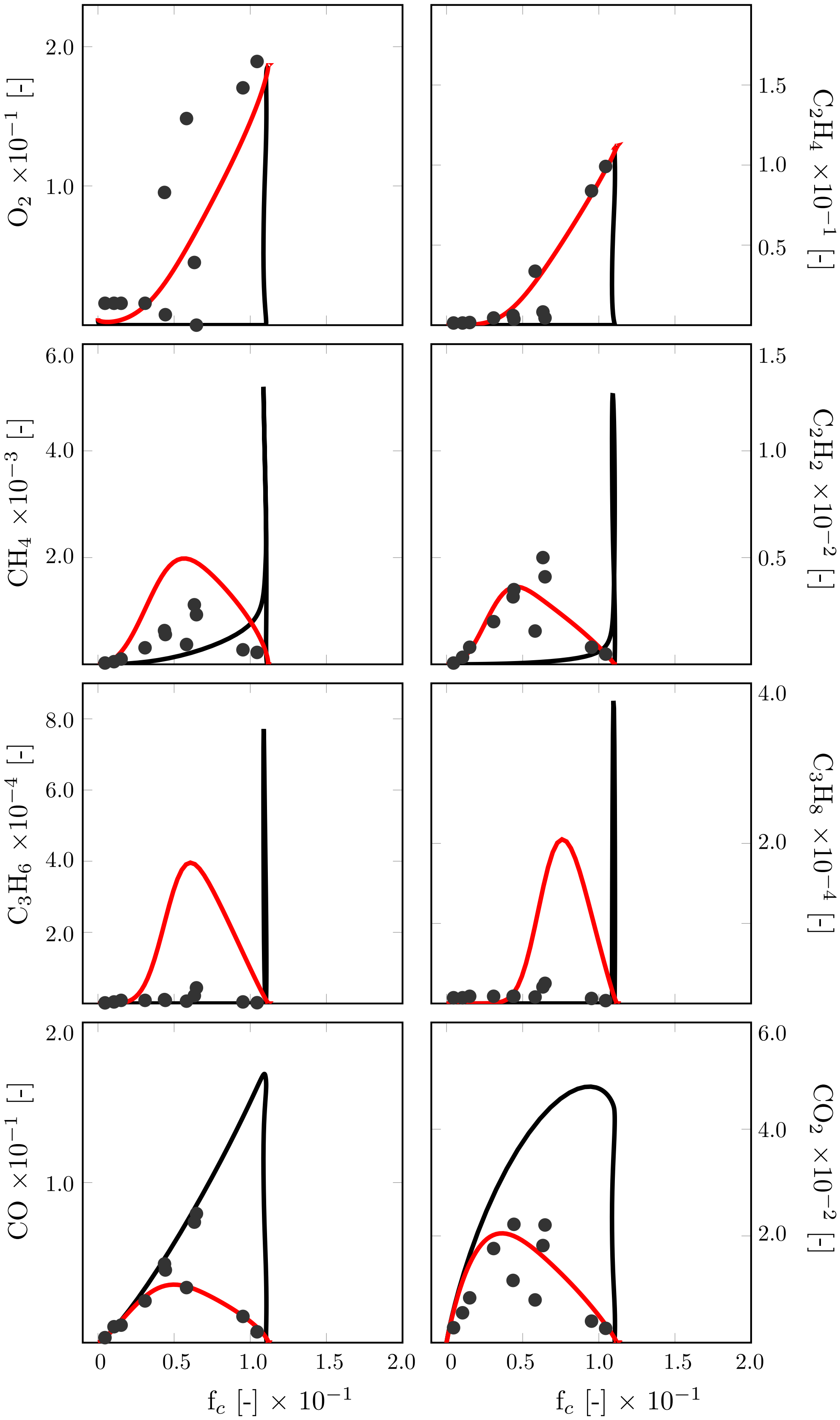

Figure 5.9. Species profile versus mixture fraction for $\phi_{UN} = 1.8$ at rates of strain of $a_T = 420\,s^{-1}$ (red) and $a_b = 120\,s^{-1}$ (black) and a burnt gas temperature of $T_{HCP} = 1500$ K. Experiments indicated by circles.

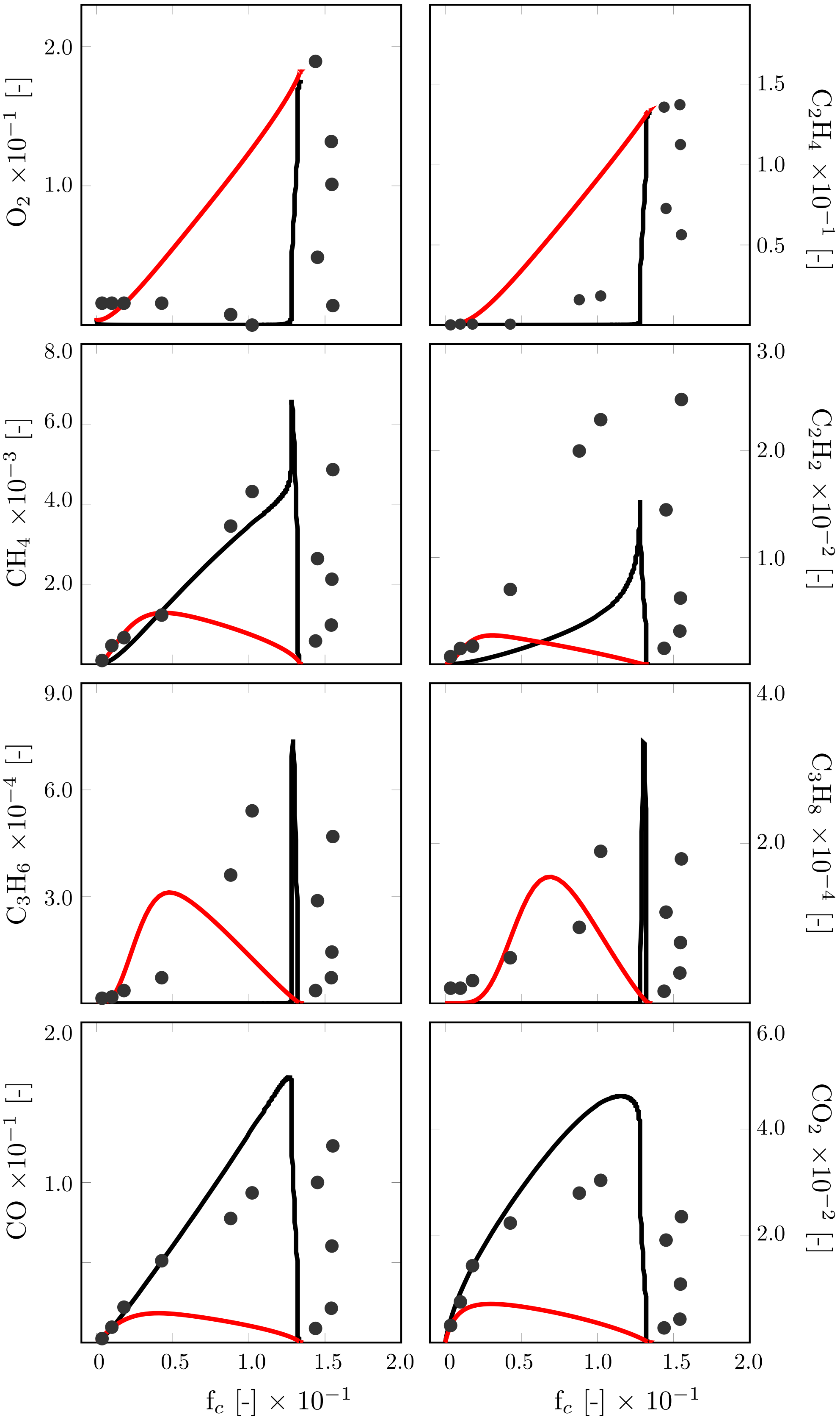

Figure 5.10. Species profile versus mixture fraction for $\phi_{UN} = 2.2$ at rates of strain of $a_T = 420\,s^{-1}$ (red) and $a_b = 120\,s^{-1}$ (black) and a burnt gas temperature of $T_{HCP} = 1500$ K. Experiments indicated by circles.

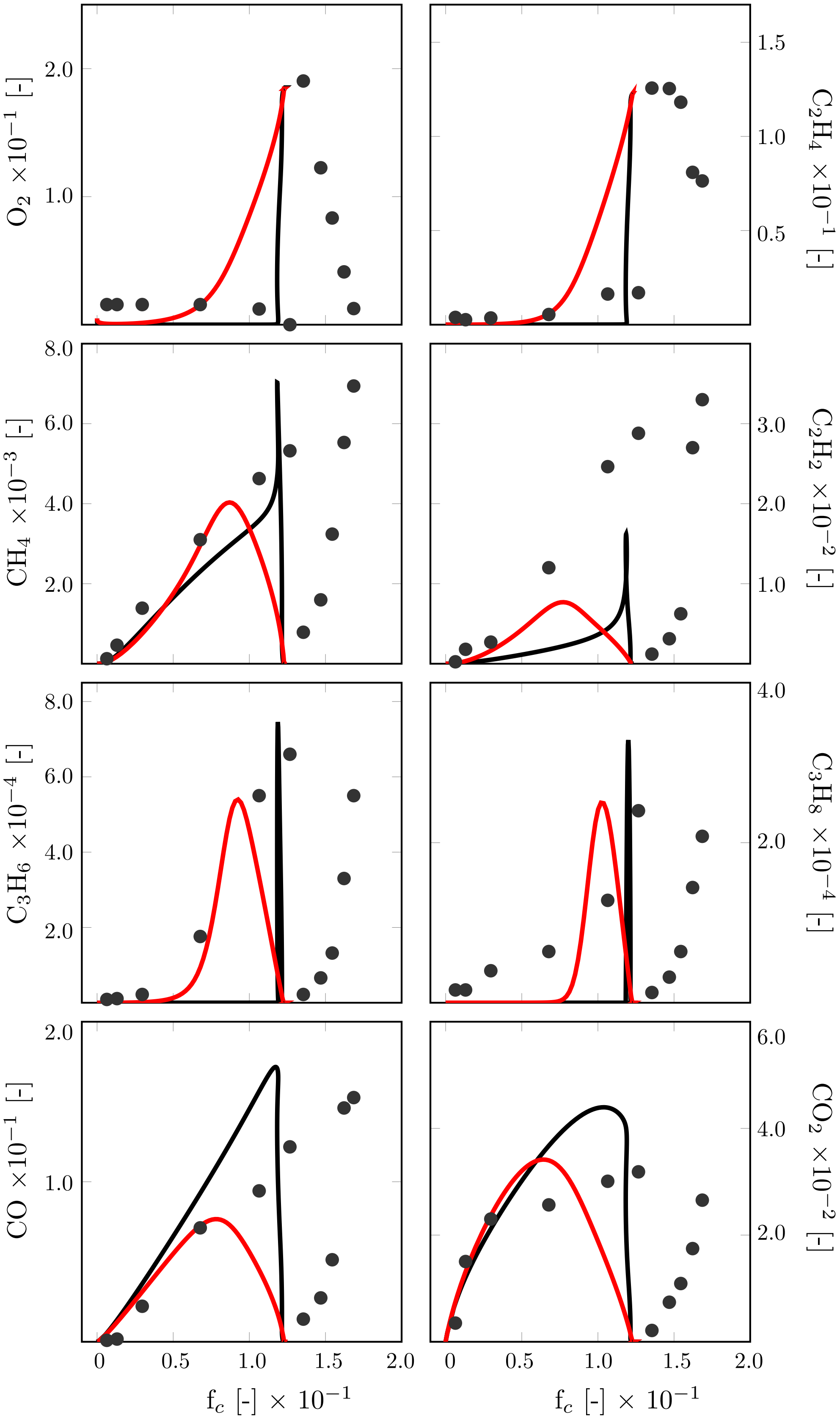

Figure 5.11. Species profile versus mixture fraction for $\phi_{UN} = 2.0$ at rates of strain of $a_T = 255\,s^{-1}$ (red) and $a_b = 80\,s^{-1}$ (black) and a burnt gas temperature of T$_{HCP}$ = 1500 K. Experiments indicated by circles.

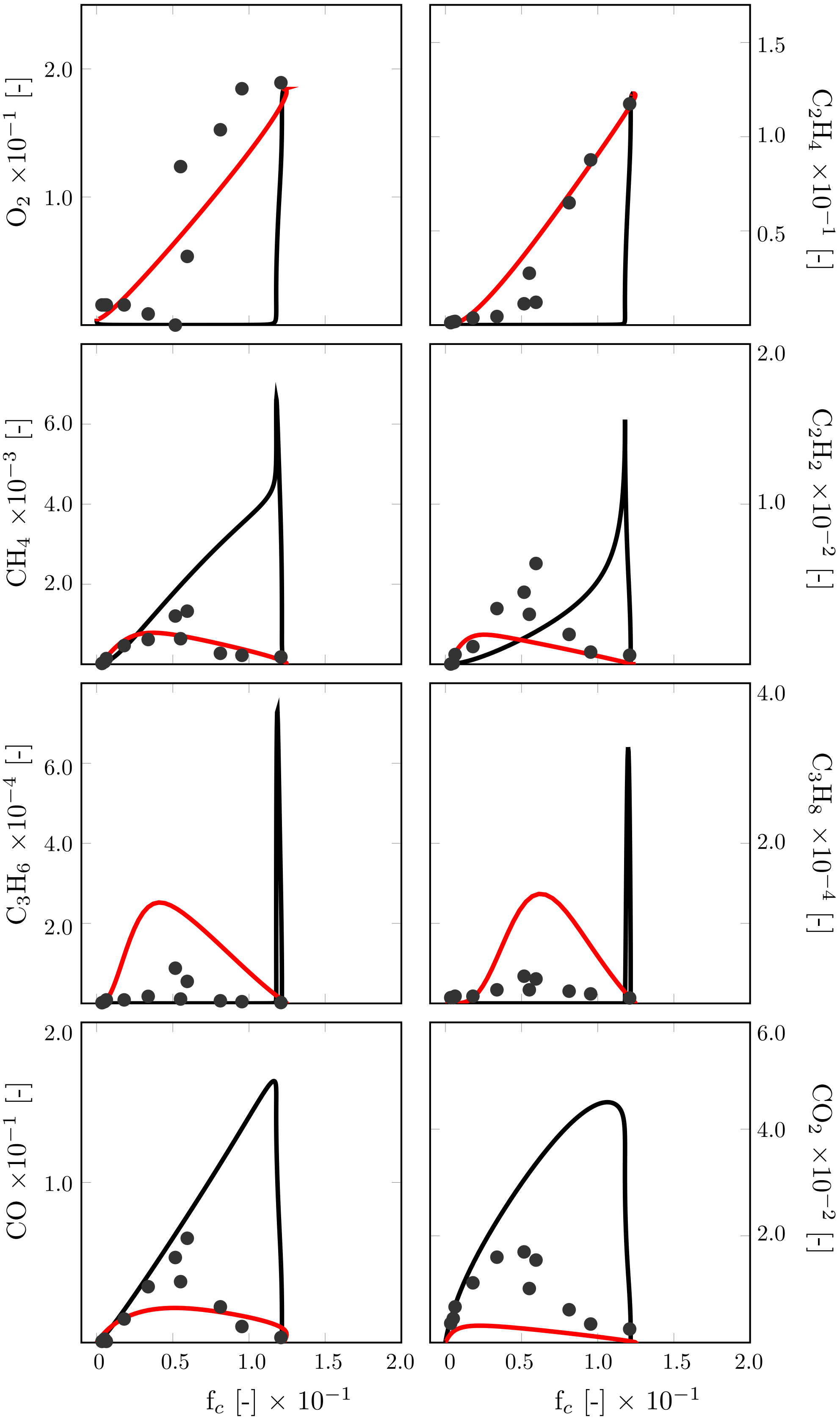

Figure 5.12. Species profile versus mixture fraction for $\phi_{UN} = 2.0$ at rates of strain of $a_T = 610\,s^{-1}$ (red) and $a_b = 160\,s^{-1}$ (black) and a burnt gas temperature of T$_{HCP}$ = 1500 K. Experiments indicated by circles.

5.4 Conclusions

The overall flame structure were investigated by obtaining major species concentrations at 11 axial sample positions along the stagnation point streamline. Measured species concentrations showed increased concentrations of intermediate species within the PAH layer of the more heavily sooting flames. The turbulence characteristics (e.g. the rate of strain on reaction layers) play a key role in soot inception process. The species profiles extend over a much broader spatial domain as a result of turbulent transport and flame-front folding [247]. It is concluded that laminar flamelet approximation may struggle to accurately predict species profiles in current turbulent flames.

The carbon based mixture fraction and reaction progress variables have been used to evaluate differences in flame structures. The determined mixture fraction and reaction progress variable profiles reinforces the selection of the reference (REF) flame at an equivalence ratio of $\phi_{UN} = 2.0$, a total rate of strain of $a_T = 420$ s^{-1} and a burnt gas temperature of $T_{HCP} = 1500$ K as a sensible choice.

Chapter 6

PAH sampling experiments

6.1 Introduction

The molecular mass growth mechanisms, including the transition from small intermediate gaseous species to large PAHs and incipient particles, is still the least understood step of soot formation, especially under turbulent combustion conditions. Besides, even approximate experimental data on concentrations of gaseous species in turbulent premixed flames under fuel–rich conditions are scarce. Because of the chaotic and unsteady nature of the flow, turbulence introduces variations of gas–phase conditions over a range of length scales and timescales.

In this Chapter, the details of the sampling process for PAH species are provided. A standardised operational procedure is used to enhance the repeatability of (i) sample collection, (ii) extraction, (iii) preparation and (iv) analysis. Each step is described precisely, and relevant discussions are presented accordingly.

6.2 Experimental steps

The sampling probe was initially placed at $X/L_I = 0.5$, where the physical and chemical evolution plays a crucial role in the formation of particulates as discussed in laser–based diagnostic experiments (see Chapter 4). Different dilution ratios are applied to identify an optimum sampling collection where minimum PAH losses are found on the sampling line. The optimum sampling condition requires a proper sampling line temperature and nitrogen dilution, which is dependent on the flame structure. When the optimum dilution ratio is established, the probe was located at various heights to provide spatial profile distribution of species over the reaction zone layer ($- 1.0 \leq X/L_I \leq + 1.5$). The impact of equivalence ratio and rate of strain on the PAHs profile distribution is further investigated. The PAH species contribution to soot nucleation is also presented for different experimental conditions.

6.3 Sample collection

The schematic of the sampling collection is shown in Fig. 6.1. The probe configuration and sampling system are discussed comprehensively in Chapter 3. A brief summary is provided in the current Chapter. The quartz probe, manufactured by Hilgenberg GmbH, features aerodynamic quenching and transfer–line nitrogen dilution. The probe tip orifice diameter is 286 μm and thus below 10% of L_I to reduce interference effects. The aerodynamic shape of the probe is based on the recommendations of Fristrom and Westenberg [242]. An opening angle of 20 degrees minimises flame disturbance while providing sufficient sample quenching [210].

Two large vacuum chambers (total volume 36.8 l), separated by a vacuum regulator, provide a constant sampling pressure of 20 mbar in the absence of pressure fluctuations. The transfer line is equipped with a pressure transducer (UNIK 5000; GE Measurement

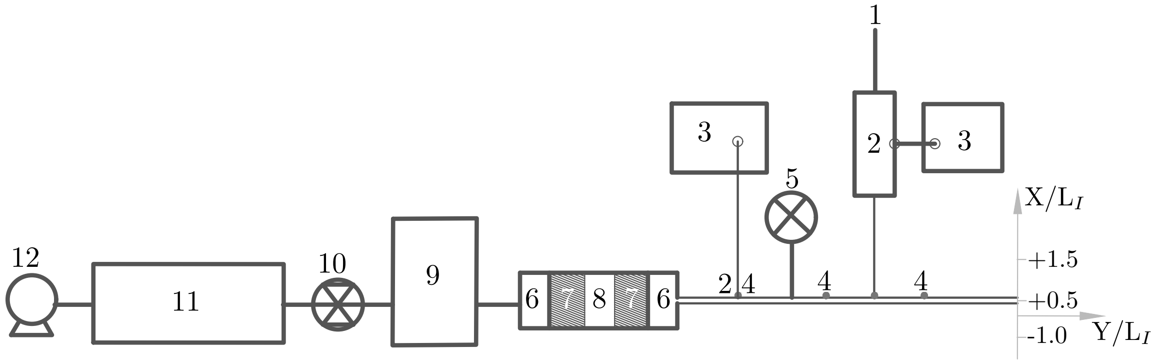

Figure 6.1. Sampling collection system used to measure PAH species over spatial locations $-1.0 \leq X/L_I \leq +1.5$. 1) Nitrogen dilution; 2) Heater; 3) PID controller; 4) Thermocouple; 5) Pressure transducer; 6) KF vacuum fitting; 7) Quartz wool; 8) XAD resin; 9) Vacuum chamber; 10) Vacuum regulator; 11) Vacuum volume; 12) Vacuum pump. The filter unit is composed of XAD–2 resin enclosed by quartz wool.

and Control), and frequent leak tests were performed to preclude sample contamination.

The wall temperature of the sampling system and the temperature of nitrogen dilution is regulated via PID controlled electric heaters. The set temperature of 523 K minimises soot agglomeration and thermophoretic, adsorption and condensation losses within the system [31, 32, 252]. The probe–tip dilution ratio corresponds to the limit where minimum species sedimentation was quantified during the extraction line (see section 6.3.2).

The diluted sample is collected on a filter unit that consists of XAD resin enclosed by two series of quartz wool as shown in Fig. 6.1. The filter unit configuration is weighed to ensure that the constant pressure differential is applied within the system between each experimental set. The weight of the filter unit configuration is listed in Table 6.1.

The sampling line assembly can be traversed in all directions using linear translation stages, and the location is calibrated using the optical setup. The ELS camera determines the X and Y position (i.e. $X/L_I = 0.5$, $Y/L_I = 0$) and the laser light sheet determines the alignment of the probe tip with the theoretical stagnation point streamline.

Table 6.1. The weight of filter unit components used in the filter unit. QW1 – The initial package of quartz wool placed at the end of transfer line; QW2 – The second package of quartz wool used to enclose XAD resin.

Components	QW1	XAD	QW2
Mass (gr)	0.3	0.58	0.25

6.3.1 Sampling process

The sampling system is preheated at atmospheric pressure to a steady–state temperature of 523 K. The probe is then moved to the measurement location and constant pressure sampling initiated by connecting the transfer line (valves 10 and 6). A sampling time of about 10,000 integral time–scales of turbulence is used (120 s) to ensure statistical independence. Sampling collection is terminated by disconnecting the probe from the vacuum system. The KF vacuum fitting is utilised to facilitate the replacement of filter packages. After dissembling KF vacuum fitting and removing the filter package, the nitrogen flows through the transfer line to remove any PAH residues and avoid any error of a set to another new sampling set. The sampling system is then moved into a new location using the manual stage. The sampling collection step is re-initiated by connecting probe to the vacuum system.

6.3.2 Optimal sampling collection

Transport efficiency is a critical factor in providing true concentrations of PAHs and particulates. Some research groups have discussed the inconsistent peak intensities on the mass spectrum from a sample to another sample. The optimum sampling conditions and an established operation procedure can minimise uncertainties within the sampling system. The impact of sampling line temperature and dilution ratio on PAH losses within the sampling system are studied. The pressure differential (between the flame and sampling pressure) is kept constant at 20 mbar. The pressure differential

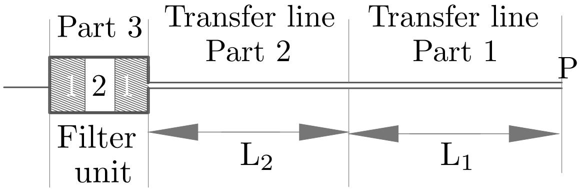

Figure 6.2. The definition of the sections of the sampling system and filter unit: (1) and (2) indicate quartz wool and XAD resin, respectively, and P the probe tip. The transfer line is split into parts. The optimum dilution ratio is at the limit where minimum species losses are found in the transfer line with species captured via the filter unit.

of 20 mbar provides minimum flame perturbation using ELS and PAH–PLIF signals as discussed in Chapter 3. The nitrogen flows are varied to provide different dilution ratios at constant ΔP = 20 mbar.

6.3.2.1 The optimal dilution ratio

The dilution ratio was calibrated using CO_2 and N_2 concentrations. The measurement probe was placed at the position (in the flame) where the maximum CO_2 concentrations were measured and nitrogen dilution was applied. Samples were collected in tedlar gas sampling bags.

The chemical analysis was performed by a gas chromatograph (Agilent 7890A) equipped with a thermal conductivity detector (TCD). A HP–PLOT Q and a HP–Molesieve column (helium carrier gas) were used to quantify CO_2 and N_2, respectively. The GC–TCD was calibrated regularly using Scotty gas mixtures (purchased from Agilent Technologies LTD) containing C_1 – C_4 hydrocarbons, CO, CO_2 and N_2. The dilution ratio (DR) was calculated according to Eq. (6.1),

$$\mathrm{DR} = \left(\frac{x_{\mathrm{CO_2,S}}}{x_{\mathrm{N_2,S}}}\right)/\left(\frac{x_{\mathrm{CO_2,DG}}}{x_{\mathrm{N_2,DG}}}\right) \tag{6.1}$$

where subscripts S and DG stand for sample and diluting gases, respectively.

Table 6.2. The quantified mole fraction of m/z = 130 at different parts of the sampling system. The ratio of extracted species to the summation of captured species on all parts is presented in brackets. The bold text is the optimal sampling condition, where minimum species losses are found in the transfer line with species is captured in the filter unit. The results are presented for REF flame at the spatial location of X/L_I = 0.5.

Variables		Mole fraction [-] $\times 10^{-4}$		
T [K]	DR [-]	Part 3	Part 2	Part 1
293	–	0.49 (9%)	1.98 (38%)	2.76 (53%)
373	–	1.84 (35%)	1.58 (30%)	1.84 (35%)
523	–	3.34 (62%)	0.91 (17%)	1.13 (21%)
523	453	4.43 (85%)	0.43 (8%)	0.33 (7%)
523	**758**	5.21 (97%)	0.04 (0.7%)	0.08 (2.3%)
523	1057	4.09 (78%)	0.35 (7%)	0.79 (15%)
523	1426	3.81 (73%)	0.58 (11%)	0.86 (16%)

6.3.2.2 Sampling line conditions

The sampling system was initially used to quantify losses in the transfer lines to ensure that species were captured on the filter unit, see Fig. 6.2, where the sampling line sections are also defined. Results are here provided for m/z = 130 and m/z = 192 and shown in Tables 6.2 and 6.3, respectively. The impact of the sampling conditions are presented for an experimental condition with a HCP temperature of 1500 K, an equivalence ratio $\phi_{UN} = 2.0$ and a rate of strain a_T = 420 s^{-1}. Species losses onto the walls of the transfer lines (Parts 1 and 2) are unacceptably high when the sampling process is using a cold transfer line and without nitrogen dilution [252] as only 9% and 5% of the total extraction for m/z = 130 and m/z = 192, respectively, are collected on the filter unit. Adsorption and condensation of species is significantly reduced when the temperature of the transfer line is increased to 523 K [291] with the detected species fraction on the filter unit increases up to a factor of ten for m/z = 192 as shown in

Table 6.3. The quantified mole fraction of m/z = 192 at different parts of the sampling system. The ratio of extracted species to the summation of captured species on all parts is presented in brackets. The bold text is the optimal sampling condition, where minimum species losses are found in the transfer line with species is captured in the filter unit. The results are presented for REF flame at the spatial location of $X/L_I = 0.5$.

Variables		Mole fraction [-] $\times 10^{-4}$		
T [K]	DR [-]	Part 3	Part 2	Part 1
293	–	0.27 (5%)	2.62 (48%)	2.62 (47%)
373	–	1.51 (27%)	1.91 (35%)	2.11 (38%)
523	–	3.05 (54%)	1.47 (26%)	1.13 (20%)
523	453	5.01 (89%)	0.41 (7%)	0.23 (4%)
523	**758**	5.58 (97%)	0.06 (1%)	0.11 (2%)
523	1057	4.49 (80%)	0.44 (8%)	0.67 (12%)
523	1426	3.76 (68%)	0.82 (15%)	0.97 (17%)

Table 6.3. However, sedimentation in the transfer lines (Parts 1 and 2) remains at 38% of the total for m/z = 130. The reason is that the temperature gradient between the sampling line and flow is high at the probe entrance [252, 292]. In order to minimise thermophoretic losses, nitrogen dilution is applied while the sampling line temperature is maintained at 523 K via multi–PID controllers.

The heated nitrogen dilution reduces species sedimentation near the sampling probe tip and along the extraction line as shown in Tables 6.2 and 6.3. The probe–tip dilution should be limited in order to minimize particle nucleation, condensation, and sedimentation in the sampling line [218]. The optimum sampling condition, resulting in a collection efficiency of 97% for both m/z = 130 and 192, is reached with a sampling line temperature of 523 K and a dilution ratio of DR = 758 for reference (REF) flame. The optimum dilution ratio is listed in Table 6.4 for each experimental conditions. The values are used in the current work to measure spatial distribution profile of PAH species over the reaction zone layer.

Table 6.4. The optimum dilution ratio used for various experimental conditions. The optimum sampling condition is a limit where minimum species losses are found on the transfer line, and species is captured via filter unit.

Experimental cases	$\phi_{UN} = 1.8$	$\phi_{UN} = 2.0$	$\phi_{UN} = 2.2$	$a_T = 255$ s^{-1}	$a_T = 610$ s^{-1}
DR [-]	423	758	1057	1726	505

6.4 Sample extraction and preparation

When the sample collection is completed, all parts are dissembled to determine sampling losses during extraction and species on the filter package. All parts are washed with Dichloromethane (DCM) to extract any condensed PAHs. When the dilution ratio is optimised for each flame condition, the washing process is only applied to the filter unit.

The extraction of PAH species from the filter unit was assessed for a number of configuration. The dissolved samples are placed on magnetic stirrer for homogenisation. Then, a Branson B-22 Ultrasonic unit is used. The samples are then centrifuged (Grant Bio PCV-2400) to remove particles and residues to prepare for GC–MS injection.

Extraction of species from the filter, or the separation of aggregated PAHs is complex [293], and different filter configurations were evaluated in terms of their PAH extraction efficiency during sonication as shown in Fig. 6.3. Samples were analysed using MS at sonication (Branson B-22 Ultrasonic) intervals of 1, 5, 24, 72 and 120 h. The filter unit–2 consists a series of quartz wool and XAD. The filter unit–1 includes a quartz fiber filter ahead of quartz wool and XAD. It was found that the extracted PAH (e.g. benzo(a)pyrene) concentrations were constant over the full range of sonication times when quartz wool filters (in the absence of quartz fibre filter) are used in the filter unit. Direct analysis of the species concentration recorded with the quartz fibre filter in place leads to incorrect conclusions. The quartz fibre filter eliminates a significant fraction of the total signal measured mass spectrometer. For instance, the placement of a quartz fibre filter ahead of the filter unit leads to a deficit of 17%

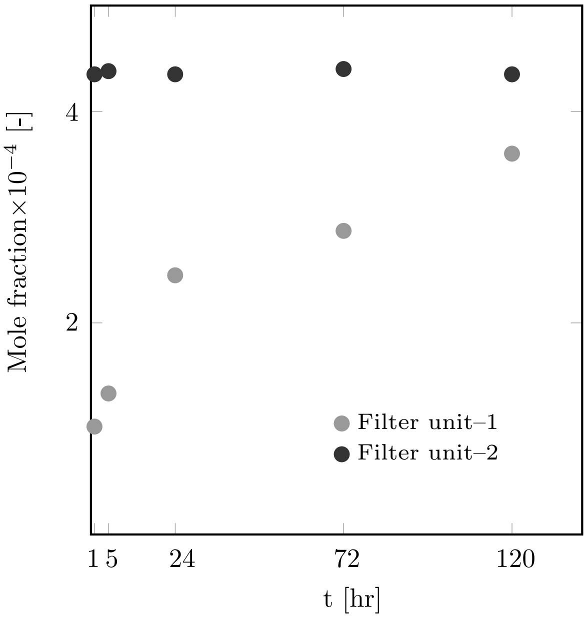

Figure 6.3. Benzo(a)pyrene (B(a)P) concentration over sonication intervals extracted from different filter units. Filter unit 1 contains XAD resin enclosed by quartz wool. Filter unit 2 consists of quartz fiber filter ahead of quartz wool and XAD resin. The equivalence ratio is at ϕ_{UN} = 2.0, rate of strain is a_T = 420 s^{-1} and burnt gas temperature is T_{HCP} = 1500 K.

remaining in the benzo(a)pyrene concentration after 120 h. The reason is that the quartz fibre can affect the signals in several ways. There could be a direct loss of particles or PAHs on the quartz fibre, which causes an overall loss of signal at all masses. The removal of volatile coatings from the particles leads to a reduced average particle size [294].

The effect of centrifuge on the B(a)P concentration is depicted in Fig. 6.4 for various rates of strain. The species reach to plateau at the end of centrifuge period (t = 10 min). Resonance–stabilised radicals can deposit/infuse on soot particles either during sample collection or in the flame [111]. Second, the composition of particulates at soot inception include aromatic structures with stacked PAHs bound together with van der Waals forces [129]. The PAH separation is carried out via the centrifuge process [295]. The infusion of PAH onto particles is significantly higher at low rates of strain and its level is proportional to the particle number concentration. The concentration of benzo(a)pyrene increases by up to five and twelve times for the REF flame (a_T = 420 s^{-1}) and highly sooting flame (a_T = 255 s^{-1}), respectively.

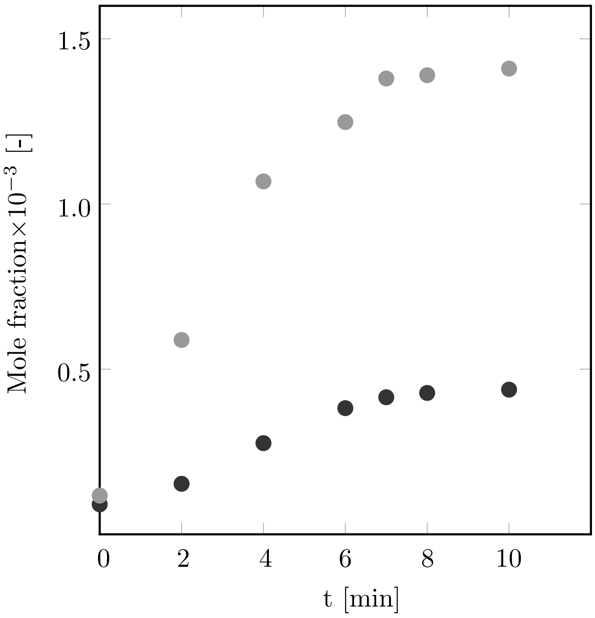

Figure 6.4. The mole fraction of benzo(a)pyrene (B(a)P) at various centrifuge time for the REF flame – $a_T = 420$ s^{-1} (black) and $a_T = 255$ s^{-1} (grey). The equivalence ratio is $\phi_{UN} = 2.0$ and burnt gas temperature is $T_{HCP} = 1500$ K. The spatial location is at $X/L_I = 0.5$ for both cases.

6.5 Sample analyses

The ion count is a non–unit parameter calibrated routinely using external and internal standard (reference) solutions. The internal standard solutions (Accustandard [Z–014J–0.5X]) are added to the liquid samples and the external standard solutions to both, separately, to account for routine variation in the response of the chromatographic system. A Select–PAH column is utilised to achieve quantitative separation of PAHs. The separation is significantly enhanced by using an optimal gas flow and the complex GC temperature profile as listed in Table 6.8. A high GC inlet temperature (T = 573 K) and a liner with glass wool are used to avoid desublimation and deposition of large PAHs within the GC [296]. In the last step of the oven program, the GC is operated at the maximum column temperature for 300 s to remove possible species residues and prepare the system for the next injection [297]. Seventeen different PAHs compounds (Accustandard [DRH–006S]) and 29 refinery gas aromatics (Accustandard [M–GRA–CAL–R/IS–R–01]) are quantified using external standard calibration with seven-point calibration curves. Standard calibration mixture of PAHs and refinery gas aromatics are listed in Table 6.5 and Table 6.6, respectively. The respective mass spectrum is shown in Fig. 6.5 and Fig. 6.6. A selection of identified compounds in the sample extracted from flame are listed in Table 6.7 and illustrated in Fig. 6.10. The NIST Library and AMDIS software are used to confirm the identification of species [298]. Results cover four intervals of the retention time (RT). The letters (a, b, c, d, e, f) refer to the internal standard solution (ISD), used to correct the MS response. There exists several isomers appearing on the mass spectrum playing significant roles in the formation of particulates. The results are provided for summation of isomers except known species are identified and confirmed using external standard calibration via the NIST library and AMDIS software.

6.6 Distribution of PAHs through the flame brush

Direct probe sampling from the flames (online sampling) leads to PAH losses within the extraction line and the filter unit and neglects PAH condensation onto soot. Samples should also include internal standard solutions to account for routine variations in the response of the chromatographic system, which is not applicable to online sampling. Therefore, optimum sampling conditions were established to minimise experimental uncertainties as outlined in Section 6.3.2. The Select–PAH column is used to quantify the major PAH species (see Table 6.7). As shown by the mass spectrum in Fig. 6.10, the mass distribution of PAH species covers the interval of $m/z = 92 - 300$ amu. The concentrations, given in Figures, correspond to the mole fractions of PAH species ($m/z = 92 - 300$ amu) in the analysed liquid sample **including** the solvent (DCM) contribution.

A direct comparison of in-situ technique and probe sampling is challenging. On the one hand, laser diagnostics cannot precisely quantify the infusion level of resonance–stabilised radicals on soot particles in the flame.

Table 6.5. Standard calibration mixture of PAH species purchased from Accustandard Accustandard [DRH–006S]. The mass spectrum is shown in Fig. 6.5. Bold texts are deuterated internal standard solutions.

ID	Name	ID	Name
a	**1,4–Dichlorobenzene**	7	Anthracene
b	**Naphthalene–D8**	8	Fluoranthene
1	Naphthalene [A2]	9	Pyrene ($C_{16}H_{10}$)
2	2–Methylnaphthalene [2–MN]	10	Benz(a)anthracene
3	Acenaphthylene	**e**	**Chrysene–D12**
c	**Acenaphthene–D10**	11	Chrysene
4	Acenaphthene	12	Benzo(b)fluoranthene
5	Fluorene	13	Benzo(k)fluoranthene ($C_{20}H_{12}$)
d	**Phenanthrene–D10**	14	Benzo(a)pyrene [B(a)P]
6	Phenanthrene ($C_{14}H_{10}$)	**f**	**Perylene–D12**

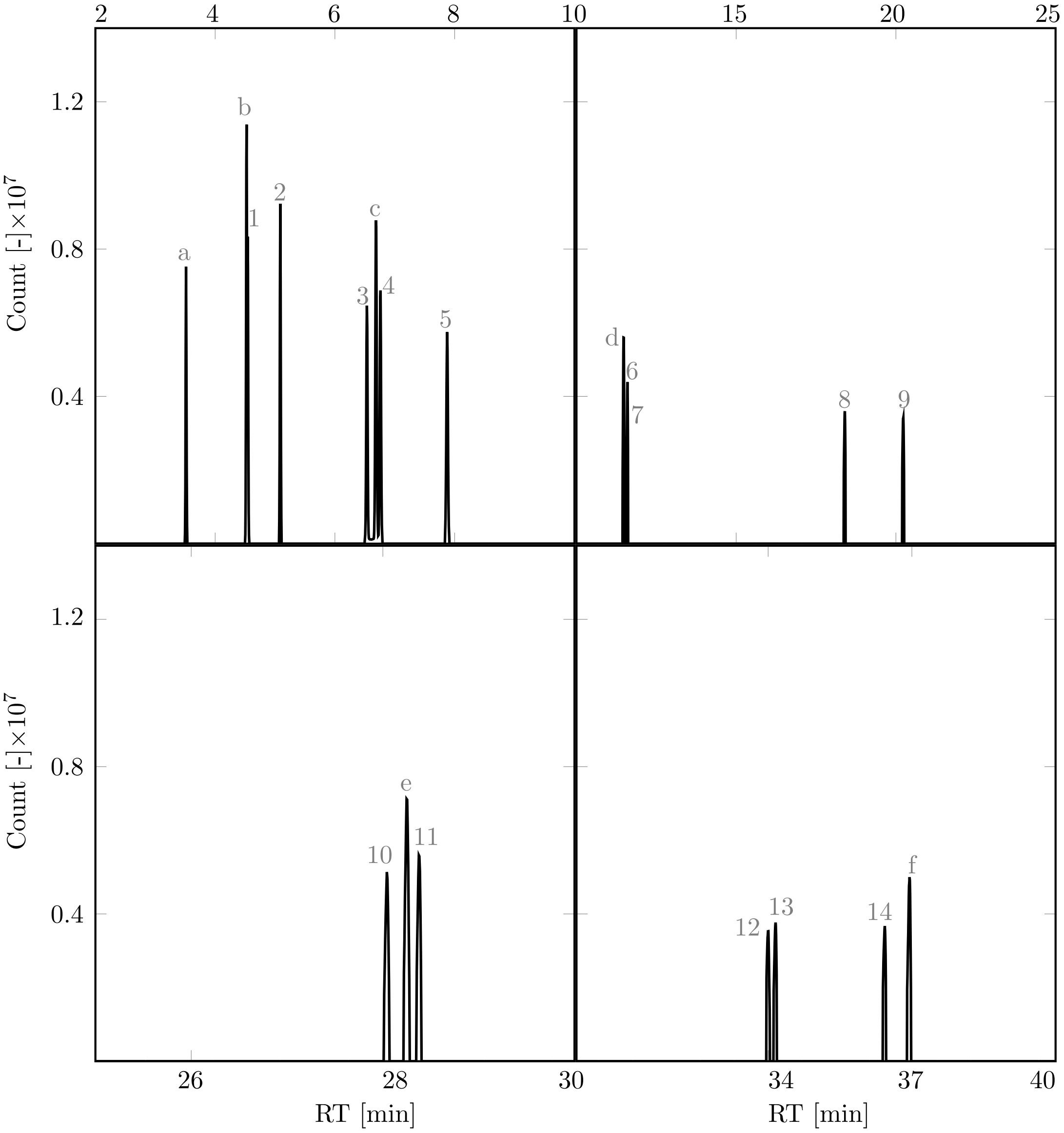

Figure 6.5. Mass spectrum from the mixture of PAH and deuterated internal standard solutios. The complete list of species is presented in Table 6.5.

Table 6.6. Standard calibration mixture of refinery gas aromatics purchased from Accustandard [M–GRA–CAL–R/IS–R–01]. The mass spectrum is shown in Fig. 6.6. Bold texts are deuterated internal standard solutions.

ID	Name	ID	Name
a	**Benzene-d6**	12	1,3,5-Trimethylbenzene
1	Benzene	13	1,2,4-Trimethylbenzene
b	**Toluene-d8**	14	1,2,3-Trimethylbenzene
2	Toluene	15	n-Butylbenzene
c	**Ethylbenzene-d10**	16	1,4-Diethylbenzene
3	Ethylbenzene	17	1,2-Diethylbenzene
4	Xylene	18	Indane
5	Xylene	19	1,2,4,5–Tetramethylbenzene
6	Xylene	20	1,2,3,5–Tetramethylbenzene
7	Isopropylbenzene	**d**	**Naphthalene-d8**
8	propylbenzene	21	Naphthalene
9	1-Methyl-3-ethylbenzene	22	Pentamethylbenzene
10	1-Methyl-2-ethylbenzene	23	2–Methylnaphthalene
11	Methyl-4-ethylbenzene	24	1–Methylnaphthalene

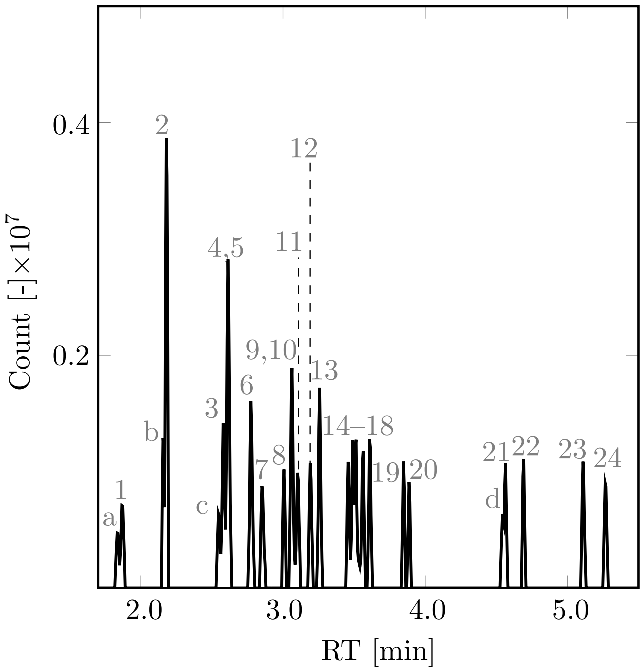

Figure 6.6. Mass spectrum from the mixture of refinery and deuterated internal standard solutions. The complete list of species is presented in Table 6.6. The mass spectrum shows the performance of PAH–select column and optimum GC conditions in the separation of isomers.

Table 6.7. The selection of identified species illustrated in Fig. 6.10. Bold texts are deuterated internal standard solutions. Grey numbers refer to species including isomers. The contribution of each species to soot nucleation is assessed for different flame structures from lightly to heavily sooting conditions.

ID	Name	ID	Name
1	m/z = 92	**d**	**Phenanthrene–D10**
a	**1,4–Dichlorobenzene**	15	Phenanthrene
2	m/z = 132	16	Anthracene
3	m/z = 130	17	m/z = 192
b	**Naphthalene–D8**	18	m/z = 206
4	Naphthalene [A2]	19	Isomer to Pyrene
5	m/z = 148	20	Pyrene [A4]
6	m/z = 146	21	m/z = 216
7	2–Methylnaphthalene [2–MN]	22	Benz(a)anthracene [B(a)A]
8	1–Methylnaphthalene [1–MN]	**e**	**Chrysene–D12**
9	Isomer to 1–MN	23	Chrysene
10	m/z = 156	24	m/z = 240
11	m/z = 154	25	Benzo(b)fluoranthene
12	m/z = 165	26	Benzo(k)fluoranthene
c	**Acenaphthene–D10**	27	Benzo(a)pyrene [B(a)P]
13	Fluorene	**f**	**Perylene–D12**
14	m/z = 170	28	m/z = 276

Table 6.8. GC–MS analysis conditions consisting of complex GC temperature and optimal gas flow to enhance quantitative separation of PAHs. P_{in} and T_{in} are the inlet pressure and temperature. A high GC inlet temperature (T = 573 K) and a liner with glass wool are used to avoid desublimation and deposition of large PAHs within the GC.

Instrument	MSD (Agilent 5975C)
Column	Select–PAH (CP7462)
Carrier	Helium, constant flow 0.94 mL/min
P_{in}	34473.8 Pa
T_{in}	573 K
Oven program	343 K for 1 min, 40 K/min to 453 K, 3 K/min to 503 K, 1.5 K/min to 508 K, 10 K/min to 553 K, 553 K for 5 min, 5 K/min to 571 K, 10 K/min to 593 K, 593 K for 5 min.

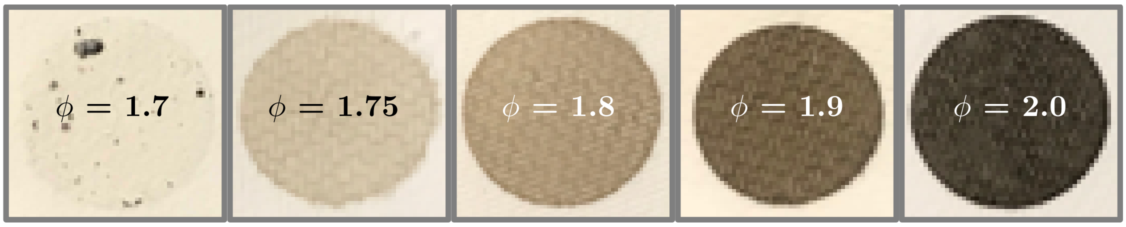

Figure 6.7. Carbon particulates deposited on the quartz filter for different equivalence ratios, illustrating heavily aggregated particles at high equivalence ratio and small dispersed particles close to the soot inception point. The gas burnt temperature is $T_{HCP} = 1500$ K and the total rate of strain is $a_T = 420$ s^{-1}.

The quantification of PAH species using LIF is a challenging task as PAHs species contain a mixture of distinct functional groups with broad spectra. The spectra of such species can overlap with each other. On the other hand, GC–MS can present the mass spectrum of species up to $m/z = 300$ amu. The given data cannot include all PAHs.

The soot loading on the filter is illustrated in Fig. 6.7 for different stoichiometries. The amount of carbon increases by up to a factor of six with increasing equivalence ratio in the range $1.75 \leq \phi_{UN} \leq 2.0$ as measured by EDX and shown in Fig. 6.8. The corresponding SEM images (Fig. 6.9) show densely aggregated particles at $\phi_{UN} = 2.0$ and small dispersed particles close to the soot inception point of $\phi_{UN} = 1.75$.

A sample of the mass spectrum extracted from the lower and upper limit of rates of strain ($a_T = 255$ and 610 s^{-1}) is shown in Fig. 6.10. The major species determined here have also been observed experimentally in other studies [40, 299, 300].

The presence of two peak sequences is noticeable among the species shown in the mass spectrum. The first sequence appears with 24 m/z units gap, which supports the role of C_2 addition via HACA style sequences followed by dehydrogenation. The growth of PAHs is further consistent with the addition of CH_2 (methylene) and CH_3 (followed by dehydrogenation) as shown by the 14 m/z gaps between PAH species. The results are consistent with the finding reported by Panariello et al. [301]. Liu et al. [302] concluded that the formation of a five–member ring are the results of the sequence of C_2H_2 addition, intramolecular hydrogen migration, CH_2 addition, and cyclization with

H elimination.

The mass spectra show that concentrations of comparatively heavy PAHs (i.e. B(a)P, m/z = 276) can build up ahead of light species [48]. From a public health perspective, the observation that soot particles become strongly infused with a Group 1 carcinogen is of significance. The importance of lighter molecules (e.g. 1–methyl naphthalene (1–MN) and m/z = 154) should not be neglected. For instance, 1–MN is a comparatively stable methyl–substituted two–ringed PAH. Schulz et al. [45] and Commodo et al. [46] suggest that methyl group substitutions make an important contribution to soot formation. As shown in this study, 1–MN is one of the major PAHs detected in the current turbulent flames. By contrast, 2–MN is present in smaller quantities suggesting a comparatively modest contribution to soot formation. Johansson et al. [122] suggest that it is crucial to consider the contributions made by all m/z = 154 isomers to the nucleation process. Reactions featuring PAHs also provide a route for mass growth [39] and structures involving C_5 rings can appear in quantities similar to, or exceeding, those based on C_6 rings [47].

The coupling between gas–phase and surface reactions [141] is an important factor and, as shown above, PAH condensation onto soot particles plays a significant role. The important note is that the PAH concentration is comparatively low before applying the centrifuge process. The centrifuge effect shows the high infusion level of PAH species into solid particulate. Interestingly, the relatively high abundance of comparatively heavy PAH (i.e. m/z = 252) are also found without using the centrifuge process at lightly sooting condition (ϕ_{UN} = 1.7) where particle formation is low as depicted in Fig. 6.7.

6.6.1 PAH sampling close to the stagnation point

Experiments were initially conducted to identify the optimum dilution range for different flame sooting conditions. The sampling point (close to the stagnation plane, i.e.

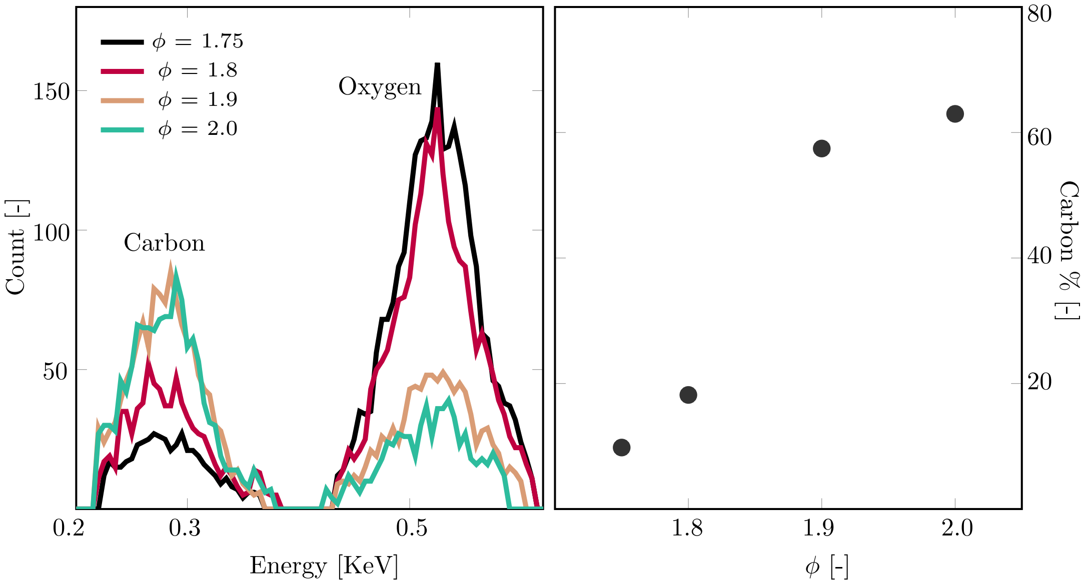

Figure 6.8. EDX analysis (left column) and carbon percentage ([Carbon]/ [Carbon+Oxygen+Silicon]) (right column) on quartz fibre filter. The analyses is conducted at a constant rate of strain of a_T = 420 s^{-1} and gas burnt temperature of T_{HCP} = 1500 K. The carbon loading on quartz fiber filter is 6 times higher for the REF flame (ϕ_{UN} = 2.0) in comparison to the soot inception case (ϕ_{UN} = 1.7).

X/L_I = 0.5) was chosen where the physical and chemical evolution plays a crucial role in the formation of particulates as confirmed by laser diagnostic experiments. Different dilution ratios are applied to identify optimum sampling collection with minimum PAH losses found in the sampling line.

Species sedimentation is also minimised during extraction line and species are captured on the filter at optimal sampling collection (see Table 6.4). The minimum species losses are achieved by applying a proper nitrogen dilution ratio (at T = 523 K) while the temperature of transfer line maintained constant at T = 523 K to reduce thermal gradient in the sampling line as discussed in Section 6.3.2.

The impact of equivalence ratio, lower nozzle HCP temperature and the bulk rate of strain on species concentrations (at X/L_I = + 0.5) is discussed below. As shown in Fig. 6.11, species concentrations increase with the equivalence ratio in a fairly linear manner. This is in contrast to the soot deposition on the quartz filters which increases sharply. This suggests that the gas phase PAH pool is significantly depleted through the soot formation process.

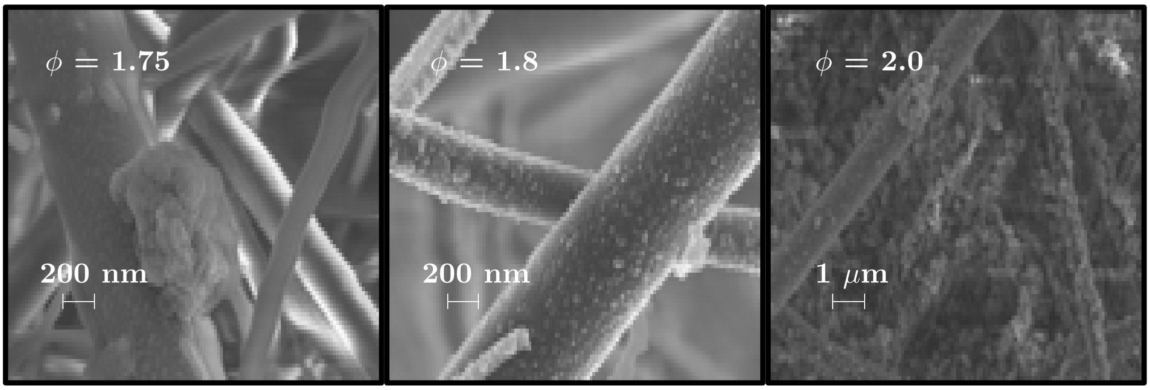

Figure 6.9. SEM images of carbon particulates on the quartz fibre filter at different equivalence ratios, showing heavily aggregated particles at high equivalence ratio and small dispersed particles close to the soot inception point. The experiments are carried out at a constant rate of strain of $a_T = 420$ s^{-1} and burnt gas temperature of $T_{HCP} = 1500$ K. The probe is located at the spatial location of $X/L_I = 0.5$.

The PAH concentrations are remarkably sensitive to increases in the rate of strain. The decrease in concentrations from $a_T = 255$ s^{-1} to 420 s^{-1} is shown in Fig. 6.12. This suggests strongly that the PAH formation chemistry is slow and that small–scale interactions between turbulence, gas-phase chemistry, and soot particles have a crucial impact on particulate formation in turbulent flames. The implication is that turbulence–chemistry interactions must be treated accurately in any modeling approach (c.f. low Damköhler number processes).

The PAH concentrations are comparatively insensitive to the lower nozzle HCP temperature as shown in Fig. 6.13. There is an increase in the species concentration when the temperature is increased from 1400 to 1500 K, which is followed by a slight decrease at 1600 K. This implies a high level of competition between the soot formation and oxidation reactions with soot oxidation starting to take precedent at temperatures of $T_{HCP} \geq 1600$ K. This is consistent with the non-intrusive laser diagnostics as discussed in Chapter 4.

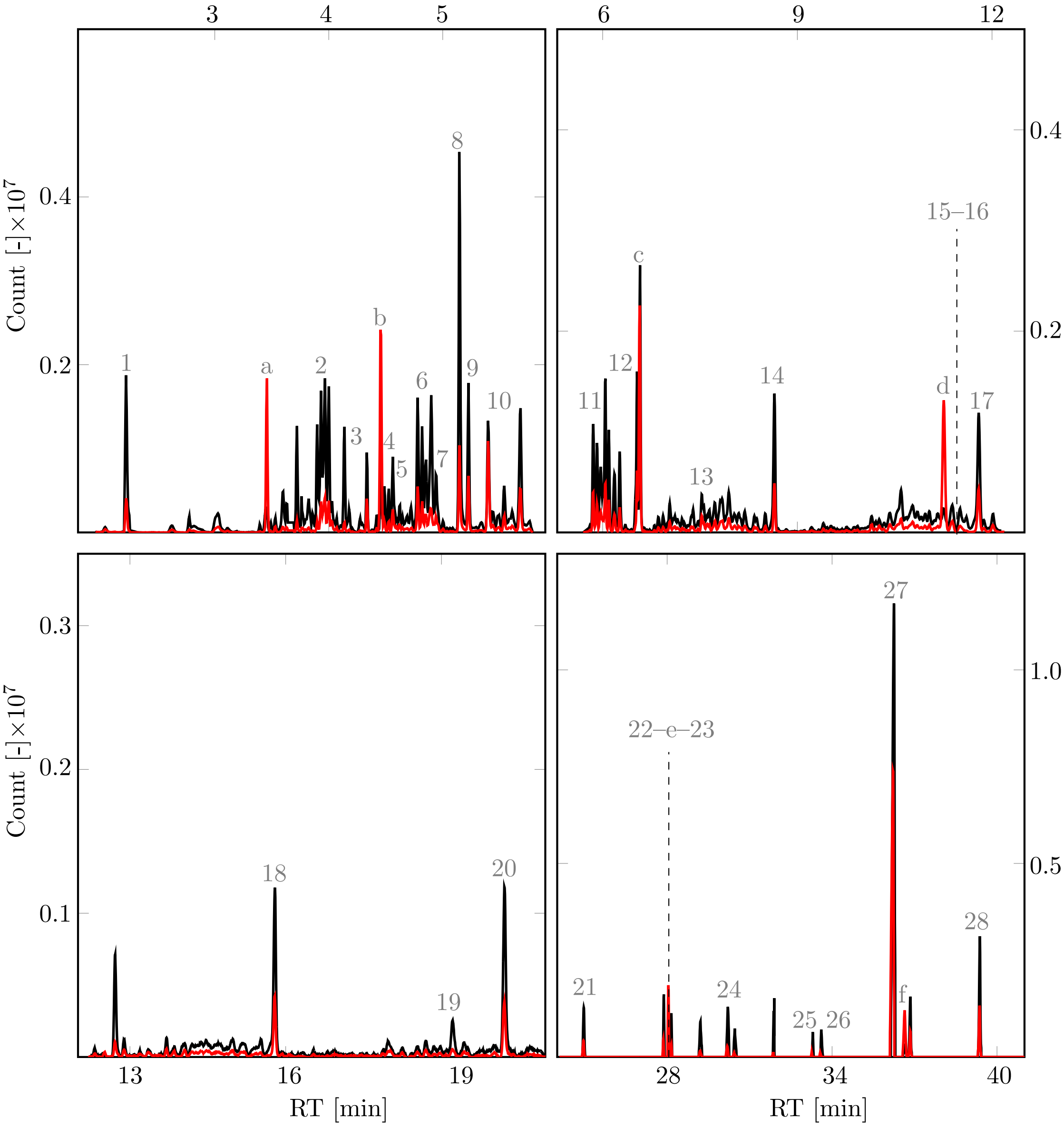

Figure 6.10. Mass spectrum extracted from low ($a_T = 255$ s^{-1} – black) and high rates of strain ($a_T = 610$ s^{-1} – red) showing the contribution of major PAH species to soot nucleation. The mass spectrum is extracted from flame for spatial location of $X/L_I = 0.5$ at a constant equivalence ratio of $\phi_{UN} = 2.0$ and burnt gas temperature of $T_{HCP} = 1500$ K. The peak labels correspond to the list presented in Table 6.7.

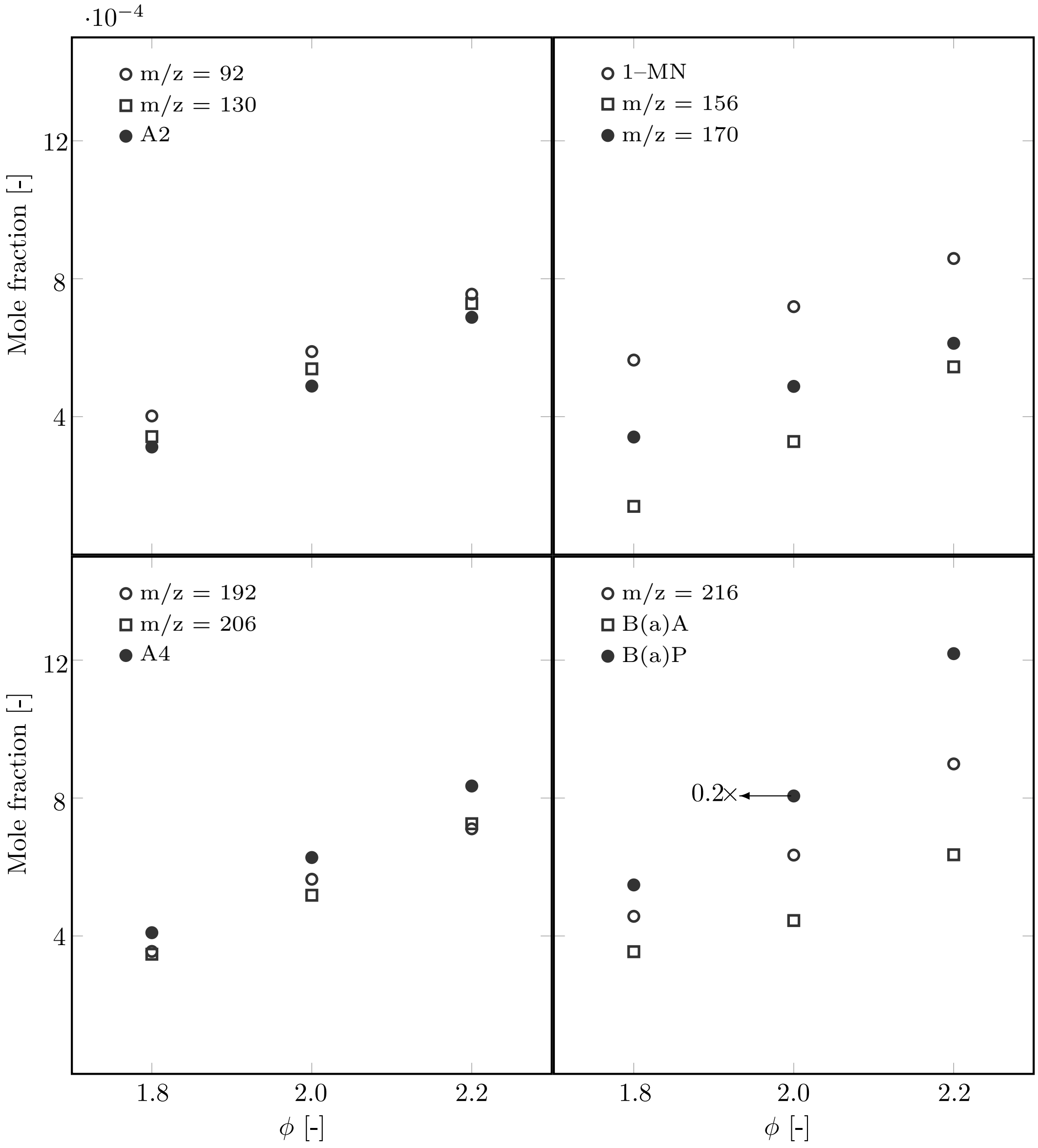

Figure 6.11. The effect of equivalence ratio on species concentration at constant rate of strain of $a_T = 420$ s^{-1} and burnt gas temperature of $T_{HCP} = 1500$ K. The probe tip is posited at the spatial location of $X/L_I = 0.5$. The respective optimum dilution (see Table 6.4) is applied to ensure minimum species losses during extraction line.

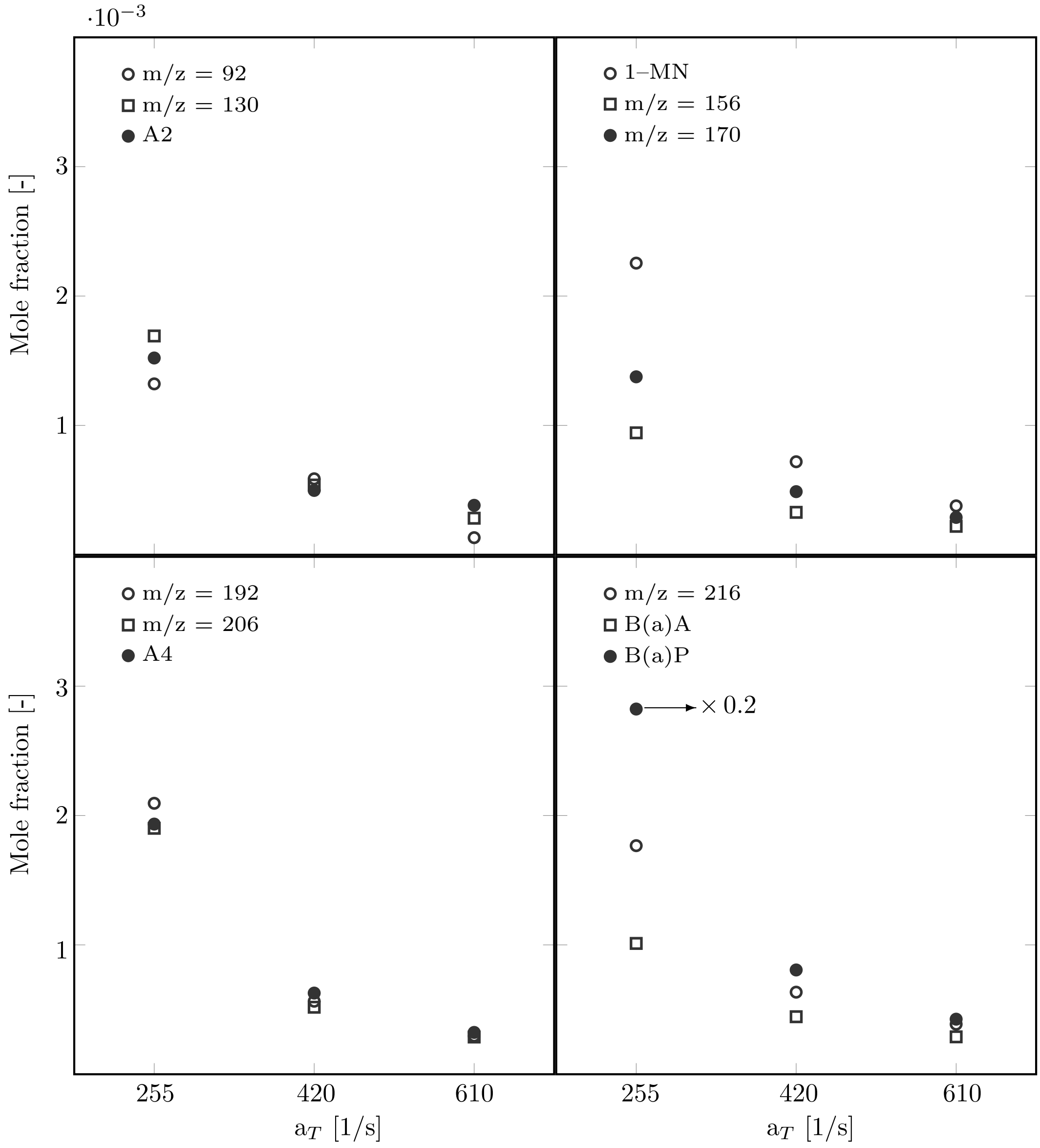

Figure 6.12. The effect of the rate of bulk strain on species concentration at a constant equivalence ratio of $\phi_{UN} = 2.0$ and burnt gas temperature of $T_{HCP} = 1500$ K. The probe tip is posited at the spatial location of $X/L_I = 0.5$. The respective optimum dilution (see Table 6.4) is applied to ensure minimum species losses during extraction line.

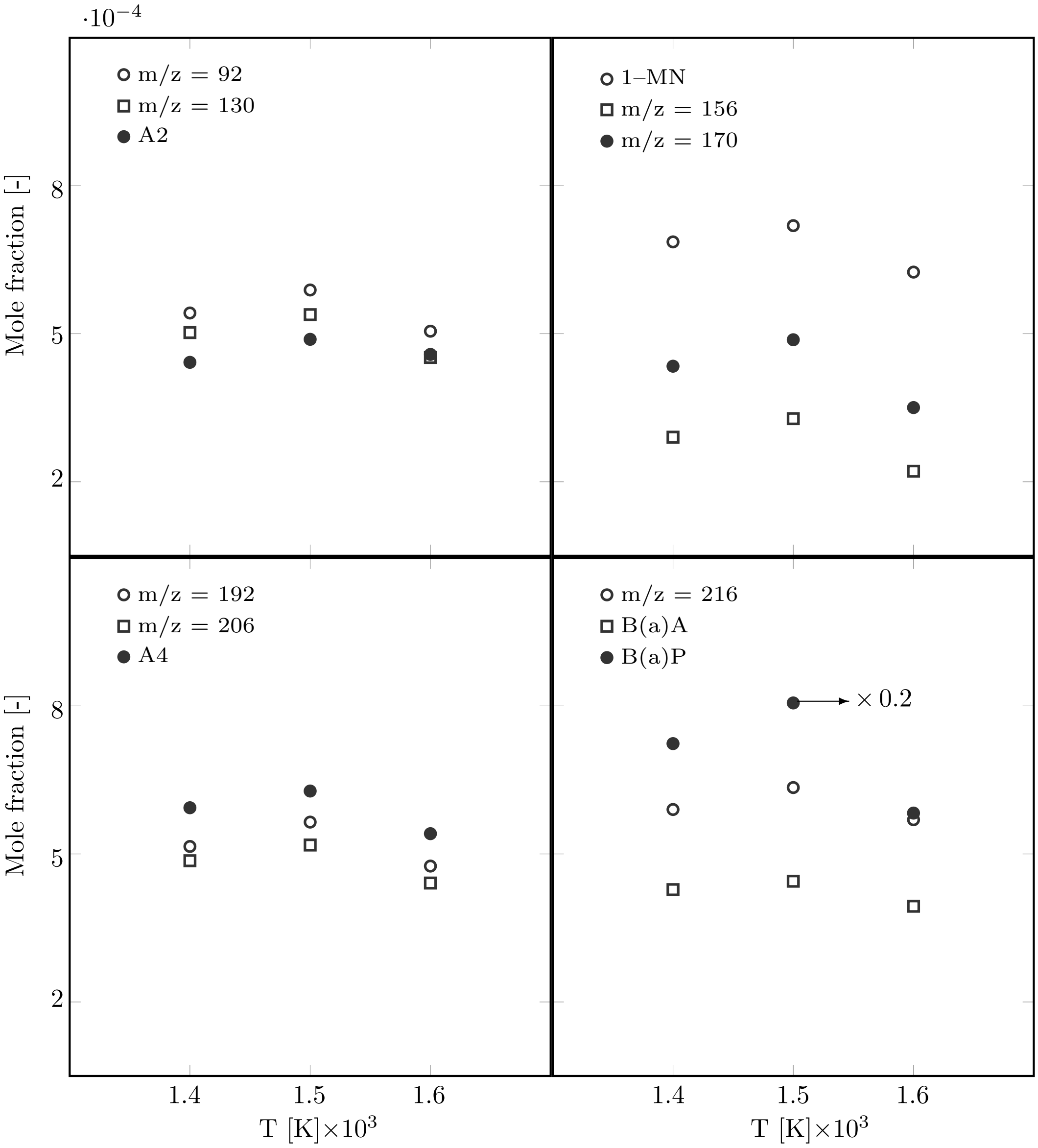

Figure 6.13. The effect of HCP from the lower nozzle temperature on species concentrations at a constant equivalence ratio of $\phi_{UN} = 2.0$ and a total rate of strain of $a_T = 420$ s^{-1}. The probe tip is posited at the spatial location of X/L$_I$ = 0.5. The respective optimum dilution (see Table 6.4) is applied to ensure minimum species losses during extraction line.

6.6.2 Spatial distribution of PAHs

The well–controlled sampling process, featuring the probe technique outlined above, was used to obtain the distribution of gaseous species within the PAH containing layer. The axial sample position was varied (6 points) along the stagnation point streamline in steps of 2 mm (i.e. about half of an integral length scale of turbulence) to include the (statistical) location of the PAH layer. A sample of the mass spectrum extracted from lightly ($\phi_{UN} = 1.8$) and heavily sooting flame ($\phi_{UN} = 2.2$) is shown in Figs. 6.14–6.15. The mass spectrum at different spatial locations are compared to $X/L_I = 0.5$, showing the distinct contributions of PAH species to soot nucleation over the reaction zone layer.

The impact of rate of strain and equivalence ratio on the spatial distribution of PAH species are shown in Figs. 6.16–6.17. It is important to note that the prevalence shown includes the solvent and correspond to the amounts present in the treated sample collected over approximately 10,000 integral time scales of turbulence. The demise of PAH is aided by the elevated temperatures found in the nearly sooting flame ($\phi_{UN} = 1.80$ and $a_T = 610$ s^{-1}) leading to enhanced oxidation. In contrast, the flames at a low rates of strain ($a_T = 255$ s^{-1}) or high equivalence ratio ($\phi_{UN} = 2.20$) are far richer and less hot than lightly sooting flames and their conditions supports the formation and survival of PAH [239].

As shown in Chapter 4, through the use of PAH–PLIF and ELS, the rate of strain has a significant impact on the formation PAHs and soot. The clear implication is that soot formation is low Da number process due to long chemical time scales. The probe measurements are consistent with the non-intrusive laser diagnostics and show a peak in PAH concentrations close to $X/L_I = 0.5$ as a result of the balance between formation and oxidation. It should again be emphasised that the reported values include the solvable amounts of condensed PAHs found on soot particles as well as on the filter units. The rate of strain shows a significant impact on the PAH species profile distribution. For a higher rate of strain ($a_T = 610$ s^{-1}), there is occasionally an initial mild increase in the mole fraction of species over axial distance from the burnt gas state to stagnation plane. This is followed by modest consumption by oxidation or, more likely, consumption by surface growth of soot particles close to the reactants. The increased residence time at lower rates of strain ($a_T = 225\,s^{-1}$) leads to a substantial increase in soot and PAH concentrations.

Mean concentration profiles of major PAHs (e.g. 1–MN, m/z = 154, m/z = 276 and B(a)P) indicate potential contributions to the formation of particulates with B(a)P present in relatively large quantities irrespective of lightly or heavily sooting conditions. It is important to note is that PAH concentrations are comparatively low before applying the centrifuge process as shown in Fig. 6.3, which indicates the importance of PAH condensation on soot particles. The concentrations of acenaphthylene and acenaphthene are consistently low from lightly to heavily sooting conditions indicating a difference balance between formation and consumption. For example, the reaction flux through these species leading to soot particles may be significant. Benzo(b)fluoranthene also reaches to a maximum at $X/L_I = 0.5$ while decreasing much faster towards both boundaries of the reaction layer.

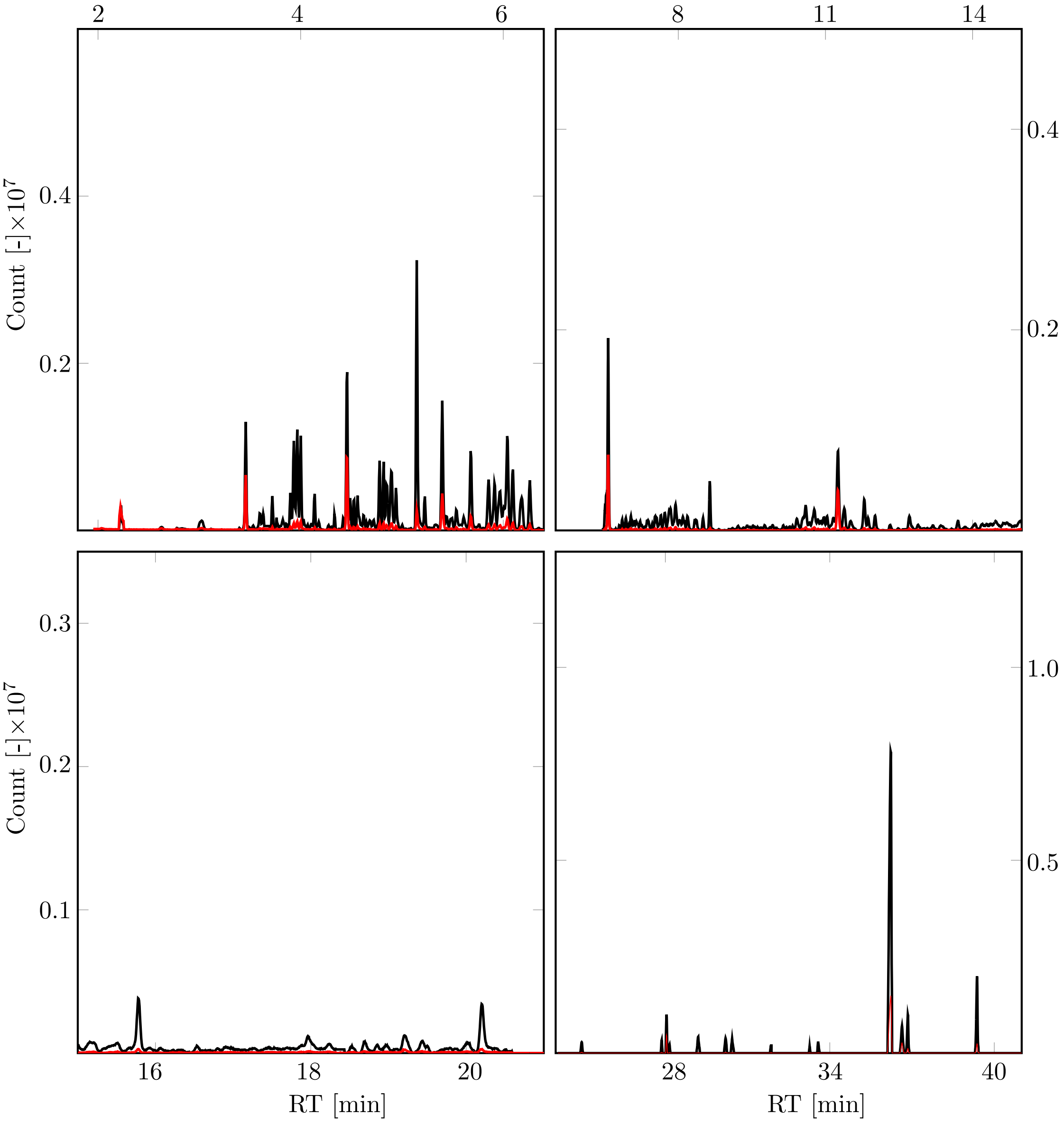

Figure 6.14. Mass spectrum extracted from the sample for the different spatial locations of X/L_I = 1.5 (red) and X/L_I = 0.5 (black) at a constant equivalence ratio of ϕ_{UN} = 1.8 and total rate of strain of a_T = 420 s^{-1}. The burnt gas temperature is constant at T_{HCP} = 1500 K.

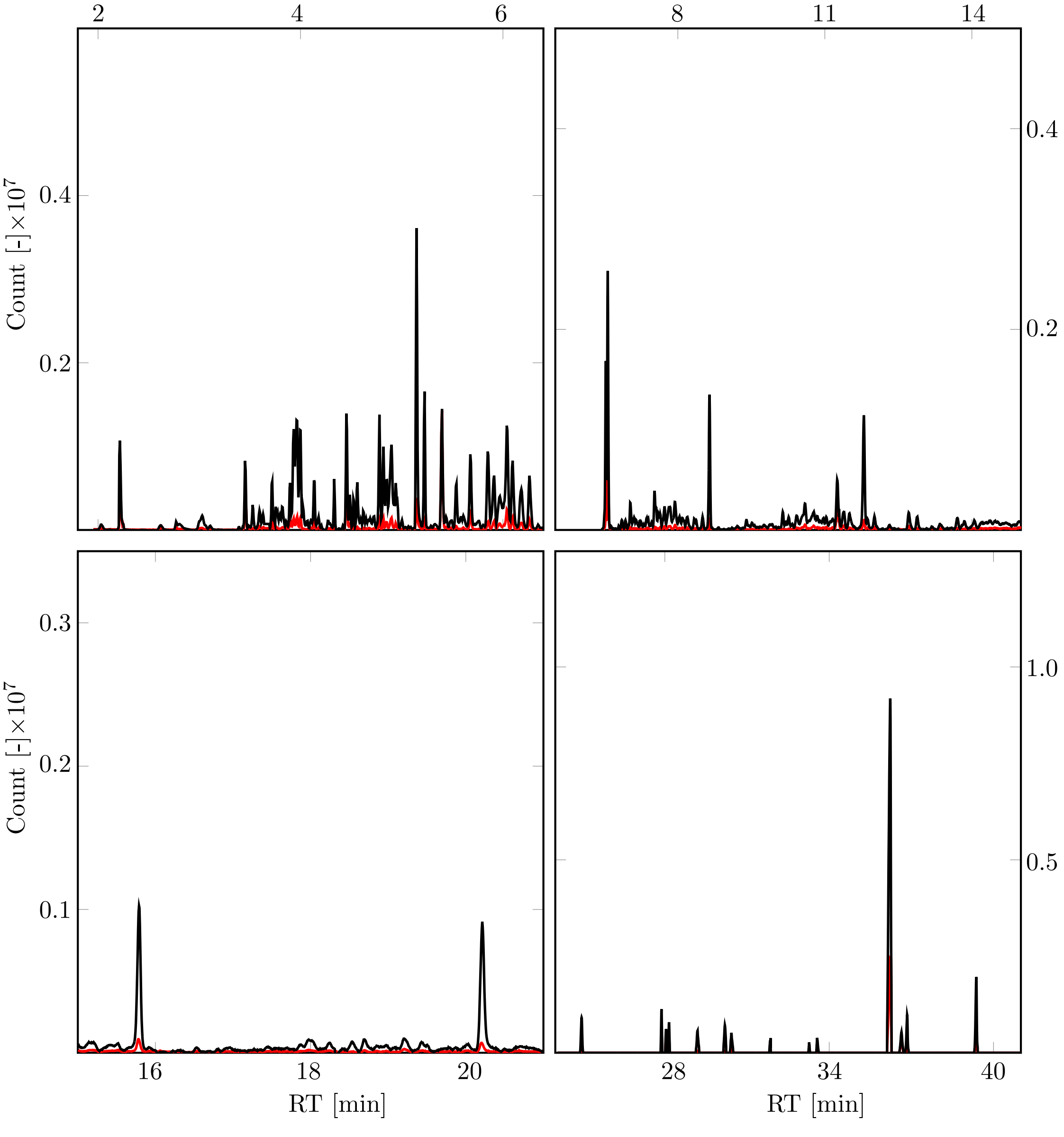

Figure 6.15. Mass spectrum extracted from the sample for the different spatial locations of X/L_I = -1.0 (red); X/L_I = 0.5 (black) at a constant equivalence ratio of ϕ_{UN} = 2.2 and total rate of strain of a_T = 420 s^{-1}. The burnt gas temperature is constant at T$_{HCP}$ = 1500 K.

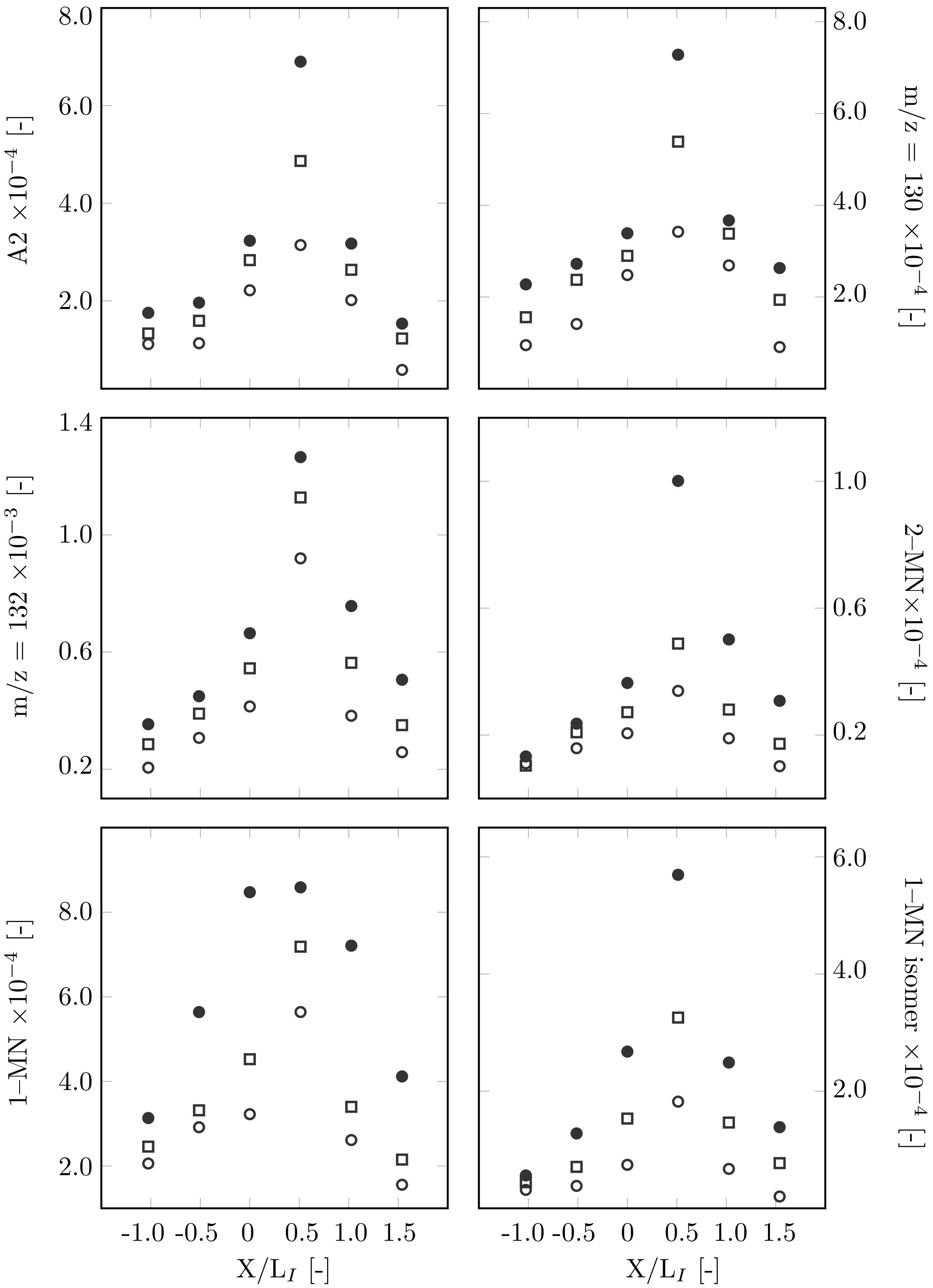

Figure 6.16. The impact of equivalence ratio on the extracted distribution of PAHs along reaction zone layer at a constant $a_T = 420\,s^{-1}$ and $T_{HCP} = 1500$ K. The concentrations correspond to the mole fractions of PAH (m/z = 92 – 300 amu) in the analysed liquid sample including the solvent (DCM) contribution. Open circle – $\phi_{UN} = 1.8$; Square – $\phi_{UN} = 2.0$; Filled circle – $\phi_{UN} = 2.2$. X/L$_I$ > 0 is towards reactants and X/L$_I$ < 0 towards the hot combustion products.

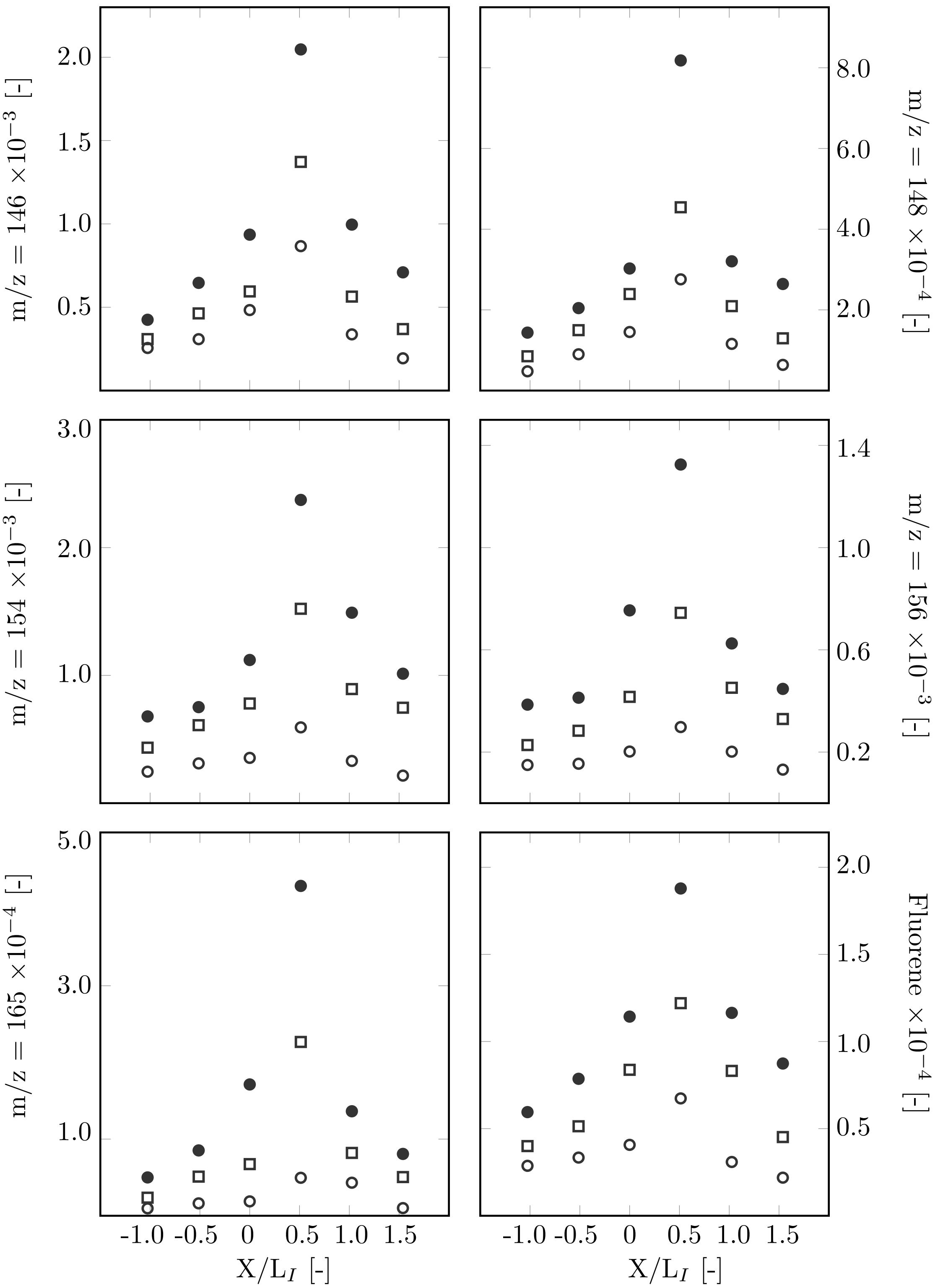

Figure 6.16 (Cont.). The impact of equivalence ratio on the extracted distribution of PAHs along reaction zone layer at a constant a_T = 420 s^{-1} and T_{HCP} = 1500 K. The concentrations correspond to the mole fractions of PAH (m/z = 92 – 300 amu) in the analysed liquid sample including the solvent (DCM) contribution. Open circle – ϕ_{UN} = 1.8; Square – ϕ_{UN} = 2.0; Filled circle – ϕ_{UN} = 2.2. X/L$_I$ > 0 is towards reactants and X/L$_I$ < 0 towards the hot combustion products.

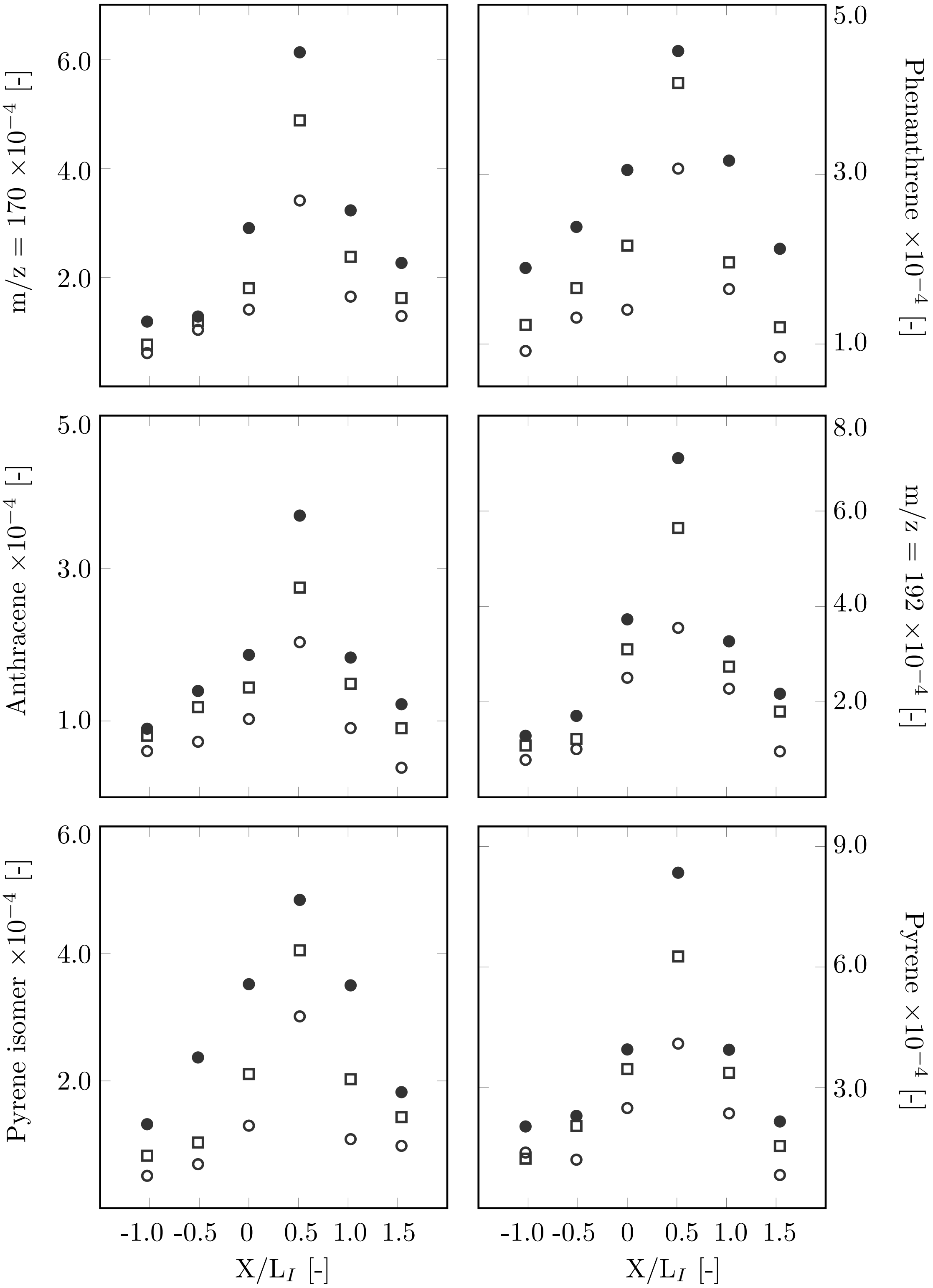

Figure 6.16 (Cont.). The impact of equivalence ratio on the extracted distribution of PAHs along reaction zone layer at a constant $a_T = 420\,s^{-1}$ and $T_{HCP} = 1500$ K. The concentrations correspond to the mole fractions of PAH (m/z = 92 – 300 amu) in the analysed liquid sample including the solvent (DCM) contribution. Open circle – $\phi_{UN} = 1.8$; Square – $\phi_{UN} = 2.0$; Filled circle – $\phi_{UN} = 2.2$. X/L$_I$ > 0 is towards reactants and X/L$_I$ < 0 towards the hot combustion products.

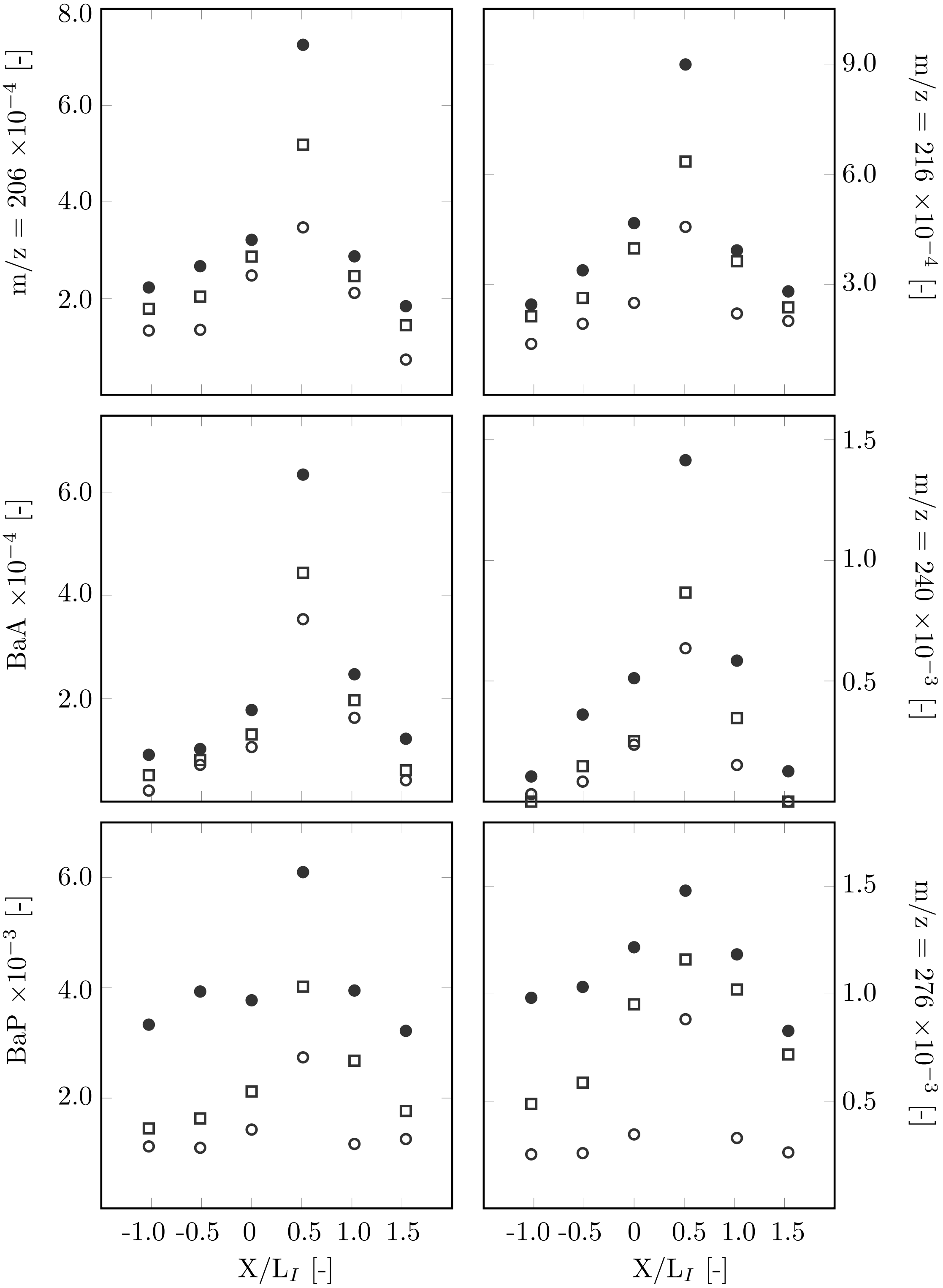

Figure 6.16 (Cont.). The impact of equivalence ratio on the extracted distribution of PAHs along reaction zone layer at a constant $a_T = 420\,s^{-1}$ and $T_{HCP} = 1500$ K. The concentrations correspond to the mole fractions of PAH (m/z = 92 – 300 amu) in the analysed liquid sample including the solvent (DCM) contribution. Open circle – $\phi_{UN} = 1.8$; Square – $\phi_{UN} = 2.0$; Filled circle – $\phi_{UN} = 2.2$. X/L$_I$ > 0 is towards reactants and X/L$_I$ < 0 towards the hot combustion products.

6.6.3 Mass distribution of PAH species

The species concentration profiles are the result of a tight balance between formation and consumption and relatively small changes in rates of specific reactions can have a significant impact. Therefore, the mass profile distribution of PAH species can shed light on the soot nucleation step. There are few reports discussing the mass species profile of incipient particle composition based on normalised ion count. The results obtained from normalised ion count can deviate from actual species contribution to soot nucleation due to routine variation in the response of the chromatographic system. In the current study, the mass distribution of species is calculated based on absolute concentration using internal and external standard calibration.

Kholghy et al. [128] state that the soot nucleation is strongly proportional to PAH concentrations. However, the probability of stabilisation depends on a number of other factors such as PAH size and orientation. It was concluded that PAHs with higher concentrations, irrespective of their sizes, have a higher chance to collide with other PAHs and form larger clusters. The study also highlighted the higher concentration of five carbon rings.

Figures 6.18 and 6.19 show the evolution of the main chemical structures involved in the soot nucleation over the entire limit of reaction zone based on the relative concentration. The mole fractions of species include the impact of chemical and physical processes such as a sequence of PAH reactions and PAH infusion on soot. The PAH reactions can play an important role in the early formation of soot precursors and provide fast routes for mass growth.

Figures 6.18 and 6.19 indicate a difference balance between formation and consumption over the reaction zone layer as a result of the reaction flux. The appearance of a high concentration of PAHs at $X/L_I = 0.5$ shows the importance of this spatial location for soot nucleation. In general, the incipient particles show the comparatively lower concentrations at the boundary of reaction zone layer (i.e. X/L_I = -1 and +1.25). The

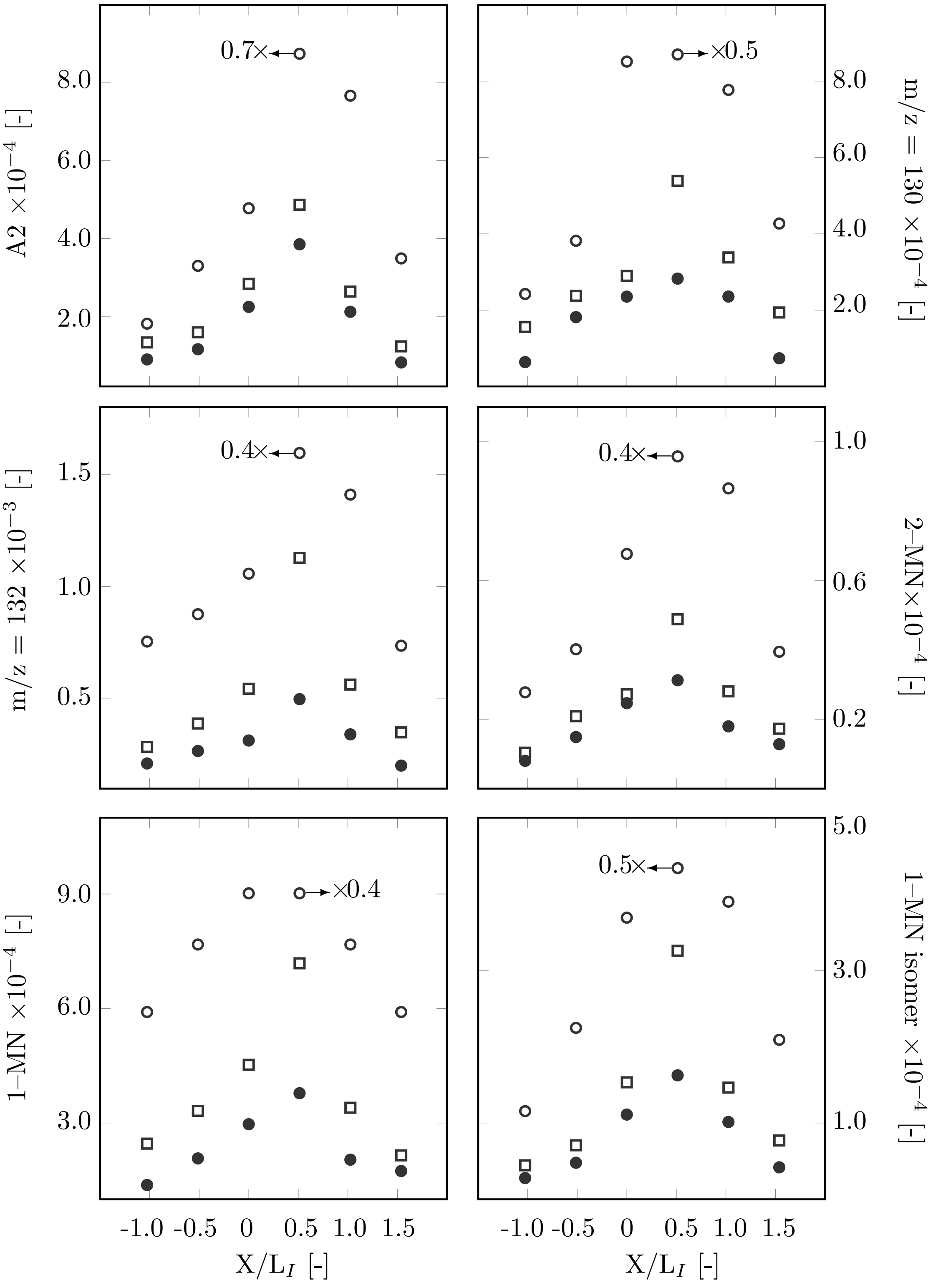

Figure 6.17. The impact of the rate of strain on the extracted distribution of PAHs along reaction zone layer for ϕ_{UN} = 2.0 and T_{HCP} = 1500 K. The concentrations correspond to the mole fractions of PAH (m/z = 92 – 300 amu) in the analysed liquid sample including the solvent (DCM) contribution. Open circle – a_T = 225 s^{-1}; Square – a_T = 420 s^{-1}; Filled circle – a_T = 610 s^{-1}. X/L$_I$ > 0 is towards reactants and X/L$_I$ < 0 towards the hot combustion products.

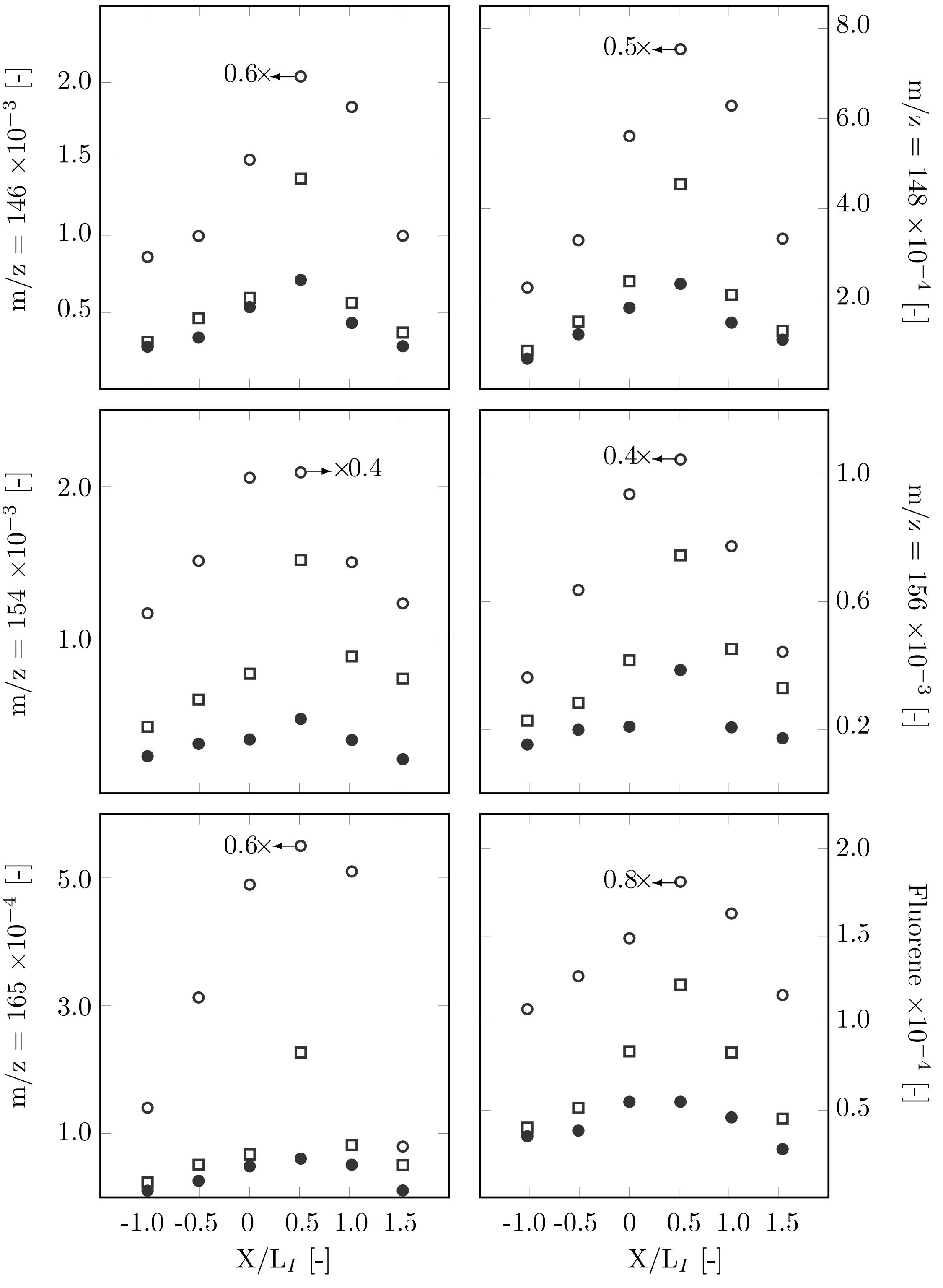

Figure 6.17 (Cont.). The impact of the rate of strain on the extracted distribution of PAHs along reaction zone layer for ϕ_{UN} = 2.0 and T_{HCP} = 1500 K. The concentrations correspond to the mole fractions of PAH (m/z = 92 – 300 amu) in the analysed liquid sample including the solvent (DCM) contribution. Open circle – a_T = 225 s^{-1}; Square – a_T = 420 s^{-1}; Filled circle – a_T = 610 s^{-1}. X/L$_I$ > 0 is towards reactants and X/L$_I$ < 0 towards the hot combustion products.

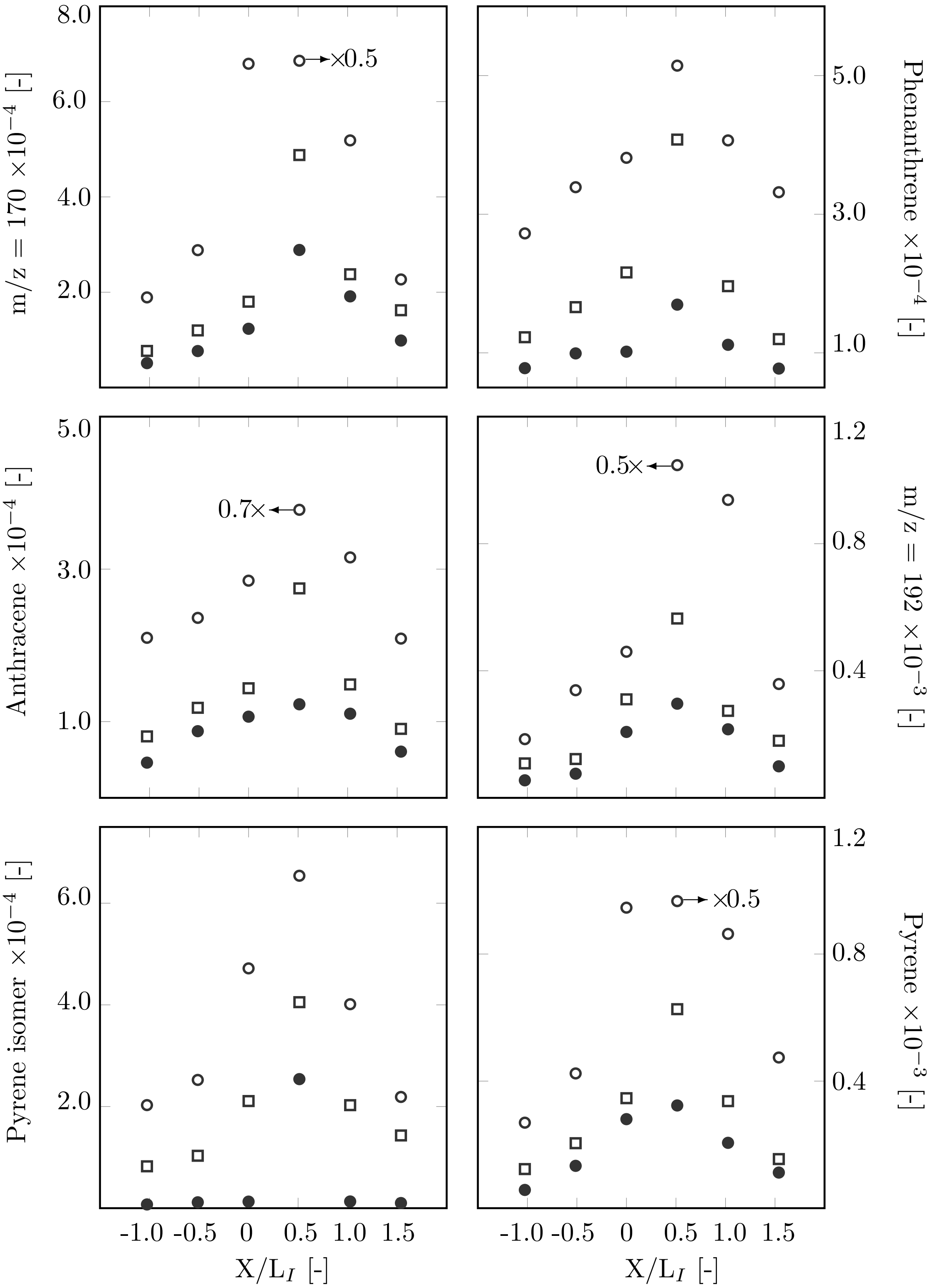

Figure 6.17 (Cont.). The impact of the rate of strain on the extracted distribution of PAHs along reaction zone layer for ϕ_{UN} = 2.0 and T_{HCP} = 1500 K. The concentrations correspond to the mole fractions of PAH (m/z = 92 – 300 amu) in the analysed liquid sample including the solvent (DCM) contribution. Open circle – a_T = 225 s^{-1}; Square – a_T = 420 s^{-1}; Filled circle – a_T = 610 s^{-1}. X/L$_I$ > 0 is towards reactants and X/L$_I$ < 0 towards the hot combustion products.

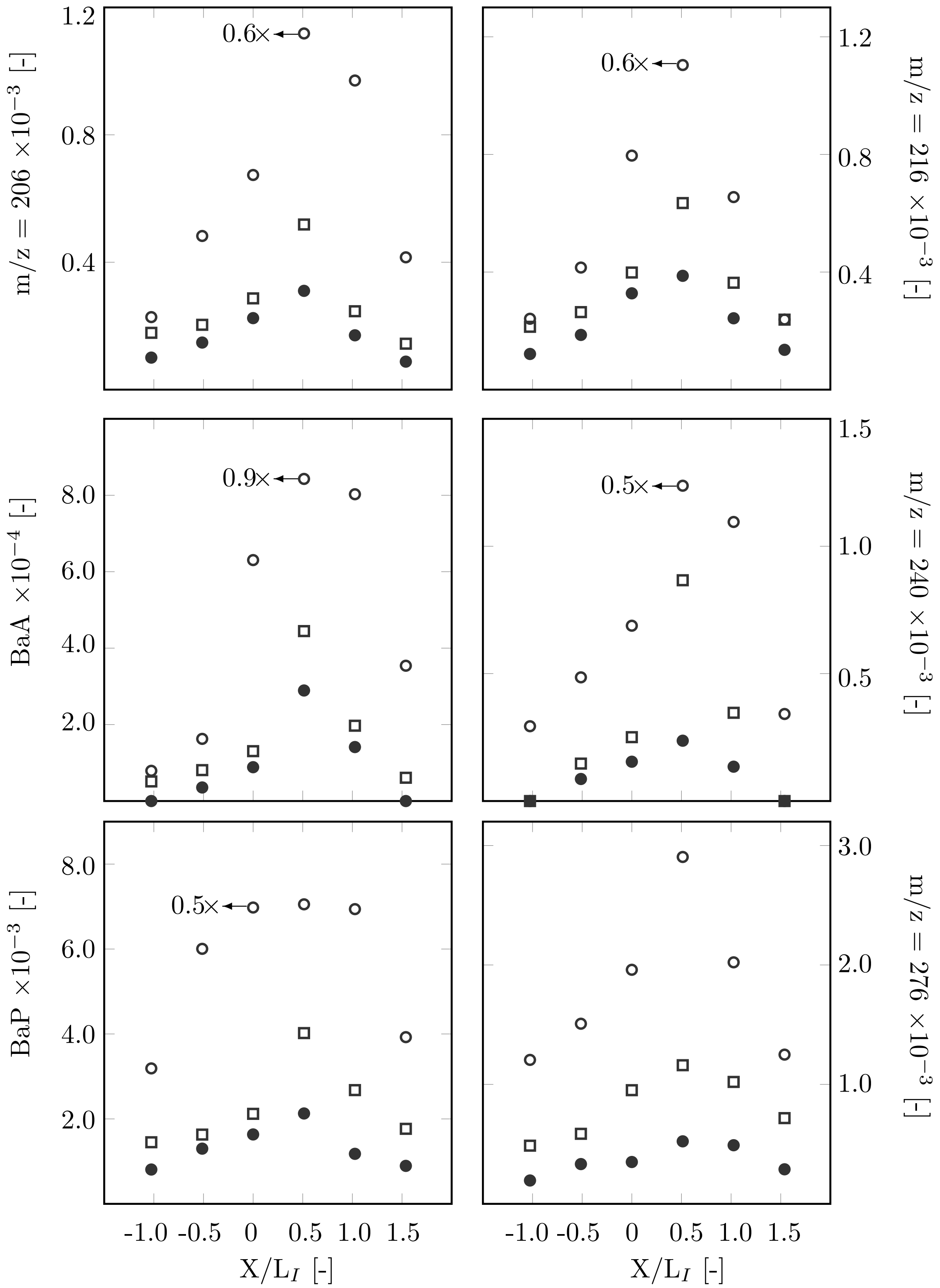

Figure 6.17 (Cont.). The impact of the rate of strain on the extracted distribution of PAHs along reaction zone layer for ϕ_{UN} = 2.0 and T_{HCP} = 1500 K. The concentrations correspond to the mole fractions of PAH (m/z = 92 – 300 amu) in the analysed liquid sample including the solvent (DCM) contribution. Open circle – a_T = 225 s^{-1}; Square – a_T = 420 s^{-1}; Filled circle – a_T = 610 s^{-1}. X/L$_I$ > 0 is towards reactants and X/L$_I$ < 0 towards the hot combustion products.

impact is more evident at lightly sooting flame condition (ϕ_{UN} = 1.8 and a$_T$ = 610 s^{-1}).

The stoichiometry of the reactant mixture (ϕ_{UN}) and the total rate of strain (a_T) have a remarkable impact on evolution of the main chemical structures involved in soot nucleation over the reaction zone layer. For instance, B(a)P shows persistently high concentrations and may account as a main contributor to soot nucleation over the entire region of the reaction zone layer irrespective of flame structures. However, the respective evolution of other species is strongly dependent on both spatial locations and sooting conditions. As an example, the relative concentration of m/z = 154, as the second highest contributor, overtakes that of m/z = 276 at X/L_I = + 0.5 and + 1.0 at ϕ_{UN} = 2.2 although the both concentrations are close at the boundaries of X/L$_I$ = -1.0 and +1.5. The concentrations of m/z = 228 and m/z = 240 appear to be higher than m/z = 276 in the region of soot inception at X/L_I = +0.5. This indicates a different balance of formation and loss mechanisms for these PAHs.

At a lower rate of strain, B(a)P still shows the highest concentration with m/z = 154 the secondary species. However, the concentration of m/z = 142 (methyl–naphthalene isomers) is particularly high with competition between m/z = 132, m/z = 142 and m/z = 146 as the third highest species. The impact of m/z = 276 is less pronounced in contrast to ϕ_{UN} = 2.2.

The current detailed information on the relative abundance of different PAHs provides a validation target for comprehensive models describing soot inception in turbulent flows. It is to be noted that the relative abundance shown includes PAH concentrations in the gas phase as well as those attached to soot particles. Given that the latter is the dominant contributor, this is necessary as the "sticking" propensity may vary for different PAH structures.

6.6.4 Total PAH concentrations

The peak ratios of the total measured PAH concentrations, shown in the mass spectrum (see Fig. 6.20), are presented in Table 6.9. The peak ratios are normalised with the corresponding maximum value for reference flame (ϕ_{UN} = 2.0, a_T = 420 s^{-1} and T_{HCP} = 1500 K). The species, appearing in the mass spectrum, cover PAH species from m/z = 92 to m/z = 300. This interval includes important PAH species contributing to soot nucleation.

As shown in Fig. 6.20, the total PAH concentration is also under the influence of the rate of strain as the peak ratio increases by a factor of 3 at highly sooting flame (a_T = 255 s^{-1}). In contrast, the soot formation process is intermittent at a higher rate of strain, and the growth rate of PAH species decreases by 52%.

The maximum peak profile shows the importance of the spatial location of X/L_I = 0.5 in the soot nucleation step. The existence of peak concentrations at X/L_I = 0.5 is also consistent with the laser–based diagnostic measurements as shown in Fig. 6.21. However, a complete comparison of the peak value is impossible because the GC/MS (probe measurement) provides species concentration up to m/z = 300, while PAHs identified using laser–based diagnostic experiments contain a mixture of distinct functional groups with broad spectra. On the other hand, the laser diagnostic method cannot distinguish the interaction between the gas–solid phase and PAH infusion level of soot particles.

Table 6.9. The peak ratio of total PAH species shown in mass spectrum. The peaks are normalised with the corresponding maximum value for the reference flame (ϕ_{UN} = 2.0, a_T = 420 s^{-1} and T_{HCP} = 1500 K).

Case	$\phi_{UN} = 1.80$	$\phi_{UN} = 2.20$	$a_T = 255\ s^{-1}$	$a_T = 610\ s^{-1}$
Peak ratio	0.65	1.44	3.05	0.48

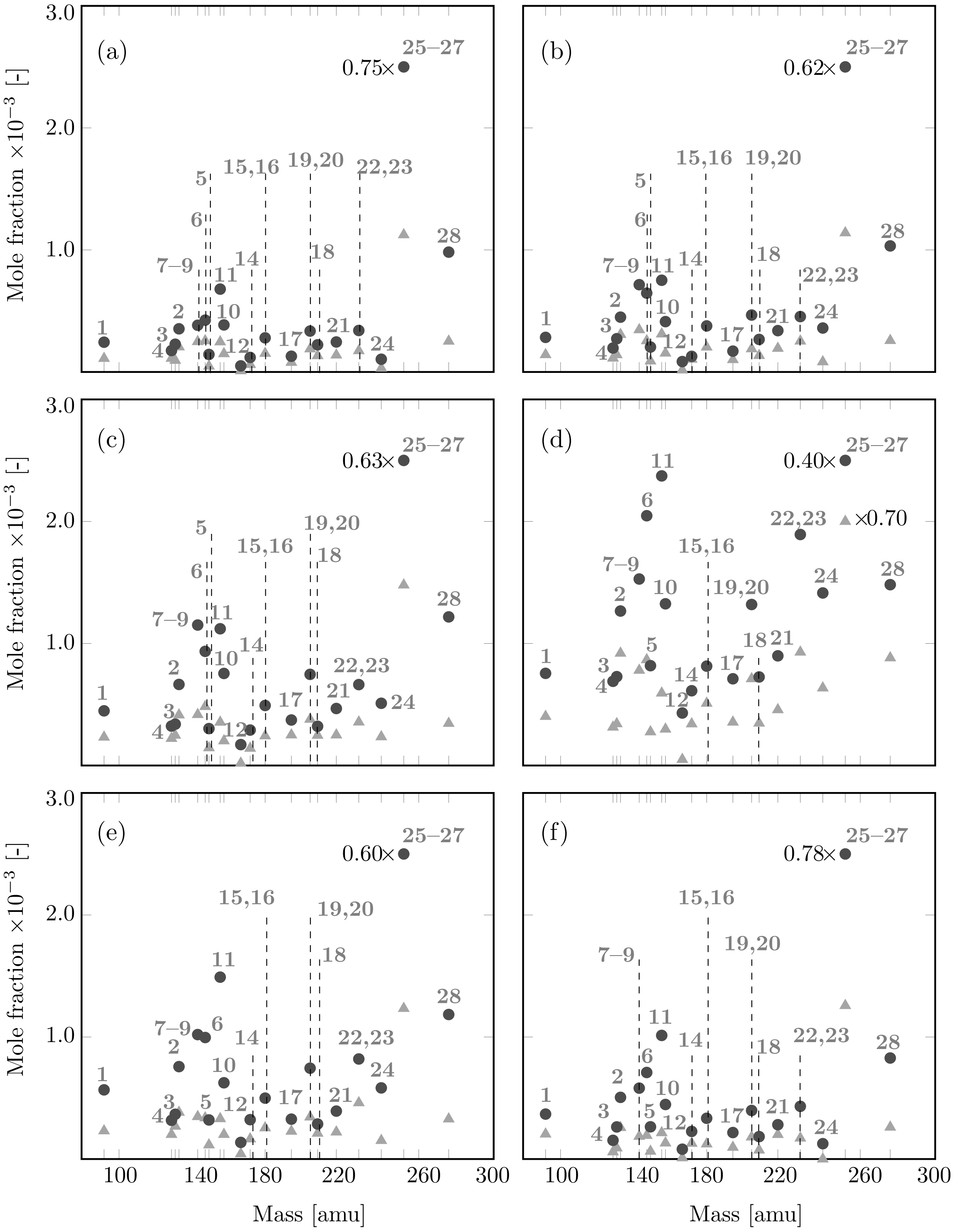

Figure 6.18. The impact of equivalence ratio on the PAH mass distribution for different spatial locations at a constant $a_T = 420\,s^{-1}$ and $T_{HCP} = 1500$ K. The label corresponds to species listed in Table 6.7. B(a)P includes the main percentage of an incipient particle composition. (a) X/L_I = - 1; (b) X/L_I = - 0.5; (c) X/L_I = 0; (d) X/L_I = + 0.5; (e) X/L_I = + 1; (f) X/L_I = + 1.5. Triangle – ϕ_{UN} = 1.8; Circle – ϕ_{UN} = 2.2.

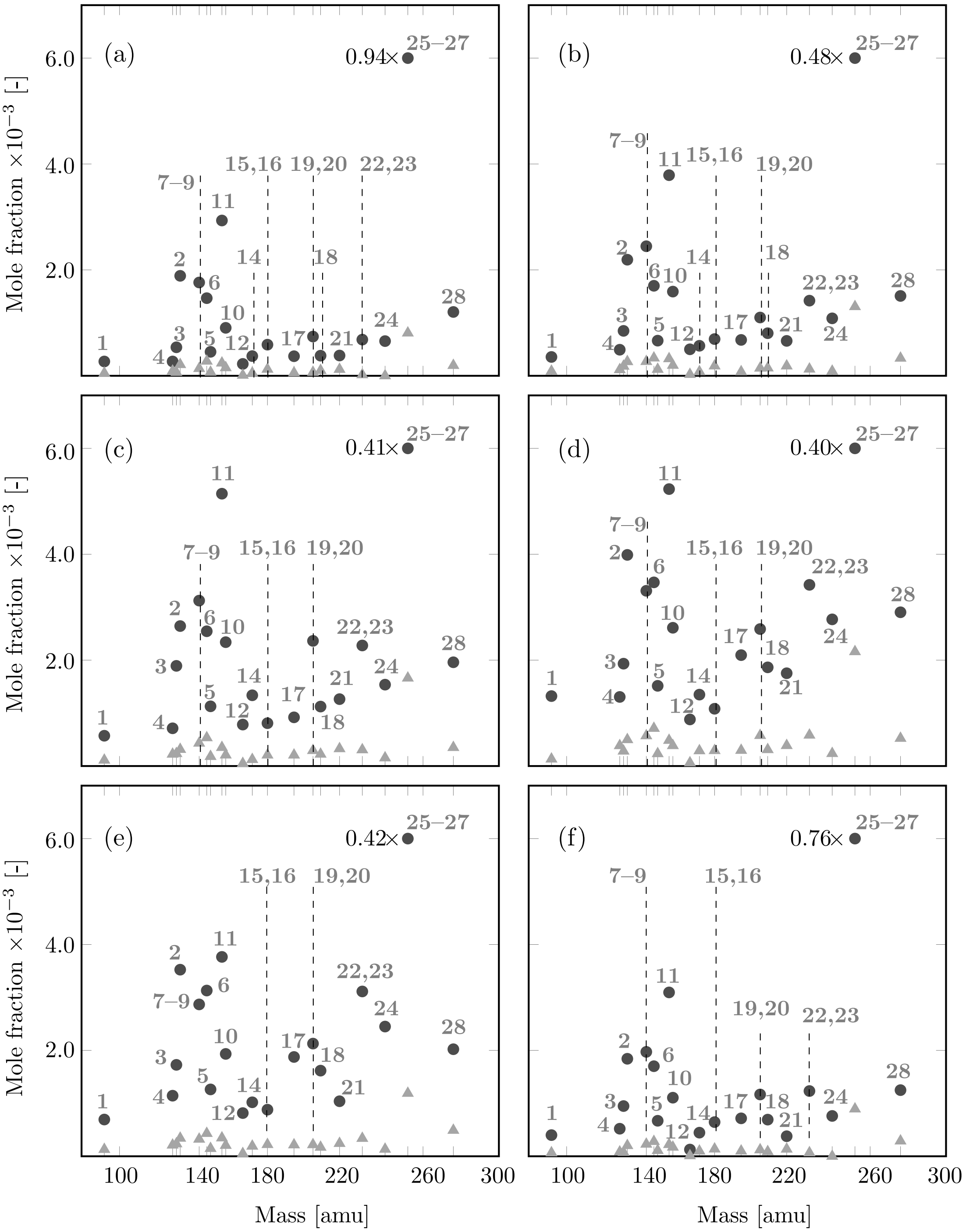

Figure 6.19. The impact of the rate of rate of strain on the PAH mass distribution for different spatial locations for ϕ_{UN} = 2.0 and T_{HCP} = 1500 K. The label corresponds to species listed in Table 6.7. B(a)P includes the main percentage of an incipient particle composition. (a) X/L_I = - 1; (b) X/L_I = - 0.5; (c) X/L_I = 0; (d) X/L_I = + 0.5; (e) X/L_I = + 1; (f) X/L_I = + 1.5. Triangle – a_T = 610 s^{-1}; Circle – a_T = 255 s^{-1}.

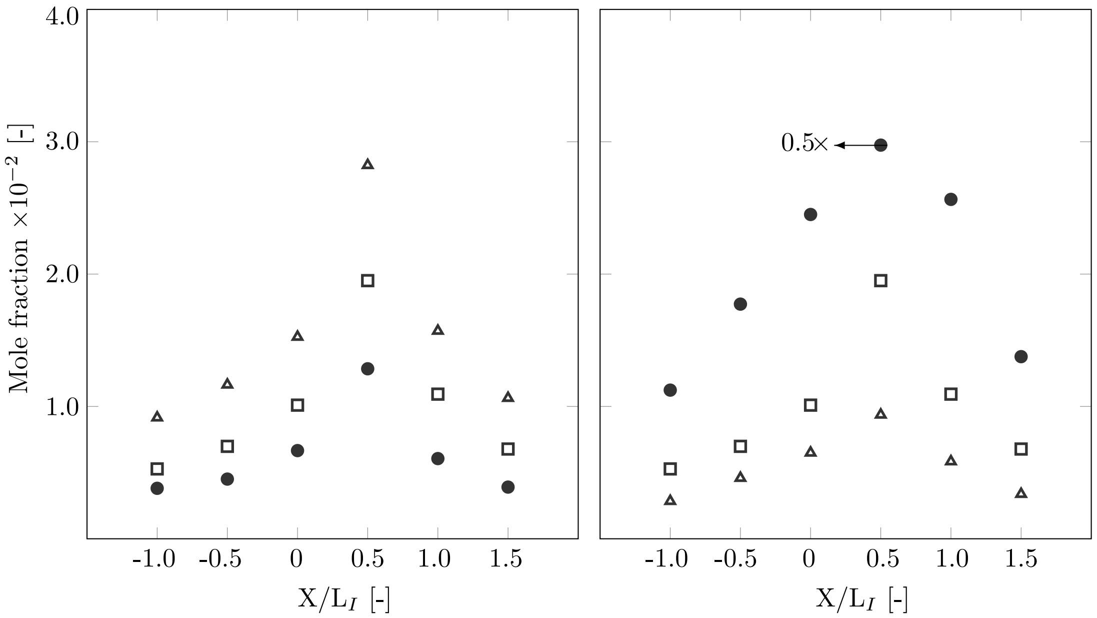

Figure 6.20. The profile distribution of total PAH species along the reaction zone layer for various equivalence ratios (left) and rates of strain (right). Left column: ϕ_{UN} = 1.8 (circle); ϕ_{UN} = 2.0 (square); ϕ_{UN} = 2.2 (triangle). Right column: a$_T$ = 610 s^{-1} (triangle); a$_T$ = 420 s^{-1} (square); a$_T$ = 255 s^{-1} (circle).

6.7 Uncertainty quantification

Figure 6.22 shows the mass spectra of two repeated samples obtained using the currently developed standardised operational procedure. The overall experimental reproducibility is calculated based on the standard deviation of five samples and suggests a high repeatability. For instance, the overall variability was estimated to 2.4% for m/z = 92 and 2.7% for m/z = 170.

The operational procedure comprises analyses of the individual repeatability of sample collection, extraction and preparation. Each step is repeated at least five times to assess the reproducibility. For example, the sample line loss of m/z = 130 reduces from 90% to 3% under optimal sampling conditions. The extraction and preparation process is complete when the species mole fractions are seen to be insensitive to the filter unit configuration and sonication/centrifuge time. At this point, the maximum standard deviation of species, for five sample iteration, is $\leqslant$ 2%. For instance, the maximum deviation of B(a)P extraction reduces to 1.4% when a filter unit consisting of quartz wool

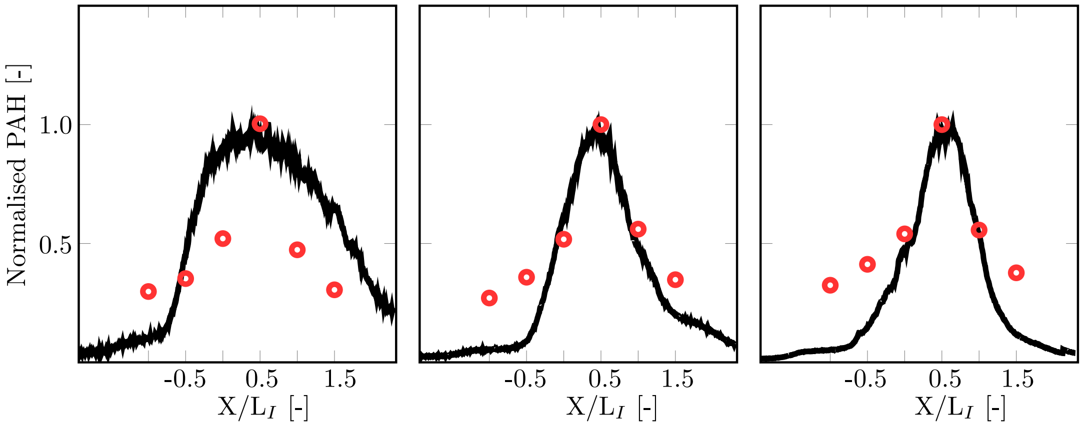

Figure 6.21. Normalised total PAH concentrations from probe measurements (circle) and PAH–PLIF signals (black line) along the centerline for different equivalence ratios of ϕ_{UN} = 1.8 (left), ϕ_{UN} = 2.0 (middle) and ϕ_{UN} = 2.2 (right). Each case is normalised by the corresponding peak. The gas burnt temperature is T$_{HCP}$ = 1500 K and rate of strain is a$_T$ = 420 s^{-1}.

and XAD is used. The optimum sample preparation, including 1 hr sonication and 10–min centrifuging, leads to a plateau in the species concentration with the maximum deviation of 1.7%. The error in each step is minimised and the process was repeated for each experimental case.

The effect of the HCP temperature on the mole fraction of species (including their error bars) are presented in Fig. 6.23. The effect of HCP temperature was also studied via using PAH–PLIF as outlined in Chapter 4. Based on the results using PAH–PLIF and probe sampling, it can be concluded that there is an increase in the PAH concentrations at $X/L_I = 0.5$ when the temperature is increased from 1400 to 1500 K, which is followed by a decrease at 1600 K. This implies a high level of competition between soot formation and oxidation reactions with soot oxidation starting to take precedent at temperatures ≥ 1600 K.

The mass spectrometer response factor (RF) is one of important parameters, that requires for the regular checking. Calibration standards for each parameter of interest are prepared by adding volumes of one or more stock standards to a vial. A known constant amount of the internal standards are added to each calibration standard and are diluted to volume with DCM. The working calibration curve, calibration factor, or

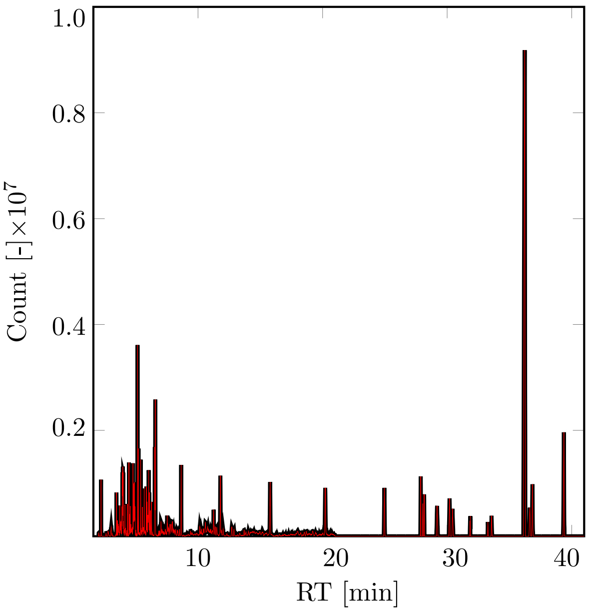

Figure 6.22. The mass spectra of two repeated samples (black and red lines) obtained using the current standardised operational procedure. The experiments were carried out at a constant equivalence ratio of $\phi_{UN} = 2.2$, total rate of strain of $a_T = 420\ s^{-1}$ and burnt gas temperature of $T_{HCP} = 1500$ K. The mass spectra of both samples were extracted at a spatial location of $X/L_I = 0.5$.

response factor must be verified on each working day by the measurement of one or more calibration standards. If the response for any parameter varies from the predicted response, the errors should be troubleshot before proceeding with the sample injection. The relative response is recorded on different days. The constant species peak area ratio reinforces the high performance of the instrument.

Online sampling can lead to significant species losses [42]. The PAH species can be easily lost along the extraction line or into the filter unit in the sampling line (to filter heavy particles) using the online sampling method. The initial analyses of PAH onto soot filter showed that some species peaks are not detected by the GC–MS when a quartz fibre filter is used. The possibility of PAH infusion is high at heavily sooting flames. Therefore, the error can be introduced into results when particles are filtered in the extraction line using the online method. The current centrifuge results substantiates this conclusion. The internal standard solutions (Accustandard [Z–014J–0.5X]) cannot be added to the liquid samples in the online sampling and there is no reference

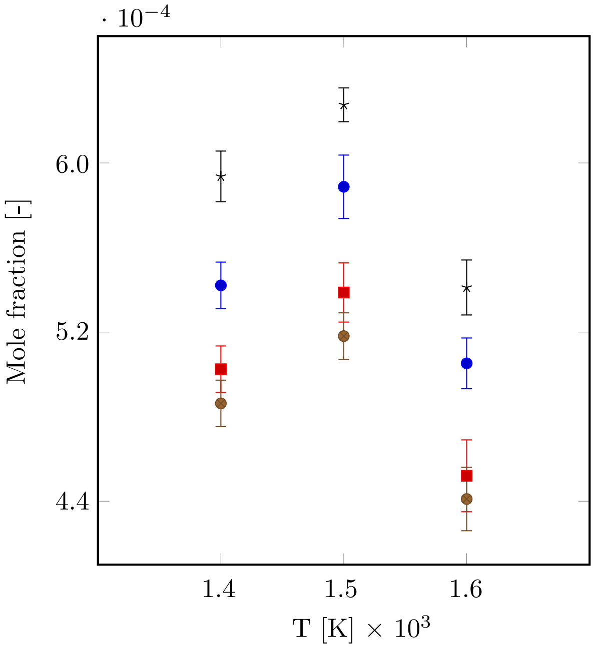

Figure 6.23. The effect of HCP temperature on the mole fraction of species (including their error bars). m/z = 92 (blue circle); m/z =130 (red square); m/z = 206 (brown circle); A4 (asterisk). The experiment is carried out at a constant total rate of strain of $a_T = 420$ s^{-1} and equivalence ratio of $\phi_{UN} = 2.0$. The probe tip is located at $X/L_I = 0.5$.

peaks to account for routine variation in the response of the chromatographic system. Method interferences may also be caused by contaminants in solvents, reagents, on glassware, and other sample processing hardware that result in discrete artefacts and elevated baselines, or both, in the detector profiles. The thorough cleaning of glass before use (for example, by acid washing, followed by heating to 300 C in a heated plate of magnetic stirrer) is implemented. Solvents and other materials are checked routinely by running laboratory reagent blanks through the GC–MS under the conditions of the analysis to establish that they are free of interfering materials. After drying and cooling, glassware is sealed and stored in a clean environment to prevent any accumulation of dust or other contaminants. The extraction line is cleaned/washed with a combination of solvents to remove adsorption of compounds on the sampling line after the completion of each experimental set. The sampling system was washed, and the solution was injected into GC/MS to ensure the efficiency of the cleaning procedure.

6.8 Conclusions

The current experimental conditions cover non–sooting to highly sooting flames with the impact of the temperature of the counterflow hot combustion products, the rate of strain and the equivalence ratio quantified. Measured species concentrations in the gas phase show gradually increased concentrations of intermediate species as the stoichiometry is increased. By contrast, the amount of soot and PAHs bound to the particles increases rapidly. For example, the amount of benzo(a)pyrene stored on particles is up to five times higher than in the gas phase for the reference flame. It has also been shown that turbulence plays a critical role in the soot inception process with a rapid reduction in PAH concentrations with increases in the rate of strain on reaction layers. The implication is that soot formation and oxidation are low Damköhler number processes with commensurate implications for modeling approaches. It has further been shown that oxidation processes become dominant with increasing HCP temperatures leading to a decline in PAH concentrations as the temperature is increased from 1500 to 1600 K. The EDX and SEM analyses were used to quantify the growth in carbon deposition.

It is shown that the mean concentration profiles are the result of a tight balance between formation and consumption of a given species and that relatively small changes in rates of specific reactions can have a significant impact, and this effect is more complicated in turbulent flames. The rate of strain exerts a substantial influence on the PAH concentrations and soot formation, that is evident based on the mass spectrum across the reaction layer.

Benzo(a)pyrene appears to have a potentially crucial impact on the formation of incipient particulates irrespective of flame conditions and spatial locations. In addition to B(a)P, the existence of isomers (m/z = 142, 154 and 276) can lead to a faster route for particle formation as their high concentration levels accelerate soot nucleation. The spatial location X/L_I = 0.5 is a representative of the point where the physical and chemical evolution plays a crucial role leading to the formation of particulates.

The current work has illustrated the need for a more comprehensive analysis for combustion processes with low Damköhler numbers. The data is expected to advance the fundamental understanding of the particle formation and oxidation process in turbulent premixed sooting flames and further support the development and validation of experimental measurements and numerical models.

Chapter 7

Particle size distribution

7.1 Introduction

Scanning mobility particle sizer (SMPS) spectrometers have frequently been used in laminar flames to measure the size distribution of polydisperse aerosols. However, there are few available experimental studies in turbulent flames due to a number of challenges in sampling processes. Roberts and co–workers [27, 64] used SMPS to measure particle size distributions (PSDs) for two turbulent non–premixed flame of Re = 10,000 and Re = 20,000. A sampling system, similar to that of Wang and co–workers [108], was used to extract particles. The higher Reynolds number flame features a comparatively shorter sooting region, while the flame heights were reported to be the same for both flames. The total soot volume concentrations were greater in the Re = 10,000 flame. Both flames exhibited a Gaussian volume concentration profile along the centerline. It was shown that the mean particle diameter increases with the distance from the nozzle outlet along the centerline and that the mean size remained below 10 nm [27]. Two stage dilution at different sampling points was recommended to reduce losses in the extraction line. In another similar study, a unimodal shape in the PSD distributions was noted for different turbulent flame conditions [64]. De Falco et al. [303] investigated the impact of air dilution levels on the particle size distribution in a premixed swirled ethylene flame. It was shown that the particle number density was significantly higher for flames without air dilution, and that the soot volume fraction increased by a factor of two in comparison to diluted flames. Olfert and co–workers [304, 305] measured particle size distributions for a buoyant turbulent diffusion flame with different fuel mixtures. The fuel mixtures was classified into light, medium and heavy based on the relative concentrations of C_1 to C_4 alkanes, carbon dioxide and nitrogen. The results showed an increase of median mobility diameter and number density with a change from light to heavy fuels. It was found that the fuel compositions had a insignificant impact on particle morphology, primary particle size and particle aggregate size.

The current Chapter describes a novel experimental process used to characterise the particle size distribution in premixed turbulent flames. The particle size distribution in turbulent premixed flames is not well understood. The current Chapter represents a well–controlled experiment that aims to advance fundamental understanding on particle inception, formation and oxidation in such flames. The facility features of a back–to–burnt opposed jet configuration with fractal grid generated turbulence and a versatile quartz glass sampling probe. The latter features aerodynamic quenching and temperature conditioned dual–port dilution (i.e. probe tip and transfer–line dilution) to minimise the particle losses during extraction.

Before proceeding within flame measurements over a range of spatial locations, it is necessary to ensure that potential errors in the sampling and measurement process are reduced as much as possible. The detailed experimental processes are hence introduced including (i) uncertainty analyses, (ii) optimal sampling conditions (range of dilution and pressure differentials), (iii) the experimental process to measure particle concentrations in the turbulent flame brush, (iv) the particle size distribution across reaction zone.

7.2 SMPS setting and parameters

The details of current SMPS system have been discussed in Chapter 3. A summary of setting in the aerosol instrument manager (AIM) software is presented in Table 7.1. TSI recommends a sheath (Q_{sh}) to aerosol (Q_p) ratio of 10:1 for optimum performance. In general, a longer scan time will result in more accurate measurements if the incoming aerosol remains stable for such a sampling period. The impact of the SMPS scanning time on the particle size distribution should be analysed for identification of the sampling time limit over which aerosol size profile distribution is stable. The sampling time is a critical factor in turbulent flames. The proper operation of the instrument for such experiments must initially be assessed for a wide range of flame. Based on initial experiments, a scan time of 120 s is chosen.

In order to reduce peak broadening, a short tube length between the differential mobility analyzer (DMA) and the condensation particle counter (CPC) is utilised based on the TSI recommendations. The time delay and purge time in the software are adjusted for the customised setups to improve accuracy. The sampling line should be disconnected from vacuum during purging (to minimise uncertainty) when particles are removed from the DMA between samples. The SMPS vacuum pump can provide an absolute suction pressure from 60 to 105 kPa using a vacuum pump when a combination of long DMA and CPC is used. The pressure differential (flame and the pressure transducer) is adjusted using a balance between the metering valve and vacuum regulator in the bypass valve and the SMPS path–line (the vacuum pressure from a pump connected to the CPC or the nano enhancer). A matrix set was established at atmospheric conditions before the sampling of particulates.

Table 7.1. SMPS analysis conditions, where P is the operating pressure and T is the operating temperature of the instrument. Q_p and Q_{sh} are the flow rates selected for the aerosol and the air sheath, respectively, t_s is scan time and t_p the purge time.

P [bar]	T [C]	Q_p [L/min]	Q_{sh} [L/min]	Q_p: Q_{sh} [-]	t_s [s]	t_p [s]
0.6–1.25	10–40	1.5	15	1:10	120	20

7.3 Flame conditions

The current target flames include a topology of soot layers in premixed turbulent flames. The flame conditions are shown in Fig. 7.1 and Table 7.2.

Photographs, shown in Fig. 7.1, illustrate the wide range of experimental conditions used to study the particle size distribution from lightly to the heavily sooting flames at different bulk rates of strain and equivalence ratios. The flame conditions, listed in Table 7.2, are chosen to provide details on the formation and oxidation of soot particulates. The experimental cases were established previously via separate analyses of GC–MS (PAH sampling experiment), and laser diagnostic techniques (ELS and PAH–PLIF). The flame with a stoichiometry of $\phi_{UN} = 1.8$ and rate of strain of $a_T = 610\ s^{-1}$ represent the lightest sooting conditions with a strongly intermittent appearance of soot. The soot layer thickness increases significantly with decreasing rate of strain and increasing equivalence ratio. This effect can be seen in Fig. 7.1 as the flames change into a brighter yellow–colour at $\phi_{UN} = 2.0$ and $\phi_{UN} = 2.2$.

7.4 The measurement process

A schematic of the experimental setup is shown in Fig. 7.2. The selected back–to–burnt opposed jet configuration features fractal grid generated turbulence and accurate control of individual parameters affecting turbulent and chemical time scales. The upper nozzle provides the premixed fuel/air mixtures that are stabilised against the lower

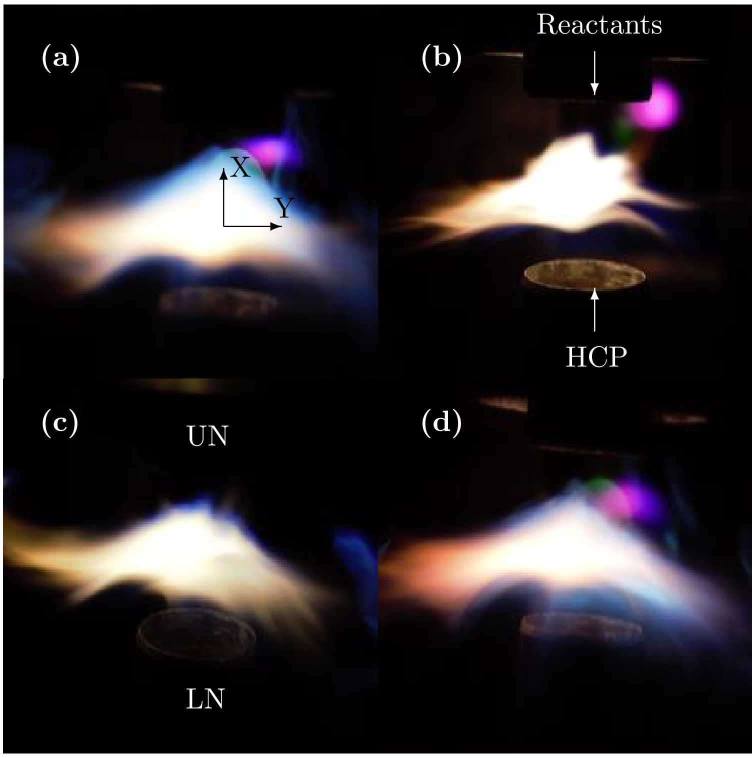

Figure 7.1. Sample photographs at different equivalence ratios (top) and total rates of strain (bottom), used to measure particle size distribution at a constant burnt gas temperature of $T_{HCP} = 1500$ K. Top row: ϕ_{UN} variation at a constant rate of strain of $a_T = 420$ s^{-1} at (a) $\phi_{UN} = 1.8$ and (b) $\phi_{UN} = 2.2$; Bottom row: Strain variation at a constant $\phi_{UN} = 2.0$ at (c) $a_T = 420$ s^{-1} (reference flame) and (d) $a_T = 610$ s^{-1}.

nozzle hot combustion products (HCP).

The sampling process is conducted using a versatile quartz glass probe featuring aerodynamic quenching and a temperature conditioned dual–port dilution (i.e. probe tip and transfer–line dilution) as outlined in Chapter 3. Dry nitrogen diluent gas at ambient temperature is injected in the dilution ports to prevent the formation of nucleation mode particles in the sampling line. The dilution ratio can be controlled by changing the sampling pressure and nitrogen dilution. The former can be adjusted by regulating the balance between the bypass pressure using a metering valve, a vacuum regulator, and the SMPS vacuum pump pressure. The latter is monitored using mass flow controllers. The gradual sample dilution (two steps) is also applied to reduce particulate losses in the extraction line. The first dilution port is used to quench/freeze particles at the probe tip. The second dilution stage is to increase the amount of total sample

Table 7.2. Experimental conditions used to study the impacts of equivalence ratio, and rate of strain on the particle size distribution across the sooting limit at a constant burnt gas temperature of $T_{HCP} = 1500$ K. The UN and LN fuels are C_2H_4 and H_2, respectively, and $\phi_{LN} = 1.0$ with $\alpha = X_{H2}/X_{N2} = 0.51$, where X indicates a mole fraction, used to control T_{HCP}, U is the upper nozzle bulk velocity and u' the velocity fluctuations. The reactant temperatures are $T_r = 320$ K, $L_I = 3.9 \pm 0.2$ mm is the integral length scale of turbulence, $Re_t = u'L_I/\nu$ the turbulent Reynolds number and $a_t = (\varepsilon_r/\nu_r)^{1/2}$ is the turbulent, $a_b = 2U/H$ the bulk and $a_T = a_t + a_b$ the total rates of strain [233]. ε_r is the rate of dissipation in the reactants and ν is fluid viscosity [234].

Variation	Reactants	HCP	Rate of Strain
ϕ_{UN} [-]	1.8, 2.0, 2.2	2.0	2.0
a_b [s^{-1}]	120	120	120, 160
a_t [s^{-1}]	300	300	300, 450
a_T [s^{-1}]	420	420	420, 610
Re_t [-]	72	72	72, 94
U [m s^{-1}]	1.8	1.8	1.8, 2.4
u' [m s^{-1}]	0.30	0.30	0.30, 0.39

dilution achievable without the choking the probe and to minimise the particles losses in the transfer line. The proper limits for individual dilution ratios (first and second port) ensure minimum losses over an interval where the mobility diameter and particle number density are insensitive to the variations in the dilution ratio. Nitrogen flows are varied to provide the required dilution ratio while the differential pressure (between flame and sampling suction) is kept constant at $\Delta P = 20$ mbar. This pressure provides the minimum flame perturbation and PAH sample losses within the sampling line [30]. A higher dilution ratio is accessible via varying pressure ΔP (at constant nitrogen flow). However, particle losses of $D_p \leq 10$ nm are seen at a differential pressure of $\Delta P > 20$ mbar.

A pressure transducer (UNIK 5000; GE Measurement and Control) is placed downstream of the probe to control the static pressure in the sampling system. A vacuum regulator and a metering valve are used to set a pressure differential of 20 mbar between the sampling line and the flame. This results in a constant sample flow rate of 3.125×10^{-6} kg/s. Two large vacuum chambers with a combined volume of 36.8 litres are also used to eliminate pressure fluctuations or gradual shifts in the sampling pressure as discussed in Chapter 3.

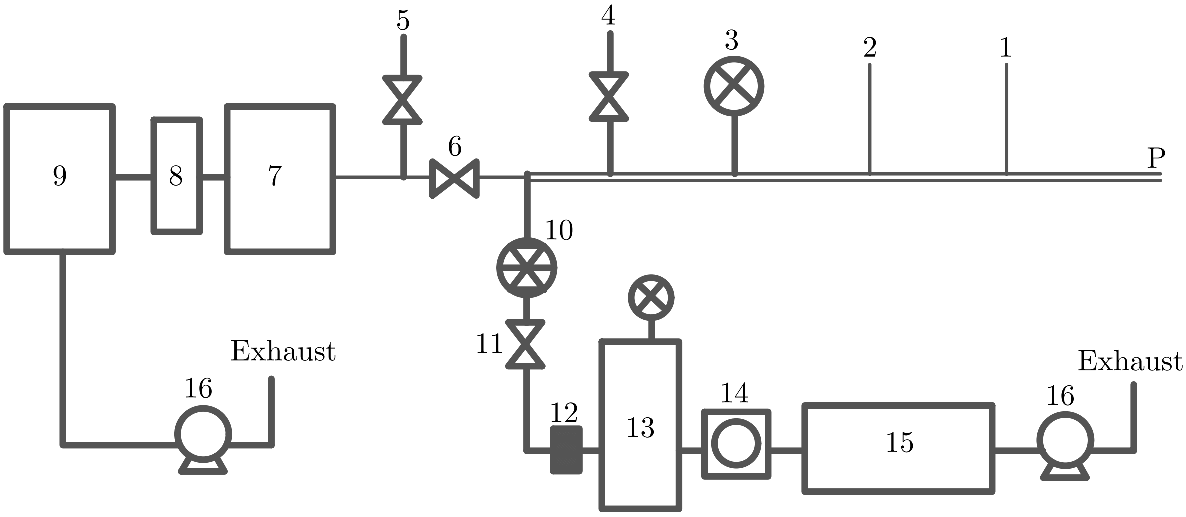

Figure 7.2. Components using in the analyses of particle size distribution . 1) Nitrogen (first port); 2) Nitrogen (second port); 3) Pressure transducer; 4,5) Bypass path; 6) Valve; 7) Electrostatic classifier; 8) DMA; 9) Particle counter (CPC and nano enhancer); 10) Metering valve; 11) Valve; 12) Filter package; 13) Vacuum chamber; 14) Vacuum regulator; 15) Vacuum volume; 16) Vacuum pump. A nano enhancer is added to CPC when the 1–nm SMPS system is applied in the experiment. "p" is the probe tip.

A sampling time of about 10,000 integral time–scales of turbulence is used (120 s) to ensure statistical independence. The length from the transfer line to SMPS is as short as possible to minimise possible losses and reduce particle residence from the sampling point to the CPC particle counter. The sampling line assembly can be traversed in all directions using linear translation stages, and the location is calibrated using the optical setup. The ELS camera determines the X and Y position (i.e. $X/L_I = 0.5$, $Y/L_I = 0$) and the laser light sheet determines the alignment of the probe tip with the theoretical stagnation point streamline.

7.4.1 Sampling process

The sampling system was tested at atmospheric pressure with the SMPS instrument at a steady–state condition. The probe is moved to the measurement location and constant pressure sampling implemented by connecting the transfer line to vacuum. The sampling collection is terminated by disconnecting the probe from the vacuum system. The purging time for DMA allows all particles to completely exit the DMA column at the end of the sampling collection step. The particles are removed from the sampling line using several valves (see numbers 4, 5 and 6 in Fig. 7.2) during the DMA purging step. Deposition of ultrafine particles on the tubing walls increases surface roughness and surface conductivity, which can potentially influence the particle size distribution between experimental sets. Nitrogen flow is injected into the sampling system using two dilution ports during DMA purging time to prevent the presence of particle on walls in the sampling system from one sampling set to another.

7.5 Probe characterisation

Losses in particle number and mass can occur through a variety of processes occurring within the sampling system, including turbulent impaction on the inlet probe, turbulent diffusion and inertial impaction on tube walls, particle coagulation or agglomeration, electrophoretic diffusion and sedimentation [220, 306]. Thermophoretic and electrostatic losses are negligible in the unheated, electrically conductive sampling lines. The operating temperature of the SMPS instrument is between 283 and 310 K. The sampling process, therefore, is performed at room temperature to reduce the impact of temperature gradients along the sampling system.

As a first step, we characterise the impact of the dilution ratio on particle size distributions for different flame conditions. The exact probe position for probe characterisation was previously identified via simultaneous CH_2O/PAH–PLIF and elastic light scattering. The probe is hence placed at a spatial location of $X/L_I = 0.5$, which corresponds to the peak soot formation layer based on the analysis of the PAH sampling and laser diagnostics experiments.

The impacts of pressure differentials (ΔP) and nitrogen dilutions (DR_1 and DR_2) on the PSD are studied, where DR_1 and DR_2 are dilution ratios used for the first and second port, respectively. The pressure differential ΔP between the sampling line and the flame, is also considered. The initial step is to identify the optimum condition for DR_1, DR_2 and ΔP, where PSD profile distribution and median mobility diameter become independent of sampling line conditions. For instance, the impact of the flow regime (laminar or turbulent) in the sampling line can lead to changes in the particle size distribution. Since a standard probe design does not exist, all steps for probe characterisation should be implemented for the relevant sampling line conditions.

7.5.1 Dilution ratio

The dilution ratio was subsequently calculated in combination with the metered nitrogen port dilution (Q_1, Q_2) and a viscosity correction [218] for a given ΔP (pressure differential) as follows (Eq. (7.1)). The data were measured using a constant volume, leak–free setup, and the flow rate through probe tip was inferred from the pressure increase.

$$DR = \left(\frac{Q_s}{Q_{air}}\right)\left(\frac{T_0}{T_s}\right)\left(\frac{\mu_{m,f}}{\mu_{air}}\right) \tag{7.1}$$

where Q_s and Q_{air} are the volumetric flow rates of dilute nitrogen gas and air sample drawn into the orifice, respectively. Since the method does not use a flame, both Q_s and Q_{air} are at the room temperature. Figure 7.3 shows the range of dilution ratios as a function of flow rate sampling pressure at a constant nitrogen flow rate. The results show consistency with the DR profile distribution as a function of ΔP presented by Camacho et al. [218]. In turbulent flames, species profiles and particle size distributions extend over a much broader spatial domain as a result of turbulent transport and flame-front folding [247]. It is reasonable to expect a different approach for the identification of optimum dilution ratio under turbulent conditions compared to in laminar flame cases. The approach here is to separately study the impacts of DR_1, DR_2, $DR_T = DR_1 + DR_2$, ΔP and flow condition (along the sampling line) on particle size distributions at the spatial location of $X/L_I = 0.5$. The experiment is repeated for

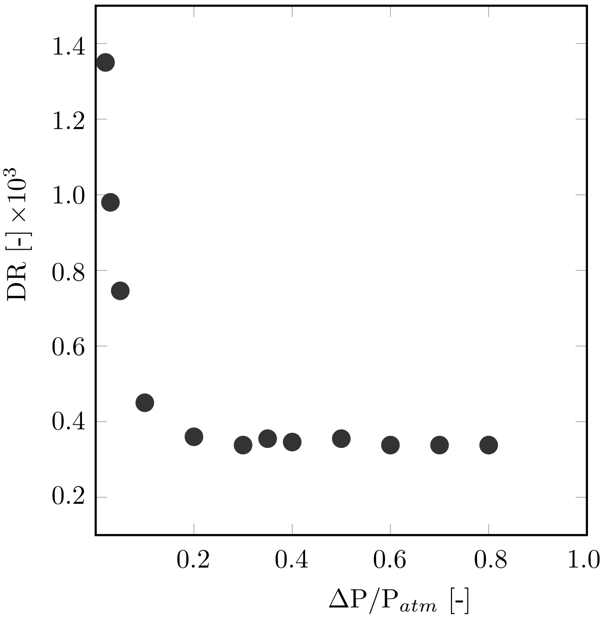

Figure 7.3. Dilution ratio as a function of pressure differential, showing a profile that is consistent with that published by Camacho et al. [218].

various conditions (ϕ_{UN} and a_T) to ensure the independence of the determined PSDs on the sampling process.

7.5.1.1 Nitrogen flow rates

The impact of nitrogen flow rates (both ports 1 and 2) on particle size function are shown in Figs. 7.5 – 7.13. The results are provided for DR_1, DR_2, DR_T and show impact on particle size distributions.

Insufficient dilution can lead to coagulation in the sampling line and skewed particle size distributions. Particles in the 6–10 nm size range appear to be lost in the sampling lines, either due to deposition or coagulation as shown in Figs. 7.5 – 7.13.

The impact of the first dilution port is presented in Figs. 7.5–7.7. The introduction of DR_1 must be carefully implemented to avoid additional particle losses through turbulent inertial or eddy impaction processes at the dilution point. The optimum DR_1 is strongly dependent on the sooting level and flame conditions. At higher dilution (i.e. $DR_1 > 1125$), all particles are lost as no PSD profile distribution is measured using

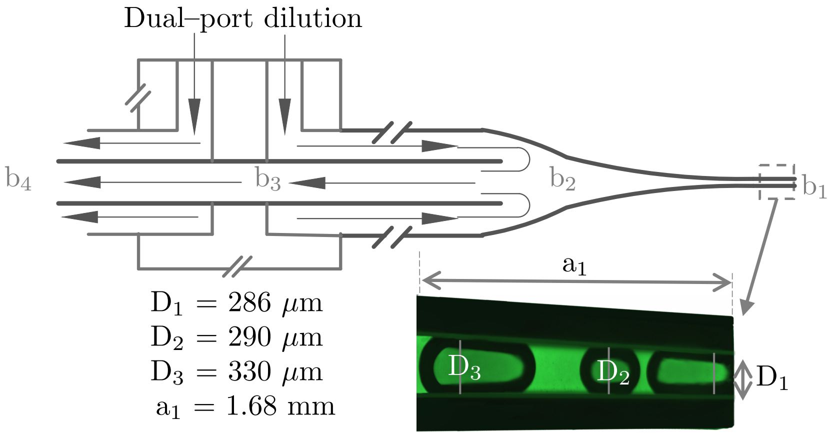

Figure 7.4. Probe configuration and dilution ports. The specified locations (b_1–b_4) are defined to represent Re number at different location along extraction line.

the SMPS. The main reasons for the particle losses are turbulent impaction, and the formation of turbulent eddies close to the inlet tip [220, 306]. The Reynolds number along the extraction line is calculated based on Eq. (7.2),

$$Re_b = \rho V D_b / \mu \tag{7.2}$$

where ρ is the density and μ the viscosity of nitrogen at the sampling temperature, V the velocity and D_b the diameter along the extraction line at different locations of b. The Reynolds numbers at different location of the sampling system (see Fig. 7.4) and particle residence time are presented in Table 7.3. The flow regime at the probe entrance is fully turbulent ($Re_b \geq 10^4$) for dilution ratios $DR_1 \geq 1125$.

The effect of the second dilution port is presented in Figs. 7.8–7.10. The second dilution is independent of flame conditions when it is chosen appropriately. For instance, the result shows that the losses are minimised when the second port dilution is chosen constant at $DR_2 = 675$. The PSD distribution shows losses of particulates in the range of 4–230 nm for $DR_2 > 675$. The reason is that improper dilution ratio at the probe tip or downstream dilution can create a pressure restriction that leads to exhaust sample stagnation within the upstream portion of transport tube [220, 306].

Table 7.3. The Re number (along the sampling system) and total residence time (t_R [ms]) (at $\Delta P = 20$ mbar), Re_b is the Reynolds numbers specified in Fig. 7.4. Re_{b_1} is 780 at $\Delta P = 20$ mbar. The total residence time is calculated from probe tip to SMPS instrument.

DR_1 [-]	DR_2 [-]	DR_T [-]	Re_{b_2} [-]	Re_{b_3} [-]	Re_{b_4} [-]	t_R [ms]
450	0	450	4198	11195	3358	62
900	0	900	8369	22318	6695	31
1125	0	1125	10454	27879	8363	25
1350	0	1350	12540	33441	10032	21
1800	0	1800	16711	44564	13369	15
225	450	675	2112	5633	5026	47
225	675	900	2112	5633	6695	37
450	450	900	4198	11195	6695	33
450	900	1350	4198	11195	10032	23
450	1125	1575	4198	11195	11700	20
450	1350	1800	4198	11195	13369	18
675	450	1125	6283	16756	8363	26
675	675	1350	6283	16756	10032	22
900	450	1350	8369	22318	10032	21
900	900	1800	8369	22318	13369	16
900	1350	2250	8369	22318	16706	14
1125	450	1575	10454	27879	11700	18
1125	675	1800	10454	27879	13369	16
1125	900	2025	10454	27879	15037	15
1125	1125	2250	10454	27879	16706	13
1350	450	1800	12540	33441	13369	16
1350	900	2250	12540	33441	16706	13
1800	450	2250	16711	44564	16706	13

7.5.1.2 Sampling line pressure

The effect of pressure differentials (between flame and sampling system) on the particulate losses in extraction line is shown in Fig. 7.14. The results show that the losses of particles ($D_p < 10$ nm) are high for $\Delta P > 20$ mbar. Particles in the $D_p < 10$ nm size range appears to be lost in the sampling lines, either due to deposition or coagulation at the probe tip. The Reynolds number at the probe tip is turbulent (i.e. $Re_{b_1} > 2300$) at pressure differentials of $\Delta P > 100$ mbar. For such pressure, loss of $D_p < 20$ nm diameter particles is severe while the loss of 30 – 230 nm particles is modest. A higher pressure difference in the sampling line leads to pronounced probe effects (flame perturbation) as discussed in Chapter 4. On the other hand, the total particle profile concentration drops at $\Delta P = 10$ mbar over the range of 6 – 230 nm. The particles with the size of $D_p \leq 10$ nm are also completely lost. This shows the critical role of differential pressure limit on the particle losses in the extraction line.

A differential pressure of $\Delta P = 20$ mbar is chosen in the current study. The constant pressure differential of $\Delta P = 20$ mbar along the sampling line reinforces stable particle sampling. The pressure differential also ensures the minimum flame perturbation and particle losses in extraction line (see Chapter 4).

The variation of mean, median mobility diameter and total number density are presented in Figs. 7.15 and 7.16 as a function of the differential pressure. The results show a comparatively constant number density for $\phi_{UN} = 2.0$ and 2.2, while the median and mean diameter increase with the suction pressure.

The higher ΔP leads to aggregation of the small particle to the larger ones for heavily sooting flames ($\phi_{UN} = 2.0$ and 2.2). On the other hand, the fluctuations in total number density with differential pressures reinforces the particle sensitivity to sampling line pressure at equivalence ratios close to soot inception ($\phi_{UN} = 1.8$). As expected, the rate of increase in the median and mean mobility diameter is significantly lower at soot inception than heavily sooting flame when differential pressure increases from $\Delta P = 20$ mbar to $\Delta P = 220$ mbar. The results show comparatively modest changes in the mean, median diameter mobility and total number density at equivalence ratios of $\phi_{UN} = 2.0$ and 2.2 for a wide limit of differential pressures.

7.5.2 Optimum sampling conditions

The approach in the current study is to apply different dilution ratios at constant differential pressure of $\Delta P = 20$ mbar. A two–stage dilution system was found to be a significant improvement over a single–stage dilution system, to reduce particle losses through the sampling line. Nitrogen flow rates should be chosen carefully. Two important effects were seen in the extraction line; (i) aggregation and (ii) condensation. The former is significant when a low level of nitrogen dilution is applied. In other words, the residence time is high enough to lead to particle aggregation. Particle diffusion to the sampling wall, leading to condensation is evident when excessive nitrogen dilution is used along the sampling line.

The optimum dilution ratio is a case where the PSD profile, mean and median mobility diameter are independent of the dilution. The loss mechanisms are minimised in an optimised range of dilution where the PSDs are seen to be insensitive to the dilution ratio. The established sampling process suggests that transmission losses should be relatively small by using the optimum dilution ratio listed in Table 7.4. Based on the above analyses, the constant dilution of $DR_2 = 675$ is chosen for the second port, while the first dilution level is dependent on the sooting flame conditions. For instance, the first dilution of DR_1 is three times higher for $\phi_{UN} = 2.0$ and 2.2 (heavily sooting flame) in comparison to lightly sooting condition (e.g. $\phi_{UN} = 1.8$).

Table 7.4. Optimum dilution ratio used in the current study. The results are for a pressure differential of $\Delta P = 20$ mbar, which is consistent with the pressure differential used in the PAH sampling experiments. Minimum particle losses and flame perturbations were found minimum at $\Delta P = 20$ mbar.

Case	DR_T	DR_1	DR_2
$a_T = 610$ [s^{-1}]	1000	325	675
$\phi_{UN} = 1.8$ [-]	900	225	675
$\phi_{UN} = 2.0$ [-]	1350	675	675
$\phi_{UN} = 2.2$ [-]	1350	675	675

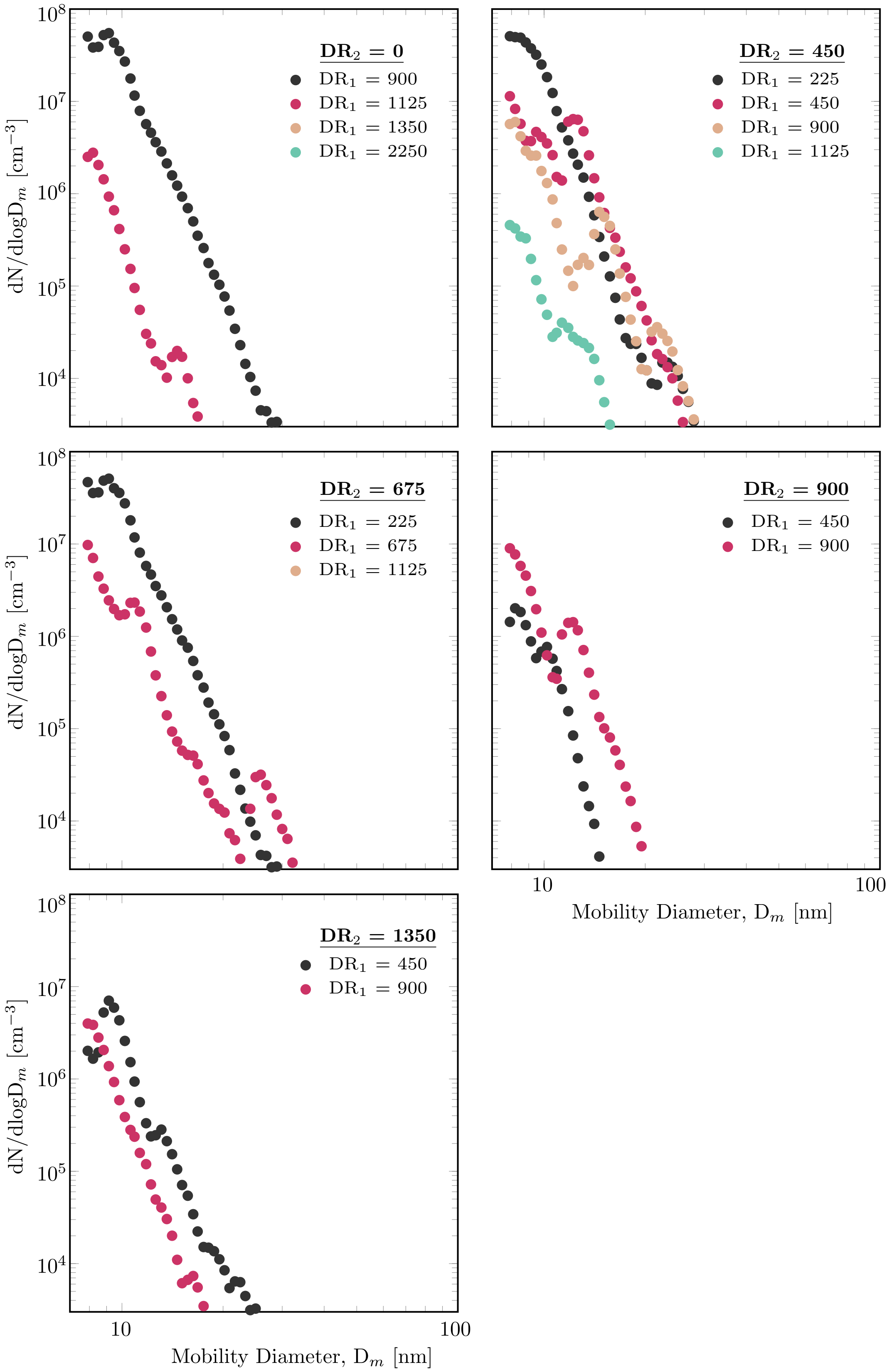

Figure 7.5. The impact of first dilution ratio (DR$_1$) on the particle size distribution at ϕ_{UN} = 1.80, a$_T$ = 420 s^{-1} and T$_{HCP}$ = 1500 K (ΔP = 20 mbar and X/L$_I$ = 0.5). Top left – DR$_2$ = 0; Top right – DR$_2$ = 450; Middle left – DR$_2$ = 675; Middle right – DR$_2$ = 900; Bottom left – DR$_2$ = 1350.

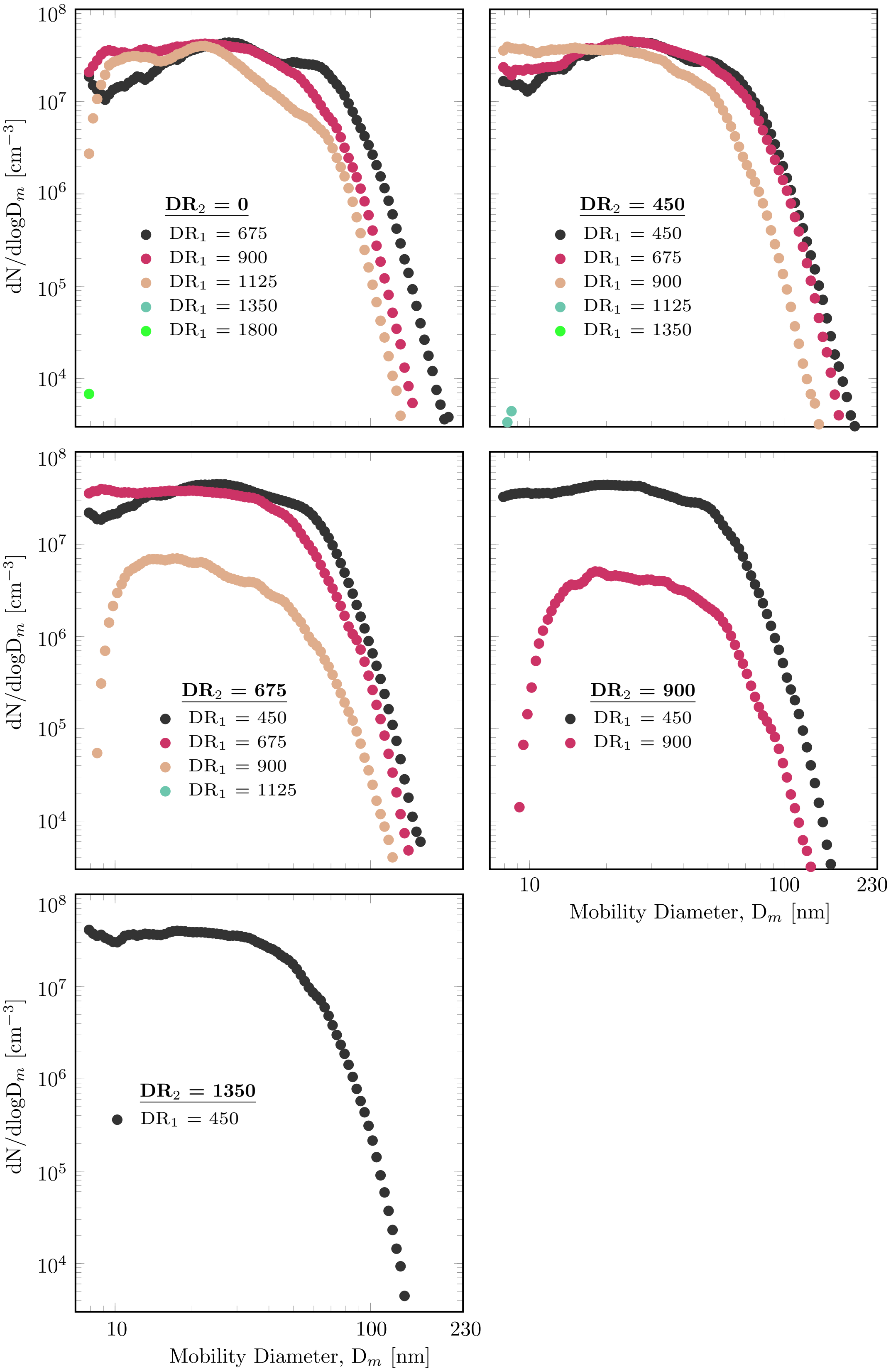

Figure 7.6. The impact of first dilution ratio (DR_1) on the particle size distribution at ϕ_{UN} = 2.0, a_T = 420 s^{-1} and T_{HCP} = 1500 K (ΔP = 20 mbar and X/L_I = 0.5). Top left – DR_2 = 0; Top right – DR_2 = 450; Middle left – DR_2 = 675; Middle right – DR_2 = 900; Bottom left – DR_2 = 1350.

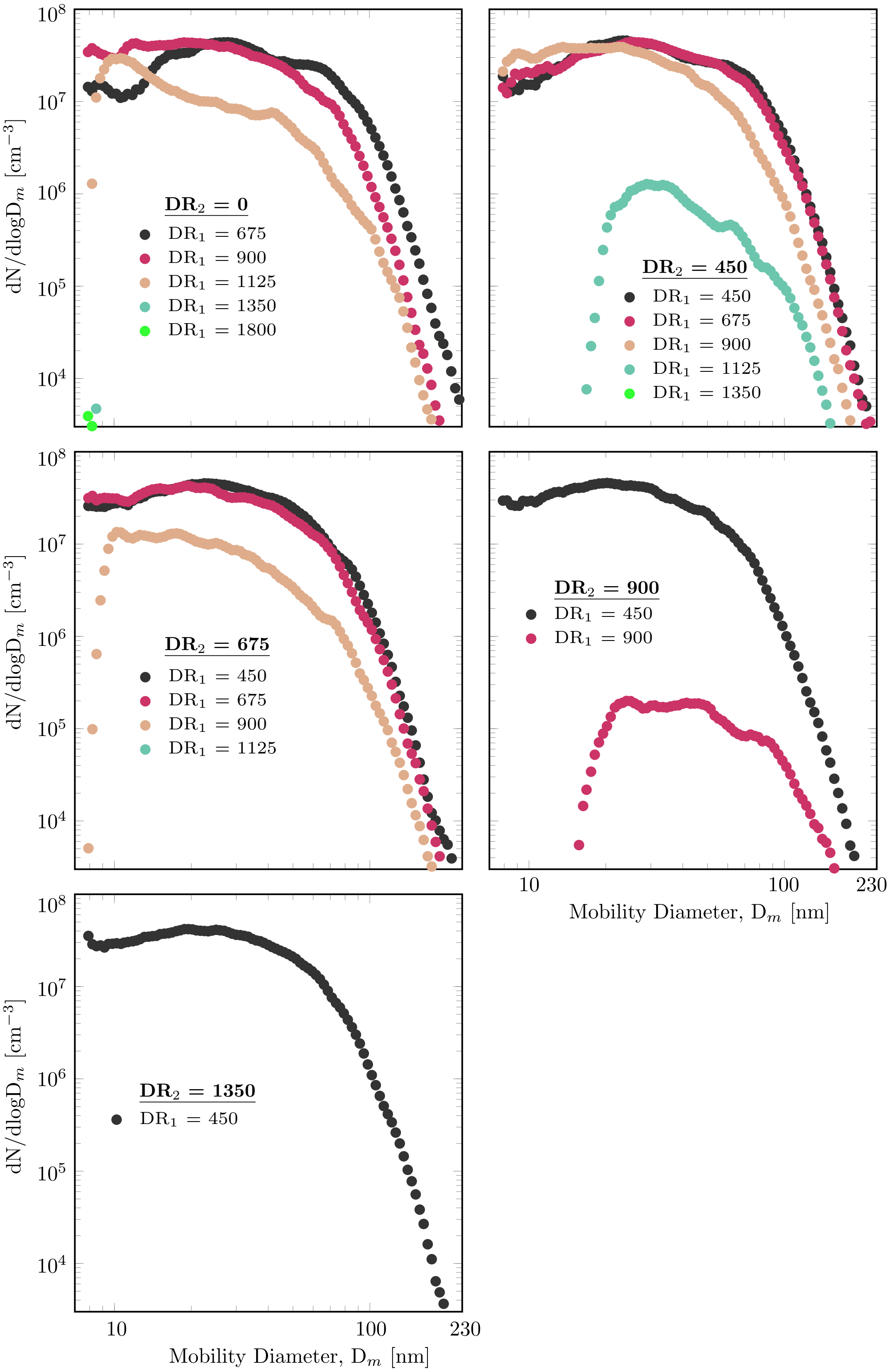

Figure 7.7. The impact of first dilution ratio (DR$_1$) on the particle size distribution at ϕ_{UN} = 2.2, a$_T$ = 420 s^{-1} and T$_{HCP}$ = 1500 K (ΔP = 20 mbar and X/L$_I$ = 0.5). Top left – DR$_2$ = 0; Top right – DR$_2$ = 450; Middle left – DR$_2$ = 675; Middle right – DR$_2$ = 900; Bottom left – DR$_2$ = 1350.

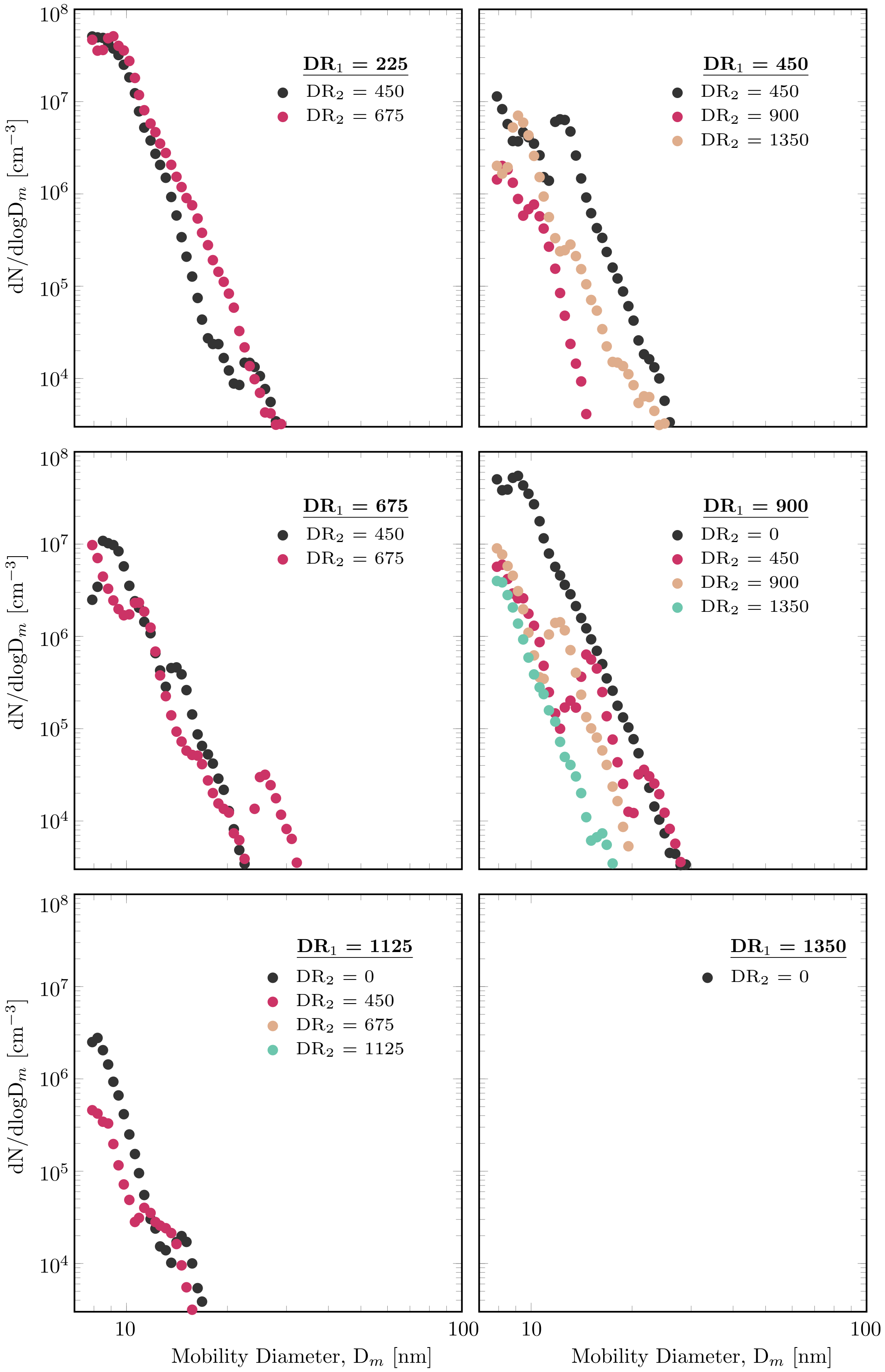

Figure 7.8. The impact of second dilution ratio (DR$_2$) on the particle size distribution at ϕ_{UN} = 1.8, a$_T$ = 420 s^{-1} and T$_{HCP}$ = 1500 K (ΔP = 20 mbar and X/L$_I$ = 0.5). Top left – DR$_1$ = 225; Top right – DR$_1$ = 450; Middle left – DR$_1$ = 675; Middle right – DR$_1$ = 900; Bottom left – DR$_1$ = 1125; Bottom right – DR$_1$ = 1350.

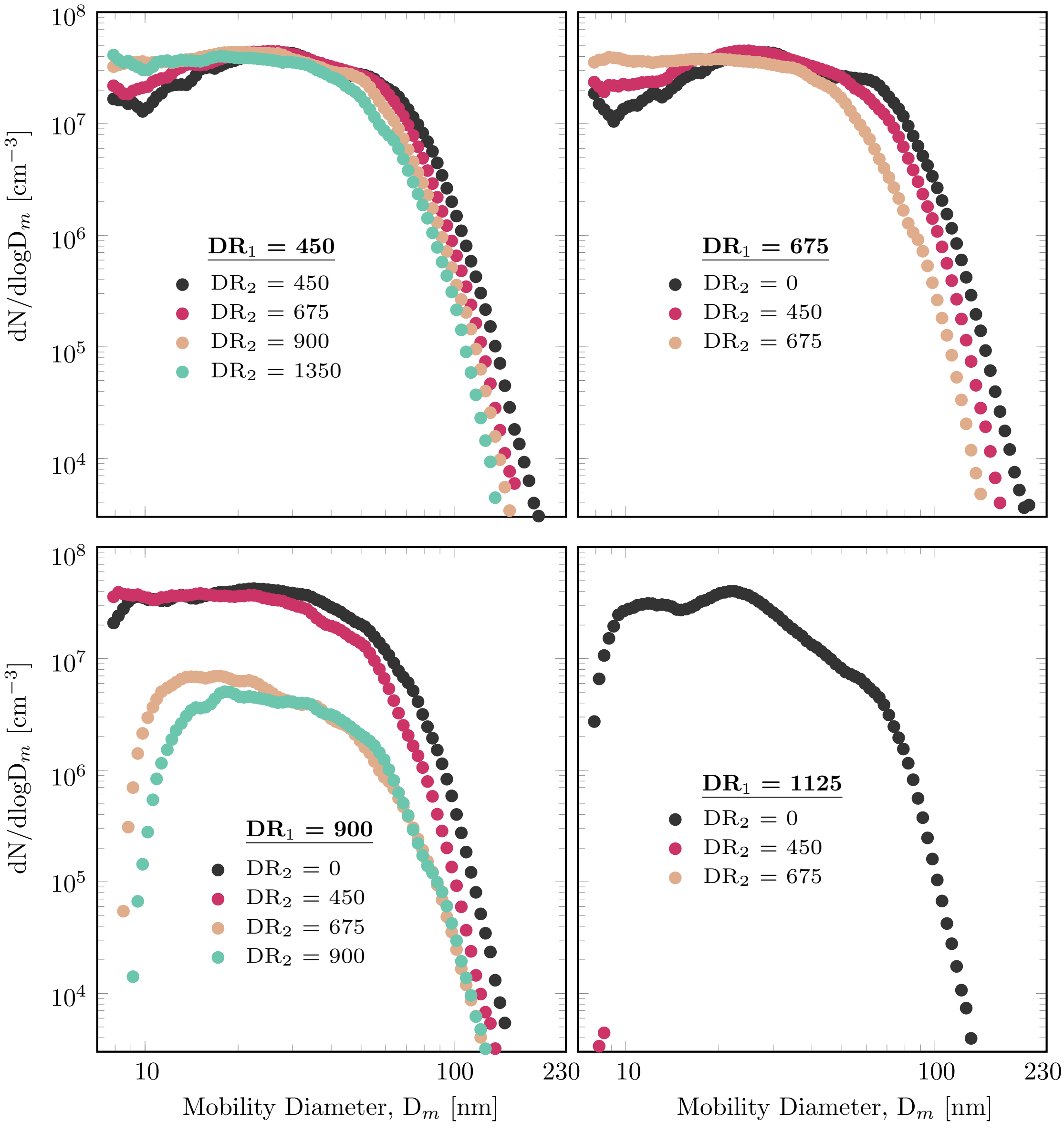

Figure 7.9. The impact of second dilution ratio (DR_2) on the particle size distribution at $\phi_{UN} = 2.0$, $a_T = 420$ s^{-1} and $T_{HCP} = 1500$ K($\Delta P = 20$ mbar and $X/L_I = 0.5$). Top left – $DR_1 = 450$; Top right – $DR_1 = 675$; Bottom left – $DR_1 = 900$; Bottom right – $DR_1 = 1125$. No PSD profile has found for $DR_1 \geq 1350$.

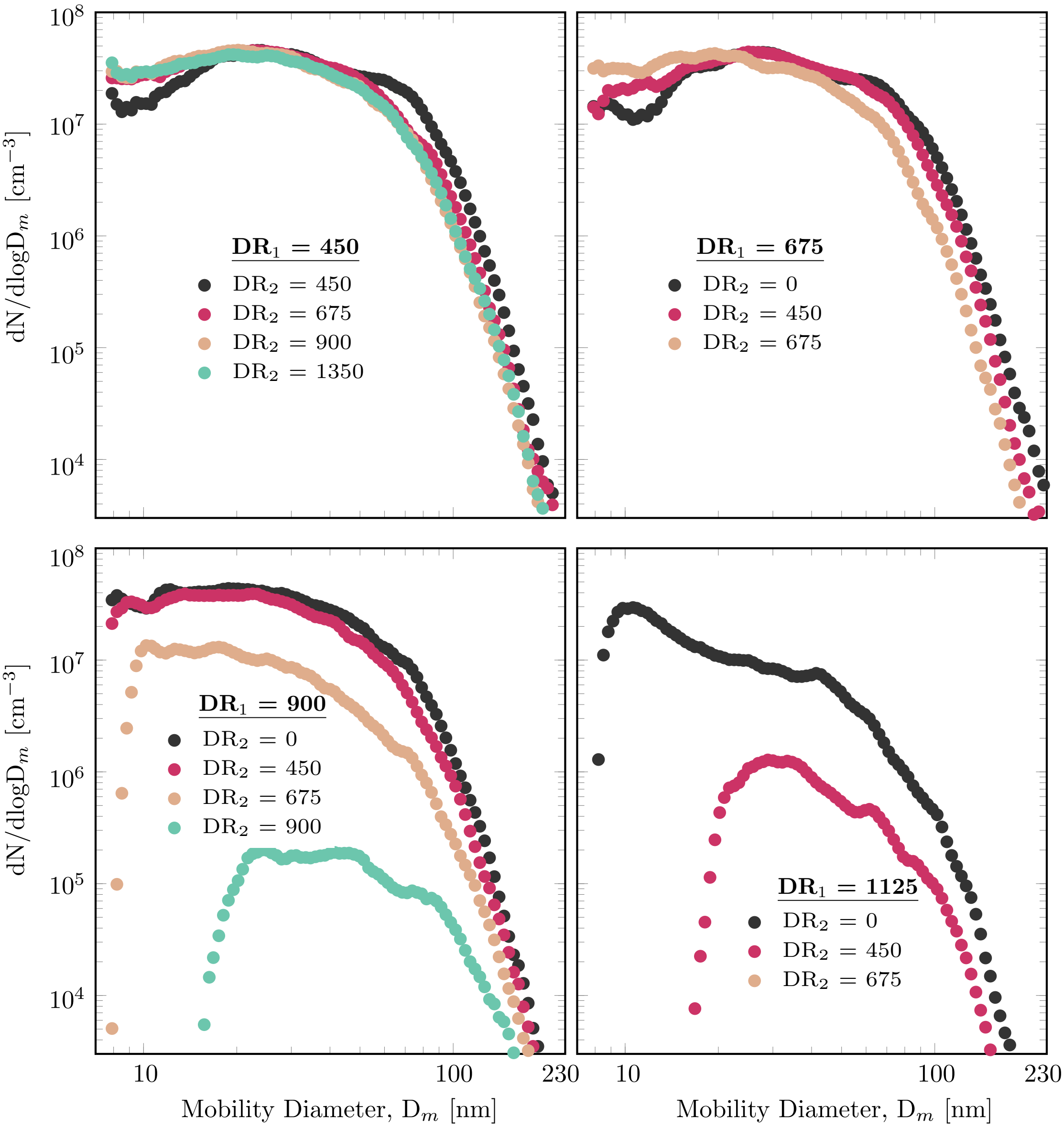

Figure 7.10. The impact of second dilution ratio (DR_2) on the particle size distribution at $\phi_{UN} = 2.2$, $a_T = 420$ s^{-1} and $T_{HCP} = 1500$ K ($\Delta P = 20$ mbar and $X/L_I = 0.5$). Top left – $DR_1 = 450$; Top right – $DR_1 = 675$; Bottom left – $DR_1 = 900$; Bottom right – $DR_1 = 1125$. No PSD profile distribution has found for $DR_1 \geq 1350$.

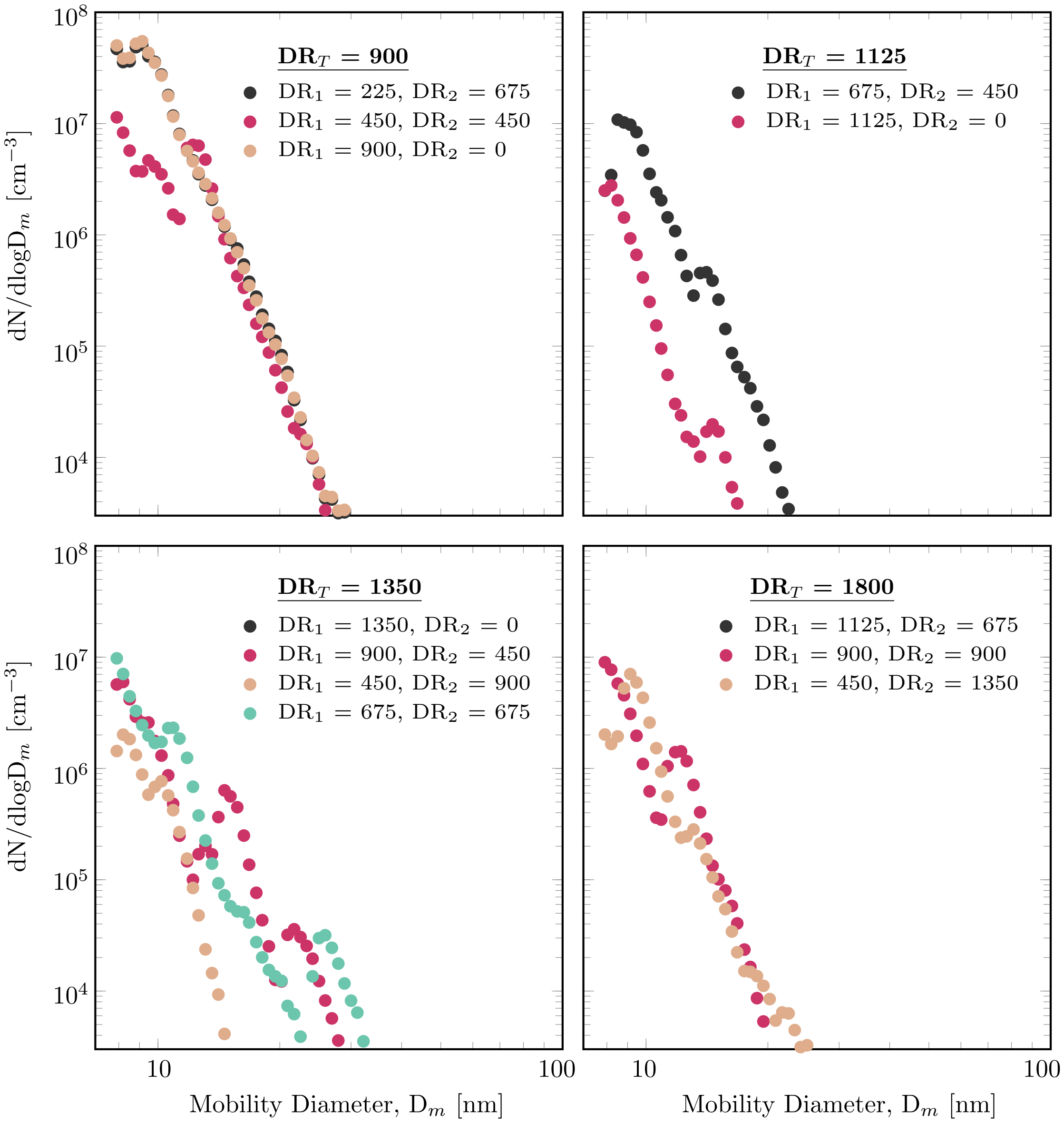

Figure 7.11. The impact of total dilution ratio (DR$_T$) on the particle size distribution at ϕ_{UN} = 1.8, a$_T$ = 420 s^{-1} and T$_{HCP}$ = 1500 K (ΔP = 20 mbar and X/L$_I$ = 0.5). The optimum dilution ratio is at DR$_T$ = 900 (DR$_1$ = 225 and DR$_2$ = 675). Top left – DR$_T$ = 900; Top right – DR$_T$ = 1125; Bottom left – DR$_T$ = 1350; Bottom right – DR$_T$ = 1800.

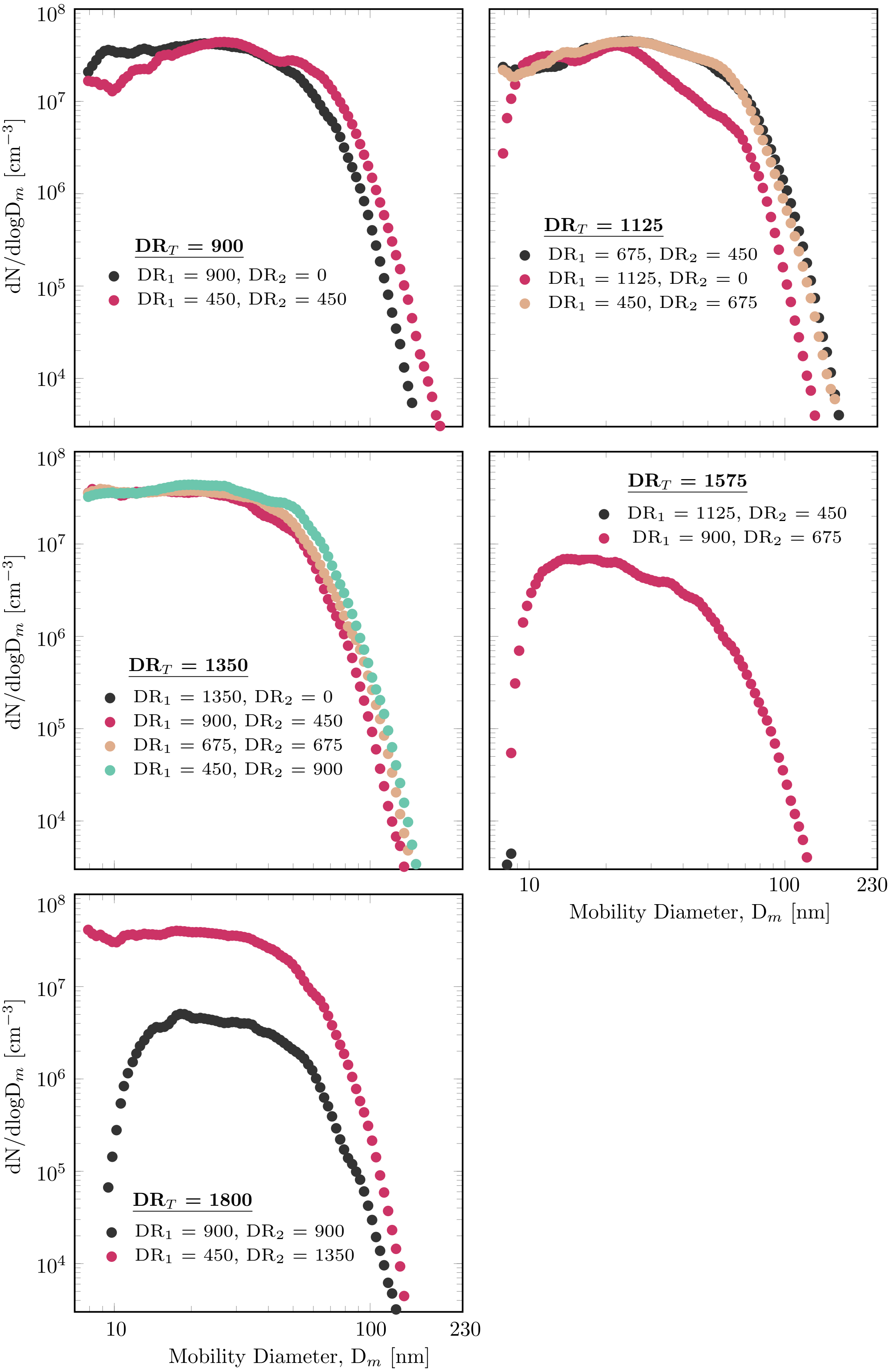

Figure 7.12. The impact of total dilution ratio (DR$_T$) on the particle size distribution at $\phi_{UN} = 2.0$, $a_T = 420\ \mathrm{s}^{-1}$ and $T_{HCP} = 1500$ K ($\Delta P = 20$ mbar and $X/L_I = 0.5$). The optimum dilution ratio is at DR$_T$ = 1350 (DR$_1$ = 675 and DR$_2$ = 675). Top left – DR$_T$ = 900; Top right – DR$_T$ = 1125; Middle left – DR$_T$ = 1350; Middle right – DR$_T$ = 1575; Bottom left – DR$_T$ = 1800.

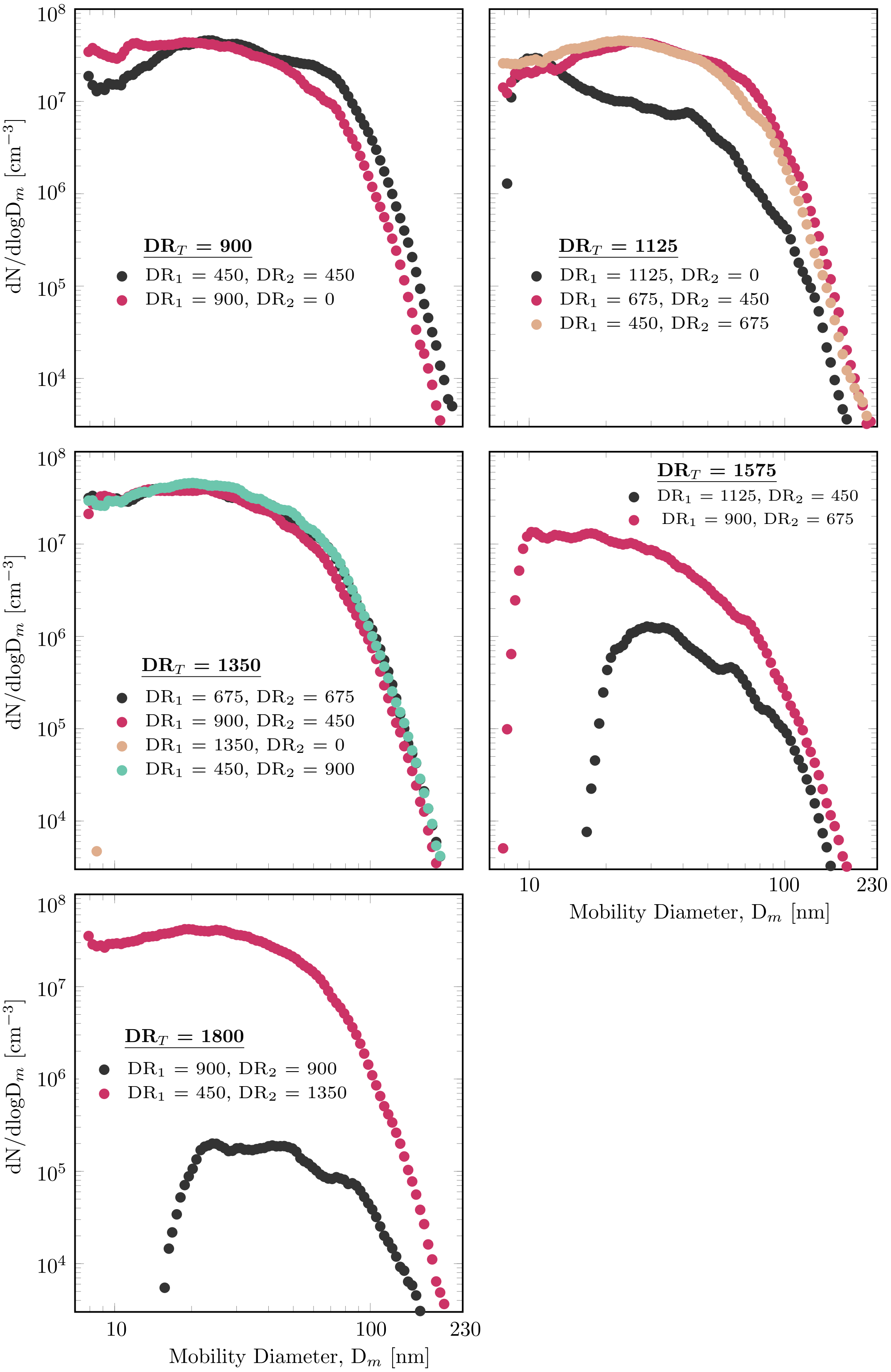

Figure 7.13. The impact of total dilution ratio (DR$_T$) on the particle size distribution at ϕ_{UN} = 2.2, a$_T$ = 420 s^{-1} T$_{HCP}$ = 1500 K (ΔP = 20 mbar and X/L$_I$ = 0.5). The optimum dilution ratio is at DR$_T$ = 1350 (DR$_1$ = 675 and DR$_2$ = 675). Top left – DR$_T$ = 900; Top right – DR$_T$ = 1125; Middle left – DR$_T$ = 1350; Middle right – DR$_T$ = 1575; Bottom left – DR$_T$ = 1800.

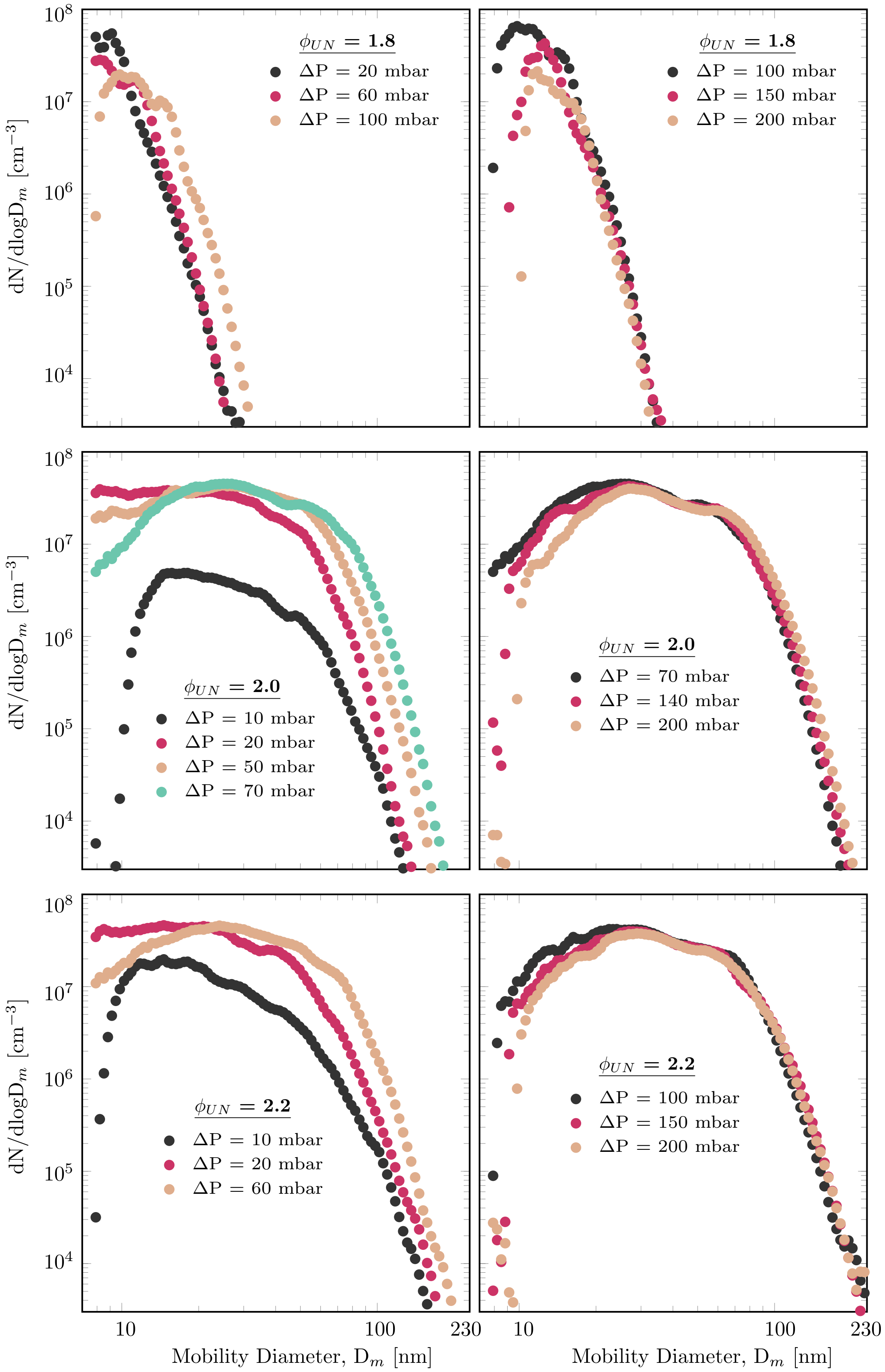

Figure 7.14. Mobility PSDFs measured as a function of ΔP (pressure differential) at X/L$_I$ = 0.5. Top row – ϕ_{UN} = 1.80 at constant DR$_T$ = 900 (DR$_1$ = 225 and DR$_2$ = 675); Middle row – ϕ_{UN} = 2.0 at constant DR$_T$ = 1350 (DR$_1$ = 675, DR$_2$ = 675); Bottom row – ϕ_{UN} = 2.2 at constant DR$_T$ = 1350 (DR$_1$ = 675, DR$_2$ = 675).

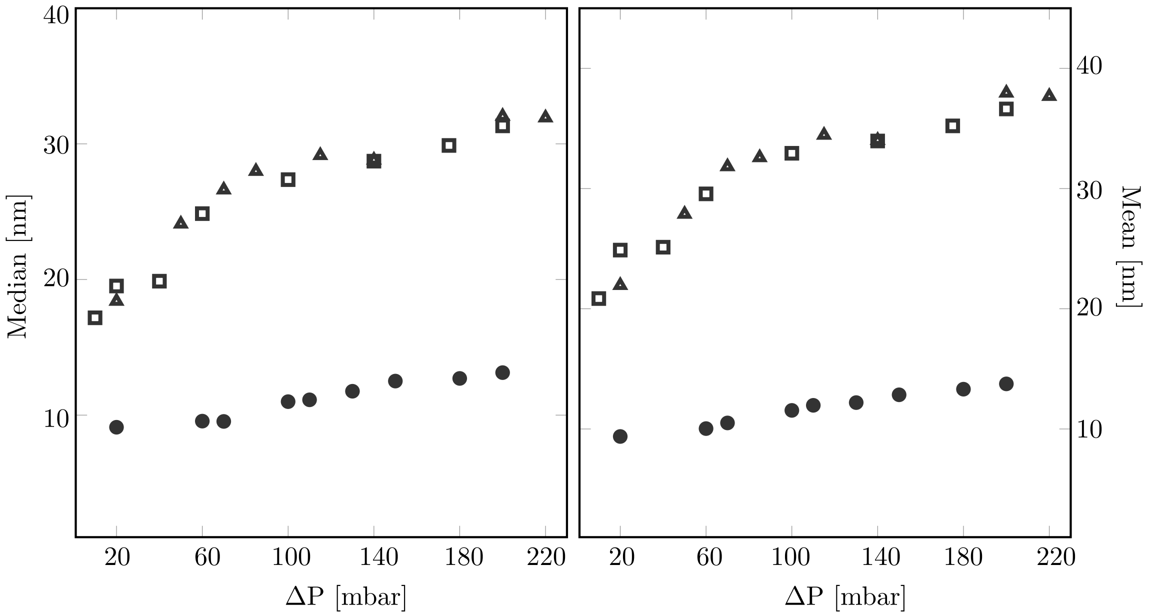

Figure 7.15. The impact of pressure differential on median (left) and mean (right) mobility diameters for different equivalence ratios of $\phi_{UN} = 1.8$ (circle); $\phi_{UN} = 2.0$ (triangle); $\phi_{UN} = 2.2$ (square). The rate of strain and burnt gas temperature is at a constant of $a_T = 420$ s^{-1} and $T_{HCP} = 1500$ K, respectively. The probe is located at $X/L_I = 0.5$.

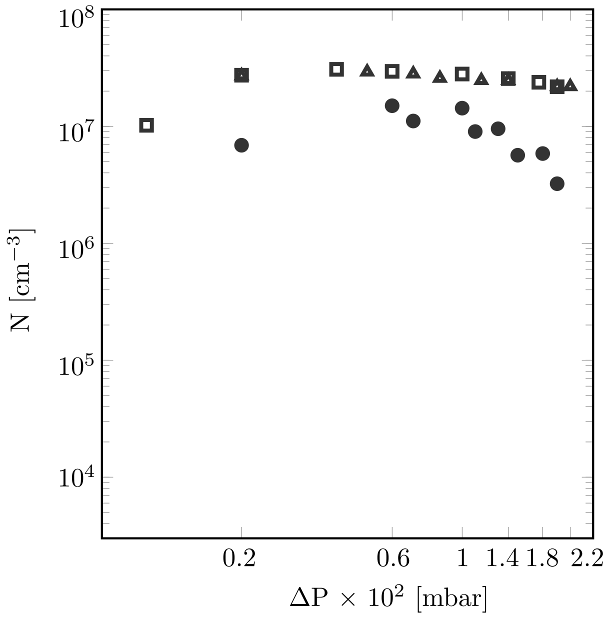

Figure 7.16. The impact of pressure differential on the total number density for different equivalence ratios of $\phi_{UN} = 1.8$ (circle); $\phi_{UN} = 2.0$ (triangle); $\phi_{UN} = 2.2$ (square). The total number density is calculated based on the division of the summed bins by the resolution per decade [253]. The rate of strain and burnt gas temperature is at a constant of $a_T = 420$ s^{-1} and $T_{HCP} = 1500$ K, respectively. The probe is located at $X/L_I = 0.5$.

Table 7.5. Some selected dilution ratios (DR_T, DR_1 and DR_2) used to study the PSD of particulates at ϕ_{UN} = 1.8, a_T = 420 s^{-1} and T_{HCP} = 1500 K for X/L_I = 0.5 and ΔP = 20 mbar. The optimum case is shown in bold font in the table. The respective median and mean mobility diameter, total number density as a function of dilution ratio are presented in Fig. 7.18 and Fig. 7.19, respectively.

ID	DR_T	DR_1	DR_2
1	675	225	450
2	900	900	0
3	**900**	**225**	**675**
4	900	450	450
5	1125	1125	0
6	1125	675	450
7	1350	1350	0
8	1350	450	900
9	1350	675	675
10	1350	900	450
11	1575	1125	450
12	1800	1125	675
13	1800	900	900
14	1800	450	1350
15	2250	2250	0

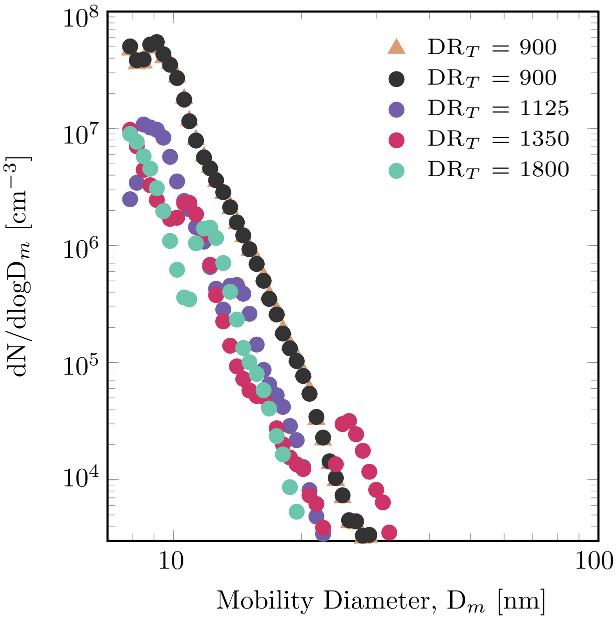

Figure 7.17. Selected mobility PSDFs measured at ϕ_{UN} = 1.8 for a spatial location of X/L_I = 0.5 and a differential pressure of ΔP = 20 mbar. The optimum dilution ratio is found at DR_T = 900 (DR_1 = 225, DR_2 = 675). Tan (DR_1 = 225, DR_2 = 675); Black (DR_1 = 900, DR_2 = 0); Violet (DR_1 = 676, DR_2 = 450); Purple (DR_1 = 675, DR_2 = 675); Sea green (DR_1 = 900, DR_2 = 900).

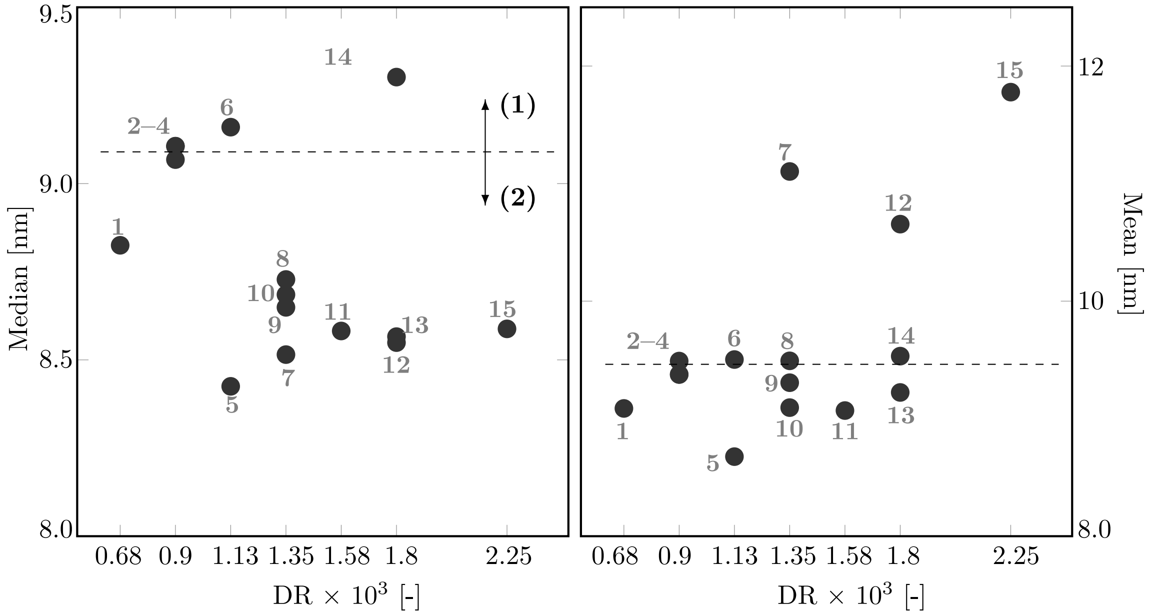

Figure 7.18. The impact of dilution ratio on median (left) and mean (right) mobility diameters of PSDs measured at $\phi_{UN} = 1.8$ and $a_T = 420$ s^{-1} for $X/L_I = 0.5$ and $\Delta P = 20$ mbar. The optimum case is found at dilution ratio of $DR_T = 900$ ($DR_1 = 225$ and $DR_2 = 675$), e.g. number 3 where (1) and (2) show the agglomeration and diffusion losses of particulates over the sampling line, respectively.

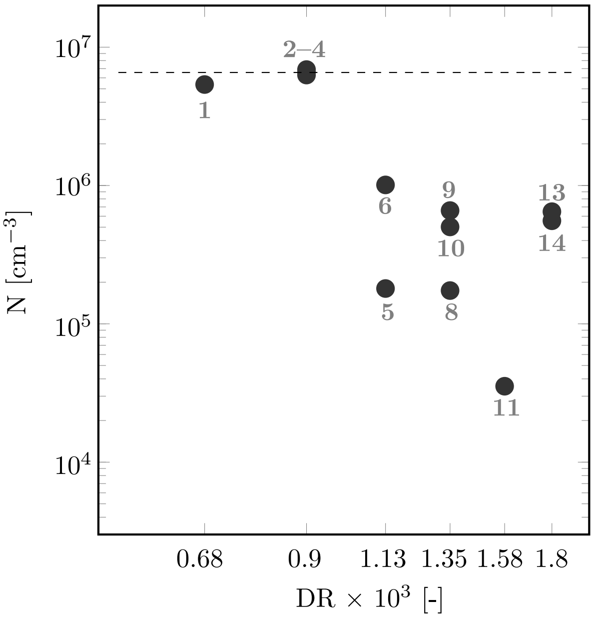

Figure 7.19. The impact of dilution ratio on total number density measured at $\phi_{UN} = 1.8$ and $a_T = 420$ s^{-1} for $X/L_I = 0.5$ and $\Delta P = 20$ mbar. The total number density is calculated based on the division of the summed bins by the resolution per decade [253]. Some cases are not presented in the figure due to particulate losses onto sampling wall of the extraction line.

Table 7.6. Some selected dilution ratio (DR_T, DR_1 and DR_2) used to the study PSD of particulates at $\phi_{UN} = 2.0$ and $a_T = 420$ s^{-1} for $X/L_I = 0.5$ and $\Delta P = 20$ mbar. The optimum case is shown in bold font in the table. The respective median and mean mobility diameter, total number density as a function of dilution ratio are presented in Fig. 7.21 and Fig. 7.22, respectively.

ID	DR_T	DR_1	DR_2
1	675	675	0
2	900	900	0
3	900	450	450
4	1125	1125	0
5	1125	450	675
6	1125	675	450
7	1350	1350	0
8	1350	450	900
9	**1350**	**675**	**675**
10	1350	900	450
11	1350	1125	225
12	1575	900	675
13	1575	1125	450
14	1800	1800	0
15	1800	450	1350
16	1800	900	900
17	1800	1125	675
18	1800	1350	450

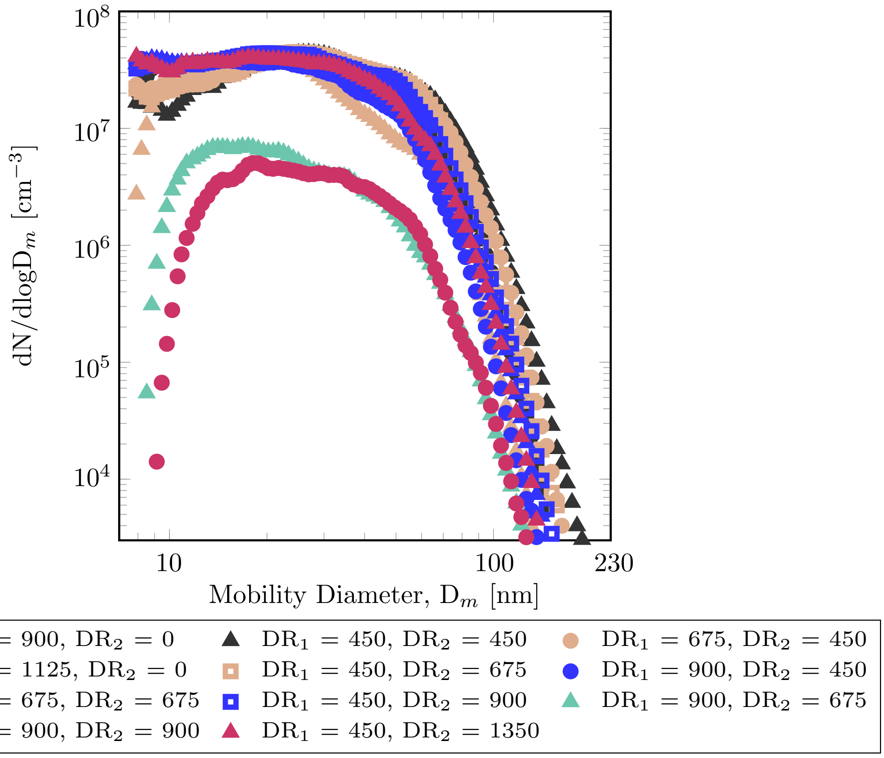

Figure 7.20. Selected mobility PSDFs measured at $\phi_{UN} = 2.0$ for a spatial location of $X/L_I = 0.5$ and a differential pressure of $\Delta P = 20$ mbar. The optimum dilution ratio is found at $DR_T = 1350$ ($DR_1 = 675$, $DR_2 = 675$). Black ($DR_T = 900$); Tan ($DR_T = 1125$); Blue ($DR_T = 1350$); Sea green ($DR_T = 1575$); Purple ($DR_T = 1800$).

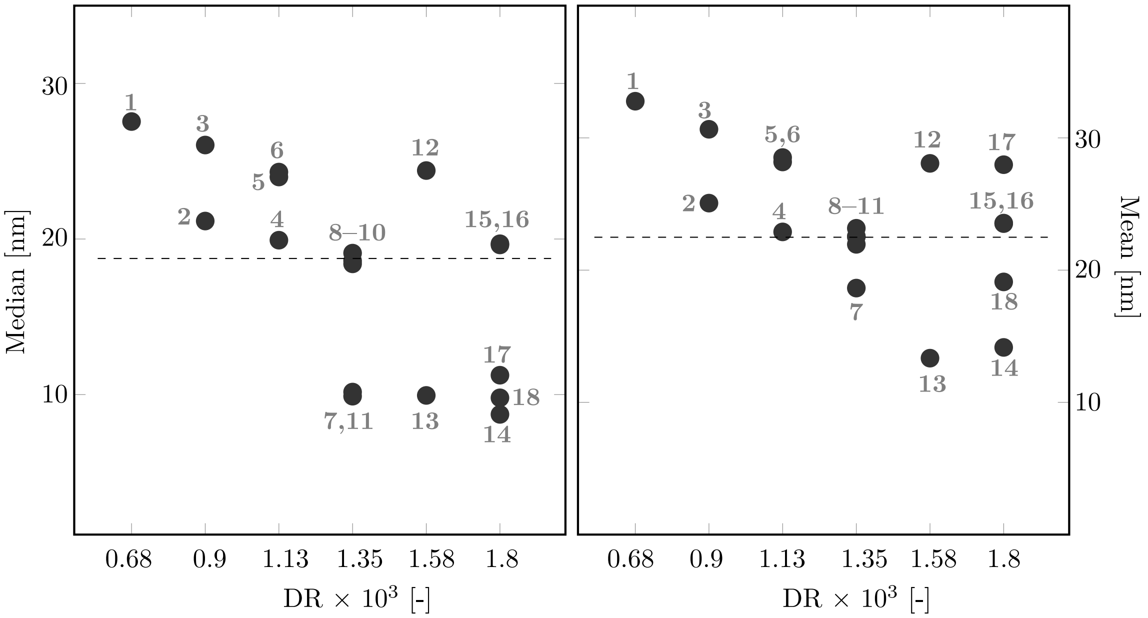

Figure 7.21. The impact of dilution ratio on median (left) and mean (right) mobility diameters of PSDs measured at $\phi_{UN} = 2.0$ and $a_T = 420$ s^{-1} for $X/L_I = 0.5$ and $\Delta P = 20$ mbar. The optimum case is found at dilution ratio of $DR_T = 1350$ ($DR_1 = 675$ and $DR_2 = 675$), e.g. number 9.

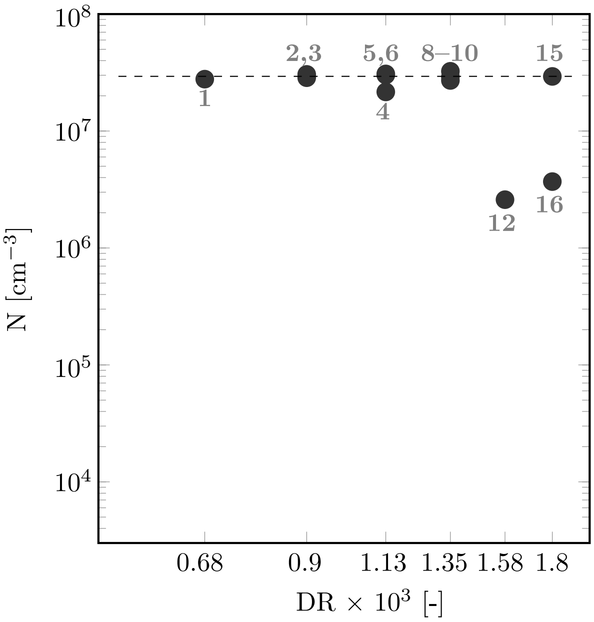

Figure 7.22. The impact of dilution ratio on total number density measured at $\phi_{UN} = 2.0$ and $a_T = 420$ s^{-1} for $X/L_I = 0.5$ and $\Delta P = 20$ mbar. The total number density is calculated based on the division of the summed bins by the resolution per decade [253]. A few more cases are not presented in the figure due to particulate diffusion losses onto sampling wall of extraction line.

Table 7.7. Some selected dilution ratio (DR_T, DR_1 and DR_2) used to study the PSD of particulates at $\phi_{UN} = 2.2$ and $a_T = 420$ s^{-1} for $X/L_I = 0.5$ and $\Delta P = 20$ mbar. The optimum case is shown in bold font in the table. The respective median and mean mobility diameter, total number density as a function of dilution ratio are presented in Fig. 7.24 and Fig. 7.25, respectively.

ID	DR_T	DR_1	DR_2
1	675	675	0
2	900	900	0
3	900	450	450
4	1125	1125	0
5	1125	450	675
6	1125	675	450
7	1350	1350	0
8	1350	450	900
9	**1350**	**675**	**675**
10	1350	900	450
11	1575	900	675
12	1575	1125	450
13	1800	1800	0
14	1800	450	1350
15	1800	900	900
16	1800	1125	675
17	1800	1350	450

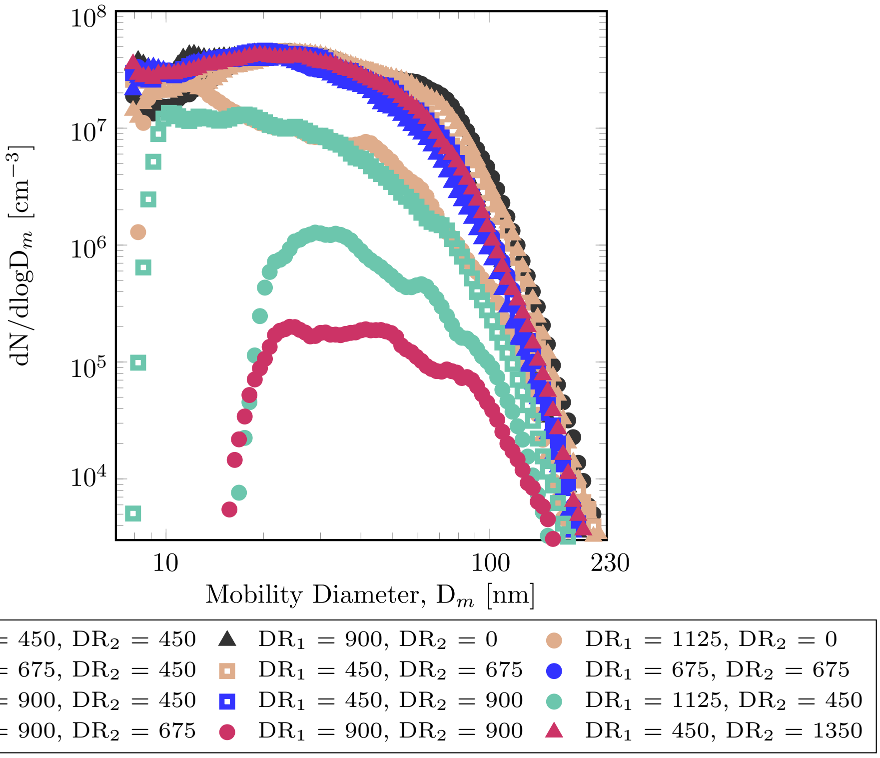

Figure 7.23. Selected mobility PSDFs measured at $\phi_{UN} = 2.2$ and $a_T = 420$ s^{-1} for a spatial location of $X/L_I = 0.5$ and a differential pressure of $\Delta P = 20$ mbar. The optimum dilution ratio is found at $DR_T = 1350$ ($DR_1 = 675$, $DR_2 = 675$). Black ($DR_T = 900$); Tan ($DR_T = 1125$); Blue ($DR_T = 1350$); Sea green ($DR_T = 1575$); Purple ($DR_T = 1800$).

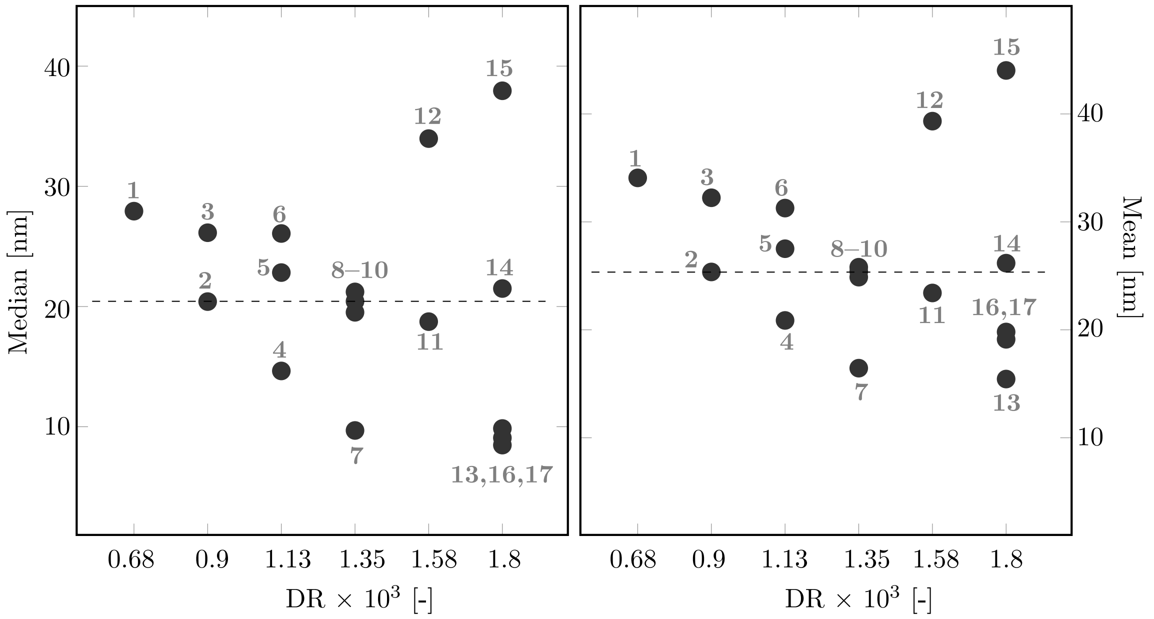

Figure 7.24. The impact of dilution ratio on median (left) and mean (right) mobility diameters of PSDs measured at $\phi_{UN} = 2.2$ and $a_T = 420$ s^{-1} for $X/L_I = 0.5$ and $\Delta P = 20$ mbar. The optimum case is found at dilution ratio of $DR_T = 1350$ ($DR_1 = 675$ and $DR_2 = 675$), e.g. number 9.

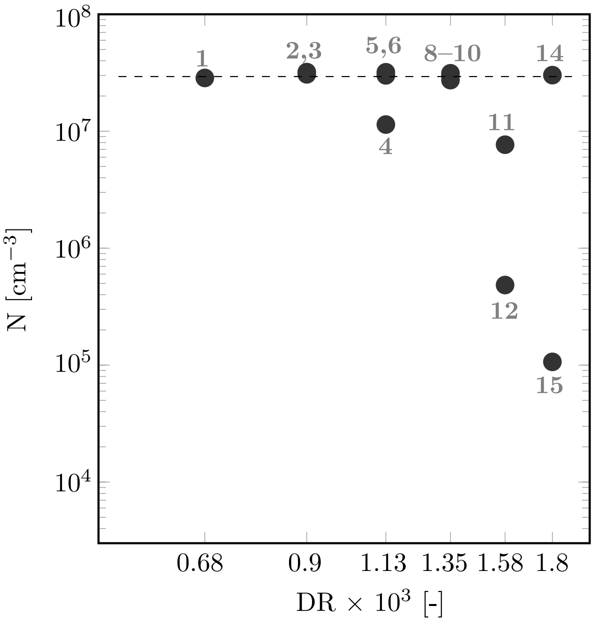

Figure 7.25. The impact of dilution ratio on total number density measured at $\phi_{UN} = 2.2$ and $a_T = 420$ s^{-1} for $X/L_I = 0.5$ and $\Delta P = 20$ mbar. The total number density is calculated based on the division of the summed bins by the resolution per decade [253]. Some cases are not presented due to particulate losses onto sampling wall of the extraction line.

7.6 Particle size distributions

Once the optimum dilution ratio (DR) has been determined, the impacts of equivalence ratio and rate of strain over reaction zone layer ($-1 \leq X/L_I \leq +1.5$) can be studied. The optimum DRs for each experimental condition are listed in Table 7.4. The sampling position is varied along the theoretical stagnation point streamline from the onset of formaldehyde formation across the soot formation layer and into the supporting hot combustion products.

SMPS scans are performed along the flame centerline at multiple axial locations with the interval of 2 mm (~ 0.5 L_I) over the reaction zone layer ($-1.0 \leqslant X/L_I \leqslant 1.5$). The scan time of about 10,000 integral time–scales of turbulence is used (120 s) to ensure statistical independence and present the consistency with PAH sampling experiments. The 1–nm SMPS system can measure particle mobility diameter in the range of 4–40 nm. The mobility diameter of $D_p > 40$ nm are also present for almost all experimental conditions. The nano DMA cannot generate a complete PSD from the measurements and, therefore, the long DMA is used to provide a broader limit of PSDs with $4 < D_p$ [nm] < 230.

The particle size distributions are provided in Figs. 7.26–7.29 for both nano and long DMA setups. The maximum discrepancy is observed within a factor of five at $D_P =$ 10 nm for $\phi_{UN} = 1.8$ at spatial location $X/L_I = 1.5$. The discrepancy is below a factor of three for all other experimental conditions. The nano DMA registers consistently higher particle concentrations. The discrepancy can stem from two main reasons. First, there are challenges in the calibration processes of each instrument. For instance, the aerosols usually used for calibration features different chemical and physical characteristics than that of soot particles in the flame [64, 307]. Second, both instruments have different transfer functions and diffusion losses due to different geometries [308]. The quantification of such instrument dependant properties is beyond the scope of the current study.

The impacts of rate of strain and equivalence ratio on the particle size distribution are shown in Fig. 7.30 and Fig. 7.31. The results were normalised with the number density over the common interval (8–40 nm) for both the 1–nm SMPS and long DMA setups to provide a comparison between experimental cases. The results highlight the important role of turbulence in the spread of particles over the reaction zone layer. A higher particle accumulation is seen for PSDs at spatial location of $X/L_I = 0$ for both lightly and heavily sooting flames. The higher residence time at the stagnation point supports the comparatively higher aggregation at the spatial location of $X/L_I = 0$.

The PSD profiles show comparatively higher particle concentrations for particle size ranges below 10 nm for the spatial location close to the reactant side. This shows that soot formation process is pronounced from reactant side to stagnation point, especially at $X/L_I = +1, +1.5$ for lightly sooting flames ($a_T = 610$ s^{-1} and $\phi_{UN} = 1.80$). However, higher aggregation is seen in the PSD profile of all flame structures when moving towards the HCP.

At higher equivalence ratios, the size distribution flattens out over a wide limit of particle size diameters. Interestingly, the PSD profiles at $\phi_{UN} = 2.2$ overlap to a single PSD over the reaction zone.

The slope of PSD profile changes from $\phi_{UN} = 2$ to $\phi_{UN} = 2.2$ with the slopes at $\phi_{UN} = 2.2$ lower between $10 \leq D_p \leq 100$ nm for the spatial location of $X/L_I \leq +0.5$. The lower PSD slope leads to lower median diameter (at $\phi_{UN} = 2.2$) for spatial locations with $X/L_I < 0.5$. On the other hand, the aggregation and total density number are proportionally correlated with the increase in the equivalence ratio.

A bimodal distribution is the result of competition between particle nucleation and particle–particle coagulation. There are few studies in turbulent flames clarifying the bimodality in the PSD profile. For instance, Chowdhury et al. [64] and De Falco et al. [303] did not observe a bimodal behaviour in the PSD profile in turbulent flows and refer the disappearance of bimodality to turbulence effects. Tian et al. [68] show that there is an intermittent shift in the calculated PSD from a unimodal to a bimodal shape in some turbulent flames. The particle size distributions measured here show a bimodal distribution for some experimental cases such as equivalence ratios of ϕ_{UN} = 2.0 and 2.2 at the spatial location of X/L$_I$ = +1.0, while the majority of PSD profiles are unimodal illustrating the dominant impact of surface growth. There should be a continuous shift between bimodal and unimodal shapes in the PSD with a transition from the existence of competition between the processes involving in oxidation, aggregation and surface growth [68].

The median and mean mobility diameter of the PSD measured over the reaction zone layer are provided in Fig. 7.32. The peak value of median and mean mobility diameters are found at the stagnation point irrespective of flame conditions. The median diameter increases by a factor of 1.6 (from 14.4 to 22.4 nm) as the rate of strain is reduced from a$_T$ = 610 s^{-1} to a$_T$ = 420 s^{-1} (i.e. the reference flame). By comparison, the median and mean mobility diameters are comparatively more influenced when the equivalence ratio is increased from ϕ_{UN} = 1.8 to ϕ_{UN} = 2.0 (i.e. the reference flame). For instance, the median and mean mobility diameters is 2.6 and 2.4 times higher for the reference flame, respectively. However, both median and mean mobility diameters reduce by 20% at the higher equivalence ratio (ϕ_{UN} = 2.2). The PSD profiles (e.g. slope) explain the lower mean and median diameters for the higher equivalence ratio at the stagnation point. The results show that median and mean diameters are higher for spatial locations towards hot combustion products due to particle aggregation. For example, the median diameter is roughly 1.5 times higher towards hot combustion products (X/L$_I$ = -1) than towards the reactants (X/L$_I$ = 1.5) for the reference flame. Roberts and co–workers [27, 64] showed that the mean mobility diameter remained below 10 nm for both flames with the Reynolds numbers of Re = 10,000 and 20,000. The mean diameter is in the range of 8.2 – 25.4 nm in the current study. The PSD profiles are broader in comparison to those obtained by Roberts and co–workers, showing the differences in the flame structures and turbulence effects. The differences in the PSD profiles reinforce the comparatively higher median and mean mobility diameters in the current study.

The total number density over the reaction zone layer is shown separately for nano (4–40 nm) and long DMA (8–230 nm) in Fig. 7.33. The total density number (4–230 nm) is depicted in Fig. 7.34 and calculated based on arithmetic averaging of the concentrations measured with the nano and the long DMA for the interval of $8 < D_p$ [nm] < 40. The total number densities are in the range of $10^6 <$ N [cm^{-3}] $< 10^8$ for the current experimental conditions, consistent with studies in turbulent flames presented by Roberts and co–workers [27, 64], and Olfert and co–workers [304, 305]. The total number density shows two distinct behaviours for lightly and highly sooting flame. For instance, the number density drops remarkably towards reactants ($X/L_I \geq +1.0$) for lightly sooting conditions ($a_T = 610$ s^{-1} and $\phi_{UN} = 1.8$). The sudden decrease in total number density is indicated by the flame photographs shown in Fig. 7.1. As an example, the lightly sooting flame ($\phi_{UN} = 1.8$) exhibits a thin pale orange zone surrounded by a thick bright blue flame with a drastically narrower soot layer. The location $X/L_I = +1.5$ corresponds to a location where mostly a bright blue flame exists. In contrast, the total number density toward reactants increases for $\phi_{UN} \geq 2.0$. The soot layer thickness increases significantly at higher equivalence ratios ($\phi_{UN} \geq 2.0$) and the flames contain a brighter yellow–colour over the entire region of reaction zone layer.

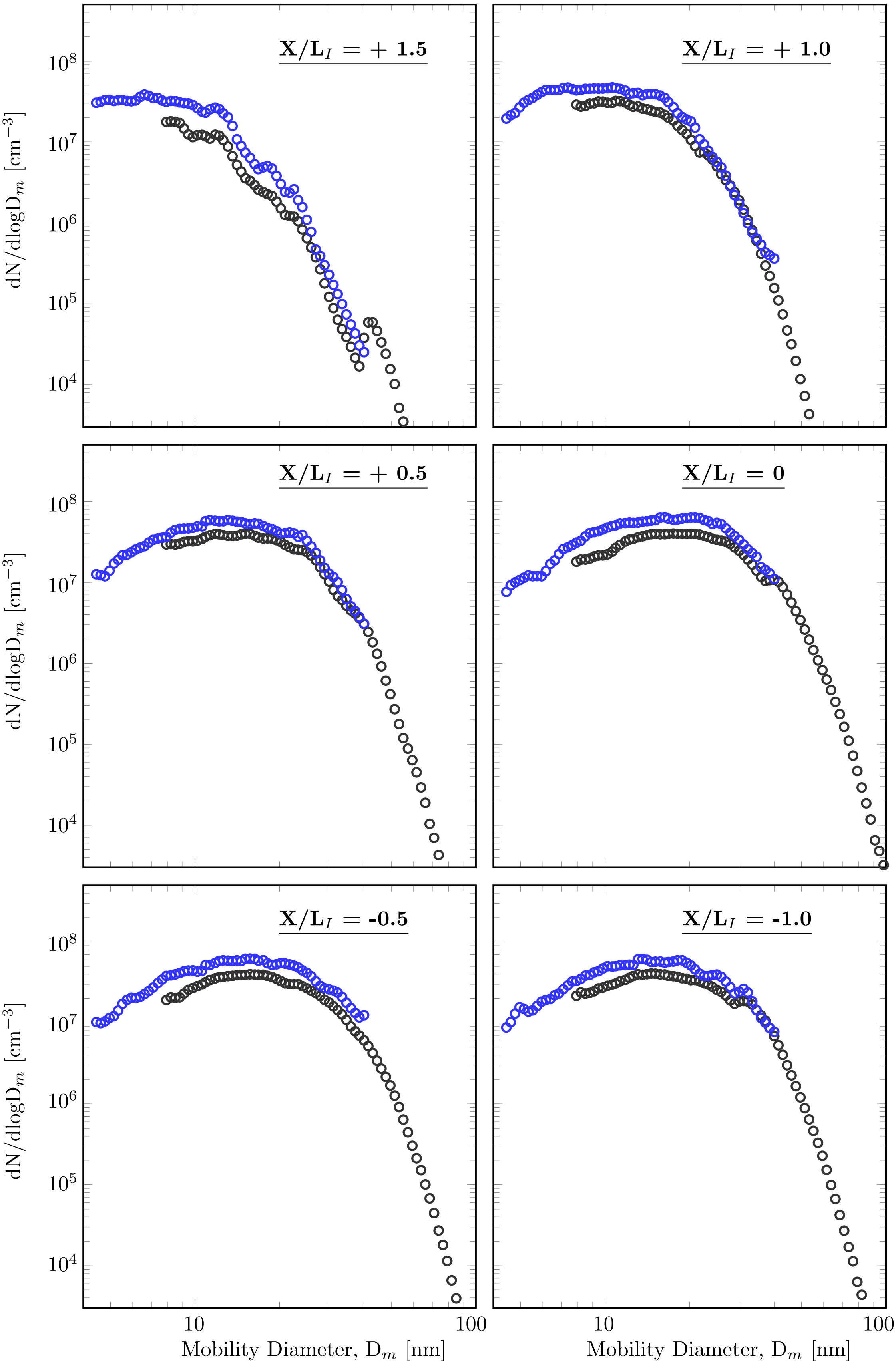

Figure 7.26. The PSD profiles for 1–nm SMPS (blue) and long DMA (black). The experiment is carried out at $\phi_{UN} = 2.0$, $a_T = 610$ s^{-1} and $T_{HCP} = 1500$ K. The nano DMA registers consistently higher concentrations for PSD profiles. Different transfer functions and diffusion losses within the DMAs explain the discrepancies between PSDs.

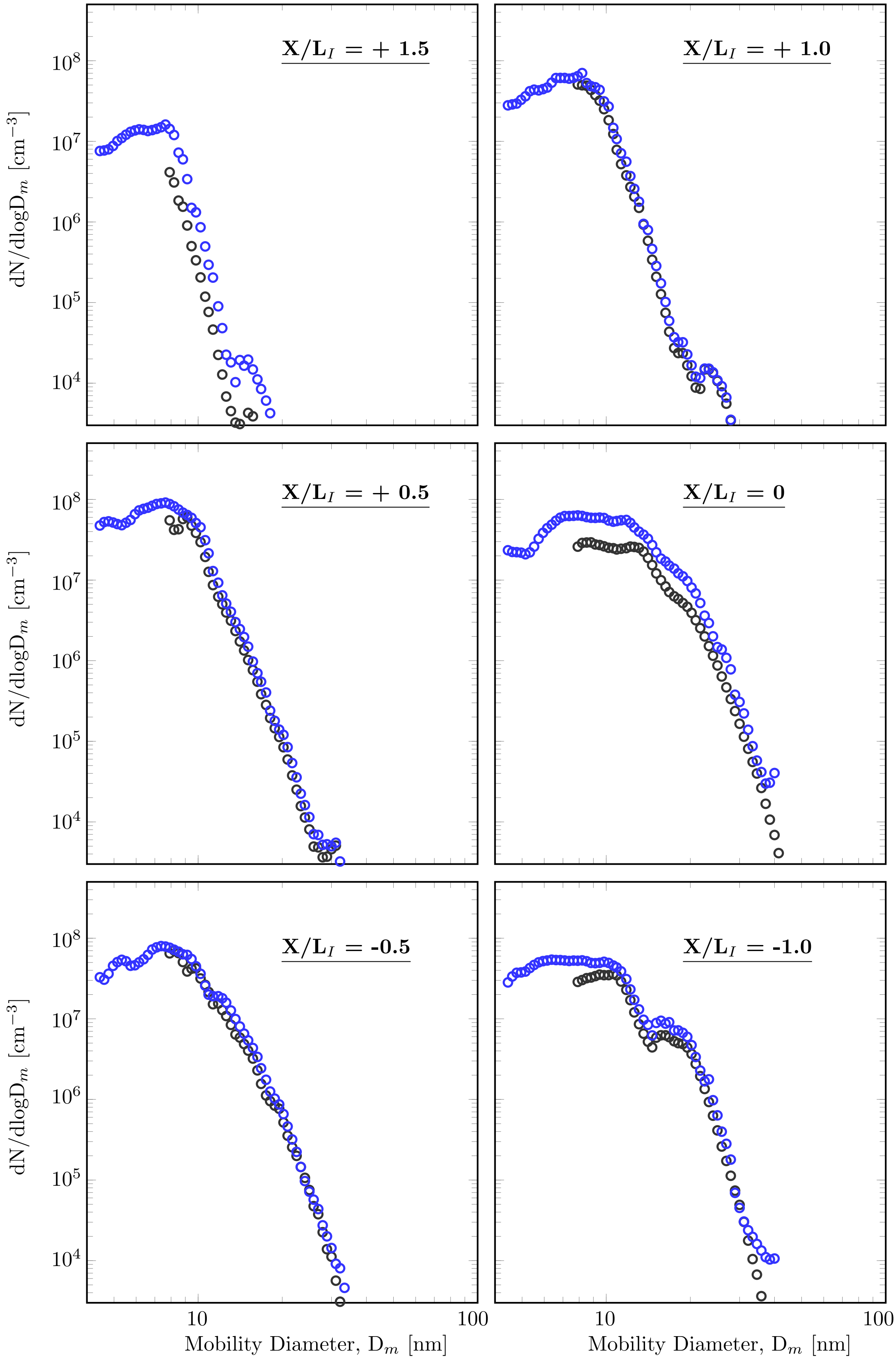

Figure 7.27. The PSD profiles for 1–nm SMPS (blue) and long DMA (black). The experiment is carried out at $\phi_{UN} = 1.8$, a$_T$ = 420 s^{-1} and T$_{HCP}$ = 1500 K. The nano DMA registers consistently higher concentrations for PSD profiles. Different transfer functions and diffusion losses within the DMAs explain the discrepancies between PSDs.

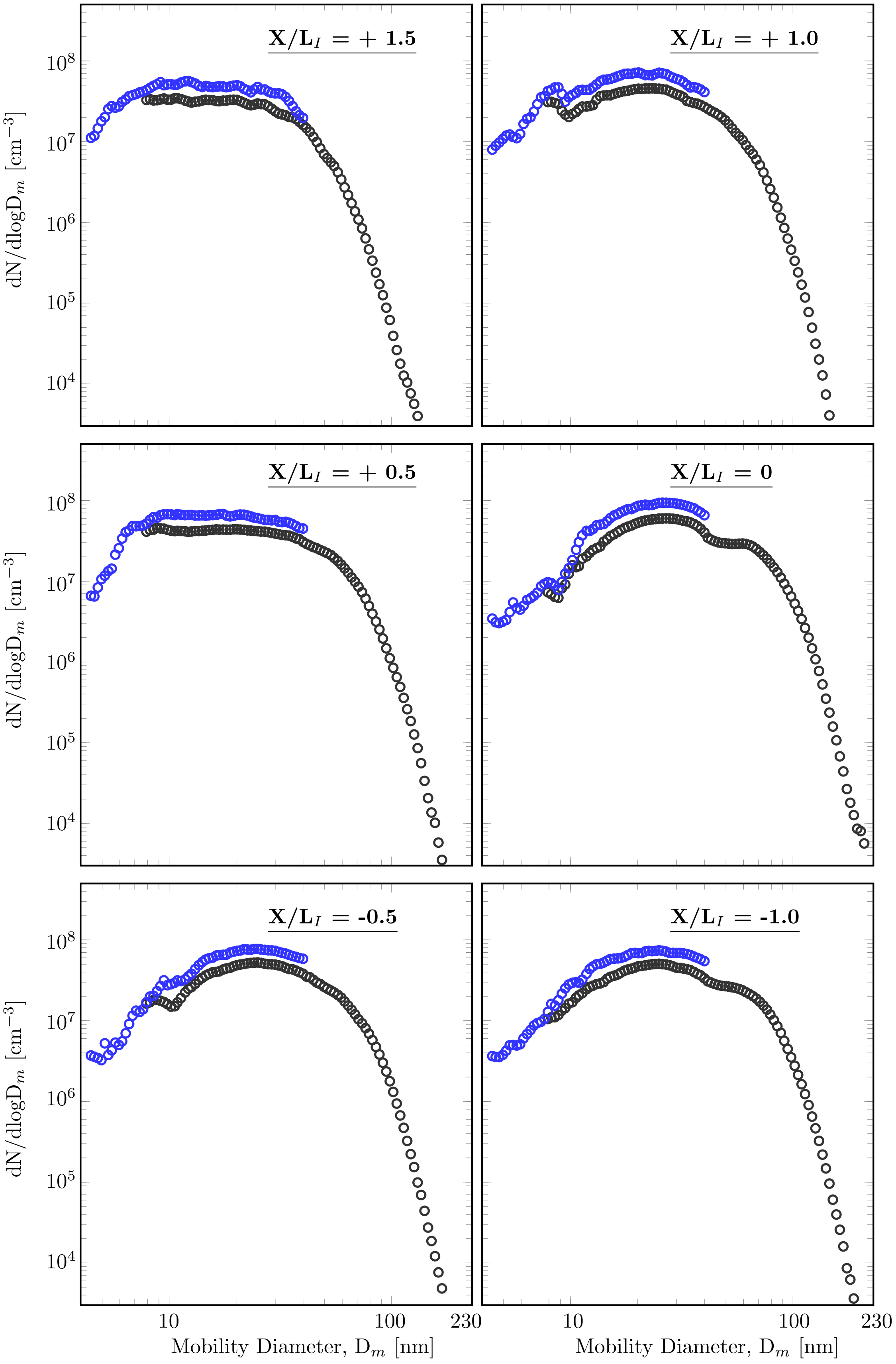

Figure 7.28. The PSD profiles for 1–nm SMPS (blue) and long DMA (black). The experiment is carried out at $\phi_{UN} = 2.0$, $a_T = 420$ s^{-1} and $T_{HCP} = 1500$ K. The nano DMA registers consistently higher concentrations for PSD profiles. Different transfer functions and diffusion losses within the DMAs explain the discrepancies between PSDs.

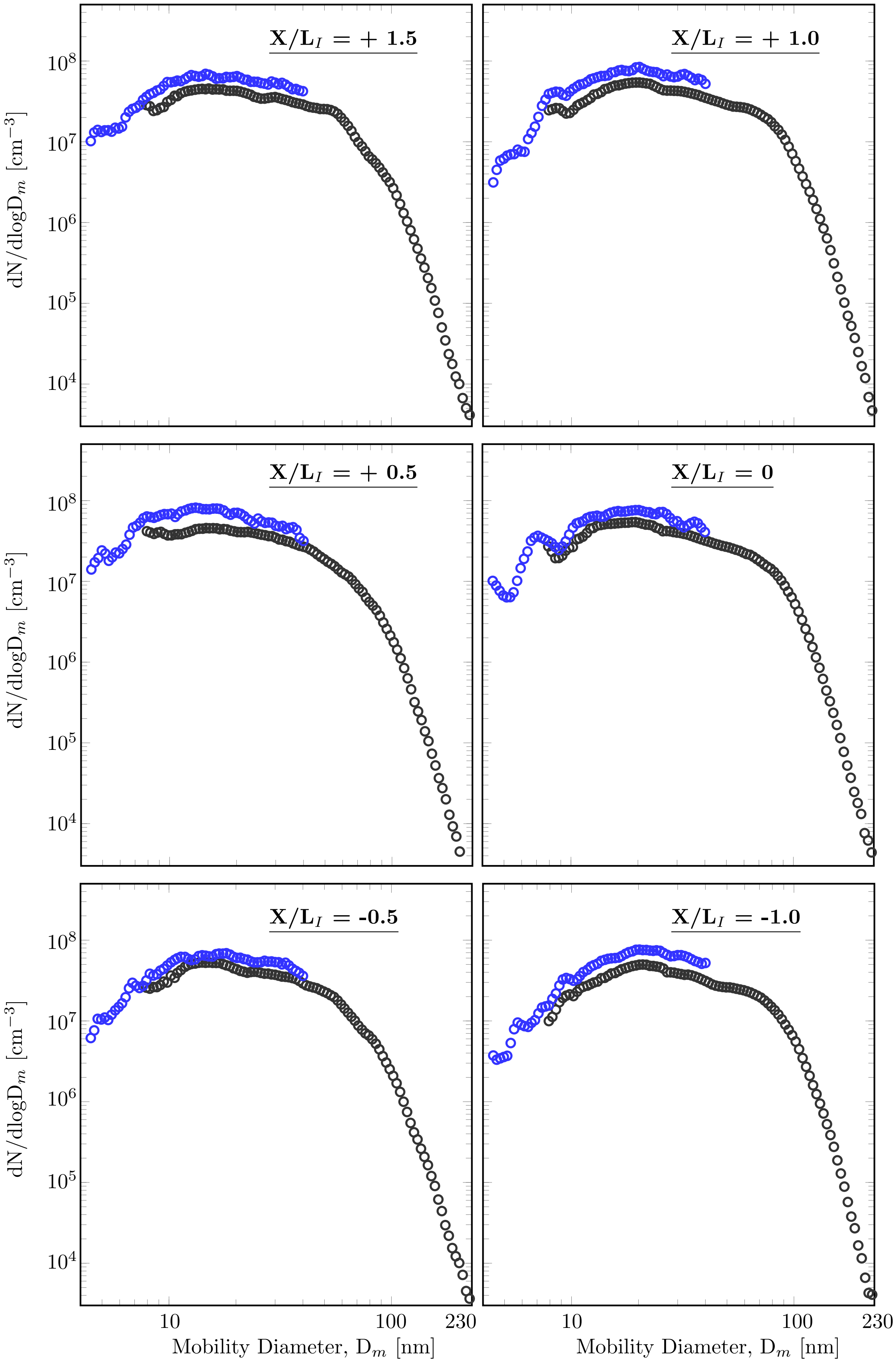

Figure 7.29. The PSD profiles for 1–nm SMPS (blue) and long DMA (black). The experiment is carried out at $\phi_{UN} = 2.2$, a$_T$ = 420 s^{-1} and T$_{HCP}$ = 1500 K. The nano DMA registers consistently higher concentrations for PSD profiles. Different transfer functions and diffusion losses within the DMAs explain the discrepancies between PSDs.

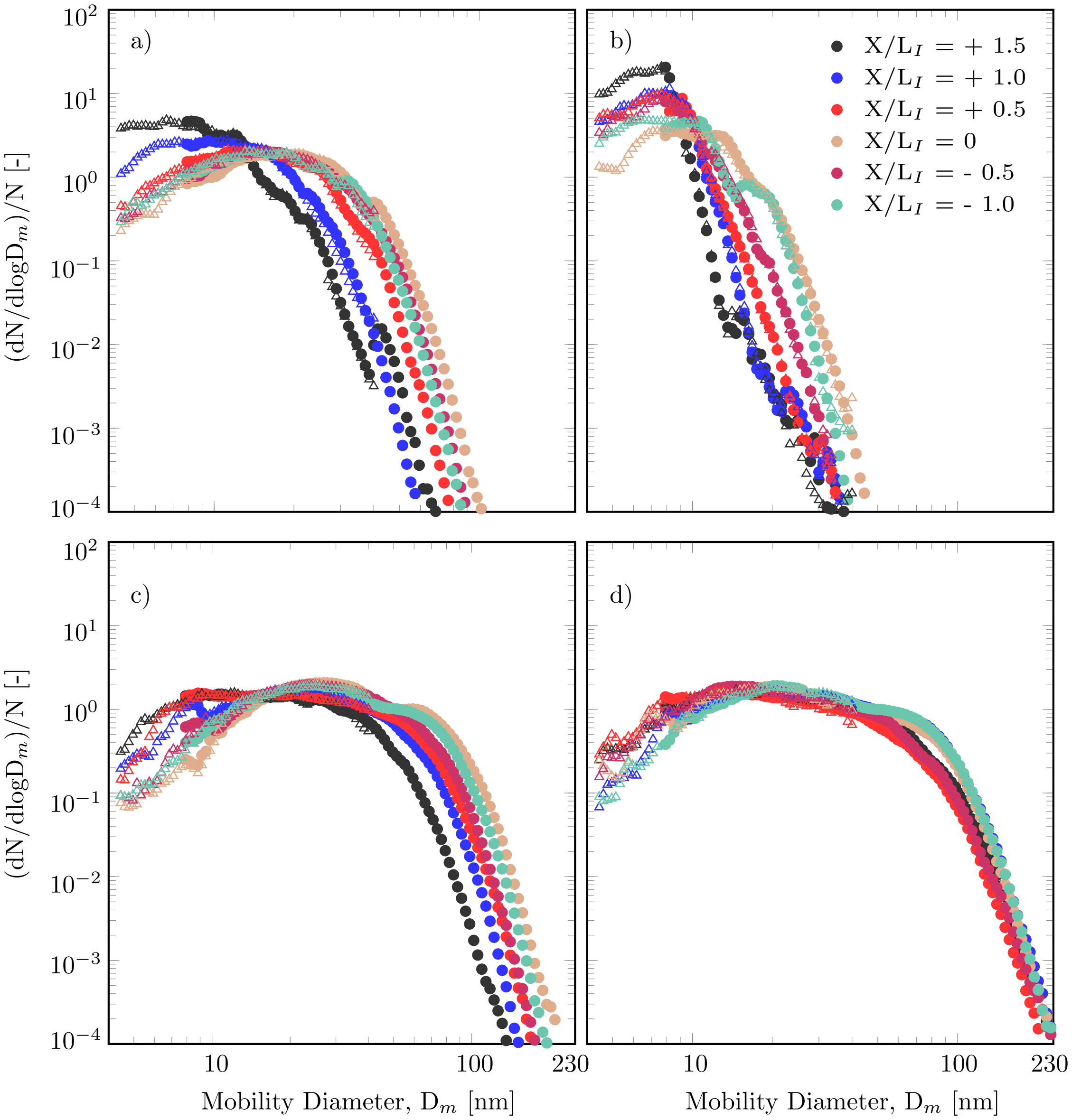

Figure 7.30. Spatial profile of particle size distribution for different flame conditions: a) $\phi_{UN} = 2.0$, $a_T = 610$ s^{-1} and $T_{HCP} = 1500$ K, b) $\phi_{UN} = 1.8$, $a_T = 420$ s^{-1} and $T_{HCP} = 1500$ K, c) $\phi_{UN} = 2.0$, $a_T = 420$ s^{-1} and $T_{HCP} = 1500$ K, d) $\phi_{UN} = 2.2$, $a_T = 420$ s^{-1} and $T_{HCP} = 1500$ K. The data are normalised with the total number density appearing over the common interval (8 – 40 nm) for 1–nm SMPS and long DMA setup. 1–nm SMPS system (4–40 nm) – triangle; long DMA (8–230 nm) – circle.

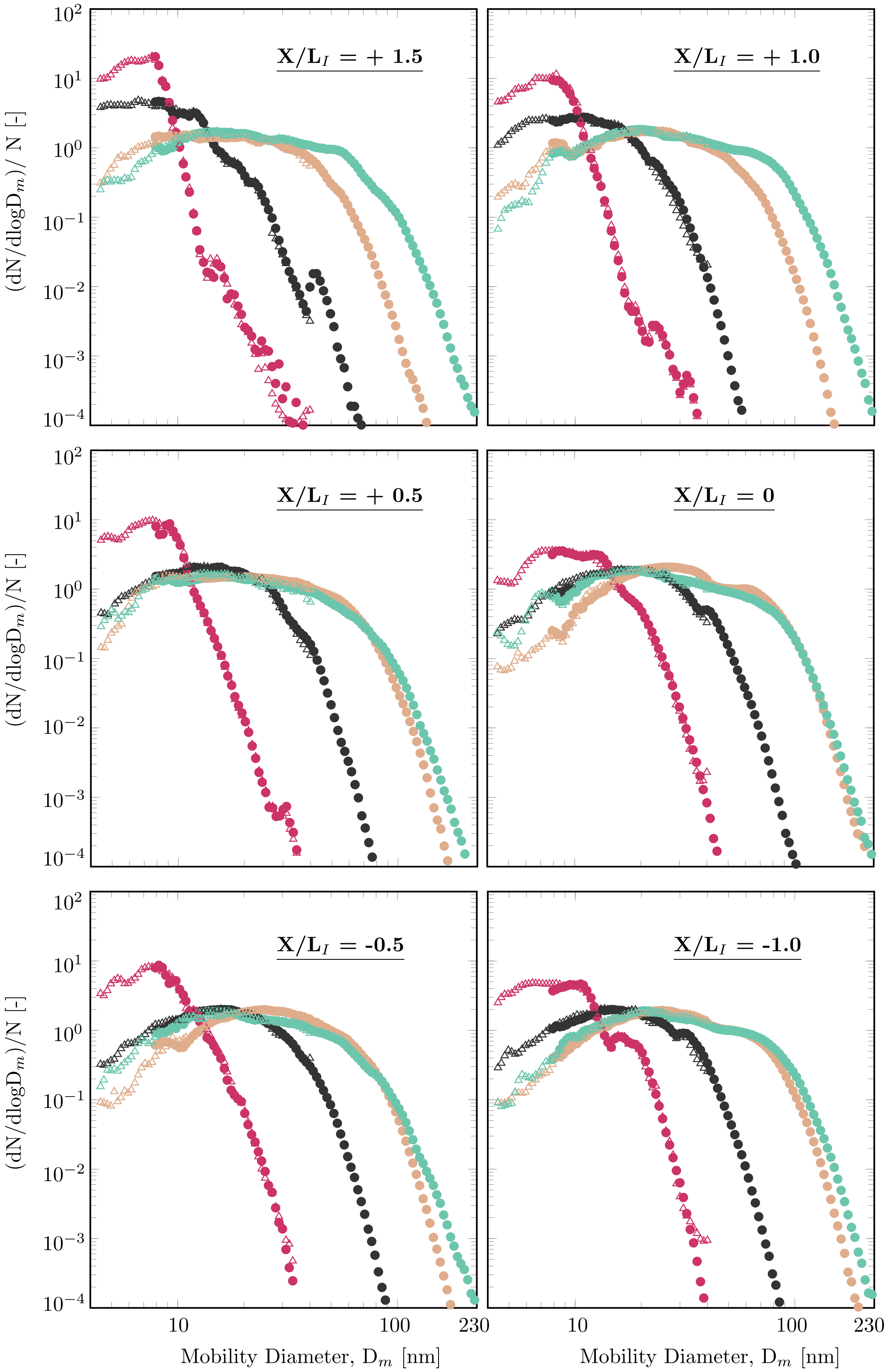

Figure 7.31. The PSDs of all data sets over the reaction zone layer. The data are normalised with the total number density appearing over the common interval (8 – 40 nm) for 1–nm SMPS and long DMA setups. Black: ϕ_{UN} = 2.0, a$_T$ = 610 s^{-1} and T$_{HCP}$ 1500 K; Purple: ϕ_{UN} = 1.8, a$_T$ = 420 s^{-1} and T$_{HCP}$ = 1500 K; Tan: ϕ_{UN} = 2.0, a$_T$ = 420 s^{-1} and T$_{HCP}$ = 1500 K; Sea green: ϕ_{UN} = 2.2, a$_T$ = 420 s^{-1} and T$_{HCP}$ = 1500 K. 1-nm SMPS system (4–40 nm): triangle; long DMA (8–230 nm): circle.

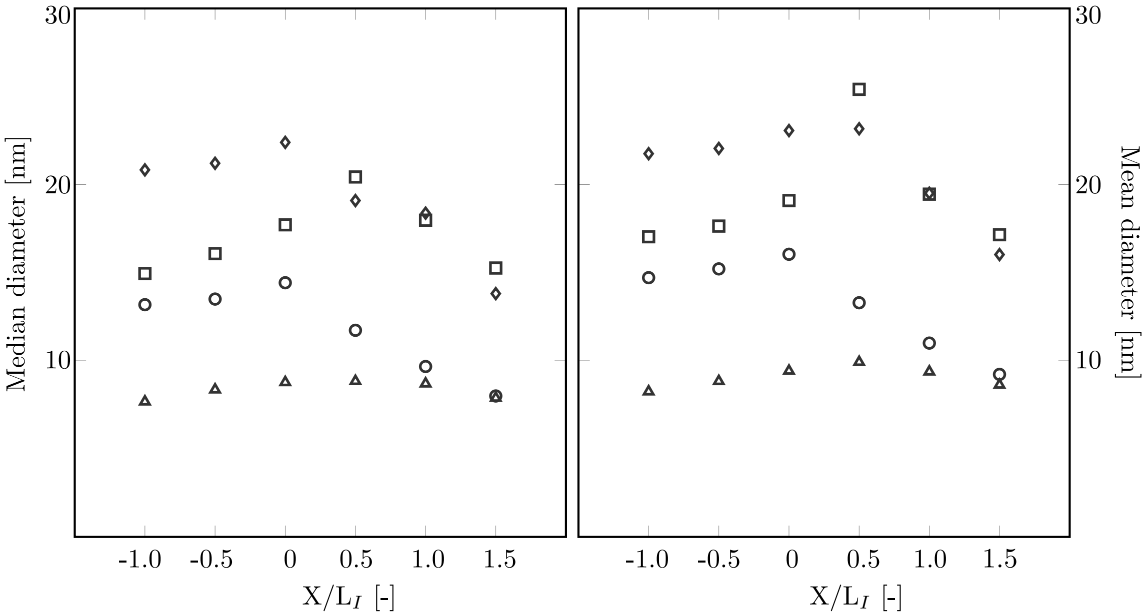

Figure 7.32. Median (left) and mean (right) mobility size diameters for various flame conditions. a$_T$ = 610 s^{-1} (circle); ϕ_{UN} = 1.8 (triangle); ϕ_{UN} = 2.0 (diamond); ϕ_{UN} = 2.2 (square). X/L$_I$ > 0 is towards reactants and X/L$_I$ < 0 towards the hot combustion products.

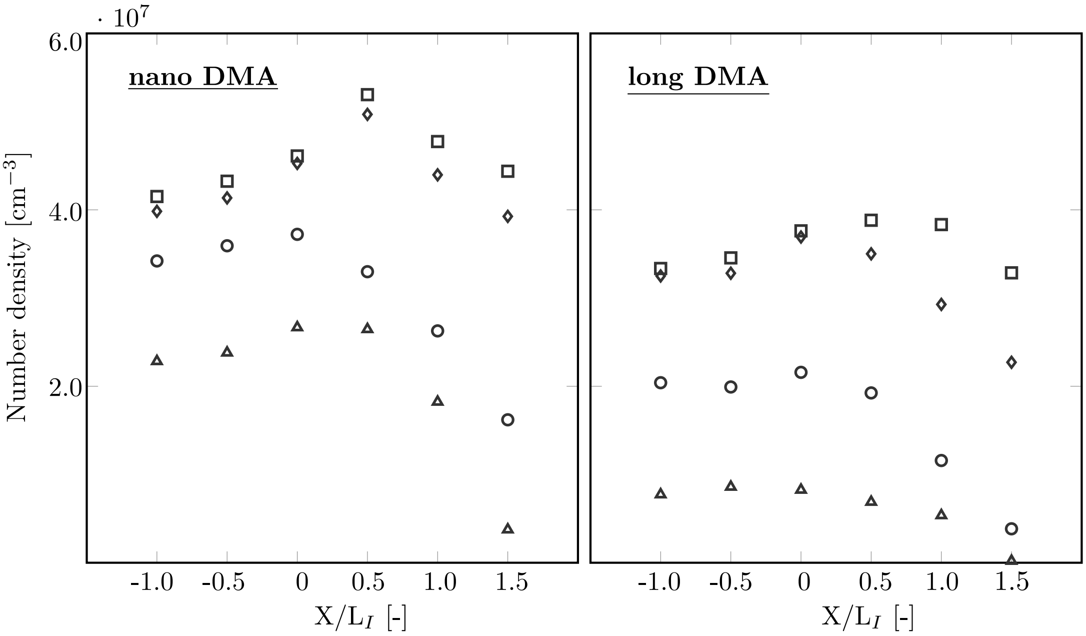

Figure 7.33. The total number densities over the reaction zone layer calculated separately for nano DMA: 4–40 nm (left) and long DMA: 8–230 nm (right). The nano DMA registers consistently higher particle concentrations for PSD profiles. The total number density is calculated based on the division of the summed bins by the resolution per decade [253]. a$_T$ = 610 s^{-1} (open circle); ϕ_{UN} = 1.8 (triangle); ϕ_{UN} = 2.0 (diamond); ϕ_{UN} = 2.2 (square). X/L$_I$ > 0 is towards reactants and X/L$_I$ < 0 towards the hot combustion products.

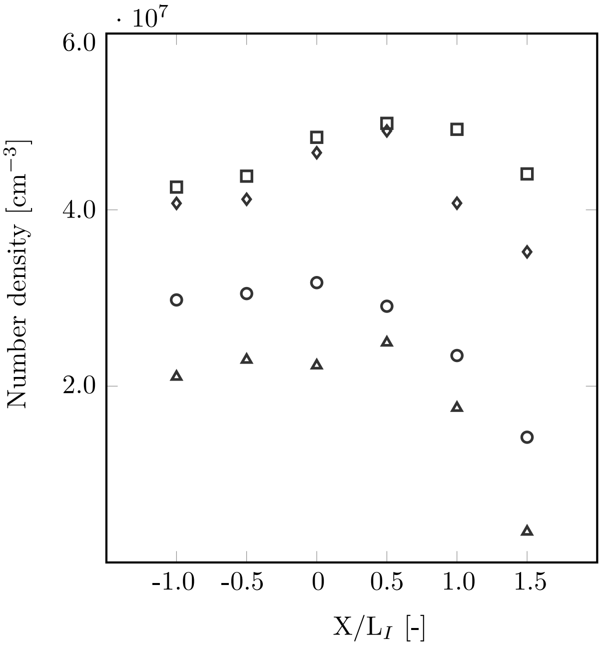

Figure 7.34. The total number densities over the reaction zone layer for different flame structures. The total number densities in the interval of $8 < D_p$ [nm] < 40 are calculated based on arithmetic averaging of the concentrations measured with nano and long DMA. $a_T = 610$ s^{-1} (open circle); $\phi_{UN} = 1.8$ (triangle); $\phi_{UN} = 2.0$ (diamond); $\phi_{UN} = 2.2$ (square). $X/L_I > 0$ is towards reactants and $X/L_I < 0$ towards the hot combustion products.

7.7 Uncertainty quantification

Carefully designed experiments are of a critical step in the characterisation of losses and uncertainties. The measured particle concentrations are no longer representative of the actual concentrations in the flame when uncertainty/error are not initially analysed. The errors can be categorised into sampling procedures and SMPS instrument functions.

Losses of soot particles between the point of the sampling and the SMPS instrument must be addressed to clarify the impact on PSDs. The most effective way to eliminate losses is to ensure sufficient and gradual dilution of the sample.

The probe effects can be minimised using appropriate sampling conditions and sampling process. For instance, the differential pressure of $\Delta P = 20$ mbar provides minimum impact on the PSDs. At higher differential pressures, the particles with mobility diameter of $D_p \leq 10$ nm are lost due to diffusion to sampling wall of extraction line. In addition,

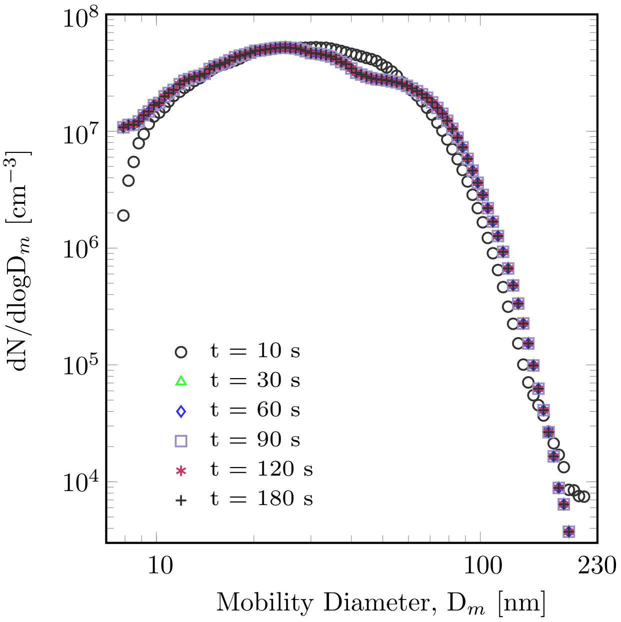

Figure 7.35. The impact of scan time on PSD ϕ_{UN} = 2.0 and a$_T$ = 420 s^{-1}. The probe tip is located at X/L$_I$ = - 1.0.

the pressure differential of 20 mbar support the minimum flame perturbation based on the laser diagnostic measurements. The probe clogging is continuously checked using the pressure transducer in the sampling system. As discussed, the probe clogging is a major problem for heavily sooting case (a$_T$ = 255 s^{-1}). This rate of strain is hence not included in the data set for SMPS experiments.

The SMPS takes time–averaged measurements, meaning that the time scale of the measurements is much greater than the time scale of turbulent fluctuations in the flame. Fig. 7.35 shows the particle distribution for different scan times. Multiple scan times are investigated, and no difference is found in the results for scan times of t > 10 s. In the current study, a scan time of 120 seconds is used. The sampling time (120 s) is consistent with PAH sampling experiments. The experimental process is repeated for different spatial locations as shown in Fig. 7.36. The results suggest high experimental repeatability.

The Aerosol Instrument Manager (AIM) supports a large number of hardware components, all fully integrated and controlled by the software. The software provides distinct features to correct the physical properties of the sample using data correction

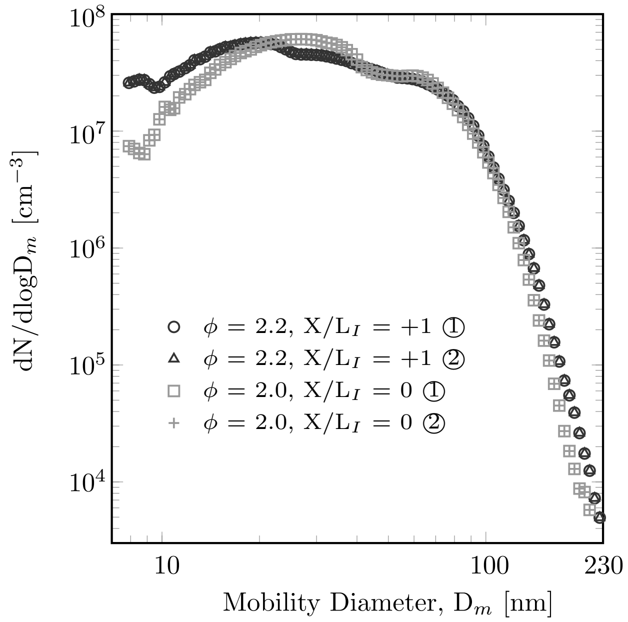

Figure 7.36. Experimental repeatability for various flame structures.

algorithms, including multiple charge and diffusion loss correction. The multiple charge correction is used to correct particles with more than one charges. The correction is mainly evident for particles with $D_p > 100$ nm. The losses in the transport path, i.e. the sampling tube upstream of the impactor, is corrected via using diffusion loss correction. This correction is of significance for particle diameters with $D_p < 100$ nm.

7.8 Conclusions

A SMPS system was used to quantify the impact of the rate of strain and equivalence ratio on the particle size distribution along the stagnation point streamline. The impact of the dilution ratio on the measured particle size distribution has been quantified. The sampling system used in the current study provides minimum sampling losses for both PAHs and particulates. The dual dilution ports used offer a significant improvement in the transport efficiencies. The determined proper balance between nitrogen flow and differential pressure reinforces minimum coagulation and turbulent diffusion losses during the extraction line.

Aggregation can happen in the sampling line and aggregation losses in the sampling line can be minimised using the optimum dilution ratios as shown. The turbulence can impact the aggregation in the flame and cause a spread particulates over spatial locations.

Bimodal PSD profiles are observed for some experimental cases including $\phi_{UN} = 2.0$ and 2.2 at the spatial location of X/L$_I$ = +1.0. The bimodality features two modes of persistent nuclei and primary soot particles separated by a trough. However, the impact of surface growth dominates as the majority of PSD profiles show unimodal shapes along the reaction zone layer. Therefore, in some cases a bimodal to unimodal shift in the PSDs between spatial locations is observed. Such a continuous transition in the particle size distribution indicates a balance between nucleation, surface growth, coagulation/aggregation and soot oxidation.

The particle number density, mean and median mobility diameter is substantially larger for heavily sooting flames than those of lightly sooting flames. The main reason is the higher aggregation load/growth for highly sooting conditions. The higher accumulation does not necessarily mean the higher particle concentration over the entire limit of PSDs. For instance, the aggregation was found higher for equivalence ratio of $\phi_{UN} =$ 2.2. However, particle concentration was lower over the particle diameter of $10 \leq D_p \leq$

100 nm as compared to reference flame for some spatial locations.

The data can significantly advance, in combination with the results from the laser-based diagnostics and GC-MS, the fundamental understanding of the particle formation and oxidation process in turbulent premixed sooting flames. The data are also of significance for the characterisation of probe designs, operational procedures and for the evaluation of experimental uncertainties in turbulent flames.

Chapter 8

Conclusions

The complexity of particulate formation in turbulent flames necessitates the use of a burner configuration featuring a well–defined boundary conditions and precise control of flow characteristics. A back–to–burnt opposed jet configuration is used to infer the impact of changes in stoichiometry ($1.7 \leq \phi_{UN} \leq 2.2$), burnt gas temperature ($1400 \leq$ T_{HCP} [K] ≤ 1700) and rates of strain ($255 \leq \mathrm{a}_T \leq 610$) on the formation of particulates in turbulent sooting ethylene–air flames. The conditions cover effectively non–sooting to highly sooting flames. A comprehensive experimental approach, featuring laser diagnostics and probe measurements, is utilised to address complex processes of soot formation/oxidation [30]. Laser diagnostic–based measurements, ELS and PAH–PLIF, were conducted to identify PAH and soot layers. A probe sampling technique was applied to quantify gaseous (GC–TCD) and PAH species (GC–MS) and particle size distribution (SMPS). The conclusions are listed for each Chapter accordingly.

Chapter 3 outlines the impact of measurement processes and uncertainties for both laser diagnostics and probe sampling. The optimal sampling conditions were developed to provide low–loss transmission lines and minimise uncertainty for measuring major gaseous, PAH species and soot particles.

- Sodium sulphate was included in the filter unit configuration to remove water vapour that can lead to significant uncertainties when measuring major gaseous species analysed using the GC–TCD.

- For the PAH sampling experiments, the system features dual–port dilution with preheated N_2 and PID controlled heated walls to minimise thermal gradients between the sample and probe walls.
- For soot particles, a parametric study on the effect of the dilution ratio on the observed particle size distribution indicates that particle losses in the sampling line can be effectively eliminated using a two–stage dilution process.
- Sample extraction definitely perturbs the flame. The probe perturbations were found higher at pressure differentials $\Delta P > 20$ mbar. The probe effect analysis shows that the mean PAH and ELS profile peak locations are not affected by the presence of the probe at a suction pressure of 20 mbar. This clearly shows that $\Delta P = 20$ mbar is a suitable pressure differential for the current probe configuration.

In Chapter 4, the impact of the turbulent flow field on the reaction zone was initially investigated by means of laser diagnostic techniques illustrating the turbulent mixing across the stagnation plane and significant reaction zone broadening.

- The laser and probe measurements show that the spatial location of $X/L_I = 0.5$ is a representative of the spatial location where the physical and chemical evolution plays a crucial role in the formation of particulates.
- The rate of strain exerts a more dominant impact on the growth of primary particle aggregates than on gaseous PAHs species. This further indicates that the chemical and physical processes leading to soot inception are comparatively slow.
- The growth of gaseous PAHs is significantly higher than that of primary particles when the equivalence ratio is increased.

- The PAH concentrations are comparatively insensitive to the lower nozzle HCP temperature, used to provide a stable flame environment.

The purpose of the work outlined in chapter 5 is to determine concentration profiles of major gaseous species under the influence of rate of strain and equivalence ratio.

- In the lightly sooting flames, the decreasing acetylene profiles parallels the decreasing profiles of PAH and are in line with the absence of detected soot [285].
- A reduction in the species formation is observed for the major hydrocarbon species including CH_4, C_2H_2, C_3H_6 and C_3H_8 as the flame shifts from the reference flame at $\phi_{UN} = 2.0$ to $\phi_{UN} = 1.80$.

In Chapter 6, the impacts of equivalence ratio and rate of strain on the spatial distribution of PAH species were quantified.

- The probe measurements show the main contributions of acetylene, m/z = 154, 1–methylnaphthalene (1–MN), m/z = 276 and benzo(a)pyrene (B(a)P) to particulate formation. For instance, B(a)P includes the main percentage of an incipient particle composition irrespective of the flame structure.
- The spatial location and flame conditions are determining factors for the competition between major species involved in the soot formation process.
- Soot samples were further processed using a centrifuge to show that soot particles are infused by significant quantifies of benzo(a)pyrene. For example, the amount of benzo(a)pyrene stored on particles is a factor of 5 and 12 higher than present in the gas phase for the reference (a_T = 420 s^{-1}) and heavily sooting flames (a_T = 255 s^{-1}), respectively.
- It is shown that the mean concentration profiles are the result of a tight balance between formation and consumption of a given species.

- The rate of strain exerts a substantial effect on the PAH concentrations and soot formation.

The particle size distribution measured using a scanning mobility particle sizer is discussed in Chapter 7.

- Soot PSDs are highly sensitive to competition among the various processes of soot formation, from nucleation to coagulation and gas–surface reactions, which in turn are strong functions of the rate of strain and equivalence ratio.
- The total number density shows two distinct behaviours from lightly to highly sooting flames. For instance, the number density suddenly decreases towards the reactants at $X/L_I = +\ 1.0$ and $+\ 1.5$ for lightly sooting conditions ($a_T = 610$ s^{-1} and $\phi_{UN} = 1.8$).
- The median and mean mobility diameters are found maximum at (close to) the stagnation point for the current flame conditions.

The current work has illustrated the need for a more comprehensive analysis for combustion processes with low Damköhler and high turbulent Reynolds number. The data is expected to advance the fundamental understanding of the particle formation and oxidation process in turbulent premixed sooting flames and further support the development and validation of experimental measurements and numerical models.

Chapter 9

Future work

A combination of experimental techniques, laser diagnostics and probe measurements, has been used to present a comprehensive description of the soot formation/oxidation process in the turbulent flame. However, there are significant deficiencies in the understanding of particle formation and evolution in turbulent flames. Some suggestions for future works are as follows:

- Addressing outstanding questions in soot chemistry will require measurements of particle characteristics, such as composition, size, fine structure, morphology, abundance, and distribution, as they evolve during combustion. Definitive conclusions on the soot formation process require numerous data analyses on different experimental configurations using various diagnostics.

- The current experimental results present glimpses on the soot nucleation and soot inception. It should be noted that the abundance includes PAH concentrations in the gas phase as well as those attached to soot particles, while the main focus of prior studies has been on PAHs in the gas phase. The presence of two peak sequences (14 and 24 m/z) among the species shown in the mass spectra supports the formation of five-member rings and their important roles in soot nucleation.

The probe measurements indicate that acetylene, 1-methylnaphthalene (1-MN), m/z = 154, m/z = 276 and benzo(a)pyrene correlate with soot formation. However, there are still gaps in the understanding of soot inception process in both laminar and turbulent flames. For instance, Johansson et al. [48] suggests that resonance-stabilised radicals (RSRs) can drive inception via chain reactions. On the other hand, the impact of PAH dimers are seen to be of significance as presented by Mercier et al. [42]. Turbulent flame calculations should be performed to provide comparisons of calculations and experiments.

- The investigation of turbulence–chemistry interactions in turbulent flames is of relevance to a large number of practical applications in the aviation and automotive industries. The study of turbulence-chemistry interactions presents a formidable challenge that promotes the use of oppose jet configurations to advance fundamental understanding. Ethylene is here used as the fuel and presents the basis for in-depth future studies of soot formation using practical fuels. Liquid fuels, e.g. n-heptane and toluene, should be included based on their significantly different chemical properties. The results will demonstrate the relative impact of fuel chemistry on the species growth mechanism, soot nucleation and particle size distributions.

- A standardised operational procedures have been developed and implemented to minimise sample losses through the collection, extraction, preparation and analyses processes for the measurements of major gaseous, PAH and soot particles. As shown, transport efficiency is a critical factor in providing true concentrations of PAHs and particulates. For instance, two dilution stage is recommended for particulate sampling at ambient temperature. However, hot nitrogen dilution at the same temperature of heated transfer line (T = 523 K) is suggested for PAH sampling process. Modeling can be performed to identify the impact of sampling line conditions on species or particle losses in the extraction line, and compare the relative PAH concentrations and absolute soot PSDs with the current turbulent flame conditions.

- As shown by laser images, combustion regimes include multiple fluid states containing PAH and soot zone layers. A multi-fluid approach, established by Hampp et al. [94], should be used to permit the identification of various intermediate fluid states. To this end, simultaneous LIF, LII and ELS techniques can be used to provide crucial insights on the nature and evolution of combustion formed particles. The combination of ELS and LII can provide inference of changes in average particle size. The distinction of nano–structure, gaseous species and heavy particles can also be possible using both PAH–PLIF and LII.

- The Select-PAH column is used to enhance selectivity towards PAHs, the separation of the isomers and the accurate analyses of PAHs. Different type of GC columns are recommended to be used to measure the concentrations of hydrocarbons with distinct functional groups (C_7–C_{24}). On the other hand, a simultaneous FID and TCD setup should be used to detect further gaseous species including CO, CO_2, O_2, O_2 and hydrocarbons from C_1 to C_6. A comprehensive list of species concentration can provide valuable data on soot formation processes.

- The current study does not include measurements of flame temperature and flow field velocities. A thermocouple cannot give a robust measurements because particles deposition onto probe leads to a high level of uncertainty. The non–intrusive techniques such as Coherent anti–Stokes Raman spectroscopy (CARS) is suggested to be used to measure the temperature profile of sooting flames. Velocity measurement is another interesting topic in the sooting flame. The main problem is the interference of seeding (e.g. Al_2O_3) with particles to measure velocity over the reaction zone layer. However, a precise PIV measurement can present valuable data for the analyses of soot formation.

- Atomic force microscopy (AFM) or transmission electron microscopy (TEM) is suggested to be utilised to determine soot structures.

- The influence of the HCP on the flames is limited to soot oxidation at the stagnation plane and heat transfer between the flame and the HCP stream. For this study, the temperature of burnt gas state is chosen in the range of 1400 – 1700 K. The temperature impact on PAH–PLIF signals and PAH species (probe sampling) are modest for T_{LN} = 1400 – 1600 K. Future experiments should cover a broader range of burnt gas temperature from 1200 – 1800 K, including both laser diagnostics and probe measurements, to include a larger data set for PAH and particle size distribution. The impact of burnt gas temperature on the bimodal or unimodal shape of PSD is of significance in turbulent flames.

- The scanning mobility particle sizer (SMPS) is suggested to pair with a centrifugal particle mass analyzer (CPMA) or aerosol particle mass analyser on a separate line to simultaneously measure particle mass and mobility diameter.

- A direct comparison of in-situ and probe sampling is challenging. On the one hand, laser diagnostics cannot precisely quantify the infusion level of resonance–stabilised radicals on soot particles in the flame. The quantification of PAH species using LIF is a challenging task as PAHs species contain a mixture of distinct functional groups with broad spectra. The spectra of such species can overlap with each other. On the other hand, GC–MS can present the mass spectrum of species up to m/z = 300 amu. The uncertainty in each technique has been minimised in the current work. However, further work using alternative laser diagnostics (e.g. LII) would be helpful.

Appendix

I.1 Soot inception

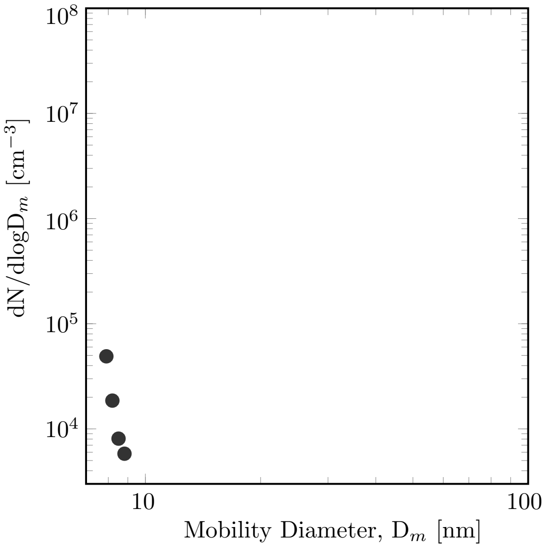

Figure I.1. The PSD profile of soot inception for equivalence ratio of $\phi_{UN} = 1.7$ at spatial location of X/L$_I$ = 0.5. The experiment is conducted at a constant burnt gas temperature of T$_{HCP}$ = 1500 K and a total rate of strain of a$_T$ = 420 s^{-1}.

I.2 Flame photograph

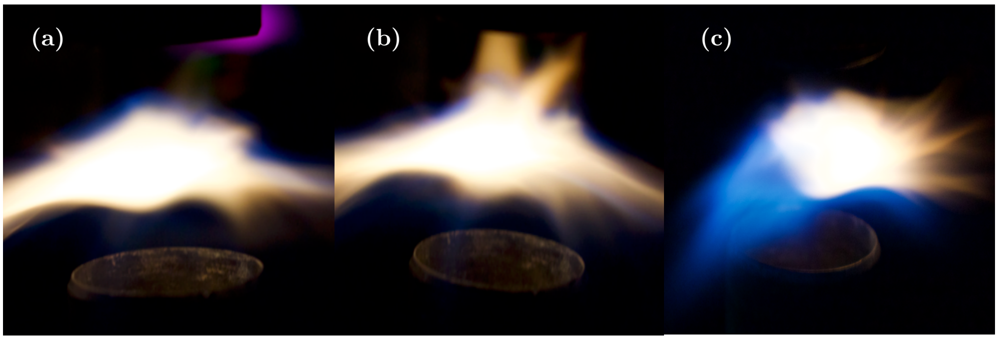

Figure I.2. Sample photographs for further study. Left column : ϕ_{UN}= 2.0, a$_T$= 420 s^{-1} and T$_{HCP}$= 1400 K; Middle column : ϕ_{UN}= 2.5, a$_T$= 420 s^{-1} and T$_{HCP}$= 1500 K; Right column : .ϕ_{UN}= 3.0, a$_T$= 492 s^{-1} and T$_{HCP}$= 1500 K.

I.3 Dilution box

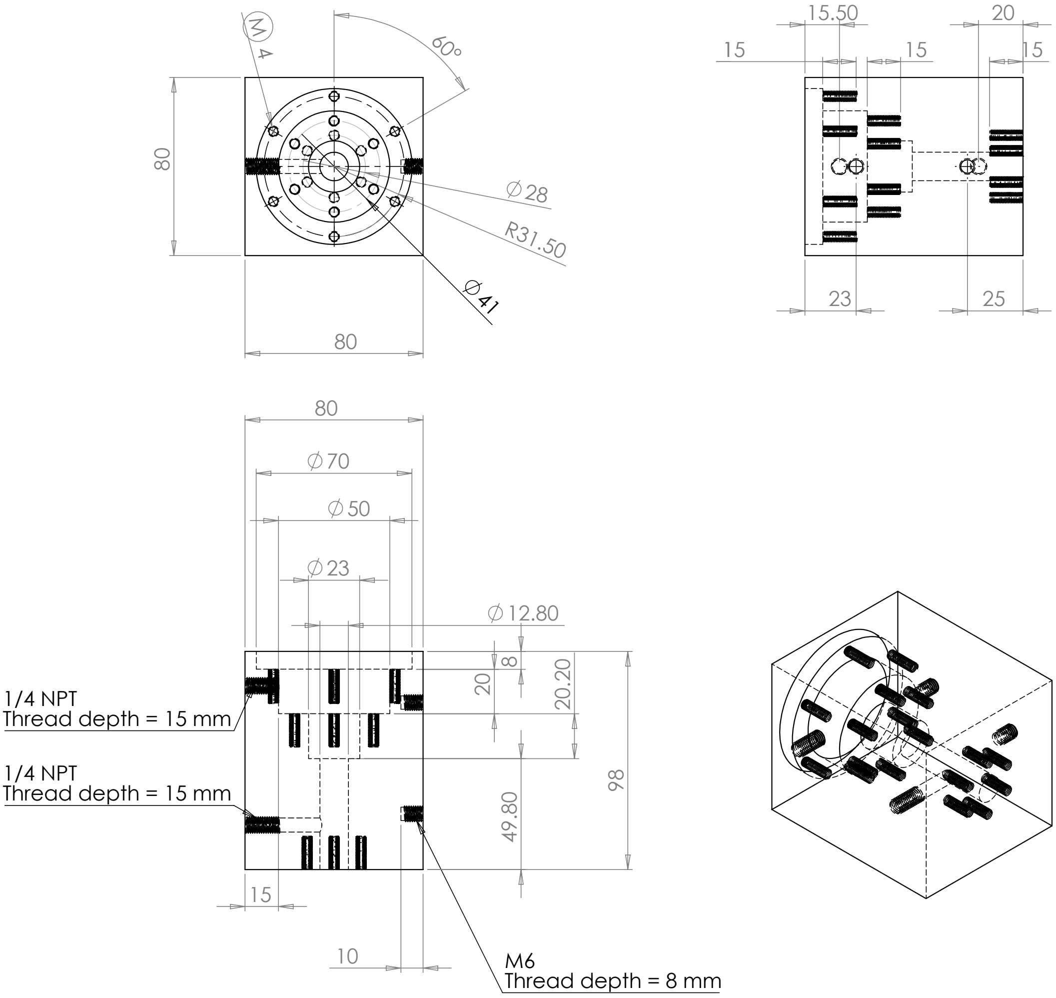

Figure I.3. The sketch of dilution box used to provide the optimum DR, minimising PAH and particle losses within the transfer line. The nitrogen flows from the dilution box into the sampling system to remove residue between experimental sets.

I.4 Desktop console–PID controller

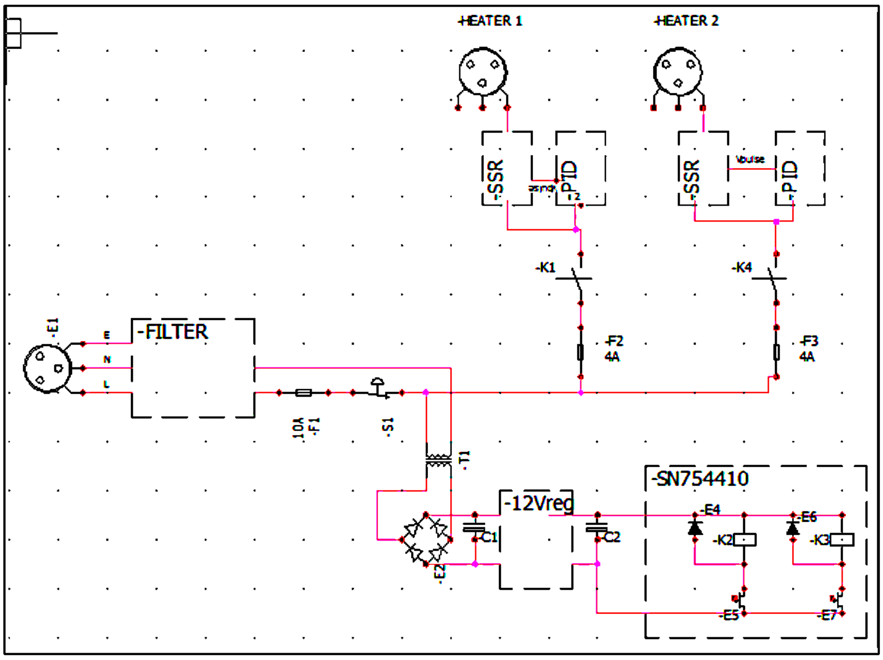

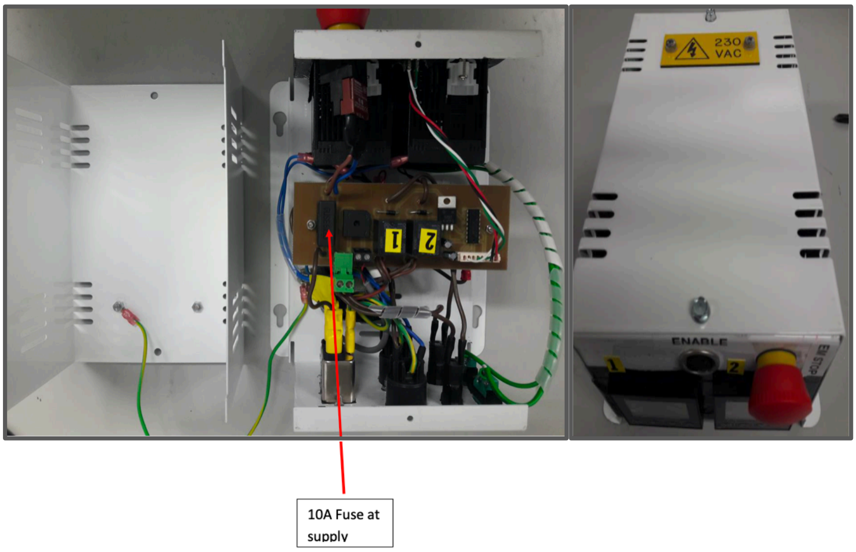

Figure I.4. The PID controller used in PAH sampling experiments to maintain the sampling line temperature constant and provide the hot nitrogen dilution. The PID provides a minimum temperature gradient during extraction line.

I.5 Major gaseous species data

Table I.1. The mole fraction of major gaseous species at different spatial locations for equivalence ratio of $1.8 \leq \phi_{UN} \leq 2.2$ at a constant rate of strain of $a_T = 420$ s^{-1}, and rate of strain of $255 \leq a_T$ [s^{-1}] ≤ 610 at a constant stoichiometry of $\phi_{UN} = 2.0$.

1	O_2 [-] $\times 10^{-1}$				
X/L$_I$	$\phi_{UN} = 1.8$	$\phi_{UN} = 2.0$	$\phi_{UN} = 2.2$	$a_T = 255$ s^{-1}	$a_T = 610$ s^{-1}
-2.5	0.157	0.157	0.157	0.157	0.157
-2	0.157	0.157	0.157	0.157	0.157
-1.5	0.157	0.157	0.157	0.157	0.157
-1	0.157	0.157	0.157	0.157	0.157
-0.5	0.075	0.157	0.075	0.122	0.087
0	0	0	0	0	0
+0.5	0.450	0.181	0.139	0.126	0.536
+1	0.953	0.674	0.486	0.412	1.237
+1.5	1.484	1.104	1.010	0.833	1.525
+2	1.704	1.398	1.318	1.225	1.845
+2.5	1.894	1.890	1.894	1.903	1.892

2	CO [-] $\times 10^{-1}$				
X/L$_I$	$\phi_{UN} = 1.8$	$\phi_{UN} = 2.0$	$\phi_{UN} = 2.2$	$a_T = 255$ s^{-1}	$a_T = 610$ s^{-1}
-2.5	0.031	0.013	0.024	0.009	0.008
-2	0.099	0.146	0.096	0.017	0.021
-1.5	0.109	0.207	0.221	0.222	0.007
-1	0.260	0.338	0.510	0.712	0.147
-0.5	0.453	0.540	0.775	0.943	0.349
0	0.806	0.852	0.935	1.218	0.531
+0.5	0.752	1.058	1.228	1.526	0.651
+1	0.491	0.762	1.001	1.461	0.381
+1.5	0.344	0.493	0.602	0.512	0.223
+2	0.163	0.208	0.214	0.274	0.100
+2.5	0.067	0.072	0.088	0.142	0.032

Table I.1. The mole fraction of major gaseous species at different spatial locations for the equivalence ratio of $1.8 \leq \phi_{UN} \leq 2.2$ at a constant rate of strain of $a_T = 420$ s^{-1}, and rate of strain of $255 \leq a_T$ [s^{-1}] ≤ 610 at a constant stoichiometry of $\phi_{UN} = 2.0$.

<u>**3**</u>	CO_2 [-] $\times 10^{-2}$				
X/L_I	$\phi_{UN} = 1.8$	$\phi_{UN} = 2.0$	$\phi_{UN} = 2.2$	$a_T = 255$ s^{-1}	$a_T = 610$ s^{-1}
-2.5	0.321	0.442	0.283	0.351	0.361
-2	0.763	1.045	0.563	1.505	0.451
-1.5	1.443	1.322	0.841	2.301	0.667
-1	2.243	2.091	1.764	2.567	1.119
-0.5	2.891	2.421	2.218	3.009	1.600
0	3.042	2.561	2.205	3.186	1.699
+0.5	2.358	2.054	1.821	2.655	1.546
+1	1.922	1.733	1.166	1.746	1.013
+1.5	1.096	1.062	0.801	1.092	0.615
+2	0.438	0.457	0.403	0.7416	0.347
+2.5	0.275	0.223	0.268	0.212	0.254

<u>**4**</u>	CH_4 [-] $\times 10^{-3}$				
X/L_I	$\phi_{UN} = 1.8$	$\phi_{UN} = 2.0$	$\phi_{UN} = 2.2$	$a_T = 255$ s^{-1}	$a_T = 610$ s^{-1}
-2.5	0.025	0.125	0.093	0.125	0.020
-2	0.049	0.187	0.464	0.462	0.061
-1.5	0.099	0.337	0.663	1.388	0.141
-1	0.312	0.875	1.227	3.100	0.465
-0.5	0.558	1.153	3.451	4.627	0.617
0	0.933	1.942	4.314	5.321	1.204
+0.5	1.116	3.038	4.861	6.941	1.326
+1	0.632	1.951	2.638	5.530	0.637
+1.5	0.372	1.637	2.124	3.239	0.273
+2	0.272	0.738	0.978	1.596	0.223
+2.5	0.223	0.375	0.581	0.786	0.182

Table I.1. The mole fraction of major gaseous species at different spatial locations for the equivalence ratio of $1.8 \leq \phi_{UN} \leq 2.2$ at a constant rate of strain of $a_T = 420$ s^{-1}, and rate of strain of $255 \leq a_T$ [s^{-1}] ≤ 610 at a constant stoichiometry of $\phi_{UN} = 2.0$.

<u>5</u>	C_2H_2 [-] $\times 10^{-2}$				
X/L$_I$	$\phi_{UN} = 1.8$	$\phi_{UN} = 2.0$	$\phi_{UN} = 2.2$	$a_T = 255$ s^{-1}	$a_T = 610$ s^{-1}
-2.5	0.006	0.001	0.071	0.024	0.001
-2	0.033	0.078	0.147	0.185	0.007
-1.5	0.084	0.353	0.168	0.271	0.061
-1	0.221	0.475	0.700	1.214	0.110
-0.5	0.353	0.917	1.998	2.462	0.348
0	0.413	1.111	2.291	2.880	0.449
+0.5	0.532	1.020	2.480	3.335	0.629
+1	0.316	0.873	1.446	2.707	0.311
+1.5	0.156	0.409	0.619	0.624	0.186
+2	0.081	0.258	0.311	0.312	0.076
+2.5	0.048	0.104	0.149	0.122	0.057

<u>6</u>	C_2H_4 [-] $\times 10^{-1}$				
X/L$_I$	$\phi_{UN} = 1.8$	$\phi_{UN} = 2.0$	$\phi_{UN} = 2.2$	$a_T = 255$ s^{-1}	$a_T = 610$ s^{-1}
-2.5	0.014	0.001	0.001	0.038	0.012
-2	0.014	0.004	0.006	0.027	0.017
-1.5	0.017	0.013	0.005	0.035	0.019
-1	0.045	0.039	0.005	0.054	0.037
-0.5	0.038	0.052	0.158	0.162	0.045
0	0.045	0.102	0.182	0.169	0.113
+0.5	0.083	0.229	0.563	0.763	0.120
+1	0.063	0.543	0.728	0.809	0.275
+1.5	0.337	1.058	1.127	1.181	0.649
+2	0.838	1.166	1.376	1.254	0.877
+2.5	0.993	1.231	1.361	1.256	1.174

Table I.1. The mole fraction of major gaseous species at different spatial locations for the equivalence ratio of $1.8 \leq \phi_{UN} \leq 2.2$ at a constant rate of strain of $a_T = 420$ s^{-1}, and rate of strain of $255 \leq a_T$ [s^{-1}] ≤ 610 at a constant stoichiometry of $\phi_{UN} = 2.0$.

<u>7</u>	C_3H_6 [-] $\times 10^{-4}$				
X/L$_I$	$\phi_{UN} = 1.8$	$\phi_{UN} = 2.0$	$\phi_{UN} = 2.2$	$a_T = 255$ s^{-1}	$a_T = 610$ s^{-1}
-2.5	0.018	0.022	0.14432	0.088	0.018
-2	0.044	0.055	0.1804	0.112	0.044
-1.5	0.088	0.110	0.361	0.227	0.088
-1	0.088	0.275	0.7216	1.762	0.088
-0.5	0.088	1.107	3.608	5.506	0.176
0	0.44	2.2	5.412	6.621	0.884
+0.5	0.224	1.925	4.690	5.524	0.556
+1	0.113	1.375	2.886	3.324	0.116
+1.5	0.066	0.825	1.443	1.324	0.066
+2	0.044	0.551	0.721	0.660	0.044
+2.5	0.022	0.275	0.361	0.223	0.022

<u>8</u>	C_3H_8 [-] $\times 10^{-4}$				
X/L$_I$	$\phi_{UN} = 1.8$	$\phi_{UN} = 2.0$	$\phi_{UN} = 2.2$	$a_T = 255$ s^{-1}	$a_T = 610$ s^{-1}
-2.5	0.072	0.132	0.194	0.161	0.072
-2	0.072	0.147	0.193	0.164	0.072
-1.5	0.091	0.125	0.285	0.406	0.091
-1	0.093	0.251	0.572	0.641	0.095
-0.5	0.092	0.437	0.954	1.287	0.176
0	0.252	0.750	1.934	2.402	0.345
+0.5	0.207	0.687	1.805	2.081	0.306
+1	0.092	0.437	1.143	1.444	0.172
+1.5	0.081	0.312	0.760	0.643	0.153
+2	0.063	0.252	0.384	0.326	0.119
+2.5	0.036	0.154	0.152	0.128	0.068

I.6 PAH species data

Table I.2. The mole fractions of PAH species at different spatial locations for the equivalence ratio of $1.8 \leq \phi_{UN} \leq 2.2$ at a constant rate of strain of $a_T = 420$ s^{-1}, and rate of strain of $255 \leq a_T$ [s^{-1}] ≤ 610 at a constant stoichiometry of $\phi_{UN} = 2.0$.

1	A2 [-] $\times10^{-4}$				
X/L$_I$	$\phi_{UN} = 1.8$	$\phi_{UN} = 2.0$	$\phi_{UN} = 2.2$	$a_T = 255$ s^{-1}	$a_T = 610$ s^{-1}
-1	1.114	1.332	1.754	2.588	0.894
-0.5	1.132	1.591	1.963	4.710	1.155
0	2.217	2.835	3.232	6.823	2.243
+0.5	3.143	4.866	6.900	12.490	3.850
+1	2.015	2.636	3.174	10.953	2.117
+1.5	0.585	1.229	1.534	4.982	0.817

2	m/z = 130 [-] $\times10^{-4}$				
X/L$_I$	$\phi_{UN} = 1.8$	$\phi_{UN} = 2.0$	$\phi_{UN} = 2.2$	$a_T = 255$ s^{-1}	$a_T = 610$ s^{-1}
-1	0.950	1.559	2.275	4.845	0.638
-0.5	1.411	2.374	2.724	7.635	1.816
0	2.478	2.897	3.389	17.027	2.354
+0.5	3.421	5.387	7.281	17.398	2.825
+1	2.688	3.381	3.669	15.541	2.356
+1.5	0.908	1.938	2.631	8.537	0.737

3	m/z = 132 [-] $\times10^{-3}$				
X/L$_I$	$\phi_{UN} = 1.8$	$\phi_{UN} = 2.0$	$\phi_{UN} = 2.2$	$a_T = 255$ s^{-1}	$a_T = 610$ s^{-1}
-1	0.205	0.285	0.354	1.888	0.212
-0.5	0.307	0.389	0.449	2.192	0.267
0	0.414	0.544	0.664	2.643	0.314
+0.5	0.919	1.127	1.265	3.987	0.498
+1	0.382	0.563	0.757	3.524	0.341
+1.5	0.258	0.350	0.505	1.842	0.202

4	2–MN [-] $\times10^{-4}$				
X/L$_I$	$\phi_{UN} = 1.8$	$\phi_{UN} = 2.0$	$\phi_{UN} = 2.2$	$a_T = 255$ s^{-1}	$a_T = 610$ s^{-1}
-1	0.110	0.103	0.132	0.693	0.087
-0.5	0.158	0.208	0.235	1.003	0.148
0	0.205	0.272	0.364	1.691	0.246
+0.5	0.339	0.488	1.001	2.393	0.312
+1	0.189	0.280	0.501	2.163	0.179
+1.5	0.101	0.172	0.307	0.986	0.127

Table I.2. The mole fractions of PAH species at different spatial locations for the equivalence ratio of $1.8 \leq \phi_{UN} \leq 2.2$ at a constant rate of strain of $a_T = 420$ s^{-1}, and rate of strain of $255 \leq a_T$ [s^{-1}] ≤ 610 at a constant stoichiometry of $\phi_{UN} = 2.0$.

5	1–MN [-] $\times10^{-4}$				
X/L$_I$	$\phi_{UN} = 1.8$	$\phi_{UN} = 2.0$	$\phi_{UN} = 2.2$	$a_T = 255$ s^{-1}	$a_T = 610$ s^{-1}
-1	2.058	2.458	3.133	14.770	1.375
-0.5	2.916	3.316	5.639	19.193	2.071
0	3.224	4.524	8.472	22.546	2.967
+0.5	5.639	7.184	8.587	22.5467	3.780
+1	2.613	3.399	7.208	19.193	2.038
+1.5	1.557	2.151	4.117	14.770	1.741

6	1–MN isomer [-] $\times10^{-4}$				
X/L$_I$	$\phi_{UN} = 1.8$	$\phi_{UN} = 2.0$	$\phi_{UN} = 2.2$	$a_T = 255$ s^{-1}	$a_T = 610$ s^{-1}
-1	0.314	0.445	0.560	2.310	0.278
-0.5	0.382	0.707	1.278	4.493	0.479
0	0.742	1.532	2.675	7.380	1.110
+0.5	1.821	3.256	5.693	8.679	1.624
+1	0.672	1.463	2.488	7.799	1.013
+1.5	0.201	0.771	1.385	4.179	0.419

7	m/z = 146 [-] $\times10^{-3}$				
X/L$_I$	$\phi_{UN} = 1.8$	$\phi_{UN} = 2.0$	$\phi_{UN} = 2.2$	$a_T = 255$ s^{-1}	$a_T = 610$ s^{-1}
-1	0.255	0.308	0.424	1.435	0.276
-0.5	0.308	0.463	0.646	1.664	0.336
0	0.483	0.594	0.935	2.493	0.534
+0.5	0.866	1.372	2.046	3.397	0.712
+1	0.337	0.563	0.995	3.065	0.432
+1.5	0.193	0.369	0.709	1.666	0.279

8	m/z = 148 [-] $\times10^{-4}$				
X/L$_I$	$\phi_{UN} = 1.8$	$\phi_{UN} = 2.0$	$\phi_{UN} = 2.2$	$a_T = 255$ s^{-1}	$a_T = 610$ s^{-1}
-1	0.477	0.850	1.436	4.502	0.675
-0.5	0.899	1.496	2.044	6.603	1.215
0	1.451	2.392	3.025	11.222	1.804
+0.5	2.756	4.542	8.181	15.072	2.334
+1	1.157	2.092	3.203	12.566	1.474
+1.5	0.636	1.295	2.641	6.673	1.095

Table I.2. The mole fractions of PAH species at different spatial locations for the equivalence ratio of $1.8 \leq \phi_{UN} \leq 2.2$ at a constant rate of strain of $a_T = 420$ s^{-1}, and rate of strain of $255 \leq a_T$ [s$^{=1}$] ≤ 610 at a constant stoichiometry of $\phi_{UN} = 2.0$.

9	m/z = 154 [-] $\times 10^{-3}$				
X/L$_I$	$\phi_{UN} = 1.8$	$\phi_{UN} = 2.0$	$\phi_{UN} = 2.2$	$a_T = 255$ s^{-1}	$a_T = 610$ s^{-1}
-1	0.246	0.434	0.678	2.932	0.241
-0.5	0.311	0.610	0.751	3.788	0.323
0	0.354	0.780	1.120	5.143	0.351
+0.5	0.593	1.521	2.373	5.230	0.485
+1	0.330	0.892	1.490	3.765	0.347
+1.5	0.215	0.747	1.013	3.094	0.222

10	m/z = 156 [-] $\times 10^{-3}$				
X/L$_I$	$\phi_{UN} = 1.8$	$\phi_{UN} = 2.0$	$\phi_{UN} = 2.2$	$a_T = 255$ s^{-1}	$a_T = 610$ s^{-1}
-1	0.149	0.227	0.385	0.905	0.152
-0.5	0.154	0.283	0.412	1.590	0.198
0	0.201	0.415	0.754	2.339	0.208
+0.5	0.297	0.744	1.325	2.611	0.385
+1	0.201	0.451	0.625	1.933	0.206
+1.5	0.131	0.329	0.447	1.106	0.172

11	m/z = 165 [-] $\times 10^{-4}$				
X/L$_I$	$\phi_{UN} = 1.8$	$\phi_{UN} = 2.0$	$\phi_{UN} = 2.2$	$a_T = 255$ s^{-1}	$a_T = 610$ s^{-1}
-1	0.096	0.235	0.523	2.338	0.105
-0.5	0.161	0.510	0.852	5.213	0.259
0	0.187	0.6735	1.712	8.156	0.486
+0.5	0.495	2.267	4.302	9.168	0.607
+1	0.431	0.819	1.363	8.500	0.511
+1.5	0.131	0.504	0.806	1.325	0.108

12	Fluorene [-] $\times 10^{-4}$				
X/L$_I$	$\phi_{UN} = 1.8$	$\phi_{UN} = 2.0$	$\phi_{UN} = 2.2$	$a_T = 255$ s^{-1}	$a_T = 610$ s^{-1}
-1	0.286	0.399	0.594	1.349	0.350
-0.5	0.333	0.513	0.786	1.586	0.383
0	0.406	0.837	1.142	1.858	0.5483
+0.5	0.673	1.220	1.878	2.263	0.548
+1	0.308	0.831	1.164	2.035	0.459
+1.5	0.218	0.451	0.873	1.450	0.277

Table I.2. The mole fractions of PAH species at different spatial locations for the equivalence ratio of 1.8 ≤ ϕ_{UN} ≤ 2.2 at a constant rate of strain of $a_T = 420$ s^{-1}, and rate of strain of 255 ≤ a_T [s^{-1}] ≤ 610 at a constant stoichiometry of $\phi_{UN} = 2.0$.

13	m/z = 170 [-] $\times 10^{-4}$				
X/L_I	$\phi_{UN} = 1.8$	$\phi_{UN} = 2.0$	$\phi_{UN} = 2.2$	$a_T = 255$ s^{-1}	$a_T = 610$ s^{-1}
-1	0.611	0.767	1.189	3.782	0.511
-0.5	1.038	1.198	1.281	5.765	0.7655
0	1.409	1.801	2.904	13.588	1.233
+0.5	3.409	4.878	6.126	13.714	2.886
+1	1.647	2.376	3.228	10.371	1.912
+1.5	1.290	1.621	2.264	4.536	0.985

14	Phenanthrene [-] $\times 10^{-4}$				
X/L_I	$\phi_{UN} = 1.8$	$\phi_{UN} = 2.0$	$\phi_{UN} = 2.2$	$a_T = 255$ s^{-1}	$a_T = 610$ s^{-1}
-1	0.917	1.225	1.896	2.723	0.779
-0.5	1.311	1.659	2.380	3.390	0.992
0	1.404	2.160	3.051	3.814	1.017
+0.5	3.067	4.077	4.454	5.143	1.695
+1	1.648	1.962	3.161	4.065	1.116
+1.5	0.848	1.198	2.122	3.317	0.773

X/L_I	$\phi_{UN} = 1.8$	$\phi_{UN} = 2.0$	$\phi_{UN} = 2.2$	$a_T = 255$ s^{-1}	$a_T = 610$ s^{-1}
-1	0.604	0.806	0.898	2.998	0.461
-0.5	0.727	1.181	1.392	3.372	0.874
0	1.024	1.437	1.865	4.069	1.064
+0.5	2.031	2.747	3.689	5.397	1.227
+1	0.906	1.487	1.830	4.505	1.103
+1.5	0.387	0.904	1.219	2.984	0.606

16	m/z = 192 [-] $\times 10^{-4}$				
X/L_I	$\phi_{UN} = 1.8$	$\phi_{UN} = 2.0$	$\phi_{UN} = 2.2$	$a_T = 255$ s^{-1}	$a_T = 610$ s^{-1}
-1	0.784	1.084	1.289	3.695	0.055
-0.5	1.008	1.222	1.706	6.775	0.076
0	2.504	3.101	3.728	9.197	0.207
+0.5	3.551	5.645	7.107	20.945	0.296
+1	2.276	2.737	3.269	18.755	0.215
+1.5	0.962	1.797	2.170	7.166	0.099

Table I.2. The mole fractions of PAH species at different spatial locations for the equivalence ratio of $1.8 \leq \phi_{UN} \leq 2.2$ at a constant rate of strain of $a_T = 420$ s^{-1}, and rate of strain of 255 $\leq a_T$ [s^{-1}] ≤ 610 at a constant stoichiometry of $\phi_{UN} = 2.0$.

17	Pyrene isomer [-] $\times10^{-4}$				
X/L_I	$\phi_{UN} = 1.8$	$\phi_{UN} = 2.0$	$\phi_{UN} = 2.2$	$a_T = 255$ s^{-1}	$a_T = 610$ s^{-1}
-1	0.508	0.823	1.318	2.028	0.073
-0.5	0.690	1.031	2.368	2.523	0.115
0	1.296	2.107	3.519	4.718	0.129
+0.5	3.014	4.052	4.844	6.540	2.539
+1	1.084	2.026	3.501	4.012	0.131
+1.5	0.978	1.431	1.823	2.188	0.101

18	Pyrene [-] $\times10^{-4}$				
X/L_I	$\phi_{UN} = 1.8$	$\phi_{UN} = 2.0$	$\phi_{UN} = 2.2$	$a_T = 255$ s^{-1}	$a_T = 610$ s^{-1}
-1	1.383	1.230	2.032	5.382	0.057
-0.5	1.205	2.045	2.296	8.482	0.133
0	2.490	3.462	3.949	18.919	0.280
+0.5	4.094	6.264	8.348	19.331	0.323
+1	2.358	3.369	3.942	17.268	0.205
+1.5	0.824	1.545	2.156	9.485	0.112

19	m/z = 206 [-] $\times10^{-4}$				
X/L_I	$\phi_{UN} = 1.8$	$\phi_{UN} = 2.0$	$\phi_{UN} = 2.2$	$a_T = 255$ s^{-1}	$a_T = 610$ s^{-1}
-1	1.332	1.784	2.225	3.795	0.101
-0.5	1.348	2.036	2.666	8.041	0.147
0	2.474	2.865	3.213	11.232	0.224
+0.5	3.471	5.185	7.255	18.637	0.310
+1	2.113	2.461	2.871	16.175	0.171
+1.5	0.731	1.442	1.837	6.924	0.087

20	m/z = 216 [-] $\times10^{-4}$				
X/L_I	$\phi_{UN} = 1.8$	$\phi_{UN} = 2.0$	$\phi_{UN} = 2.2$	$a_T = 255$ s^{-1}	$a_T = 610$ s^{-1}
-1	1.386	2.137	2.457	4.019	0.121
-0.5	1.933	2.636	3.387	6.921	0.186
0	2.501	3.983	4.671	13.267	0.327
+0.5	4.569	6.346	8.987	18.400	0.387
+1	2.212	3.635	3.929	10.915	0.242
+1.5	2.012	2.381	2.814	3.977	0.135

Table I.2. The mole fractions of PAH species at different spatial locations for the equivalence ratio of $1.8 \leq \phi_{UN} \leq 2.2$ at a constant rate of strain of $a_T = 420$ s^{-1}, and rate of strain of $255 \leq a_T$ [s^{-1}] ≤ 610 at a constant stoichiometry of $\phi_{UN} = 2.0$.

21	BaA [-] $\times 10^{-4}$				
X/L$_I$	$\phi_{UN} = 1.8$	$\phi_{UN} = 2.0$	$\phi_{UN} = 2.2$	$a_T = 255$ s^{-1}	$a_T = 610$ s^{-1}
-1	0.214	0.512	0.910	0.8790	0
-0.5	0.714	0.809	1.021	1.807	0.354
0	1.060	1.305	1.77	7.004	0.885
+0.5	3.544	4.446	6.354	9.364	2.892
+1	1.629	1.970	2.474	8.918	1.412
+1.5	0.414	0.609	1.22	3.93	0

22	m/z = 240 [-] $\times 10^{-3}$				
X/L$_I$	$\phi_{UN} = 1.8$	$\phi_{UN} = 2.0$	$\phi_{UN} = 2.2$	$a_T = 255$ s^{-1}	$a_T = 610$ s^{-1}
-1	0.0308	0	0.104	0.587	0
-0.5	0.083	0.146	0.360	0.970	0.086
0	0.235	0.251	0.512	1.376	0.154
+0.5	0.635	0.866	1.415	2.474	0.236
+1	0.151	0.346	0.584	2.190	0.134
+1.5	0	0	0.125	0.683	0

23	B(a)P [-] $\times 10^{-3}$				
X/L$_I$	$\phi_{UN} = 1.8$	$\phi_{UN} = 2.0$	$\phi_{UN} = 2.2$	$a_T = 255$ s^{-1}	$a_T = 610$ s^{-1}
-1	1.124	1.450	3.332	6.378	0.808
-0.5	1.099	1.631	3.933	12.009	1.299
0	1.429	2.119	3.774	13.955	1.634
+0.5	2.739	4.021	6.098	14.106	2.128
+1	1.168	2.678	3.951	13.880	1.177
+1.5	1.257	1.766	3.219	7.850	0.894

24	m/z = 276 [-] $\times 10^{-3}$				
X/L$_I$	$\phi_{UN} = 1.8$	$\phi_{UN} = 2.0$	$\phi_{UN} = 2.2$	$a_T = 255$ s^{-1}	$a_T = 610$ s^{-1}
-1	0.252	0.487	0.982	1.205	0.195
-0.5	0.2575	0.586	1.0329	1.508	0.332
0	0.345	0.951	1.217	1.959	0.350
+0.5	0.882	1.160	1.481	2.904	0.523
+1	0.3283	1.021	1.185	2.022	0.491
+1.5	0.261	0.718	0.827	1.249	0.289

Bibliography

[1] B. Dudley, BP Statistical Review of World Energy, Technol. Rep. June, British Petroleum, 2015.

[2] U.S. Energy Information Administration (EIA), January 2020.

[3] N. Armaroli, V. Balzani, Towards an electricity–powered world, Energy Environ. Sci. 4 (2011) 3193–3222.

[4] https://www.economist.com/science-and-technology/2016/12/10/how–clean–is–solar–power

[5] D. Mulvaney, Solar's green dilemma, IEEE Spectrum 51 (2014) 30–33.

[6] International Energy Agency, Commissioned EV and energy storage lithium–ion battery cell production capacity by region, and associated annual investment, 2010–2022.

[7] International Energy Outlook 2013, U.S. Energy Information Administration, US Department of Energy, Washington DC 20585, DOE/EIA– 0484 (2013) July.

[8] R. S. Barlow, Laser diagnostics and their interplay with computations to understand turbulent combustion, Proc. Combust. Inst. 31 (2007) 49–75.

[9] S. C. Peter, Reduction of CO_2 to Chemicals and Fuels: A solution to global warming and energy crisis, ACS Energy Lett. 3 (2018) 1557–1561.

[10] Paris agreement to the United Nations framework convention on climate change, Dec. 12, 2015, T. I. A. S. No. 16–1104.

[11] G. Popkin, How much can forests fight climate change?, Nature 565 (2019) 280–282.

[12] S. Masala, T. Ahmed, C. Bergvall, R. Westerholm, Improved efficiency of extraction of polycyclic aromatic hydrocarbons (PAHs) from the National Institute of Standards and Technology (NIST) Standard Reference Material Diesel Particulate Matter (SRM 2975) using accelerated solvent extraction, Anal. Bioanal. Chem. 401 (2011) 3305–3315.

[13] M. Arienzo, M. Toscanesi, M. Trifuoggi, L. Ferrara, C. Stanislao, C. Donadio, V. Grazia, D. V. Gionata, F. Carella, Contaminants bioaccumulation and pathological assessment in Mytilus galloprovincialis in coastal waters facing the brownfield site of Bagnoli, Italy, Marine Pollution Bulletin 140 (2019) 341–352.

[14] M. D. Avakian, B. Dellinger, H. Fiedler, B. Gullet, C. Koshland, S. Marklund, The origin, fate, and health effects of combustion by–products: a research framework, Environ. Health. Perspect. 110 (2002) 1155–1162.

[15] Regulatory impact analyses for the particulate matter and ozone national ambient air quality standards and proposed regional haze rule. Washington, DC: US Environmental Protection Agency; 1997, http://www.epa.gov/ttn/oartg/naaqsfin/ria.html.

[16] R. E. Cochran, I. P. Smoliakova, A. Kubatova, Detection of nitrated and oxygenated polycyclic aromatic hydrocarbons using atmospheric pressure chemical ionization high resolution mass spectrometry, Int. J. Mass Spectrom. 15 (2016) 6–17.

[17] M. Shrivastava, S. Lou, A. Zelenyuk, R. C. Easter, R. A. Corley, B. D. Thrall, P. J. Rasch, J. D. Fasta, S. L. Massey, Simonich, H. Shen, S Tao, Proc. Natl. Acad. Sci. 114 (2017) 1246–1251.

[18] C. S. McEnally, L. D. Pfefferle, B. Atakan, K. Kohse–Höinghaus, Studies of aromatic hydrocarbon formation mechanisms in flames: Progress towards closing the fuel gap, Prog. Energ. Combust. 32 (2006) 247–294.

[19] C. E. Bostrom, P. Gerde, A. Hanberg, B. Jernstrom, C. Johansson, T. Kyrklund, A. Rannug, M. Tornqvist, K. Victorin, R. Westerholm, Cancer risk assessment, indicators,

and guidelines for polycyclic aromatic hydrocarbons in the ambient air, Environ. Health Perspect. Suppl. 110 (2002) 451–488.

[20] K. O. Johansson, F. E. Gabaly, P. E. Schrader, M. F. Campbell, H. A. Michelsen, Evolution of particle surface and bulk maturity level during soot growth and oxidation in a flame, Aerosol Sci. Technol. 51 (2017) 1333–1344.

[21] F. Weiland, P. T. Nilsson, H. Wiinikka, R. Gebart, A. Gudmundsson, M. Sanati, Online characterization of syngas particulates using aerosol mass spectrometry in entrained flow biomass gasification, Aerosol Sci. Technol. 48 (2014) 1145–1155.

[22] R. J. Delfino, C. Sioutas, and S. Malik, Potential role of ultrafine particles in associations between airborne particle mass and cardiovascular health, Environ. Health Perspec. 113 (2005) 934–946.

[23] United States Environmental Protection Agency, Regulations for emissions from vehicles and engines, https://www.epa.gov/regulations–emissions–vehicles–and–engines/regulations–onroad–vehicles–and–engines.

[24] A. Violi, H. Michelsen, N. Hansen, K. Wilson, Developing a predictive model for the chemical composition of soot nanoparticles, United States. doi:10.2172/1351404.

[25] G. Blanquart, H. Pitsch, Analyzing the effects of temperature on soot formation with a joint volume–surface–hydrogen model, Combust. Flame 156 (2009) 1614–1626.

[26] M. A. Schiener, R. P. Lindstedt, Transported probability density function based modelling of soot particle size distributions in non–premixed turbulent jet flames, Proc. Combust. Inst. 37 (2019) 1049–1056.

[27] W. R. Boyette, S. Chowdhury, W. L. Roberts, Soot particle size distribution functions in a turbulent non–premixed ethylene-nitrogen flame, Flow Turbul. Combust. 98 (2017) 1173–1186.

[28] F. Hampp, R. P. Lindstedt, Quantification of combustion regime transitions in premixed turbulent DME flames, Combust. Flame 182 (2017) 248–268.

[29] F. Hampp, S. Shariatmadar, R. P. Lindstedt, Quantification of low Damköhler number turbulent premixed flames, Proc. Combust. Inst. 37 (2019) 1047–1054.

[30] H. Shariatmadar, F. Hampp, R. P. Lindstedt, Quantification of PAH concentrations in premixed turbulent flames crossing the soot inception limit, In press, Proc. Comb. Inst. 38 (2020).

[31] A. D. Abid, J. Camacho, D. A. Sheen, H. Wang, Quantitative measurement of soot particle size distribution in premixed flames–The burner–stabilized stagnation flame approach, Combust. Flame 156 (2009) 1862–1870.

[32] C. Gu, H. Lin, J. Camacho, B. Lin, C. Shao, R. Li, H. Gu, B. Guan, Z. Huang, H. Wang, Particle size distribution of nascent soot in lightly and heavily sooting premixed ethylene flames, Combust. Flame 165 (2016) 177–187.

[33] M. Commodo, S. Violi, A. D' Anna, A. D' Alessio, C. Allouis, F. Beretta, P. Minutolo, Soot and nano–particle formation in laminar and turbulent flames, Comb. Sci. Technol. 179 (2007) 387–400.

[34] A. D' Anna, M. Commodo, S. Violi, C. Allouis, J. Kent, Nano organic carbon and soot in turbulent non-premixed ethylene flames, Proc. Combust. Inst. 31 (2007) 621–629.

[35] A. Bhargava, P. R. Westmoreland, MBMS analysis of a fuel–lean ethylene flame, Combust. Flame 115 (1998) 456–467.

[36] J. H. Werner, T. A. Cool, Kinetic model for the decomposition of DMMP in a hydrogen/oxygen flame, Combust. Flame 117 (1998) 78–98.

[37] R. P. Lindstedt, B. B. O. Waldheim, Modeling of soot particle size distributions in premixed stagnation flow flames, Proc. Combust. Inst. 34 (2013) 1861–1868.

[38] A. Raj, M. Sander, V. Janardhanan, M. Kraft, A study on the coagulation of polycyclic aromatic hydrocarbon clusters to determine their collision efficiency, Combust. Flame 157 (2010) 523–534.

[39] K. O. Johansson, F. E. Gabaly, P. E. Schrader, M. F. Campbell, H. A. Michelsen, Evolution of maturity levels of the particle surface and bulk during soot growth and oxidation in a flame, Aerosol. Sci. Technol. 51 (2017) 1333–1344.

[40] K. O. Johansson, T. Dillstrom, P. Elvati, M. F. Campbell, P. E. Schrader, D. M. Popolan–Vaida, N. K. Richards–Henderson, K. R. Wilson, A. Violi, H. A. Michelsen, Radical–radical reactions, pyrene nucleation, and incipient soot formation in combustion, Proc. Combust. Inst. 36 (2017) 799–806.

[41] T. Dillstrom, A. Violi, The effect of reaction mechanisms on the formation of soot precursors in flames, Combust. Theor. Model. 21 (2017) 23–34.

[42] X. Mercier, O. Carrivain, C. Irimiea, A. Faccinetto, E. Therssen, Dimers of polycyclic aromatic hydrocarbons: the missing pieces in the soot formation process, Phys. Chem. Chem. Phys. 21 (2019) 8282–8294.

[43] N. M. Marinov, W. J. Pitz, C. K. Westbrook, M. J. Castaldi, S. M. Senkan, Modeling of aromatic and polycyclic aromatic hydrocarbon formation in premixed methane and ethane flames, Combust. Sci. Technol. 116 (1996) 211-287.

[44] P. Liu, Z. Li, A. Bennett, H. Lin, S. M. Sarathy, W. L. Roberts, The site effect on PAHs formation in HACA–based mass growth process, Combust. Flame 199 (2019) 54–68.

[45] F. Schulz, M. Commodo, K. Kaiser, G. De Falco, P. Minutolo, G. Meyer, A. D' Anna, L. Gross, Insights into incipient soot formation by atomic force microscopy, Proc. Combust. Inst. 37 (2019) 885–892.

[46] M. Commodo, K. Kaiser, G. D. Falco, P. Minutolo, F. Schulz, A. D' Anna, L. Gross, On the early stages of soot formation: Molecular structure elucidation by high–resolution atomic force microscopy, Combust. Flame 205 (2019) 154–164.

[47] R. P. Lindstedt, Modeling of the chemical complexities of flames, Proc. Combust. Inst. 27 (1998) 269–285.

[48] K. O. Johansson, M. P. Head–Gordon, P. E. Schrader, K. R. Wilson, H. A. Michelsen, Resonance–stabilized hydrocarbon–radical chain reactions may explain soot inception and growth, Sci. 361 (2018) 97–100.

[49] P. Liu, Z. Li, W. L. Roberts, The growth of PAHs and soot in the post–flame region, Proc. Combust. Inst. 37 (2019) 977–984.

[50] M. Sander, R. I. A. Patterson, A. Braumann, A. Raj, M. Kraft, Developing the PAH-PP soot particle model using process informatics and uncertainty propagation, Proc. Combust. Inst. 33 (2011) 675–683.

[51] A. G. G. M. Tielens, Interstellar polycyclic aromatic hydrocarbon molecules, annu. rev. astro. 46.060407.145211.

[52] Q. Mao, D. Hou, K. H. Luo, X. You, Dimerization of polycyclic aromatic hydrocarbon molecules and radicals under flame conditions, J. Phys. Chem. A 122 (2018) 8701–8708.

[53] F. Bisetti, G. Blanquart, M. E. Mueller, and H. Pitsch, On the formation and early evolution of soot in turbulent nonpremixed flames, Combust. Flame 159 (2012) 317–335.

[54] A. Raj, Z. Tan, D. Zhu, E. Croiset, J. Z. Wen, On the particle evolution in iron pentacarbonyl loaded counterflow methane–air flame, Combust. Flame 194 (2018) 1–14.

[55] N. A. Eaves, S. B. Dworkin, M. J. Thomson, Assessing relative contributions of PAHs to soot mass by reversible heterogeneous nucleation and condensation, Proc. Combust. Inst. 36 (2017) 935–945.

[56] B. Zhao, Z. Yang, Z. Li, M. V. Johnston, and H. Wang, Particle size distribution function of incipient soot in laminar premixed ethylene flames: effect of flame temperature, Proc. Combust. Inst. 30 (2005) 1441–1448.

[57] L. A. Sgro, A. D. Filippo, G. Lanzuolo, A. D' Alessio, Characterization of nanoparticles of organic carbon (NOC) produced in rich premixed flames by differential mobility analysis, Proc. Combust. Inst. 31 (2007) 631–638.

[58] M. L. Botero, S. Mosbach, M. Kraft, Sooting tendency of paraffin components of diesel and gasoline in diffusion flames, Fuel 126 (2014) 8–15.

[59] K. Gleason, F. Carbone, A. Gomez, Effect of temperature on soot inception in highly controlled counterflow ethylene diffusion flames, Combust. Flame 192 (2018) 283–294.

[60] W. Meier, X. R. Duan, P. Weigand, Reaction zone structures and mixing characteristics of partially premixed swirling CH_4/air flames in a gas turbine model combustor, Proc. Combust. Inst. 30 (2005) 835–842.

[61] S. B. Pope, Turbulent Flows. Cambridge, UK: Cambridge Univ. Press (2000).

[62] R. O. Fox, Computational models for turbulent reacting flows. Cambridge, UK: Cambridge Univ. Press (2003).

[63] R. P. Lindstedt, S. A. Louloudi, Joint–scalar transported PDF modeling of soot formation and oxidation, Proc. Combust. Inst. 30 (2005) 775–782.

[64] S. Chowdhury, W. R. Boyette, W. L. Roberts, Time–averaged probability density functions of soot nanoparticles along the centerline of a piloted turbulent diffusion flame using a scanning mobility particle sizer, J. Aerosol Sci. 106 (2017) 56–67.

[65] M. E. Mueller, H. Pitsch, LES model for sooting turbulent nonpremixed flames, Combust. Flame 159 (2012) 2166–2180.

[66] C. S. Yoo, H. G. Im, Transient soot dynamics in turbulent nonpremixed ethylene–air counterflow flames, Proc. Combust. Inst. 31 (2007) 701–708.

[67] K. P. Geigle, W. O' Loughlin, R. Hadef, W. Meier, Visualization of soot inception in turbulent pressurized flames by simultaneous measurement of laser–induced fluorescence of polycyclic aromatic hydrocarbons and laser–induced incandescence, and correlation to OH distributions, Appl. Phys. B. 119 (2015) 717–730.

[68] L. Tian, M. A. Schiener, R. P. Lindstedt, Fully coupled sectional modelling of soot particle dynamics in a turbulent diffusion flame, In press, Proc. Comb. Inst. 38 (2020).

[69] X. Dong, G. J. Nathan, S. Mahmoud, P. J. Ashman, D. Gu, and B. B. Dally, Global characteristics of non–premixed jet flames of hydrogen hydrocarbon blended fuels, Combust. Flame 162 (2015) 1326–1335.

[70] S. M. Mahmoud, G. J. Nathan, P. R. Medwell, B. B. Dally, and Z. T. Alwahabi, Simultaneous planar measurements of temperature and soot volume fraction in a turbulent non–premixed jet flame, Proc. Combust. Inst. 35 (2015) 1931–1938.

[71] S. M. Mahmoud, G. J. Nathan, Z. T. Alwahabi, Z. W. Sun, P. R. Medwell, and B. B. Dally, The effect of exit strain rate on soot volume fraction in turbulent non–premixed jet flames, Proc. Combust. Inst. 36 (2017) 889–897.

[72] S. M. Mahmoud, G. J. Nathan, Z. T. Alwahabi, Z. W. Sun, P. R. Medwell, B. B. Dally, The effect of exit Reynolds number on soot volume fraction in turbulent non–premixed jet flames, Combust. Flame 187 (2018) 42–51.

[73] J. Zhang, C. R. Shaddix, and R. W. Schefer, Design of model–friendly turbulent non–premixed jet burners for C_{2+} hydrocarbon fuels, Rev. Sci. Instrum. 82 (2011) 074101.

[74] J. B. Michael, P. Venkateswaran, C. R. Shaddix, and T. R. Meyer, Effects of repetitive pulsing on multi–kHz planar laser–induced incandescence imaging in laminar and turbulent flames, Appl. Opt. 54 (2015) 3331–3344.

[75] M. E. Mueller, Q. N. Chan, N. H. Qamar, B. B. Dally, H. Pitsch, Z. T. Alwahabi, and G. J. Nathan, Experimental and computational study of soot evolution in a turbulent nonpremixed bluff body ethylene flame, Combust. Flame 160 (2013) 1298–1309.

[76] S. Deng, M. E. Mueller, Q. N. Chan, N. H. Qamar, B. B. Dally, Z. T. Alwahabi, G. J. Nathan, Hydrodynamic and chemical effects of hydrogen addition on soot evolution in turbulent nonpremixed bluff body ethylene flames, Proc. Combust. Inst. 36 (2017) 807–814.

[77] K. P. Geigle, R. Hadef, and W. Meier, Soot formation and flame characterization of an aero–engine model combustor burning ethylene at elevated pressure, J. Eng. Gas Turbines Power 136 (2014) 021505.

[78] K. P. Geigle, M. Köhler, W. O' Loughlin, and W. Meier, Investigation of soot formation in pressurized swirl flames by laser measurements of temperature, flame structures and soot concentrations, Proc. Combust. Inst. 35 (2015) 3373–3380.

[79] B. Merci, D. Roekaerts, and B. Naud, Study of the performance of three micromixing models in transported scalar PDF simulations of a piloted jet diffusion flame ("Delft Flame III"), Combust. Flame 144 (2006) 476–493.

[80] N. H. Qamar, Z. T. Alwahabi, Q. N. Chan, G. J. Nathan, D. Roekaerts, and K. D. King, Soot volume fraction in a piloted turbulent jet non–premixed flame of natural gas, Combust. Flame 156 (2009) 1339–1347.

[81] M. Köhler, K. P. Geigle, W. Meier, B. M. Crosland, K. A. Thomson, and G. J. Smallwood, Sooting turbulent jet flame: characterization and quantitative soot measurements, Appl. Phys. B, 104 (2011) 409–425.

[82] M. Köhler, K. P. Geigle, T. Blacha, P. Gerlinger, and W. Meier, Experimental characterization and numerical simulation of a sooting lifted turbulent jet diffusion flame, Combust. Flame 159 (2012) 2620–2635.

[83] T. Plessing, N. Peters, J. G. Wünning, Laser optical investigation of highly preheated combustion with strong exhaust gas recirculation, Proc. Combust. Inst. 27 (1998) 3197–3204.

[84] J. A. Wünning, J. G. Wünning, Flameless oxidation to reduce thermal NO-formation, Prog. Energy Combust. Sci. 23 (1997) 81–94.

[85] F. Hampp, R. P. Lindstedt, Quantification of fuel chemistry effects on burning modes in turbulent premixed flames, Combust. Flame 218 (2020) 134–149.

[86] F. E. Marble, Recent advances in the aerospace sciences, in: C. Casci, C. Bruno, eds. Springer US, Boston, MA, 1985, ISBN 978-1-4684-4300-4, 395–413.

[87] N. Peters, Turbulent combustion, Cambridge University Press, Cambridge, 2000.

[88] K. Seshadri, N. Peters, The inner structure of methane–air flames, Combust. Flame 81 (1990) 96–118.

[89] K. Yamamoto, S. Isii, M. Ohnishi, Local flame structure and turbulent burning velocity by joint PLIF imaging, Proc. Combust. Inst. 33 (2011) 1285–1292.

[90] P. Geipel, Experimental research on turbulent reacting flows using gaseous and liquid fuels, Ph.D. thesis, Imperial College London, 2009.

[91] B. Zhou, C. Brackmann, Z. Li, M. Alden, X. S. Bai, Thin reaction zone and distributed reaction zone regimes in turbulent premixed methane/air flames: Scalar distributions and correlations, Combust. Flame 175 (2017) 220–236.

[92] L. P. H. de Goey, T. Plessingb, R. T. E. Hermanns, N. Peters, Analysis of the flame thickness of turbulent flamelets in the thin reaction zones regime, Proc. Combust. Inst. 30 (2005) 859–866.

[93] D. B. Spalding, Multi–fluid models of turbulent combustion, in: CTAC95 Conference, Melbourne, 1995.

[94] F. Hampp, Quantification of combustion regime transitions, PhD thesis, Imperial College, May 2016, url: http://hdl.handle.net/10044/1/32582.

[95] M. Fairweather, W. P. Jones, H. S. Ledin, R. P. Lindstedt, Predictions of soot formation in turbulent, non-premixed propane flames, Proc. Combust. Inst. 24 (1992) 1067–1074.

[96] M. Fairweather, W. P. Jones, R. P. Lindstedt, Predictions of radiative transfer from a turbulent reacting jet in a cross–wind, Combust. Flame 89 (1992) 45–63.

[97] M. A. Schiener, Stochastic modelling of soot in turbulent combustion, PhD thesis, Imperial College, March 2018.

[98] R. P. Lindstedt, L. Q. Maurice, Detailed kinetic modelling of toluene combustion, Combust. Sci. Technol. 120 (1996) 119-167.

[99] K. C. Kalvakala, V. R. Katta, S. K. Aggarwal, Effects of oxygen–enrichment and fuel unsaturation on soot and NOx emissions in ethylene, propane, and propene flames, Combust. Flame 187 (2018) 217–229.

[100] H. S. Hura, I. Glassman, Fuel oxygen effects on soot formation in counterflow diffusion flames, Combust. Sci. Technol. 53 (1987) 1–21.

[101] Y. Wang, S. H. Chung, Effect of strain rate on sooting limits in counterflow diffusion flames of gaseous hydrocarbon fuels: Sooting temperature index and sooting sensitivity index, Combust. Flame 161 (2014) 1224–1234.

[102] P. Dagaut, A. Ristori, A. E. Bakali, M. Cathonnet, Experimental and kinetic modeling study of the oxidation of n–propylbenzene, Fuel 81 (2002) 173-184.

[103] B. C. Choi, S. K. Choi, S. H. Chung, Soot formation characteristics of gasoline surrogate fuels in counterflow diffusion flames, Proc. Combust. Inst. 33 (2011) 609–616.

[104] M. L. Botero, S. Mosbach, J. Akroyd, M. Kraft, Sooting tendency of surrogates for the aromatic fractions of diesel and gasoline in a wick-fed diffusion flame, Fuel 153 (2015) 31–39.

[105] M. L. Botero, S. Mosbach, M. Kraft, Sooting tendency and particle size distributions of n-heptane/toluene mixtures burned in a wick-fed diffusion flame, Fuel 169 (2016) 111–119.

[106] L. Zepeng, H. M. F. Amin, L. Peng, W. Yu, C. Suk H., W. L. Roberts, Effect of dimethyl ether (DME) addition on sooting limits in counterflow diffusion flames of ethylene at elevated pressures, Combust. Flame 197 (2018) 463–470.

[107] H. Lin, C. Gua, J. Camacho, B. Lin, C. Shao, R. Lia, H. Gu, B. Guan, H. Wang, Z. Huanga, Mobility size distributions of soot in premixed propene flames, Combust. Flame 172 (2016) 365–373.

[108] J. Camacho, A. V. Singh, W. Wang, R. Shan, E. K. Y. Yapp, D. Chen, M. Kraft, H. Wang, Soot particle size distributions in premixed stretch–stabilized flat ethylene–oxygen–argon flames, Proc. Combust. Inst. 36 (2017) 1001–1009.

[109] R. Hadef, K. P. Geigle, W. Meier, M. Aigner, Soot characterization with laser-induced incandescence applied to a laminar premixed ethylene/air flame, Int. J. Therm. Sci. 49 (2010) 1457–1467.

[110] L. Figura, A. Gomez, Structure of incipiently sooting ethylene/nitrogen counterflow diffusion flames at high pressures, Combust. Flame 161 (2014) 1587–1603.

[111] V. Raman, R. O. Fox, Modeling of fine–particle formation in turbulent flames, Annu. Rev. Fluid Mech. 48 (2016) 159–190.

[112] H. Bockhorn, Soot formation in combustion: Mechanisms and Models, 1994.

[113] M. Frenklach, Reaction mechanism of soot formation in flames, Phys. Chem. Chem. Phys 4 (2002) 2028–2037.

[114] Z. A. Mansurov, Soot formation in combustion processes (Review), Combust. Explos. Shock Waves 41 (2005) 727–744.

[115] M. Frenklach, D. W. Clary, W. C. Gardiner, J. Stephen, E. Stein, Detailed kinetic modeling of soot formation in shock-tube pyrolysis of acetylene, Symposium (International) on Combustion 20 (1985) 887–901.

[116] M. Frenklach, W. C. Gardiner, E. Stein, D. W. Clary, T. Yuan, Mechanism of soot formation in acetylene–oxygen mixtures, Combust. Sci. Technol. 50 (1986) 79–115.

[117] M. Frenklach, J. Warnatz, Detailed Modeling of PAH Profiles in a Sooting Low–Pressure Acetylene Flame, Combust. Sci. Technol. 51 (1987) 265–283.

[118] M. Frenklach, H. Wang, Detailed modeling of soot particle nucleation and growth, Symposium (International) on Combustion, 23 (1991) 1559–1566.

[119] H. Wang, Formation of nascent soot and other condensed–phase materials in flames, Proc. Combust. Inst. 33 (2011) 41–67.

[120] S. E. Stein and A. Fahr, High–temperature stabilities of hydrocarbons, J. Phys. Chem. 89 (1985) 3714–3725.

[121] K. M. Leung and R. P. Lindstedt, Detailed Kinetic Modeling of $C_1 - C_3$, Alkane Diffusion Flames, Combust. Flame 102 (1995) 129–160.

[122] K. O. Johansson, J. Y. W. Lai, S. A. Skeen, D. M. Popolan–Vaida, K. R. Wilson, N. Hansen, A. Violi, H. A. Michelsen, Soot precursor formation and limitations of the stabilomer grid, Proc. Combust. Inst. 35 (2015) 1819–1826.

[123] P. Elvati, A. Violi, Thermodynamics of poly–aromatic hydrocarbon clustering and the effects of substituted aliphatic chains, Proc. Combust. Inst. 34 (2013) 1837–1843.

[124] H. W. Kroto, J. R. Heath, S. C. O' Brien, R. F. Curl, R. E. Smalley, C60: Buckminsterfullerene, Nat. 318 (1985) 162–163.

[125] M. Frenklach, L. B. Ebert, Comment on the proposed role of spheroidal carbon clusters in soot formation, J. Phys. Chem. 92 (1988) 561–563.

[126] A. D' Anna, Combustion–formed nanoparticles, Proc. Combust. Inst. 32 (2009) 593–613.

[127] A. D' Anna, Detailed kinetic modeling of particulate formation in rich premixed flames of ethylene, Energy Fuels 22 (2008) 1610–1619.

[128] M. R. Kholghy, G. A. Kelesidis, S. E. Pratsinis, Reactive polycyclic aromatic hydrocarbon dimerization drives soot nucleation, Phys. Chem. Chem. Phys. 20 (2018) 10926–10938.

[129] H. A. Michelsen, Probing soot formation, chemical and physical evolution, and oxidation: A review of in–situ diagnostic techniques and needs, Proc. Combust. Inst. 36 (2017) 717–735.

[130] I. M. Kennedy, The evolution of a soot aerosol in a counterflow diffusion flame, Combust. Flame 68 (1987) 1–16.

[131] J. Appel, H. Bockhorn, M. Frenklach, Kinetic modeling of soot formation with detailed chemistry and physics: laminar premixed flames of C_2 hydrocarbons, Combust. Flame 121 (2000) 122–136.

[132] M. Saffaripour, A. Veshkini, M. Kholghy, M. J. Thomson, Experimental investigation and detailed modeling of soot aggregate formation and size distribution in laminar coflow diffusion flames of Jet A–1, a synthetic kerosene, and n–decane, Combust. Flame 161 (2014) 848–863.

[133] A. Veshkini, N. A. Eaves, S. B. Dworkin, M. J. Thomson, Application of PAH–condensation reversibility in modeling soot growth in laminar premixed and nonpremixed flames, Combust. Flame 167 (2016) 335–352.

[134] N. A. Eaves, S. B. Dworkin, M. J. Thomson, The importance of reversibility in modeling soot nucleation and condensation processes, Proc. Combust. Inst. 35 (2015) 1787–1794.

[135] W. Pejpichestakul, E. Ranzi, M. Pelucchi, A. Frassoldati, A. Cuoci, A. Parente, T. Faravelli, Examination of a soot model in premixed laminar flames at fuel–rich conditions, Proc. Combust. Inst. 37 (2019) 1013–1021.

[136] A. D' Anna, M. Commodo, M. Sirignano, P. Minutolo, R. Pagliara, Particle formation in opposed–flow diffusion flames of ethylene: An experimental and numerical study, Proc. Combust. Inst. 32 (2009) 793–801.

[137] P. Mitchell, M. Frenklach, Monte carlo simulation of soot aggregation with simultaneous surface growth–why primary particles appear spherical, Symposium (International) on Combustion 27 (1998) 1507–1514.

[138] P. Mitchell, M. Frenklach, Particle aggregation with simultaneous surface growth, Phys. Rev. E. 67 (2003) 061407.

[139] M. Balthasar, M. Frenklach, Monte–Carlo simulation of soot particle coagulation and aggregation: the effect of a realistic size distribution, Proc. Combust. Inst. 30 (2005) 1467–1475.

[140] G. A. Kelesidis, E. Goudeli, S. E. Pratsinis, Morphology and mobility diameter of carbonaceous aerosols during agglomeration and surface growth, Carbon 121 (2017) 527–535.

[141] M. Frenklach, Z. Liu, R. I. Singh, G. R. Galimova, Va. N. Azyazov, A. M. Mebel, Detailed, sterically–resolved modeling of soot oxidation: Role of O atoms, interplay with particle nanostructure, and emergence of inner particle burning, Combust. Flame 188 (2018) 284–306.

[142] B. R. Stanmore, J. F. Brilhac, P. Gilot, The oxidation of soot: a review of experiments, mechanisms and models, Carbon 39 (2001) 2247–2268.

[143] A. Cavaliere, R. Barbella, A. Ciajolo, A. D' Anna, R. Ragucci, Fuel and soot oxidation in diesel-like conditions, Symposium (International) on Combustion 25 (1994) 167–174.

[144] L. Delfau, P. Michaud, A. Barassin, Formation of Small and Large Positive Ions in Rich and Sooting Low–Pressure Ethylene and Acetylene Premixed Flames, Combust. Sci. Technol. 20 (1979) 165–177.

[145] M. Sirignano, A. Collina, M. Commodo, P. Minutolo, A. D' Anna, Detection of aromatic hydrocarbons and incipient particles in an opposed–flow flame of ethylene by spectral and time–resolved laser induced emission spectroscopy, Combust. Flame 159 (2012) 1663–1669.

[146] M. S. Celnik, M. Sander, A. Raj, R. H. West, M. Kraft, Modelling soot formation in a premixed flame using an aromatic-site soot model and an improved oxidation rate, Proc. Combust. Inst. 32 (2009) 639–646.

[147] M. Sirignano, D. Bartos, M. Conturso, M. Dunn, A. D' Anna, A. R. Masri, Detection of nanostructures and soot in laminar premixed flames, Combust. Flame 176 (2017) 299–308.

[148] D. Bartos, M. Sirignano, M. J. Dunn, A. D' Anna, A. R. Masri, Soot inception in laminar coflow diffusion flames, Combust. Flame 205 (2019) 180–192.

[149] M. Commodo, G. De Falco, A. Bruno, C. Borriello, P. Minutolo, A. D' Anna, Physicochemical evolution of nascent soot particles in a laminar premixed flame: from nucleation to early growth, Combust. Flame 162 (2015) 3854–3863.

[150] P. Minutolo, G. Rusciano, L. A. Sgro, G. Pesce, A. Sasso, A. D' Anna, Surface enhanced Raman spectroscopy (SERS) of particles produced in premixed flame across soot threshold, Proc. Combust. Inst. 33 (2011) 649–657.

[151] M. Commodo, G. Tessitore, G. De Falco, A. Bruno, P. Minutolo, A. D' Anna, Further details on particle inception and growth in premixed flames, Proc. Combust. Inst. 35 (2015) 1795–1802.

[152] F. Ossler, L. Vallenhag, S. E. Canton, J. B. A. Mitchell, J. L. L. Garrec, M. Sztucki, S. d. Stasio, Dynamics of incipient carbon particle formation in a stabilized ethylene flame by in-situ extended–small–angle–and wide–angle X–ray scatterin, Carbon 51 (2013) 1–19.

[153] J. B. A. Mitchell, J. L. LeGarrec, G. Saidani, F. Lefeuvre, S. di Stasio, Synchrotron Radiation studies of additives in combustion, III: Ferrocene, Energy Fuels 27 (2013) 4891–4898.

[154] J. B. A. Mitchell, S. di Stasio, J. L. LeGarrec, A. I. Florescu–Mitchell, T. Narayanan, M. Sztucki, Small angle x–ray scattering study of flame soot nanoparticle aggregation and restructuring, J. Appl. Phys. 105 (2009) 124904.

[155] F. Ossler, Measurements of the structures of nanoparticles in flames by in-situ detection of scattered x-ray radiation, J. Appl. Phys. 98 (2005) 114317.

[156] F. Ossler, S. E. Canton, L. R. Wallenberg, A. Engdahl, S. Seifert, J. P. Hessler, R. S. Tranter, Measurements of structures and concentrations of carbon particle species in premixed flames by the use of in–situ wide angle X–ray scattering, Carbon 96 (2016) 782–798.

[157] M. Alfe, B. Apicella, R. Barbella, J. N. Rouzaud, A. Tregrossi, A. Ciajolo, Structure–property relationship in nanostructures of young and mature soot in premixed flames, Proc. Combust. Inst. 32 (2009) 697–704.

[158] C. S. McEnally, L. D. Pfefferle, Experimental study of nonfuel hydrocarbons and soot in coflowing partially premixed ethylene/air flames, Combust. Flame 121 (2000) 575–592

[159] C. R. Shaddix, T. C. Williams, L. G. Blevins, R. W. Schefer, Flame structure of steady and pulsed sooting inverse jet diffusion flames, Proc. Combust. Inst. 30 (2005) 1501–1508.

[160] B. Yang, U. O. Koylu, Soot processes in a strongly radiating turbulent flame from laser scattering/extinction experiments, J. Quant. Spectrosc. Radiat. Transfer 93 (2005) 289–299.

[161] F. Ossler, S. E. Canton, J. Larsson, X–ray scattering studies of the generation of carbon nanoparticles in flames and their transition from gas phase to condensed phase, Carbon 47 (2009) 3498–3507.

[162] H. Wang, B. Zhao, B. Wyslouzil, K. Streletzky, Small–angle neutron scattering of soot formed in laminar premixed ethylene flames, Proc. Combust. Inst. 29 (2002) 2749–2757.

[163] F. Goulay, P. E. Schrader, L. Nemes, M. A. Dansson, H. A. Michelsen, Photochemical interferences for laser-induced incandescence of flame-generated soot, Proc. Combust. Inst. 32 (2009) 963–970.

[164] F. Liu, G. J. Smallwood, Relationship between soot volume fraction and LII signal in AC–LII: effect of primary soot particle diameter polydispersity, Appl. Phys. B. 112 (2013) 307–319.

[165] C. M. Sorensen, J. Cai, N. Lu, Light–scattering measurements of monomer size, monomers per aggregate, and fractal dimension for soot aggregates in flames, Appl. Opt. 31 (1992) 6547–6557.

[166] J. Reimann, S. A. Kuhlmann, S. Will, 2D aggregate sizing by combining laser–induced incandescence (LII) and elastic light scattering (ELS), Appl. Phys. B. 96 (2009) 583–592.

[167] M. Sztucki, T. Narayanan, In-situ study of aggregation of soot particles in an acetylene flame by small-angle x–ray scattering, J. Appl. Phys. 101 (2007) 114304.

[168] J. B. A. Mitchell, J. L. L. Garrec, A. I. Florescu–Mitchell, S. D. Stasio, Small–angle neutron scattering study of soot particles in an ethylene–air diffusion flame, Combust. Flame 145 (2006) 80–87.

[169] B. Zhao, K. Uchikawa, H. Wang, A comparative study of nanoparticles in premixed flames by scanning mobility particle sizer, small angle neutron scattering, and transmission electron microscopy, Proc. Combust. Inst. 31 (2007) 851–860.

[170] M. Leschowski, K. A. Thomson, D. R. Snelling, C. Schulz, G. J. Smallwood, Combination of LII and extinction measurements for determination of soot volume fraction and estimation of soot maturity in non-premixed laminar flames, Appl. Phys. B. 119 (2015) 685–696.

[171] S. D. Stasio, P. Massoli, M. Lazzaro, Retrieval of soot aggregate morphology from light scattering/extinction measurements in a high–pressure high–temperature environment, J. Aerosol Sci. 27 (1996) 897–913.

[172] K. Hayashida, K. Amagai, K. Satoh, M. Arai, Experimental analysis of soot formation in sooting diffusion flame by using laser–induced emissions, J. Eng. Gas Turbines Power. 128 (2006) 241–246.

[173] F. Cignoli, S. Benecchi, G. Zizak, Simultaneous one–dimensional visualization of OH, polycyclic aromatic hydrocarbons, and soot in a laminar diffusion flame, Opt. Lett. 17 (1992) 229–231.

[174] J. H. Frank, A. Shavorskiy, H. Bluhm, B. Coriton, E. Huang, D. L. Osborn, In-situ soft X–ray absorption spectroscopy of flames, Appl. Phys. B 117 (2014) 493–499.

[175] R. L. Vander Wal, Laser–induced incandescence: excitation and detection conditions, material transformations, and calibration. Appl. Phys. B. Laser. Opt. 96 (2009) 601–611.

[176] R. P. Bambha, H. A. Michelsen, Effects of aggregate morphology and size on laser-induced incandescence and scattering from black carbon (mature soot), J. Aerosol. Sci. 88 (2015) 159–181.

[177] E. Cenker, G. Bruneaux, T. Dreier, C. Schulz, Determination of small soot particles in the presence of large ones from time–resolved laser–induced incandescence, Appl. Phys. B. 118 (2015) 169–183.

[178] D. R. Snelling, O. Link, K. A. Thomson, G. J. Smallwood, Measurement of soot morphology by integrated LII and elastic light scattering, Appl. Phys. B. 104 (2011) 385–397.

[179] B. M. Crosland, K. A. Thomson, M. R. Johnson, Instantaneous in–flame measurement of soot volume fraction, primary particle diameter, and aggregate radius of gyration via auto–compensating laser–induced incandescence and two-angle elastic light scattering, Appl. Phys. B. 112 (2013) 381–393.

[180] S. D. Iuliis, F. Cignoli, S. Benecchi, G. Zizak, Determination of soot parameters by a two-angle scattering–extinction technique in an ethylene diffusion flame, Appl. Opt. 37 (1998) 7865–7874.

[181] J. J. Murphy, C. R. Shaddix, Influence of scattering and probe-volume heterogeneity on soot measurements using optical pyrometry, Combust. Flame 143 (2005) 1–10.

[182] C. B. Stipe, B. S. Higgins, D. D. Lucas, C. P. Koshland, R. F. Sawyer, Soot detection using excimer laser fragmentation fluorescence spectroscopy, Proc. Combust. Inst. 29 (2002) 2759–2766.

[183] G. S. Humphries, J. Dunn, M. M. Hossain, M. Lengden, I. S. Burns, J. D. Black, A simple photoacoustic method for the in-situ study of soot distribution in flames, Appl. Phys. B 119 (2015) 709–715.

[184] A. Bohlin, C. J. Kliewer, Direct coherent Raman temperature imaging and wide-band chemical detection in a hydrocarbon flat flame, J. Phys. Chem. Lett. 6 (2015) 643–649.

[185] S. Jahangirian, C. S. McEnally, A. Gomez, Experimental study of ethylene counterflow diffusion flames perturbed by trace amounts of jet fuel and jet fuel surrogates under incipiently sooting conditions, Combust. Flame 156 (2009) 1799–1809.

[186] F. Carbone, A. Gomez, The structure of toluene–doped counterflow gaseous diffusion flames, Combust. Flame 159 (2012) 3040–3055.

[187] F. Carbone, A. Gomez, Experimental study on the structure of opposed flow gaseous diffusion flames doped with n–decane, Combust. Flame 161 (2014) 453–464.

[188] J. K. Lefkowitz, J. S. Heyne, S. H. Won, S. Dooley, H. H. Kim, F. M. Haas, S. Jahangirian, F. L. Dryer, Y. Ju, A chemical kinetic study of tertiary-butanol in a flow reactor and a counterflow diffusion flame, Combust. Flame 159 (2012) 968–978.

[189] L. Tosatto, B. L. Mantia, H. Bufferand, P. Duchaine, A. Gomez, Chemical structure of a methane counterflow diffusion flame perturbed with the addition of either JP–8 or a jet fuel surrogate, Proc. Combust. Inst. 32 (2009) 1319–1326.

[190] F. Carbone, A. Gomez, Chemical effects of 1,2,4–Trimethyl benzene addition in counterflow gaseous diffusion flames, Proc. Combust. Inst. 34 (2013) 1025–1033.

[191] S. Jahangirian, S. Dooley, F. M. Haas, F. L. Dryer, A detailed experimental and kinetic modeling study of n–decane oxidation at elevated pressures, Combust. Flame 159 (2012) 30–43.

[192] M. Saffaripour, P. Zabeti, M. Kholghy, M. J. Thomson, An Experimental Comparison of the Sooting Behaviour of Synthetic Jet Fuels, Energy Fuels 25 (2011) 5584–5593.

[193] J. B. Thianer, L. Nett, S. Zhou, Y. Preibisch, H. Hollert, C. Achten, Identification of 7–9 ring polycyclic aromatic hydrocarbons in coals and petrol coke using High performance liquid chromatography – Diode array detection coupled to Atmospheric pressure laser ionization – Mass spectrometry (HPLC–DAD–APLI–MS), Environ. Pollut. 252 (2019) 723–732.

[194] N. Hansen, M. Schenk, K. Moshammer, K. KohseHöinghaus, Investigating repetitive reaction pathways for the formation of polycyclic aromatic hydrocarbons in combustion processes, Combust. Flame 180 (2017) 250–261.

[195] S. A. Skeen, B. Yang, H. A. Michelsen, J. A. Miller, A. Violi, N. Hansen, Studies of laminar opposed-flow diffusion flames of acetylene at low-pressures with photoionization mass spectrometry, Proc. Combust. Inst. 34 (2013) 1067–1075.

[196] S. A. Skeen, H. A. Michelsen, K. R. Wilson, D. M. Popolan, A. Violi, N. Hansen, Near–threshold photoionization mass spectra of combustion-generated high–molecular–weight soot precursors, J. Aerosol Sci. 58 (2013) 86–102.

[197] L. Luo, R. You, Y. Liu, J. Yang, Y. Zhu, W. Wen, Y. Pan, F. Qi, W. Huang, Gas–Phase Reaction Network of Li/MgO–Catalyzed Oxidative Coupling of Methane and Oxidative Dehydrogenation of Ethane, ACS Catal. 9 (2019) 2514–2520.

[198] C. Russo, B. Apicella, A. Tregrossi, M. M. Oliano, A. Ciajolo, Thermophoretic sampling of large PAH ($C \geqslant 22$–24) formed in flames, Fuel 263 (2020) 116722.

[199] A. Raj, K. Pan, H. Qi, H. Zhu, J. Z. Wen, E. Croiset, Effects of an iron pentacarbonyl additive on counterflow natural gas and ethanol flames, Energy Fuels 29 (2015) 5361–5371.

[200] J. H. Choi, C. H. Hwang, S. K. Choi, S. M Lee, W. J. Lee, S. H. Jang, Seul–Hyun Park, Impacts of hydrogen addition on micro and nanostructure of soot particles formed in C2H4/air counter diffusion flames, Int. J. Hydrogen Energy 41 (2016) 15852–15858.

[201] S. S. Hou, D. H. Chung, T. H. Lin, High–yield synthesis of carbon nano–onions in counterflow diffusion flames, Carbon 47 (2009) 938–947.

[202] T. X. Li, H. G. Zhang, F. J. Wang, Z. Chen, K. Saito, Synthesis of carbon nanotubes on Ni–alloy and Si–substrates using counterflow methane–air diffusion flames, Proc. Combust. Inst. 31 (2007) 1849–1856.

[203] H. M. F. Amin, A. Bennett, W. L. Roberts, Determining fractal properties of soot aggregates and primary particle size distribution in counterflow flames up to 10 atm, Proc. Combust. Inst. 37 (2019) 1161–1168.

[204] L. Figura, F. Carbone, A. Gomez, Challenges and artifacts of probing high–pressure counterflow laminar diffusion flames, Proc. Combust. Inst. 35 (2015) 1871–1878.

[205] F. Carbone, F. Cattaneo, A. Gomez, Structure of incipiently sooting partially premixed ethylene counterflow flames, Combust. Flame 162 (2015) 4138–4148.

[206] F. Carbone, A. Gomez, Chemical interactions between 1,2,4–trimethylbenzene and n-decane in doped counterflow gaseous diffusion flames, Proc. Combust. Inst. 35 (2015) 761–769.

[207] F. Carbone, K. Gleason, A. Gomez, Pressure effects on incipiently sooting partially premixed counterflow flames of ethylene, Proc. Combust. Inst. 36 (2017) 1395–1402.

[208] J. C. Biordi, C. P. Lazzara, J. F. Papp, Molecular beam mass spectrometry applied to determining the kinetics of reactions in flames. I. Empirical characterization of flame perturbation by molecular beam sampling probes, Combust. Flame 23 (1974) 73–82.

[209] J. F. Pauwels, M. Carlier, P. Devolder, L. R. Sochet, Experimental and numerical analysis of a low pressure stoichiometric methanol–air flame, Combust. Sci. Technol. 64 (1989) 97–117.

[210] U. Struckmeier, P. Oβwald, T. Kasper, L. Böhling, M. Heusing, M. Köhler, A. Brockhinke, K. Kohse–Höinghaus, Sampling probe influences on temperature and species concentrations in molecular beam mass spectroscopic investigations of flat premixed low–pressure flames, Z. Phys. Chem. 223 (2009) 503–537.

[211] U. Niemann, R. Seiser, K. Seshadri, Ignition and extinction of low molecular weight esters in nonpremixed flows, Combust. Theor. Model. 14 (2010) 875–891.

[212] A. Ergut, S. Granata, J. Jordan, J. Carlson, J. B. Howard, H. Richter, Y. A. Levendis, PAH formation in one–dimensional premixed fuel–rich atmospheric pressure ethylbenzene and ethyl alcohol flames, Combust. Flame 144 (2006) 757–772.

[213] A. Faccinetto, High sensitivity detection of polycyclic aromatic hydrocarbons desorbed from soot particles using laser desorption/laser ionisation/time–of–flight mass spectrometry. An approach for studying the soot growth process in flames, Universite Lille, December 2009.

[214] P. H. Joo, B. Gigone, E. A. Griffin, M. Christensen, O. L. Gulder, Soot primary particle size dependence on combustion pressure in laminar ethylene diffusion flames, Fuel 220 (2018) 464–470.

[215] J. Moran, J. Cuevas, F. Liu, J. Yon, A. Fuentes, Influence of primary particle polydispersity and overlapping on soot morphological parameters derived from numerical TEM images, Powder Technol. 330 (2018) 67–79.

[216] M. Saffaripour, L. L. Tay, K. A. Thomson, G. J. Smallwood, B. T. Brem, L. Durdina, M. Johnson, Raman spectroscopy and TEM characterization of solid particulate matter emitted from soot generators and aircraft turbine engines, Aerosol Sci. Technol. 51 (2017) 518–531.

[217] M. L. Botero, D. Chen, S. Gonzalez-Calera, D. Jefferson, M. Kraft, HRTEM evaluation of soot particles produced by the non-premixed combustion of liquid fuels, Carbon 96 (2016) 459–473.

[218] J. Camacho, C. Liu, C. Gu, H. Lin, Z. Huang, Q. Tang, X. You, C. Saggese, Y. Li, H. Jung, L. Deng, I. Wlokas, H. Wang, Mobility size and mass of nascent soot particles in a benchmark premixed ethylene flame, Combust. Flame 162 (2015) 3810–3822.

[219] C. H. Huang, R. L. Vander Wal, Effect of soot structure evolution from commercial jet engine burning petroleum based JP–8 and synthetic HRJ and FT fuels, Energy Fuels 27 (2013) 4946–4958.

[220] B. E. Anderson, A. J. Beyersdorf, C. H. Hudgins, J. V. Plant, K. L. Thornhill, E. L. Winstead, L. D. Ziemba, R. Howard, E. Corporan, R. C. Miake–Lye, S. C. Herndon, M. Timko, E. Wood, W. Dodds, P. Whitefield, D. Hagen, P. Lobo, W. B Knighton, D. Bulzan, K. Tacina, C. Wey, R. Vander Wal, A. Bhargava, J. Kinsey, D. S. Liscinsky, Alternative aviation fuel experiment (AAFEX); NASA/TM-2011–217059; Hanover, MD, February 2011.

[221] A. Violi, A. D' Anna, A. D' Alessio, A. F. Sarofim, Modeling aerosol formation in opposed-flow diffusion flames, Chemosphere 10 (2003) 1047–1054.

[222] K. H. H. Goh, P. Geipel, R. P. Lindstedt, Lean premixed opposed jet flames in fractal grid generated multiscale turbulence, Combust. Flame 161 (2014) 2419–2434.

[223] K. H. H. Goh, P. Geipel, F. Hampp, R. P. Lindstedt, Flames in fractal grid generated turbulence, Fluid Dyn. Res. 45 (2013) 061403.

[224] M. Smooke, I. Puri, K. Seshadri, A comparison between numerical calculations and

experimental measurements of the structure of a counterflow diffusion flame burning diluted methane in diluted air, Proc. Combust. Inst. 21 (1986) 1783–1792.

[225] R. P. Lindstedt, D. S. Luff, J. H. Whitelaw, Velocity fields of fuel lean premixed turbulent opposed jet flames, Proc. Combust. Inst. 31 (2007) 1459–1466.

[226] E. Mastorakos, A. M. K. P. Taylor, J. H. Whitelaw, Extinction of turbulent counterflow flames with reactants diluted by hot products, Combust. Flame 102 (1995) 101–114.

[227] J. Du, R. L. Axelbaum, The effect of flame structure on soot–particle inception in diffusion flames, Combust. Flame 100 (1995) 367–375.

[228] K. H. H. Goh, P. Geipel, F. Hampp, R. P. Lindstedt, Regime transition from premixed to flameless oxidation in turbulent JP–10 flames, Proc. Combust. Inst., 34 (2013) 3311–3318.

[229] D. Geyer, A. Kempf, A. Dreizler, J. Janicka, Turbulent opposed–jet flames: A critical benchmark experiment for combustion LES, Combust. Flame 143 (2005) 524–548.

[230] P. Geipel, K. H. H. Goh, R. P. Lindstedt, Fractal–generated turbulence in opposed jet flows, Flow Turbul. Combust. 85 (2010) 397–419.

[231] K. H. H. Goh, P. Geipel, R. P. Lindstedt, Turbulent transport in premixed flames approaching extinction, Proc. Combust. Inst. 35 (2015) 1469–1476.

[232] F. Hampp, R. P. Lindstedt, Strain distribution on material surfaces during combustion regime transitions, Proc. Combust. Inst. 36 (2017) 1911–1918.

[233] K. H. H. Goh, Investigation of conditional statistics in premixed combustion and the transition to flameless oxidation in turbulent opposed jets, Ph.D. thesis, Imperial College London, 2013.

[234] W. K. George, H. J. Hussein, Locally axisymmetric turbulence, J. Fluid Mech. 233 (1991) 1–23.

[235] S. B. Pope, Turbulent Flows, vol. 12, Cambridge University Press, 2001, ISBN 9780511840531.

[236] N. Peters, Laminar flamelet concepts in turbulent combustion, Twenty-first Symposium (International) on Combustion (1986) 1231–1250.

[237] L. W. Kostiuk, K. N. C. Bray, T. C. Chew, premixed turbulent combustion in counter-flowing streams, Combust. Sci. Technol. , 64(4–6), (1989) 233â€“41.

[238] F. Hampp, K. H. H. Goh, R. P. Lindstedt, The reactivity of hydrogen enriched turbulent flames, Process Saf. Environ. Prot. 143 (2020) 66–75.

[239] L. Wheatley, Y. A. Levendis, P. Vouros, Exploratory study on the combustion and PAH emissions of selected municipal waste plastics, Environ. Sci. Technol. 27 (1993) 2885–2895.

[240] R. E. Majors, D. E. Wilmington, Sample preparation fundamentals for chromatography, Agilent Technologies, www.agilent.com/cs/library/primers/Public/5991–3326EN–SPHB.pdf.

[241] M. V. Heitor, A. L. N. Moreira, Thermocouples and sample probes for combustion studies, Prog. Energ. Combust. Sci. 19 (1993) 259–278.

[242] R. M. Fristrom, and A. A. Westenberg, Flame structures, McGraw–Hill, New York, 1965.

[243] M. S. P. Kahandawala, M. J. DeWitt, E. Corporan, S. S. Sidhu, Ignition and emission characteristics of surrogate and practical jet fuels, Energy Fuels 22 (2008) 3673–3679.

[244] F. N. Egolfopoulos, N. Hansen, Y. Ju, K. Kohse–Höinghaus, C. K. Law, F. Qi, Advances and challenges in laminar flame experiments and implications for combustion chemistry, Prog. Energ. Combust. Sci 43 (2014) 36–67.

[245] P. Desgroux, L. Gasnot, J. F. Pauwels, L. R. Sochet, Correction of LIF temperature measurements for laser absorption and fluorescence trapping in a flame, Appl. Phys. B 61 (1995) 401–407.

[246] O. I. Smith, An experimental study of probe distortions to the structure of one–dimensional flames, Combust. Flame 63 (1986) 19–29.

[247] B. Coriton, J. H. Frank, A. Gomez, Interaction of turbulent premixed flames with combustion products: Role of stoichiometry, Combust. Flame 170 (2016) 37–52.

[248] P. Desgroux, X. Mercier, B. Lefort, R. Lemaire, E. Therssen, J. F. Pauwels, Soot volume fraction measurement in low-pressure methane flames by combining laser-induced incandescence and cavity ring-down spectroscopy: Effect of pressure on soot formation, Combustion and Flame 155 (2008) 289–301.

[249] D. C. Rapp, Soot formation: species measurements and analysis in laminar coflow coannular diffusion flames. PhD Thesis. Pennsylvania State University; 1996.

[250] Agilent 5975 Series MSD, Operation Manual.

[251] C. Betrancourt, F. Liu, P. Desgroux, X. Mercier, A. Faccinetto, M. Salamanca, L. Ruwe, K. Kohse–Höinghaus, D. Emmrich, A. Beyer, A. Golzhauser, T. Tritscher, Investigation of the size of the incandescent incipient soot particles in premixed sooting and nucleation flames of n-butane using LII, HIM, and 1 nm–SMPS, Aerosol Sci. Technol. 51 (2017) 916–935.

[252] J. Mei, M. Wang, X. You, C. K. Law, Quantitative measurement of particle size distributions of carbonaceous nanoparticles during ethylene pyrolysis in a laminar flow reactor, Combust. Flame 200 (2019) 15–22.

[253] TSI Scanning Mobility Particle Sizer Spectrometer 3938, https://tsi.com/products/particle-sizers/particle-size-spectrometers/scanning-mobility-particle-sizer-spectrometer-3938/

[254] A. C. Eckbreth, Laser diagnostic for combustion temperature and species, CRC Press, 1988, ISBN 9056995324.

[255] I. Namer, R. W. Schefer, Error estimates for Rayleigh scattering density and temperature measurements in premixed flames, Exp. Fluids 3 (1985) 1–9.

[256] F. A. Jenkins, H. E. White, Fundamentals of Optics, vol. 45, McGraw Hill, 1951, ISBN 0070323305.

[257] F. Q. Zhao, H. Hiroyasu, The applications of laser Rayleigh scattering to combustion diagnostics, Prog. Energy Combust. Sci. 19 (1993) 447–485.

[258] P. O. Witze, S. Hochgreb, D. Kayes, H. A. Michelsen, C. R. Shaddix, Time–resolved laser–induced incandescence and laser elastic scattering measurements in a propane diffusion flame, Appl. Opt. 40 (2001) 2443–2452.

[259] R. J. Santoro, H. G. Semerjian, Soot formation in diffusion flames: Flow rate, fuel species and temperature effects, Symposium (International) on Combustion 20 (1985) 997–1006.

[260] B. Axelsson, R. Collin, P. E. Bengtsson, Laser–induced incandescence for soot particle size and volume fraction measurements using online extinction calibration, Appl. Phys. B 72 (2001) 367–372.

[261] N. J. Kempema, M. B. Long, Quantitative Rayleigh thermometry for high background scattering applications with structured laser illumination planar imaging, Appl. Opt. 53 (2014) 6688–6697.

[262] H. Oltmann, J. Reimann, S. Will, Wide–angle light scattering (WALS) for soot aggregate characterization. Combust. Flame 157 (2010) 516–522.

[263] J. P. Schwarz, A. E. Perring, M. Z. Markovic, R. S. Gao, S. Ohata, J. Langridge, Technique and theoretical approach for quantifying the hygroscopicity of black–carbon–containing aerosol using a single particle soot photometer. J. Aerosol. Sci. 81 (2015) 110–126.

[264] H. A. Michelsen, C. Schulz, G. J. Smallwood, S. Will, Laser–induced incandescence: particulate diagnostics for combustion, atmospheric, and industrial applications, Prog. Energy Combust. Sci. 51 (2015) 2–48.

[265] J. R. Lakowicz, SpringerLink, Principles of fluorescence spectroscopy, Springer US, Boston, MA, 2006.

[266] A. Bruno, C. de Lisio, P. Minutolo, A. D' Alessio, Evidence of fluorescent carbon nanoparticles produced in premixed flames by time–resolved fluorescence polarization anisotropy, Combust. Flame 151 (2007) 472–481.

[267] F. Ossler, T. Metz, M. Alden, Picosecond laser–induced fluorescence from gas–phase polycyclic aromatic hydrocarbons at elevated temperatures. I. Cell measurements, Appl. Phys. B 72 (2001) 465–478.

[268] S. Bejaoui, X. Mercier, P. Desgroux, E. Therssen, Laser induced fluorescence spectroscopy of aromatic species produced in atmospheric sooting flames using UV and visible excitation wavelengths, Combust. Flame 161 (2014) 2479–2491.

[269] Z. Chi, B. M. Cullum, D. L. Stokes, J. Mobley, G. H. Miller, M. R. Hajaligol, T. Vo–Dinh, Laser-induced fluorescence studies of polycyclic aromatic hydrocarbons (PAH) vapors at high temperatures, Spectrochimica Acta Part A: Molecular and Biomolecular Spectroscopy 57 (2001) 1377–1384.

[270] R. K. Hanson, R. M. Spearrin, C. S. Goldenstein, Spectroscopy and optical diagnostics for gases. 2016: Springer.

[271] M. Tamura, P. A. Berg, J. E. Harrington, J. Luque, J. B. Jeffries, G. P. Smith, D. R. Crosley, Collisional quenching of CH(A), OH(A), and NO(A) in low pressure hydrocarbon flames. Combust. Flame 114 (1998) 502–514.

[272] F. Beretta, V. Cincotti, A. D' Alessio, P. Menna, Ultraviolet and visible fluorescence in the fuel pyrolysis regions of gaseous diffusion flames, Combust. Flame 61 (1985) 211–218.

[273] I. Berlman, Handbook of florescence spectra of aromatic molecules, 2nd ed. New York: Academic Press; 1971.

[274] LaVision, Davis 8.1 Software, Product Manual 1003001.

[275] P. Saisirirat, F. Foucher, S. Chanchaona, C. M. Rousselle, Spectroscopic Measurements of Low–Temperature Heat Release for Homogeneous Combustion Compression Ignition (HCCI) n–heptane/Alcohol Mixture Combustion, Energy Fuels 24 (2010) 5404–5409.

[276] S. H. Won, S. Dooley, F. L. Dryer, Y. Ju, Kinetic effects of aromatic molecular structures on diffusion flame extinction, Proc. Combust. Inst. 33 (2011) 1163–1170.

[277] P. Zhang, Y. Kang, Z. Wu,, X. Lu, Q. Wang, L. Mei, Effect of dimethyl ether addition on soot formation dynamics of ethylene opposed–flow diffusion flames, Ind. Eng. Chem. Res. 58 (2019) 8370–8386.

[278] B. Zhou, C. Brackmann, Z. Li, M. Alden, X. S. Bai, Simultaneous multi–species and temperature visualization of premixed flames in the distributed reaction zone regime, Proc. Combust. Inst. 35 (2015) 1409–1416.

[279] Y. C. Chen, N. Peters, G. A. Schneemann, The detailed flame structure of highly stretched turbulent premixed Methane-Air flames, Combust. Flame 107 (1996) 223–244.

[280] G. Blanquart, Chemical and statistical soot modelling, Ph. D. thesis, Stanford University, 2008.

[281] A. Gomez, G. Sidebotham, I. Glassman, Sooting behavior in temperature-controlled laminar diffusion flames. Combust. Flame 58 (1984) 45–57.

[282] K. Dewa, K. I. Ono, A. Watanabe, K. Takahashi, Y. Matsukawa, Y. Saito, Y. Matsushita, H. Aoki, K. Era, T. Aoki, T. Yamaguchi, Evolution of size distribution and morphology of carbon nanoparticles during ethylene pyrolysis, Combust. Flame 163 (2016) 115–121.

[283] H. F. Calcote, Mechanisms of soot nucleation in flames–a critical review, Combust. Flame 42 (1981) 215–242.

[284] A. Ergut, Y. A. Levendis, H. Richter, J. B. Howard, J. Carlson, The effect of equivalence ratio on the soot onset chemistry in one-dimensional, atmospheric–pressure, premixed ethylbenzene flames, Combust. Flame 151 (2007) 173–195.

[285] C. Duwig, B. Li, Z. S. Li, M. Alden, High resolution imaging of flameless and distributed turbulent combustion, Combust. Flame 159 (2012) 306–316.

[286] Y. Minamoto, N. Swaminathan, Scalar gradient behaviour in MILD combustion, Combust. Flame 161 (2014) 1063–1075.

[287] A. E. Bakali, D. Boufflers, C. Betrancourt, P. Desgroux, Experimental and numerical investigation of atmospheric laminar premixed n–butane flames in sooting conditions, Fuel 211 (2018) 548–565.

[288] T. Hulek, R. P. Lindstedt, Computations of steady–state and transient premixed turbulent flames using pdf methods, Combust. Flame 104 (1996) 481–504.

[289] D. C. Haworth, M. C. Drake, S. B. Pope, R. J. Blint, The importance of time–dependent flame structures in stretched laminar flamelet models for turbulent jet diffusion flames, Proc. Combust. Inst. 22 (1989) 589–97.

[290] J. H. Kent, D. Honnery, Prediction of particulates in turbulent diffusion flames by conditional moment closure, Combust. Sci. Technol. 54 (1987) 33–397.

[291] P. Lobo, D. E. Hagen, P. D. Whitefield, D. J. Alofs, Physical characterization of aerosol emissions from a commercial gas turbine engine, J. Propul. Power. 23 (2007) 919–929.

[292] H. W. Wong, Z. Yu, M. T. Timko, S. C. Herndon, E. R. Blanco, R. C. Miake–Lye, R. P. Howard, Design parameters for an aircraft engine exit plane particle sampling system, J. Eng. Gas. Turb. Power. 133 (2010) 021501–1.

[293] C. Giorio, C. Bortolini, I. Kourtchev, A. Tapparo, S. Bogialli, M. Kalberer, Direct target and non–target analysis of urban aerosol sample extracts using atmospheric pressure photoionisation high–resolution mass spectrometry, Chemosphere 224 (2019) 786–795.

[294] K. O. Johansson, J. Zador, P. Elvati, M. F. Campbell, P. E. Schrader, N. K. Richards–Henderson, K. R. Wilson, A. Violi, H. A. Michelsen, Critical assessment of photoionization efficiency measurements for characterization of soot-precursor species, J. Phys. Chem. A 121 (2017) 4475–4485.

[295] G. R. Salazar–Banda, M. A. Felicetti, J. A. S. Goncalves, J. R. Coury, M. L. Aguiar, Determination of the adhesion force between particles and a flat surface, using the centrifuge technique, Powder. Technol. 173 (2007) 107–117.

[296] K. A. Anderson, M. J. Szelewski, G. Wilson, B. D. Quimby, P. D. Hoffman, Modified ion source triple quadrupole mass spectrometer gas chromatograph for polycyclic aromatic hydrocarbon analyses, J. Chromatogr. A. 1419 (2015) 89–98.

[297] A. Mueller, N. Ulrich, J. Hollmann, C. E. Z. Sanchez, U. E. Rolle–Kampczyk, M. V. Bergen, Characterization of a multianalyte GC–MS/MS procedure for detecting and quantifying polycyclic aromatic hydrocarbons (PAHs) and PAH derivatives from air particulate matter for an improved risk assessment, Environ. Pollut. 255 (2019) 112967.

[298] A. J. Bergmann, G. L. Points, R. P. Scott, G. Wilson, K. A. Anderson, Development of quantitative screen for 1550 chemicals with GC–MS, Anal. Bioanal. Chem. 410 (2018) 3101–3110.

[299] K. H. Homann, Angewandte Chemie International Edition, 37 (1998) 2434–2451.

[300] B. Oktem, M. P. Tolocka, B. Zhao, H. Wang, M. V. Johnston, Chemical species associated with the early stage of soot growth in a laminar premixed ethylene–oxygen–argon flame, Combust. Flame 142 (2005) 364–373.

[301] M. Panariello, B. Apicella, M. Armenante, A. Bruno, A. Ciajolo, N. Spinelli, Analysis of polycyclic aromatic hydrocarbon sequences in a premixed laminar flame by on–line time–of-flight mass spectrometry. Rapid. Commun. Mass. Spectr. 22 (2008) 573–581.

[302] P. Liu, H. Lin, Y. Yang, C. Shao, B. Guan, Z. Huang, Investigating the role of CH_2 radicals in the HACA mechanism. J. Phys. Chem. A. 119 (2015) 3261–3268.

[303] G. D. Falco, I. E. Helou, P. M. de Oliveira, M. Sirignano, R. Yuan, A. D' Anna, E. Mastorakos, Soot particle size distribution measurements in a turbulent ethylene swirl flame, In press, Proc. Comb. Inst. 38 (2020).

[304] M. Kazemimanesh, R. Dastanpour, A. Baldelli, A. Moallemi, K. A. Thomson, M. A. Jefferson, M. R. Johnson, S. N. Rogak, J. S. Olfert, Size, effective density, morphology, and nano-structure of soot particles generated from buoyant turbulent diffusion flames, J. Aerosol Sci. 132 (2019) 22–31.

[305] U. Trivanovica, T. A. Sipkens, M. Kazemimanesh, A. Baldelli, A. M. Jefferson, B. M. Conrad, M. R. Johnson, J. C. Corbin, J. S. Olfert, S. N. Rogak, Morphology and size of soot from gas flares as a function of fuel and water addition, Fuel 279 (2020) 118478.

[306] C. C. Wey, B. E. Anderson, C. Hudgins, C. Wey, X. Li-Jones, E. Winstead, L. K. Thornhill, P. Lobo, D. Hagen, P. Whitefield, P. E. Yelvington, S. C. Herndon, T. B. Onasch, R. C. Miake–Lye, J. Wormhoudt, W. B. Knighton, R. Howard, D. Bryant, E. Corporan, C. Moses, D. Holve, W. Dodds, 2006, Aircraft particle emission experiment APEX, NASA Technical Report No. NASA/TM-2006–214382.

[307] B. Sarangia, S. G. Aggarwala, P. K. Gupta, Performance check of particle size standards within and after shelf–life using differential mobility analyzer, J. Aerosol Sci. 103 (2017) 24–37.

[308] H. Mai, R. C. Flagan, Scanning DMA data analysis I. classification transfer function, Aerosol Sci. Technol. 52 (2018) 1382–1399.